PRECIPITATION IN AN AUSTENITIC STEEL CONTAINING NIOBIUM AND NITROGEN

by

Marilene Carvalho

Clare Hall

Cambridge

A dissertation submitted for the degree of

Doctor of Philosophy in the University of Cambridge

March 1985

Dedicated to my parents

Preface

This dissertation, which is submitted for the degree of Doctor of Philosophy in the University of Cambridge, describes research work carried out in the Department of Metallurgy and Materials Science under the supervision of Professor R.W.K. Honeycombe between October 1980 and April 1984. Except where due acknowledgement is made to previous work, this work is to the best of my knowledge original and has been performed without collaboration. No part of this dissertation has been or is currently being submitted for any other qualification at this or any other university. This dissertation contains less than sixty thousand words.

M. Carvalho

March 1985

Summary

The precipitation behaviour of a commercial austenitic stainless steel, REX 734, containing large additions of nitrogen and niobium, has been investigated. The stability of the steel was examined with respect to the formation of various carbide, nitride and intermetallic phases, during ageing treatment and under welding conditions.

The relevant published work on precipitation in austenitic stainless steels and welding joints is reviewed and the experimental techniques used are described.

After solution treatment at 1300°C, six different phases precipitated in the steel during ageing between 600-1000°C: Z phase, $M_{23}C_6$, χ phase, σ phase, Cr_2N and ϕ phase. The structures, morphology and composition of the precipitating phases were determined and the precipitation sequences established. Z phase was the first formed phase at all ageing temperatures and occurred at grain boundaries, twin boundaries and on dislocations in the austenitic matrix. Intragranular Z phase always showed a consistent orientation relationship with the austenitic matrix. The $M_{23}C_6$ carbide precipitation followed that of Z phase and was observed in the temperature range 600-800°C. The high nitrogen content of the steel was found to slow down the $M_{23}C_6$ precipitation. This effect appears to be related to the fact that nitrogen is not soluble in the carbide. χ phase precipitation was detected at higher temperatures and longer ageing times than for $M_{23}C_6$ carbide formation, and was found to be associated with $M_{23}C_6$ particles. The χ phase precipitation was more dominant than that of σ phase which precipitates only at 900°C. Cr_2N precipitation occurred at grain boundaries after long ageing times in the temperature range 800-900°C, usually following the dissolution of $M_{23}C_6$ particles. Finally, a face-centred cubic ϕ phase was observed at 1000°C which formed around Z phase particles.

In the as-welded condition a duplex structure ($\gamma+\delta$) was usually observed in the fusion zones. The δ ferrite, which resulted from segregation during the solidification process, was found to increase in volume fraction with decreasing nitrogen content in the weld deposits when the welding process was changed. The intermetallic χ and σ phases were found to precipitate exclusively at the γ/δ interfaces. The presence of δ ferrite enhanced the precipitation of these intermetallic phases which formed in preference to $M_{23}C_6$ and Cr_2N which were absent in the welds. Precipitation of Z phase was observed on dislocations in the austenitic matrix.

A discussion on the precipitation behaviour of REX 734 is presented and conclusions are drawn from the results obtained. Finally suggestions are made concerning possible future work.

Acknowledgements

I would like to express my gratitude to my supervisor, Professor R.W.K. Honeycombe for the provision of laboratory facilities and for his advice and encouragement throughout the course of the project. I am grateful to Dr A.A. Wells and Dr T.G. Gooch for providing all the materials used in this investigation, and welding services at the Welding Institute. Dr A.J. Bourdillon deserves a special mention for kindly providing me with his expertise and helping me with Electron Energy Loss Spectroscopy (EELS) analysis. I would also like to mention Dr H.K.D.H. Bhadeshia for stimulating discussions and encouragement, and Dr R.A. Ricks with whom I had helpful discussions on electron microscopy techniques in my second year. It is also a pleasure to acknowledge Mr J. Leader's technical assistance.

I would like to thank the Conselho Nacional de Desenvolvimento Cientifico e Tecnologico (CNP_q) and Secretaria de Tecnologia Industrial do Ministerio da Industria e Comercio (STI/MIC) in Brazil for the provision of a scholarship and maintenance grant for the period of this research work. I also wish to thank Miss R. Leach for the English corrections and Miss S. Seal for carefully typing this dissertation.

Finally, I wish to express my deep appreciation to Richard and Katie for their interest in my education and for their loving support. Were it not for their dedicated support abroad, I might not have had the opportunity to pursue this research work.

M. Carvalho

March 1985

Clare Hall

Cambridge

CONTENTS

1. INTRODUCTION

Austenitic stainless steels are used frequently in highly corrosive environments, such as those found in the petrochemical and chemical industries and in marine applications. A major problem often associated with these alloys is that during welding, or slow cooling from high temperatures, or ageing of the material in the temperature range 550-900°C, chromium-rich carbide, $M_{23}C_6$, is found to precipitate[1], reducing the concentration of chromium in the matrix to such an extent that the corrosion resistance of the alloy is reduced. This is particularly true at the grain boundaries, where enhanced precipitation and the resulting chromium depletion can lead to intergranular corrosion. Furthermore, grain boundary precipitation of $M_{23}C_6$ (the M components are metallic atoms, notably chromium) causes room temperature embrittlement, which becomes more pronounced at lower temperatures.

The addition of stabilizing elements, such as Nb or Ti, has been found to be the most effective method of alleviating the problem. The carbides of these elements form, in preference to the chromium carbides, and thereby prevent chromium depletion leading to grain boundary corrosive attack[2].

Alternatively, the carbon content of the alloy can be reduced to a level (~ 0.03 wt %) at which the precipitation of the carbides is no longer a serious problem. Unfortunately, carbon in interstitial solid solution makes an important contribution to the strength of these steels at room temperature,[3] and its removal requires some compositional modifications to compensate for the loss in strength. Carbon also stabilizes austenite and its removal requires an increase in Ni content, or of some other austenite-stabilizing element, to ensure a completely austenitic structure at ambient temperatures.

It is not surprising, therefore, that attention has been increasingly directed towards nitrogen as a potential alloying element in austenitic stainless steels, as nitrogen confers similar benefits to carbon but

without the detrimental effects which accompany the use of carbon.

The earliest work on the development of nitrogen containing austenitic stainless steel was in Germany[4] during World War II, and made use of the austenite-stabilizing characteristic of this element (e.g. as a substitute for Ni). The modern approach involves steels containing at least 8 wt % and usually 10 wt % or more Ni; the purpose of the addition of N is to produce higher strength levels, particularly with respect to proof stress, without increasing the concentration of metallic alloying elements.

Recently a combination of high Cr with N and Nb additions[5,6], in commercial austenitic steels, has been shown to give good weldability, adequate general corrosion resistance and excellent pitting corrosion. Improvements of creep properties in austenitic stainless steels have been achieved by the addition of boron, N and V[7-9] or Ti[9,10] or Nb[8-11].

In addition, nitrogen-rich steels are claimed to be more stable with respect to the formation of embrittling phases such as sigma[12-13], which may form during welding, especially if multi-run techniques are used since the effective time for precipitation is increased in such cases. Recently Tuma[14] showed that the presence of N, even in relatively small amounts (0.1 wt %), reduces precipitation of $M_{23}C_6$ without suppressing it entirely, and also partially modifies the amount of the types of phases precipitated. However, relatively little is known about the nature of precipitation in austenitic stainless steels containing large quantities of nitrogen together with a nitride-forming element other than chromium, and this is particularly the case in welding applications.

The aim of the present project was to investigate the thermal stability of a commercial austenitic stainless steel containing additions of nitrogen and niobium, during ageing as well as under welding conditions, with respect to the formation of various carbides, nitrides and intermetallic phases.

2. CARBIDES AND INTERMETALLIC COMPOUNDS IN AUSTENITIC STAINLESS STEELS

2.1 Introduction

The chemistry of commercial austenitic stainless steels is usually adjusted to meet specific design parameters consistent with service life demands. Austenitic stainless steels are widely used in corrosive environments, often at elevated temperatures. They are also an important group amongst the construction steels because they do not undergo a ductile/brittle transition which causes so many problems in ferritic steels. In order to preserve the face-centred cubic austenite phase at room temperature, and achieve corrosion resistance and adequate mechanical properties, sufficient alloying elements have to be added. Therefore, it would be constructive to make a brief review of the constitution of austenitic stainless steels and precipitation in austenite. In this chapter, consideration will be given to published information regarding the occurrence of common carbides (e.g. $M_{23}C_6$, MC) and intermetallic compounds (e.g. σ, χ, Laves phases) found in alloys related to the base alloy chosen for the experimental work, 21 wt % Cr, 9 wt % Ni.

2.2 Constitution of γ Stainless Steel

The constitution diagrams pertaining directly to the study of iron-base austenitic alloys of technical interest are complex, since at least four components are involved. In practice, predictions regarding the constitution of these alloys must normally be based largely on the information provided by the relevant binary and ternary systems.

The binary iron-chromium equilibrium diagram (Fig 2.1)[15] shows that the largest phase field is the b.c.c substitutional solid solution of chromium in iron, analogous to the α ferrite formed in the Fe-C system. The ferrite is normally referred to as delta ferrite, because in these

steels the phase can have a continuous existence from the melting point to room temperature if the Cr content is high enough. The other phases which occur in the binary Fe-Cr system are austenite (a face-centred cubic, paramagnetic phase) and σ phase (a tetragonal intermetallic phase). The diagram shows that chromium restricts the occurrence of the γ-loop, and this favours the formation of ferrite. Many other common substitutional alloying elements have the same effect as chromium in restricting the formation of γ-iron, causing the γ-area of the diagram to contract, for example. Silicon, molybdenum, aluminium, titanium, vanadium and niobium fall into this category and are known as ferrite stabilizers.

The addition of an interstitial element, carbon (Fig 2.2)[16] or nitrogen (Fig 2.3)[17] , to the binary alloy extends the γ-loop to higher chromium contents, and also widens the (α+γ) phase field up to 0.3 wt % of either C or N. There is little evidence to compare their relative effectiveness, but comparison of the slopes of the lower boundaries of the γ phase fields in the Fe-C and Fe-N binary system[18] suggests that carbon is the more effective austenite-stabilizing element. Both elements are the most effective solid solution strengtheners available.

The other effect of carbon and nitrogen is to introduce carbides and nitrides to the structure, as indicated in Figs 2.2 and 2.3. In the austenitic steels $M_{23}C_6$ is the most significant carbide formed, and it can have a substantial detrimental influence on corrosion resistance. In this respect, nitrogen is more useful as it can reduce[14] the precipitation of $M_{23}C_6$. Moreover, the proof strength of a Cr-Ni austenitic steel at concentrations up to 0.25 wt % N can be nearly doubled[3]. However, the presence of nitrides such as Cr_2N and CrN can also impair the corrosion resistance of austenitic stainless steels containing high nitrogen.

The extent of the sigma-phase field in Fe-Cr-Ni ternary system is reduced by the addition of either carbon or nitrogen[19]. This is probably not because of the effect of these elements on the relative stabilities of the γ and σ phases, but rather because stable compounds are preferentially formed with chromium. In this way the matrix is depleted of chromium and is therefore less liable to form the sigma phase. However, workers such as Weiss and Stickler[20] have proposed that "less stable" chromium-rich

phases may act as favourable nucleation sites for σ phase precipitation in austenitic stainless steels. The authors have provided evidence for the nucleation of σ phase at $M_{23}C_6$ particles which were in the process of dissolving.

The important substitutional alloying elements in steel which extend the γ field are nickel and manganese (Fig 2.4)[17]. When sufficient alloying element is added, it is possible to preserve the face-centred cubic austenite at room temperature, either in a stable or metastable condition. In practice the equilibrium state is difficult to attain in the low temperature range since the rate of diffusion is quite low. Under normal cooling rates insufficient time is allowed for this equilibrium to be attained, and a marked hysteresis between the transformation temperatures on heating and cooling may be seen in the iron-nickel transformation diagram (Fig 2.5)[21]. This means that, at a temperature of, say, 500°C, there is a range of compositions, approximately 9-19 wt % of Ni, in which the transformation does not proceed in either direction. It is this temperature hysteresis effect which is the basis of the austenitic class of stainless steels, since it allows the production of such steels with less austenite stabilizer than would be predicted from the equilibrium phase diagram.

As the most common alloying additions to the stainless steel have ferrite forming tendencies (except Mn, C and N), the nickel content is usually increased to compensate for it. This explains why the low C grades of austenitic steel tend to have quite a high level of nickel. Although manganese expands the γ-loop and could, therefore, be used instead of nickel, it is not as strong as a γ-former being only about half as effective, so higher concentrations would be required.

Thus, although the austenitic steels are based upon the Fe-Cr-Ni ternary system, in more exacting service conditions, e.g. at elevated temperatures, in corrosive environments and for welded structures, additional chemistry adjustments are often necessary to surmount the inherent instability of some grades of austenitic steels.

Molybdenum is frequently added to austenitic stainless steels to enhance the corrosion resistance and elevated temperature strength of the steel. An example of the use of Mo in this class of steel is AISI type 316 alloy, which contains about 2 wt % Mo. However, molybdenum is a ferrite stabilizer and so significant adjustments to the chromium and nickel levels are needed to compensate for the molybdenum additions, to ensure that the structure remains wholly austenitic.

The effect of various elements on the basic structure of chromium-nickel stainless steels is often reported as "Cr equivalents" if the elements stabilize ferrite and "Ni equivalent" if they stabilize austenite, as follows, in wt %[22]

$$\text{Cr equivalent} = \text{Cr} + 2(\text{Si}) + 1.5(\text{Mo}) + 5(\text{V}) + 5.5(\text{Al}) + 1.75(\text{Nb}) + 1.5(\text{Ti}) + 0.75(\text{W})$$

$$\text{Ni equivalent} = \text{Ni} + \text{Co} + 0.5(\text{Mn}) + 0.3(\text{Cu}) + 30(\text{C}) + 25(\text{N})$$

Similar equations have been applied in the form of the Schaeffler diagram[23], as in Fig 2.6. Although originally intended for use with air-cooled weld deposits - where it is frequently important to predict the structure in order to avoid weld defects and excessive localized corrosive attack - this diagram can be employed to estimate the phases that will be present in stainless steels when compositions are changed.

Many of the lesser alloyed austenitic steels could more properly be termed metastable austenitic. These leaner face-centred cubic austenites tend to transform to martensite, either by cold working or by cooling to below room temperature. Two of the common martensitic products in stainless steels are the body-centred cubic α-martensite and the hexagonal closed packed ε-martensite. These martensites are different from the distorted tetragonal structure found in the Fe-C system. While such martensites are of interest in the development of very high strength stainless steels their appearance in the truly austenitic stainless steel is usually avoided because of their deleterious effects on ductility[22].

2.3 Precipitation of Carbides in Austenite

As we have seen in the previous section, the addition of carbon to the binary alloy Fe-Cr not only expands the γ-loop but also introduces carbides to the structure. The solubility of carbon in Cr-Ni stainless steels is around 0.08 wt % at 1100°C falling to 0.02 wt % at 800°C, and substantially less at 600°C. This means that even steels with very low carbon contents (around 0.03 wt %) will tend to precipitate carbides.

The most significant carbides formed in these steels are the $M_{23}C_6$ and MC carbides. The latter arises on addition of strong carbide-forming elements such as Nb or Ti to the steel. This will result in the preferential formation of their respective carbides NbC or TiC, and will therefore remove the carbon from solid solution and so prevent $M_{23}C_6$ formation, which has the effect of reducing the corrosion of the alloy.

2.3.1 $M_{23}C_6$

The $M_{23}C_6$ type carbides have been found for chromium and manganese. The structure is complex cubic containing 92 metal atoms of Cr or Mn and 29 carbon atoms per unit cell, with a lattice parameter of about 10.60 Å. The chromium-rich carbide which forms in high chromium ferritic steels and in chromium nickel austenitic steels will tend to precipitate after appropriate treatment, e.g. solution treatment at 1100°C followed by ageing between 550-900°C. Other metallic atoms, notably Fe, Mo, Ni, W and Mn, can replace Cr atoms to varying degrees in the $Cr_{23}C_6$ lattice. In Table 2.1 are listed the composition and lattice parameter of $M_{23}C_6$ which have been reported to occur in austenitic stainless steels.

In the early stages of precipitation $M_{23}C_6$ nucleates at grain boundaries as discrete angular particles, and often as complex dendritic arrays which form initially at boundary intersections. The most frequently occurring form of grain boundary precipitate is discontinuous[27-29], where individual precipitate particles only form at the advancing interface with the required diffusion of solute taking place along the grain boundary. The $M_{23}C_6$ carbide also nucleates on non-coherent twin boundaries at approximately the same time as it does on

Table 2.1 Crystal structure and compositions of $M_{23}C_6$ in aged Type 316L and 316 austenitic stainless steels.

PHASE	SYSTEM	LATTICE PARAMETER IN A, (a)	COMPOSITION	LITERATURE REF.
$M_{23}C_6$	f.c.c.	10.680	$(Cr_{17}Fe_{4.5}Mo_{1.5})C_6$	(24)
		10.638	$(FeCr)_{23}C_6$; $Cr_{23}C_6$	(25)(26)
		10.569 to 10.676	$(Cr_{16}Fe_5Mo_2)C_6$	(20)

grain boundaries, whereas it does not normally form on coherent twin boundaries[30]. However, under the influence of quenching stresses or by deliberate deformation at room or elevated temperature, dislocations which move to the coherent twin boundaries provide sites for nucleation of $M_{23}C_6$[27]. The particles have been reported to have a parallel cube-cube orientation relationship with one of the neighbouring austenite grains and the edges which develop on one side of the particle (growing into the non cube-cube austenite grain) are parallel to {111} planes[27,31-33]. On the basis of the matching of the atom planes, Lewis and Hattersley[27] and Beckitt and Clark[32] showed that mismatch is minimal between the two lattices on {111} planes. In agreement with this consideration, precipitate/matrix interfaces on those planes have been reported for dislocation nucleated precipitates[27,32].

The heterogeneous precipitation of the complex $M_{23}C_6$ also occurs intragranularly on dislocations[27,32] and as matrix-dot particles[34]. Lewis and Hattersley and Beckitt and Clark have studied the process of carbide formation involving nucleation of $M_{23}C_6$ on dislocations, which form during the quench, or are generated by the prismatic punching mechanism around growing particles to relieve stresses arising from the differential thermal expansion of particle and matrix. This results in the formation of stringers of particles having <110> matrix axis. Both lattices, precipitate and matrix, have cubic symmetry and differ in lattice

parameter approximately by a factor of 3. Electron diffraction evidence invariably shows a cube-cube orientation relationship between the two phases:

$$\{100\}\ M_{23}C_6\ //\ \{100\}\ \gamma$$
$$\langle 010\rangle\ M_{23}C_6\ //\ \langle 010\rangle\ \gamma$$

$M_{23}C_6$ particles usually appear to be geometric in shape with {111} planar interfaces which are explained in terms of the similarity in atomic configuration between planes parallel to {111} $M_{23}C_6$ and that of {111} γ, there being only a minor difference in atomic population together with an average mismatch of only 1.3% parallel to the plane[27].

Singhal and Martin[34] have shown that $M_{23}C_6$ carbide precipitation also occurs within the grains in the absence of dislocations as dot-like particles showing strain field contrast. It was suggested that vacancies play an important role in the formation of the dot-like particles, since regions near the grain boundaries are free of these precipitates. On subsequent ageing the particles grow rapidly along <110> directions leading to the formation of a Widmanstätten precipitate structure with {111} planes interface. The orientation relationship is the same as for the dislocation nucleated particles.

Two other morphological forms of intragranular $M_{23}C_6$ carbides, triangular and rhombohedral, have been noted by Colclough[35]. They appear to nucleate independently of any other feature, but there has been no discussion on their nucleation, growth and morphology. In the case of triangular-section particles, the sides of the triangle are parallel to the austenite slip band traces which indicates they are {111} type faces. The angular rhombohedral-shaped particles were seen only occasionally at ageing temperatures below 900°C. Similar observations have been reported by White and Le May[36] in stainless steel AISI type 310, aged at 825°C for 100 hrs.

2.3.2 MC

The addition of strong carbide-forming elements, such as Nb or Ti, largely reduces or eliminates the formation of $M_{23}C_6$. The carbides of these elements form in preference to the chromium-rich carbides and thus

prevent the chromium depletion effect which leads to corrosive attack. Furthermore, by appropriate heat treatments, very fine dispersions of these more stable carbides can be obtained which contribute substantially to the strength of the steel, particularly at elevated temperatures.

The amount of the stabilizing element added to the steel is in excess of that required by simple stoichiometric factors because: (i) any nitrogen in solution would form nitrides or carbo-nitrides with the stabilizing elements, thereby reducing the overall effect of the carbon getter; (ii) niobium and titanium may also precipitate as other phases e.g. Lave phase Fe_2Nb, Fe_2Ti, which would again reduce the effectiveness of the stabilizing-element addition.

The solubility of NbC, TiC and VC is sufficient in austenite at 1100-1300°C to allow their redistribution by solution treatment in this range, followed by quenching, then ageing in the range 650-850°C. The carbide structure is face-centred cubic of the NaCl crystal type and the lattice parameter will change with variations in carbon or nitrogen contents. They exist over a range of stoichiometric $MC_{0.6}$-$MC_{1.0}$, Table 2.2. The modes of precipitation so far observed are as follows: grain boundary; dislocations; stacking faults; matrix. The relative predominance of the different modes of precipitation depends on several factors, which differ as the heat treatments and compositions of the steels are modified, and the compositions of the carbide phases changed.

Table 2.2 (After Goldschmidt)[25]. Lattice parameters of NaCl-type carbides found in austenite

NOMINAL COMP	RANGE OF STOICHIOMETRY	RANGE OF LATTICE PARAMETER A, (a)	% DIFF. in a. from austenite
VC	$VC_{0.75}$ - $VC_{0.96}$	4.1360 - 4.1820	16.5
TiC	$TiC_{0.61}$ - $TiC_{1.0}$	4.3127 - 4.3280	20.6
TaC	$TaC_{0.7}$ - $TaC_{0.99}$	4.4100 - 4.4555	24.1
NbC	$NbC_{0.77}$ - $NbC_{0.99}$	4.4318 - 4.4707	24.5
HfC	$HfC_{0.51}$ - $HfC_{1.0}$	4.6190 - 4.6430	29.3
ZrC	$ZrC_{0.55}$ - $ZrC_{0.95}$	4.6910 - 4.6983	30.9

The grain boundary precipitation of MC carbides usually occurs at a later stage than that of $M_{23}C_6$ as a result of the more rapid diffusion of chromium in austenite at low ageing temperature. However, after a long time at 800°C and above there will be a tendency for the chromium-rich carbides to dissolve[37] and be replaced by the MC carbides.

Nucleation of MC precipitates on dislocations is extensive in austenitic stainless steels. The relationship between precipitate and matrix has been found for several of the MC carbides e.g. NbC, TiC and VC, and is shown to be of cube-cube type:

$$\{111\}\ MC\ //\ \{111\}\ \gamma,\ \langle 1\bar{1}0\rangle\ MC\ //\langle 1\bar{1}0\rangle\gamma.$$

Because of this precise relationship it is assumed that all the MC particles in the early stages of growth are likely to be coherent with the austenite. Since all the MC carbide room temperature lattice parameters are substantially greater than those of austenite (from about 16% in the case of VC to 25% in the case of Nb, (Table 2.2)) a flux of vacancies into the precipitates is needed to reduce the local internal stresses resulting from the growth of the carbide. This is mainly provided by the climb process of dislocations which is most efficient if it occurs on {110} planes. In the process of climbing the dislocations act repeatedly as nucleation sites for further precipitation, resulting in sheets of fine precipitates[38].

Stacking fault precipitation has been found with most of the MC carbides, NbC[39,40], TiC[39,41], VC[38,42], TaC[43], as thin discs in Cr-Ni austenites. These discs lie on {111} planes and all four variants are normally observed, forming a pseudo-Widmanstätten structure. The stacking fault forms by the basic dislocation reaction[44]: $a/2\ \langle 110\rangle \rightarrow a/3\ \langle 111\rangle + a/6\ \langle 11\bar{2}\rangle$ and extents by the climb of Frank dislocations, providing a flux of vacancies which are available to the precipitate. The particles nucleate on the $a/3\ \langle 111\rangle$ dislocation and accept vacancies to lower the internal stresses; as a result the stacking fault grows, eventually escapes from the particles, and is again free to provide new nucleation sites. This stacking fault precipitation can occur side by side with normal nucleation on undissociated dislocation.

The random matrix precipitation is the rarest to be encountered, but it has been observed in Nb[45] and V containing steels[38,41,42,46] where the fine MC particles still have the same cube/cube orientation relationship, though they are not nucleated on dislocations. The nucleation of these particles is apparently related to the formation of vacancies[41] since it occurs after high ageing temperatures and rapid quenching - high vacancy supersaturation in the austenite matrix.

2.4 Intermetallic Precipitation in Austenite

The large number of intermetallic compounds which exist in transition metal systems is reduced considerably if attention is restricted to the phases which have been observed in austenitic stainless steels, and this subject has been reviewed by Decker and Floreen[47]. These intermetallic compounds are mainly σ phase, χ phase, Laves phase, γ', η phase, β phase and G phase. In the present work consideration will be given to the phases which are more likely to form in low carbon austenitic stainless steels related to the base alloy chosen for the experimental work, 21Cr 9Ni (wt %). The phases are σ phase, χ phase and Laves phase, the latter occurring when additions of Ti or Nb (in excess of that needed to combine with the carbon) or Mo are made to the steel. In Table 2.3 are listed the compositions and lattice parameters of σ, χ and Laves phase which have been reported to occur in low carbon austenitic stainless steels. Precise factors which determine the occurrence of the intermetallic phases are complex, but may include such factors as electron/atom ratios, atomic size factors and co-ordination numbers. The situation in which these phases precipitate is further complicated by the fact that they rarely form singly so that competition for the main atomic species also becomes an important factor.

2.4.1 σ Phase

This phase appears to be the most investigated intermetallic phase in austenitic stainless steels because of its adverse effect on mechanical properties. It was first reported by Bain and Griffiths[53] and later has received adequate review by Hall and Algie[48]. The phase is tetragonal in

Table 2.3 Crystal structure and compositions of intermetallic phases in low carbon austenitic stainless steels

PHASE	SYSTEM	LATTICE PARAMETERS in Å		c/a	COMPOSITION	LITERATURE REF.
		a	c			
Sigma (σ)	tetragonal	8.799	4.544	0.516	FeCr	(48)
		9.188	4.812	0.523	FeMo; Fe(CrMo)	(48)
		8.883	4.599	0.517	$(FeNi)_x(CrMo)_y$	(20)
Chi (χ)	b.c.c	8.920			$Fe_{36}Cr_{12}Mo_{10}$	(49)(50)
		8.862			$(FeNi)_{36}Cr_{18}Mo_4$	(24)
Laves (η)	hexagonal	4.744	7.725	1.628	Fe_2Mo	(51)
		4.827	7.866	1.629	Fe_2Nb	(52)

structure with the unit cell containing 30 atoms, and has a variable composition, Table 2.3. There is evidence that the stability of the sigma phase depends on both atomic size and electron configuration. Large differences in atomic size do not favour the formation of this phase, and the size ratios for the known binary sigma phases fall between the limits 0.93-1.15. In the Cr-Ni austenitic steels, σ formation is encouraged by increasing Cr above 17wt%, and is discouraged by an increase in nickel content.

Precipitation of σ phase in fully austenitic stainless steel has been observed at grain boundaries[54,55] and incoherent twin boundaries[55,56], but there is some doubt whether coherent twin boundaries also act as sites for sigma formation[57]. For full development of σ, long term ageing seems essential. In steels containing some ferrite or in which ferrite forms transiently during ageing, σ forms via the ferrite when the interface α/γ boundary presumably provides appropriate high energy nucleation sites[56]. The role of the α/γ interface in the nucleation of σ is particularly clear in the case of duplex stainless steels where the σ phase precipitation kinetics are enhanced[58,59]. The ferrite, being richer in chromium, is preferentially absorbed during the growth of sigma. The addition of

alloying elements such as Mo[60] and Ti[61] achieves a further acceleration of sigma formation.

It has been suggested that $M_{23}C_6$ acts as a nucleus for σ[62,63], but there is also evidence to the contrary[55]. However, more recently, Weiss and Stickler[20] have provided evidence for the nucleation of σ at $M_{23}C_6$ particles which were in the process of dissolving, and also on oxide particles within the austenite grains. The following orientation relationship was frequently observed:

$$\{111\}\ \gamma\ //\ \{001\}\ \sigma,\ \langle 0\bar{1}1\rangle\ \gamma\ //\ \langle 140\rangle\ \sigma,$$

confirming earlier results[64,49].

The effect of cold work on σ phase formation in austenitic stainless steels has been studied extensively[20,35,54,55]. All investigators found that cold work accelerates the formation of σ phase, presumably by increasing diffusion rates, as there is little evidence for the nucleation of σ on dislocations or dislocations pile-ups. However, the increased amounts of σ phase resulting from cold deformation have been associated with the increased amount of lattice defects such as stacking faults or twins, which are the sites of σ phase nucleation[20,65]. Further acceleration is achieved when recrystallization takes place, which provides more boundary area for precipitation[55,66,67].

2.4.2 χ Phase

The χ phase as determined by Kasper[50] has a bcc α-Mn type crystal structure and is believed to be a carbon-dissolving compound[25]. This phase is known to occur in many transition metal systems usually associated with σ phase. In the Fe-Cr-Ni-Mo system, the lattice parameter of the χ phase was reported[50] to be a=8.920 A, corresponding to a composition of $Fe_{36}Cr_{12}Mo_{10}$ (Table 2.3). However, χ phase was found to vary appreciably in composition with a high tolerance for metal interchange and, in the presence of carbon, an amount of molybdenum was reported[25]. The χ phase has been frequently detected in 316 type austenitic steel[20,24,55,68-70], a typical composition being $(Fe,Ni)_{36}Cr_{18}Mo_4$ with a=8.862 A [24]. Weiss and Stickler[20] have shown that

in low carbon steels χ phase formation precedes that of σ, but the formation curves tended to be at higher temperatures and longer times than those for carbide phases. In higher carbon steels, χ and σ precipitate in the same temperature range as $M_{23}C_6$ (650-900°C). Lai and Meshkat[71], studying the precipitation kinetics of χ phase in a 316 type alloy, suggested that the precipitation rate of the phase at 750° and 815°C follows a single relationship of the form $V=fn(t/\tau)$, where V is the volume fraction of the χ phase formed in a time t, and τ is a "characteristic time" which is dependent upon the ageing temperature.

The χ particles nucleate preferentially at grain boundaries, and depletion of the surrounding matrix in molybdenum and chromium has been detected by electron beam microanalysis on a type 316 stainless steel[20]. Nucleation at incoherent twin boundaries has frequently been observed, but only occasionally at coherent twins[20,72]. In the boundaries χ particles were frequently observed in close contact with remnants of $M_{23}C_6$ particles. After ageing for more than 1500 hrs at 815°C, numerous fine, rod-shaped χ phase particles were observed intragranularly. The morphology of the particles ranges from rod-shaped to globular massive particles similar in appearance to σ phase, but can also be found with an acicular morphology[72].

Cold work, as in the case of σ, accelerates the formation of χ phase[20,55,73], but it can be suppressed[67] by early nucleation of σ which competes for the necessary alloying elements (Cr,Mo). In austenitic steels where deformation causes ε-martensite to form, during subsequent ageing, χ precipitates predominantly within the grains on the ε phase[74]. A single orientation relationship has been determined between the austenitic matrix and the precipitate:

$$\{111\}\ \gamma\ //\ \{110\}\ \chi$$
$$\langle 01\bar{1}\rangle\ \gamma\ //\ \langle\bar{1}10\rangle\ \chi$$
$$\langle\bar{2}11\rangle\ \gamma\ //\ \langle 001\rangle\ \chi$$

The χ phase forms as small rods on the matrix planes {110}, {111} and {211}.

2.4.3 Laves Phase

The hexagonal intermetallic Laves phase has been identified in austenitic stainless steels with the formula Fe_2A where A is reported as molybdenum[20,69,75] and as Nb[52,76]; see Table 2.3. The Fe_2Mo variant is commonly a minor constituent in molybdenum-austenitic stainless steels. Frequently it is found to precipitate intragranularly, but only occasionally in grain boundaries. This Laves phase exists at 815°C and below in a range of 18Cr 12Ni (wt %) steels with 2-2.5 wt % Mo, when the precipitate, together with carbide dispersions, contributes to the mechanical strength at elevated temperatures[20].

The Fe_2Nb Laves phase has been reported to occur in the temperature range 750°-950°C in 18Cr-9Ni-2Nb (wt %) steel[76]. Similar results were obtained by Denham and Silcock[52], where the unit cell dimensions of their Laves phase varied according to the level of niobium in the alloy of base composition, 16 wt % Cr, 16 wt % Ni. This work also showed that the Laves phase usually precipitated with an orientation relationship with the austenite matrix, which was:

$$(0001)Fe_2Nb//(111)\gamma \text{ and } (10\bar{1}0)Fe_2Nb//(\bar{1}10)\gamma.$$

The nucleation of the phase was observed to be slow but the growth reaction rapid.

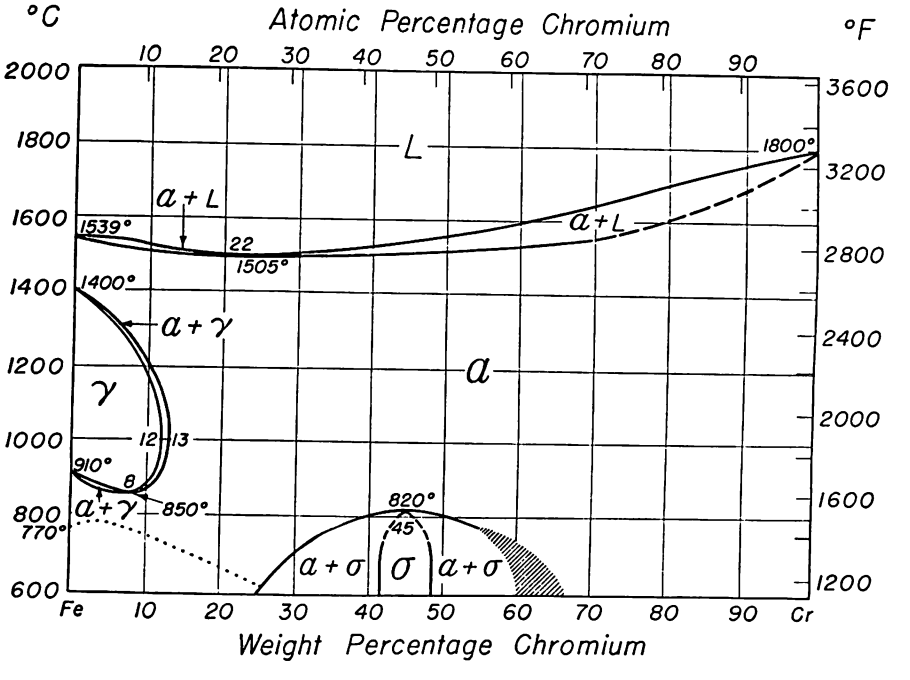

Fig 2.1 The Fe-Cr equilibrium diagram. (Metals Handbook)[15].

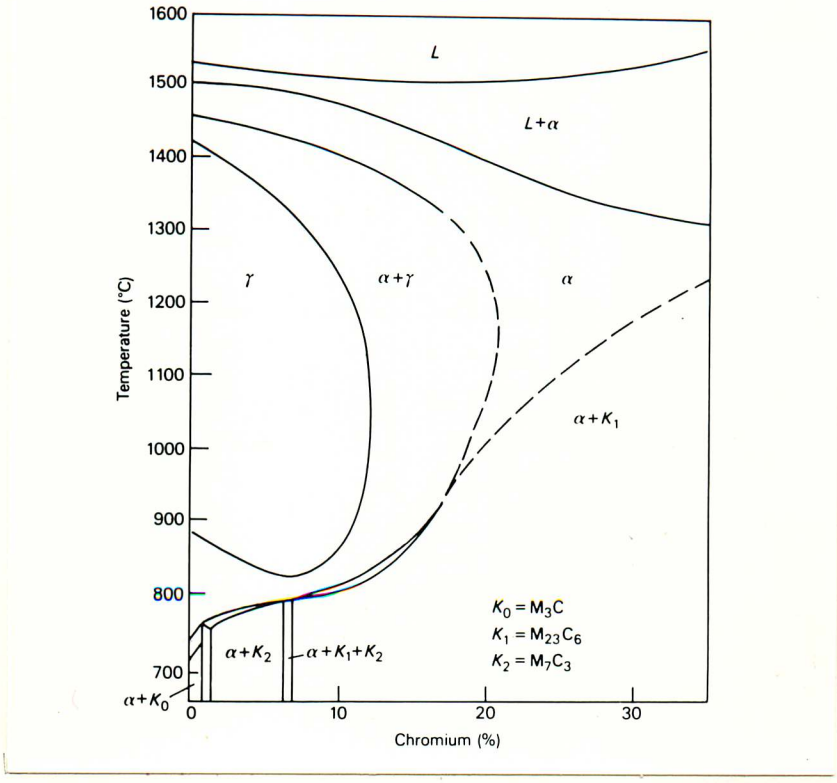

Fig 2.2 Effect of carbon on the Fe-Cr diagram at 0.05 wt % C. (Colombier and Hoffman)[16].

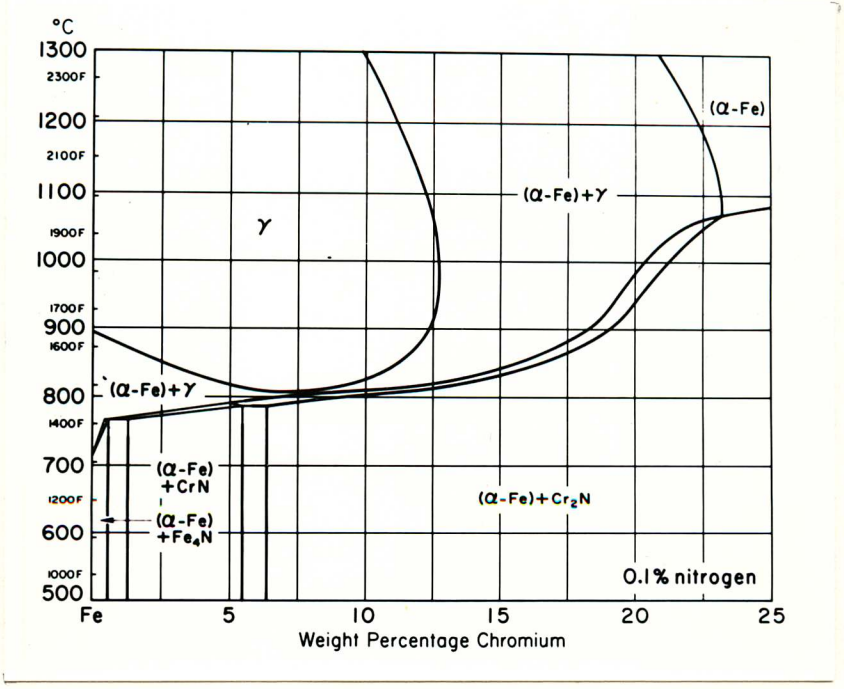

Fig 2.3 Effect of nitrogen on the Fe-Cr diagram at 0.1 wt % N. (Metals Handbook)[17].

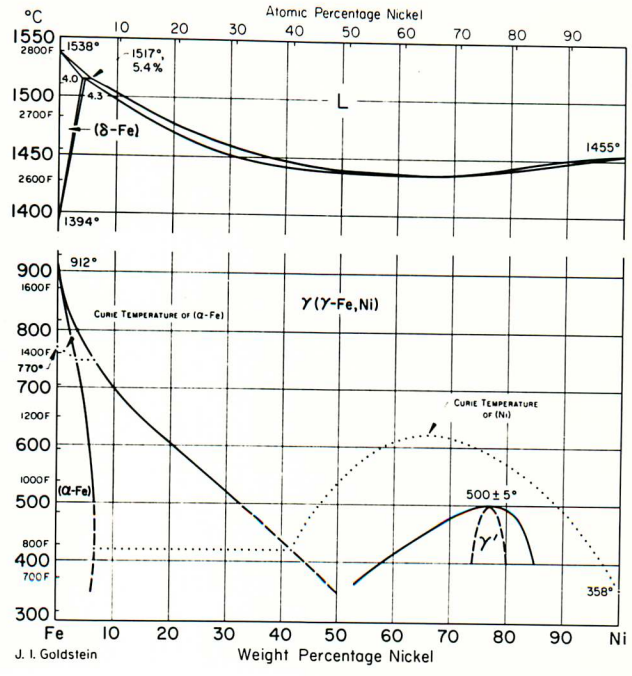

a

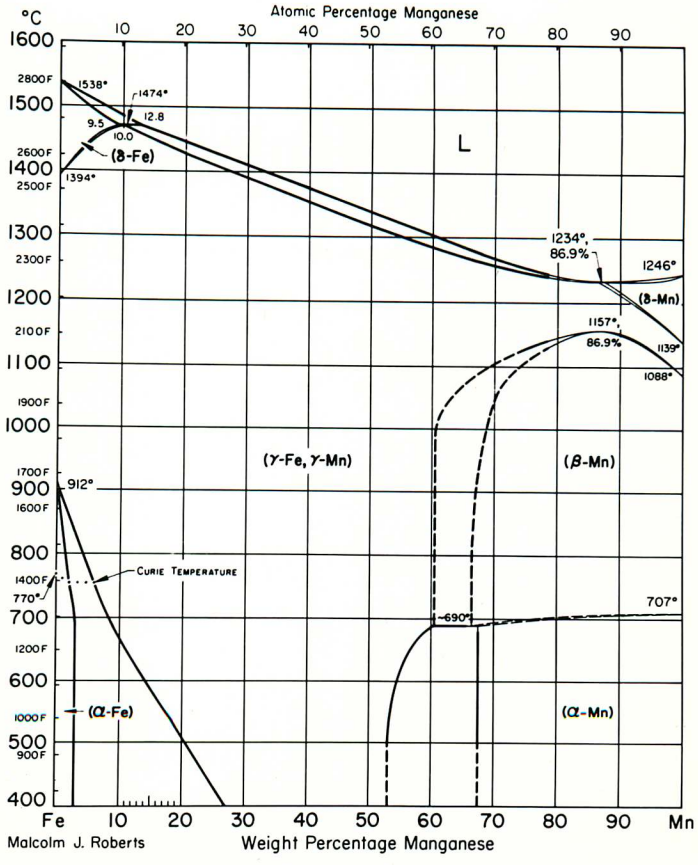

b

Fig 2.4 (a) The Fe-Ni equilibrium diagram. (b) The Fe-Mn equilibrium diagram (Metals Handbook)[17].

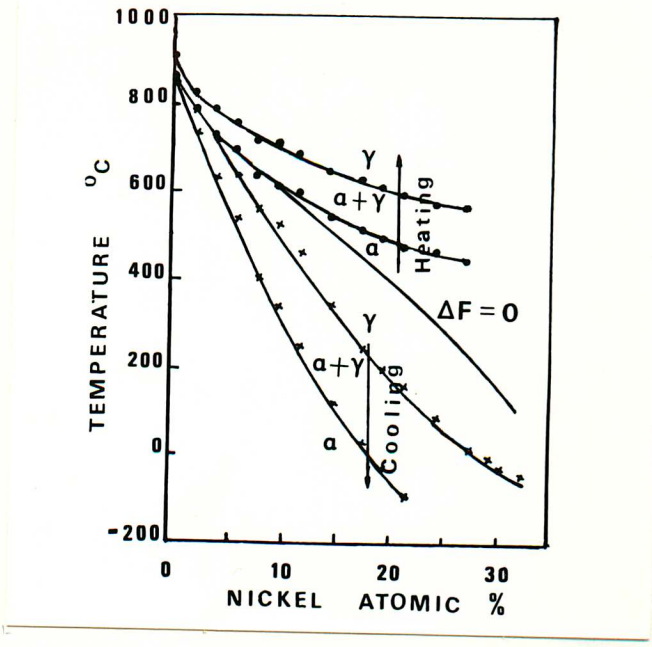

Fig 2.5 Portion of the Fe-Ni phase diagram. (Jones and Pumphrey)[21].

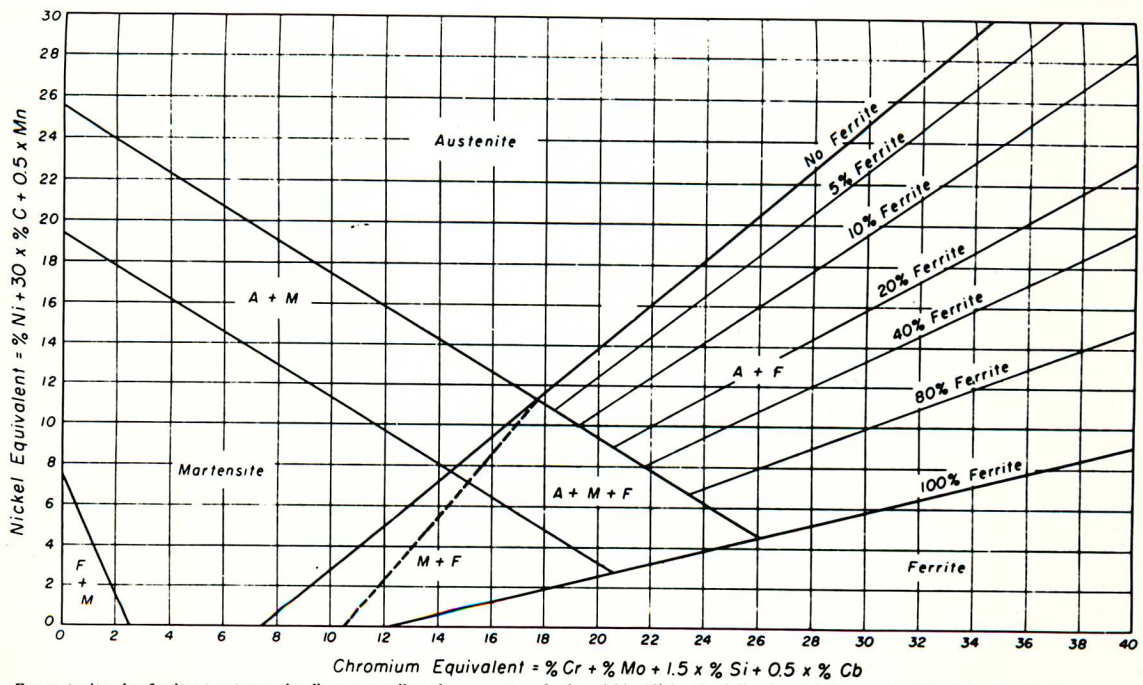

For austenite-plus-ferrite structures, the diagram predicts the percentage ferrite within 4% for the following stainless steels: 308, 309, 309 Cb, 310, 312, 316, 317, 318 (316 Cb), and 347. Dashed line is the martensite/M + F boundary modification by Eberhard Leinhos, "Mechanische Eigenschaften und Gefugeausbildung von mit Chrom und Nickel legiertem Schweissgut," VEB Deutscher Verlag fur Grundstoffindustrie, Leipzig, 1966.

Fig 2.6 Constitution diagram (Schaeffler diagram) for stainless steel weld metal (Metal Progress Data Book)[23]

3. NITRIDES IN AUSTENITIC STAINLESS STEELS

3.1 Introduction

The crystal chemistry and the occurrence of nitrides in steels has received adequate review by Jack and Jack[77], where the characteristics of nitrogen are emphasized and related to the behaviour of carbon. As described in the previous chapters there are several reasons for making additions of nitrogen to stainless steels. The similarities between carbon and nitrogen are well known; however in comparison with carbon the role of nitrogen in stainless steel has been neglected, and insufficient is known about the nucleation, growth and morphology of nitrides in high nitrogen stainless steels.

As we have seen in the previous chapter, the addition of nitrogen to the binary alloy Fe-Cr not only expands the γ-loop but also introduces nitrides to the structure. The maximum solubility of nitrogen in equilibrium with austenite is 2.8 wt % with respect to γ'-Fe_4N for which the corresponding equilibrium pressure of gaseous nitrogen is about 10^4 atm. In Cr-Ni stainless steels the solubility of nitrogen is higher than that of carbon (Fig 3.1)[78], thus providing substantial opportunity for precipitation of nitrides. The most significant nitrides formed in Cr-Ni high nitrogen containing steels are Cr_2N and CrN. Addition of strong nitride-forming elements such as Nb, Ti and V result in the formation of their respective nitrides or possibly ternary nitrides (Table 3.1), in preference to that of Cr_2N and CrN. In this chapter, consideration will be given to the published information regarding the occurrence of nitrides in austenitic stainless steels.

Table 3.1 Nitrides observed in aust ice
parameters data from Ref

PHASE	SYSTEM	STRUCTU TYPE			
Cr_2N	hexagonal	Ni_3N			
CrN	cubic	NaCl(B_1)			
δ"-NbN_{1+x}	cubic	NaCl(B_1)			
TiN_{1-x}	cubic	NaCl(B_1)	4.2259		
V-N ?	tetragonal b.c		2.970	3.395	1.143
V_2N	hexagonal		4.907	4.539	1.081
VN_{1-x}	cubic	NaCl(B_1)	4.1398		
M_6N Cr_3Nb_3N[80]	f.c.c		11.31		
NbCrN[26] (Z-phase)	tetragonal		3.037	7.391	2.434

3.2 Chromium Nitrides: CrN, Cr_2N

In chromium-nickel austenitic stainless steels containing high nitrogen both Cr_2N and CrN can precipitate, but the hexagonal Cr_2N predominates[82] on ageing in the temperature range 650-900°C. The predominance of Cr_2N over CrN can be seen from the Fe-Cr diagram in Fig 2.3 and the phase diagram in Fig 3.2, where in the range of austenitic stainless steel, the equilibrium is between austenite and Cr_2N in the absence of other strong nitride-forming elements. The modes of precipitation of Cr_2N observed in austenitic stainless steels are as follows: grain boundary, twin boundary and matrix. The relative

predominance of the different modes of precipitation appear to depend on several factors, which differ as the heat treatment and composition of the steels are modified.

Nakagawa and Otoguro[83] have studied low carbon (0.02 wt %) steels with 18Cr-12Ni-2Mn (wt %) to which 0.16 and 0.21 wt % N were added. On ageing $M_{23}C_6$ still precipitated at the boundaries, and there was some evidence for the intragranular precipitation of Cr_2N. At higher nitrogen contents (> 0.5 wt % N) ageing at 700°C produced a cellular reaction at the grain boundary[84] giving a lamellar form of Cr_2N, with depletion of the austenite in nitrogen, which as a result transformed partially to martensite on cooling. In chromium-nickel cast stainless steel containing nitrogen, the precipitation of Cr_2N is observed in interdendritic regions[85], where metallic segregation locally increases as the nitrogen content of the alloy increases.

More recent work[86-91] on 25Cr-28Ni-2Mo (wt %) steel with 0.1 wt % carbon and 0.2-0.6 wt % nitrogen has included long term (up to 5000 hrs) ageing treatments in the range 600-900°C. With 0.36 wt % of N in this steel, only intergranular precipitation of Cr_2N occurs on both grain and twin boundaries[87]. Intragranular precipitation of Cr_2N takes place when the nitrogen concentration exceeds 0.45 wt %. The number density of the intragranular Cr_2N precipitates has found to be of the order of $10^{17} m^{-3}$ and the particles are uniformly distributed. At higher nitrogen contents the intragranular precipitation density does not increase significantly. One other characteristic feature of the microstructure of these nitrogen-containing steels is that both perfect and faulted dislocation loops are formed[86]. These loops have a density of about $10^{20} m^{-2}$. However, dislocation loops or other dislocations introduced by deformation were not found to be very favourable sites[89] for the precipitation of Cr_2N. Additions of 0.3 wt % of phosphorus greatly enhanced the intragranular precipitation of Cr_2N, and produced uniform dispersion of this precipitate[91]. Since regions near the grain boundaries are free of this precipitate it was suggested that the nucleation of these particles is related to the formation of vacancies. It appears that phosphorus enhances the clustering of vacancies and prolongs the excess vacancy life time, thereby promoting the aggregation of solute atoms and vacancies

forming the nucleus[45].

Mukherjee and Nijhawan[92] observed Cr_2N precipitation in Cr-Mn-N austenitic steels in the temperature range 500-800°C. They found that the precipitation reactions during ageing were considerably influenced by the carbon and nitrogen contents of the alloy. Cr_2N and $M_{23}C_6$ will form together during ageing depending on the carbon/nitrogen ratio. With C/N ratio below 0.15 only Cr_2N is observed for all temperatures and ageing time up to 1000 hrs; for C/N ratios between 0.15-0.30, Cr_2N and $M_{23}C_6$ are observed at 500°C, while at higher ageing temperatures only Cr_2N is detected. A carbon/nitrogen ratio above 0.3 gives Cr_2N and $M_{23}C_6$ at higher ageing temperatures and $M_{23}C_6$ only at lower ageing temperatures. In agreement with other work[14,37] the results obtained by Mukherjee and Nijhawan[92] indicate that an increase in nitrogen content or high ageing temperatures reduce the precipitation of $M_{23}C_6$. This is due to the fact that at high temperatures and long ageing treatments there will be a tendency for the chromium carbide to dissolve and be replaced by more stable precipitate (e.g. Cr_2N in high nitrogen austenitic steels, Fig 3.2). Furthermore, no evidence has been found for the solubility of nitrogen in the $M_{23}C_6$ carbide.

The exposure of austenitic steels to air at high temperatures (> 600°C) leads to the absorption of high nitrogen concentrations particularly at points where the oxide layer is deficient. For example a nitrogen content of 1.9 wt % has been found under the oxide layer in a 16Cr13Ni (wt %) steel[93] containing 0.7 wt % Nb after creep testing for 30,000 hrs at 700°C. The nitride in this case, Cr_2N, formed a coarse Widmanstätten distribution, although discontinuous precipitation is sometimes observed. Other workers[94] have detected both CrN and Cr_2N. The discontinuous precipitation is attributed to regions of high nitrogen supersaturation often closely associated with cracks in the creep failure zone. Dulis[28] has found that the transition from continuous to discontinuous precipitation is dependent both on ageing temperature and composition. In Cr-Ni-Mn steels the discontinuous reaction is favoured by increasing nitrogen content and high ageing temperatures, whereas continuous precipitation reaction is favoured by increasing carbon content.

Cr_2N is not a common precipitate in the commercial AISI Type 300 series of stainless steels for two reasons: (i) the nitrogen levels tend to be low in these steels so that any subsequent precipitation in the steel will remove the nitrogen from the solution, because the nitrogen would replace some of the carbon in the carbides; (ii) if other strong carbide or nitride forming elements are present in the steel, they will form in preference to that of chromium.

3.3 Nitrides of Stabilizing Elements

There is less information on the precipitation of alloy nitrides other than chromium e.g. VN, NbN, TiN, Z phase, occurring in chromium-nickel austenitic stainless steels. Bungardt et al[95] examined in detail the effect of nitrogen on the properties of 18Cr16Ni (wt %) austenitic steel with and without 3.5 wt % Mo and 0.12 wt % nitrogen. On the addition of 0.5 wt % V, they obtained at all ageing temperatures hexagonal $(CrV)_2N$ isomorphous with Cr_2N. A further addition of 0.1 wt % Nb led to the replacement of this nitride by a phase referred to as Z-phase which they referred to as NbCrN. This has since been verified by later work[80,96] which has shown it to have a tetragonal structure.

Hull and Stickler[97] have reported the precipitation of vanadium nitride, VN_x, during high temperature creep testing of 16Cr 20Ni 10Mn 2.3Mo (wt %) steels containing 0.3-0.6 wt % V and 0.04-0.2 wt % N. The precipitate VN_x has a tetragonal structure with lattice parameter a=2.98 A, c=3.78 A, and occurs as a fine dispersed phase in the austenitic matrix. This precipitation appears to contribute to increases in the rupture and creep strengths, which reach maximum values when 0.12-0.19 wt % N is added to the alloy. In austenitic stainless type steel AISI 316 L, containing 0.12 wt % N, 0.4 wt % V and 0.005 wt % B, improved creep properties have also been achieved[7] by fine precipitation of VN_{1-x} on dislocations. The vanadium nitride particles on dislocation are found to retain their small size after long creep testing times. However, it has been observed that the VN particles coarsen considerably during ageing at 750°C[100]. Thorvaldsson and Dunlop[99] have shown that, in Cr-Ni austenitic stainless steels containing stabilizing additions of V, Nb or Ti with

carbon between 0.02-0.55 wt % and nitrogen between 0.02-0.47 wt %, the MN particles coarsen faster than the equivalent MC. This is due to the higher solubility of nitrides in austenite in the presence of chromium. Previous work[9,100] has indicated that chromium diminishes the activity of both carbon and nitrogen in austenite, therefore increasing its stability. This effect is found to be considerably greater for nitrogen than for carbon. The first precipitation reaction observed in the Cr-Ni austenitic steels studied by Thorvaldsson and Dunlop is that of $M_{23}C_6$ at grain boundaries at 750°C ageing temperature. On further ageing precipitation of VN occurs on dislocations in steels containing V additions and high nitrogen content. These particles were spheroidal and obeyed a similar cube/cube orientation relationship with the austenitic matrix as that of the isomorphous VC.

Borland[80] carried out an investigation of precipitation reactions in 18Cr 12Ni (wt %) austenitic steels containing between 0.02-0.15 wt % N to which Nb, Ti and V were added separately. In the Nb-N alloys the precipitation reactions were complex and showed no less than three nitrides forming on ageing between 700-800°C after solution treatment at 1300°C:

1) NbN, face-centred cubic, a = 4.39 Å
2) M_6N, face-centred cubic, a = 11.31 Å
3) Z-phase, tetragonal, a = 3.037 Å c = 7.391 Å with composition suggested NbCrN

The NbN phase is normally the first precipitate to form, and its morphology follows that of the isomorphous NbC precipitate in so far as it nucleates on grain boundaries, undissociated dislocations, in association with stacking faults and also in the matrix[101]. The M_6N precipitate represented by the formula $(Fe,Cr)_3Nb_3N$ is found to be the most stable form of nitride in the high-Nb alloys (1.2 wt % Nb), and is undissolved after solution treatment at 1300°C. M_6N also precipitates during prolonged ageing when it has been observed as sheets which have replaced the NbN stacking fault precipitate. The crystal sheets of M_6N were observed on {111} planes with a cube-cube relationship with the matrix. The matrix precipitation in the Nb-N alloys was very complex, comprising all three phases: NbN, Z phase and the hexagonal Laves phase, NbM_2, with lattice parameters a=4.85 Å, c=15.86 Å.

In similar alloys containing titanium the isomorphous TiN phase was found, but it appeared to be much less soluble than NbN at 1300°C. On ageing at 700°C and 800°C some precipitate on dislocations was observed, and on prolonged ageing at 800°C, a Laves phase Fe_2Ti made its appearance.

The Z-phase, a mixed niobium-chromium nitride, has been reported[80,95,96] to occur in Nb-N austenitic stainless steels, and full identification of the tetragonal Z-phase unit cell was established by Jack and Jack[102]. Recently, Colclough[35] has given detailed information about the Z-phase precipitation reaction in a commercial austenitic stainless steel, Nitronic 50. In Nitronic 50 steel (0.04% C, 21.5% Cr, 12.5% Ni, 2.2% Mo, 4.9% Mn, 0.18% Nb, 0.18% V and 0.24% N, all in wt %) five phases formed on ageing between 600°-1000°C after solution treatments at 1200°C; Z-phase, σ phase, $M_{23}C_6$, Cr_2N and a b.c.c α' phase. The stable tetragonal Z-phase with composition NbCrN and lattice parameter a=3.03 Å, c=7.37 Å occurs over a temperature range 700°-1000°C. It is the first precipitate to form and nucleates on grain boundaries, twin boundaries, dislocations and matrix. The particles are rounded particles which, on growing, developed into cuboids in the later stages of ageing, and are commonly seen to decorate dislocations in a characteristic "propeller" morphology. In the temperature range (500 -900°C) where the $M_{23}C_6$ and σ phase occur, it is found that they form at grain boundaries around the Z-phase. Frequently, during the rapid process of growth the $M_{23}C_6$ and σ phase particles engulf the small equiaxed Z-phase particles which delineate the position of the original grain boundary. The intragranular Z-phase cuboids are semi-coherent and have a fixed orientation relationship with the matrix:

$$\{001\}\ Z\ \text{phase}\ //\ \{001\}\ \gamma$$
$$\langle 110\rangle\ Z\ \text{phase}\ //\ \langle 100\rangle\ \gamma$$

Colclough[35] has also observed that in Nitronic 50 steel, with varying levels of prior deformation followed by ageing, the precipitation of Z-phase occurs quickly on the deformed substructure and precedes any recrystallization reaction. Once the material has recrystallized, further Z-phase and σ phase precipitation occurs.

The identification of Z phase as a nitride, and its stability in high nitrogen niobium steels, raises the question of its occurrence in low

nitrogen Cr-Nb austenitic stainless steels. Hughes[96] has indicated that a nitrogen content greater than 0.06 wt % is necessary before the phase can be detected in 18Cr 10Ni wt % austenitic stainless steel in the presence of NbC. Although the exact limit of nitrogen content could be argued, the Z phase precipitation has not been observed in niobium austenitic stainless steels containing nitrogen below 0.05 wt %. Furthermore, according to Borland's work[80] it seems likely that the content of niobium in the steel would affect the preferential formation of either niobium binary nitride (NbN) or niobium ternary nitride, Z phase, (CrNbN). A reduction in Nb content (1.2 to 0.6 wt %) in a 18Cr 12Ni (wt %) containing 0.09 wt % N increased the amount of Z phase matrix precipitation and reduced the NbN stacking fault precipitates[80].

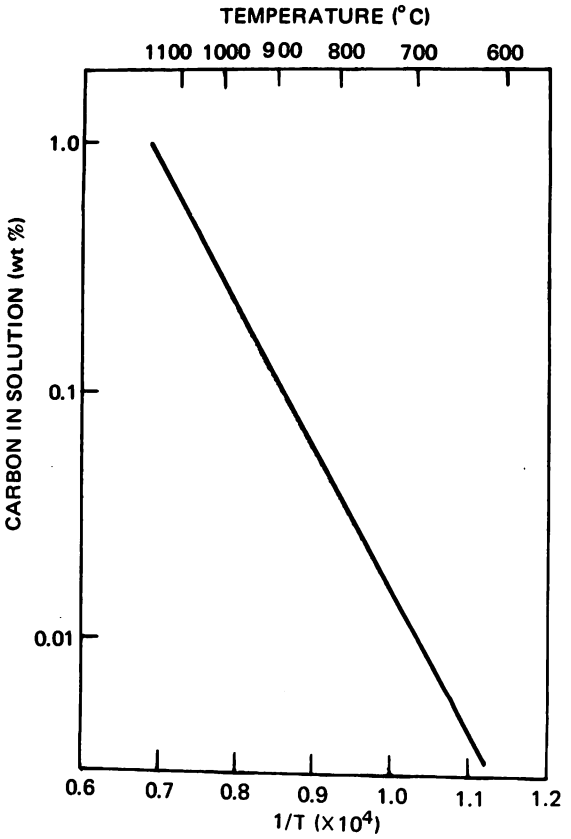

a

	Solid solubility (wt %)	
Temperature (°C)	Type 304	Type 308
838	0.125	0.115
866	0.145	0.132
893	0.177	0.165
927	0.190	–
954	0.258	0.254
982	0.281	0.273
1010	–	0.297

b

Fig 3.1 (a) Approximate solubility of carbon in 18 Cr, 10Ni, Fe (wt %) alloys[78]. (b) Solubility of nitrogen in types 304 and 308 stainless steels[78].

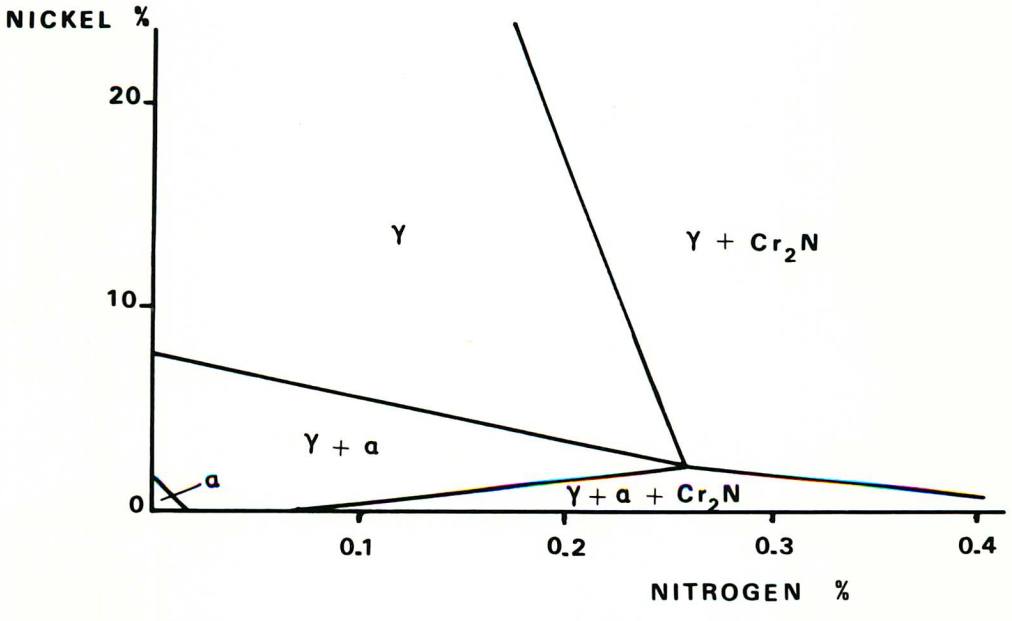

Fig 3.2 Fe-18Cr-Ni-N equilibrium diagram at 900°C. (T. Masumoto and Y. Imai)[81].

4. STRUCTURAL CHANGES DURING WELDING

4.1 Introduction

The structural changes occurring during welding are largely dependent on the alloy composition (plates and filler metal) and on the weld thermal cycle or post-weld heat treatment to which the weldments are subject. Two distinctive zones can be initially identified in welding, the fused zone or weld metal and the heat affected zone. In order to interpret the transformation occurring in the former, attention should be paid to the solidification behaviour of the weld pools which play an important role in the final microstructure of the fused zone; while in the latter, the structure is solely determined by the alloy composition of the plates and the thermal history of the alloy. Therefore, the following section of this chapter presents a concise survey of the basic principles of weld pool solidification to indicate the current state of theory and experiment and to emphasize those areas of particular importance in the study of weld pool solidification. This second section is followed by a review of the phenomenological observations of the solidification behaviour of austenitic stainless steel fusion welds, paying particular attention to the development of duplex structure. Finally a complementary review of Chapter 2 on precipitation behaviour in austenitic stainless steel is applied to weld deposits and the heat affected zone.

4.2 Welding Pool Solidification

4.2.1 Growth Initiation and Development of Grain Structure

During the usual solidification process, the transformation of a liquid phase to a solid normally occurs by a process of nucleation and growth. The creation of solid nuclei and the growth of the solid from

these nuclei can proceed at a finite rate only if the system is undercooled below the equilibrium reaction temperature. In the fusion welding process, however, the nucleation event is not significant since a solid-liquid interface is always present and growth may occur from the partially melted crystals of the parent plate. This process of growth at the fusion boundary generates grains in the weld metal having the same crystallographic orientation as the immediately contiguous parent plate grains across the fusion boundary[103-105]. On this basis it seems that the growth initiation event in the weld pool solidification does not present a significant energy barrier.

In the weld pool the initial growth of partially melted grains from the parent plate is followed by the development of columnar grains in a competitive growth process analogous to that observed in ingot solidification. The columnar grains show a strong preferred orientation which corresponds with the favourable crystallographic direction of the dend ritic growth, i.e. <100> in cubic metals[106]. Solidification usually proceeds along the favourable growth direction oriented most closely to the direction of the maximum thermal gradient in the melt[104,107], e.g. parallel to the direction of the normal to the boundary. Thus, the form of the competitive growth process in a given material is uniquely controlled by the weld pool geometry[103,108,109]. The latter is found to change with variations in welding parameters, e.g. welding speed, welding current.

The overall solidification macrostructure of a weld pool, usually dominated by columnar grains, is determined in general solely by the nature of the competitive growth process between adjacent columnar grains. Columnar-to-equiaxed growth transitions are comparatively rare during welding since generation of nuclei is limited and their survival is difficult under very high temperatures such as those obtained in the liquid during welding. However, at high welding speeds [110,111] and high alloy content[111], equiaxed dendrites have been observed in the region of the centre line of the pool, where solidification rates are highest and the thermal gradients flattest[105], as will be seen later. High welding speeds encourage equiaxed growth because of the overlap of the regions of solute accumulation ahead of the converging solidification fronts at the centre of the tear-shaped pools formed at rapid welding speeds. This

provides a region of the weld pool suited to the growth of fragments (high solute concentration, high solidification rate, temperature gradient give rise to undercooling) ahead of the melt as the weld pool progresses along the parent plate.

4.2.2 Growth Substructures

The solidification substructures, e.g. cellular, cellular dendritic substructures, produced in welds are found to be related to the growth rate and the temperature gradient in the liquid ahead of the growing interface[107]. A steep thermal gradient together with low solidification rates tends to reduce the extent of undercooling ahead of the interface, thus favouring cellular growth. At high solidification rates, together with shallow thermal gradient, the dendritic mode is favoured as the extent of undercooling is increased. The local solidification rate at any point on the pool boundary (Fig 4.1) is given by the following expression

$$R = \frac{Rn}{\cos(\theta'-\theta)} = \frac{V \cos\theta}{\cos(\theta'-\theta)} \qquad 105$$

where Rn is the growth rate in a direction normal to the isotherm; V is the welding speed, θ is the angle between the normal to the tangent to the pool at the point considered and the welding direction, and θ' is the angle between the welding direction and the direction of favoured growth (the crystal growth is anisotropic). The solidification rate in welding is greatest on the weld pool centre line where $\theta = 90°$, and the temperature gradients are almost shallow because of the distance from the welding heat source. Conversely at the weld pool edge the solidification rate is lowest.

This variation in both local solidification rate and thermal gradient in a single weld on moving around the fusion boundary from the side to weld centre line, causes a progressive change in solidification structure across an individual bead. As a result, a range of growth substructures can be observed in melt pools[112] and in individual beads, particularly at relatively high welding speeds[110,111]. At speeds used in normal welding practice only a gradual increase in the dendritic nature of the substructure is observed on moving across the weld bead.

4.2.3 Segregation

Segregation accompanies both cellular and dendritic growth modes and may extend over distances of the grain diameter or less (microsegregation). The degree of segregation and distribution of the segregate depends on the mode of the growth and the dimensions of the cells or dendrites, whichever are present. The basic mechanism of solute segregation is found to be the same in both ingot and weld solidification[113] and, just as in ingots, microsegregation is more pronounced in a weld bead, the more dendritic is the solidification mode[114]. A cellular structure, however, leads to minimization of both the degree of segregation and the mean distance of segregate distribution[107] (where this distance is defined as the distance between solute-rich regions). These conditions are schematically represented in Fig 4.2. The nature and extent of dendritic and cellular solute segregation can alter the form of the final microstructure of the weld deposit when solid-phase transformation occurs after solidification. This effect will be seen in the following section where the formation of δ ferrite in austenite stainless steel weld deposits is reviewed.

Grain boundary segregation, more properly considered as macrosegregation (extending more than several diameters), occurs either by solute accumulation in grain boundary grooves (Fig 4.3) or by the impingement of two interfaces growing with a growth component normal to each other (Fig 4.4). Segregation at grain boundary will be greater than that encountered within the substructure composing the grains, and both Miller[113] and Bell[115] have identified the existence of such enhanced grain boundary segregation during welding. This is particularly true where the outward growing grains from both sides of a weld impinge at the centre line and tend to trap the solute-rich liquid (Fig 4.4). This is found to be most marked for welding conditions which produce a steep angle of abutment between the columnar grains at the weld centre[116], e.g. high welding speeds or low welding currents. Weld deposits under these conditions are found to be more susceptible to solidification cracking[116]. A marked increase in cracking susceptibility is observed when low melting point impurities, such as phosphorus and sulphur, segregate and are concentrated at the regions of grain impingement[117]. Additionally, the

enhanced level of solute and impurity segregation at the centre of the bead can under certain conditions impair the toughness of the weld deposit[118].

4.3 Duplex Structure in Austenitic Weld Deposits

The solidification sequences and solid state transformation leading to the observed final duplex microstructure in austenitic stainless steel have been the subject of extensive investigation but different interpretations have arisen[119-129]. From the results obtained on as-cast and welded structures it is now clear that several austenitic stainless steels are either partially or completely ferritic just below the solidus line. The final duplex microstructure at room temperature is strongly dependent on the solid state transformation of ferrite to austenite and minor variations in composition.

Suutala et al[123] have proposed a model for weld metal solidification sequence in austenitic stainless steels which is supported by the work by Fredriksson[121] concerning directional solidification of an austenitic stainless steel of type 304. The solidification sequence proposed by Suutala has been defined according to the ratio Creq/Nieq of the Schaeffler diagram (Fig 2.6). The microstructures are classified depending on the leading phase during solidification, e.g. primary δ ferrite or primary austenite (Fig 4.5). When the ratio Creq/Nieq ≤ 1.48 (type A welds)[130] the austenite is the leading phase and δ ferrite, if any, solidifies from the rest of the melt between the cells or dendrites so that the solidification takes a eutectic character (Fig 4.5a and 4.5b). The δ ferrite is stabilized by segregation effects and retained at room temperature on a vermicular morphology at the interdentritic areas. No definite orientation relationship has been found between the austenite and the vermicular ferrite[130].

In welds with 1.48 ≤ Creq/Nieq ≤ 1.95 (type B welds)[125] the δ ferrite is the leading phase and austenite solidifies from the rest of the melt (Fig 4.5c and 4.5d). The austenite formed between the ferrite dendrites peritectically or eutectically grows into the melt and into the ferrite as

the temperature goes down. The growth of austenite into ferrite occurs taking either an equiaxed or lath morphology, depending on the cooling rate or temperature of transformation, and is accompanied by partitioning of elements, notably chromium and nickel, which has been measured by electron microprobe. As the reaction progresses, the ferrite dendrite core becomes richer in chromium, stabilizing the ferrite, which is retained at room temperature, showing a vermicular or lath morphology.

The mechanism of the $\delta \rightarrow \gamma$ solid state transformation, particularly at the above-compositional range, is a controversial issue. While a number of authors [120-126] reported that the ferrite to austenite transformation is a diffusion-controlled reaction, Lippold and Savage[128,129] have proposed that, for the cooling rate observed in welds, the ferrite transforms to austenite by a diffusionless massive transformation. According to this interpretation, the microsegregation observed at room temperature is produced during the liquid-to-solid transformation (Fig 4.6), with no further redistribution of elements during cooling of the solid to room temperature. However, recent work by Leone and Kerr[131] has given evidence of a diffusion-controlled $\delta \rightarrow \gamma$ transformation occurring in both Gas Tungsten Arc Welds and cast austenitic stainless steels in which the primary phase during solidification is ferrite. Working with stainless steels of composition between Region II and Region IV in the Cr-Ni 68 wt % Fe phase diagram (Fig 4.7), Leone has examined the development of the microstructure and the composition variations at different temperatures below the solidus line by quenching the specimen. The solid state ferrite to austenite transformation occurs by a diffusion-controlled process, in which Ni diffuses in ferrite towards the advancing austenite, and Cr is rejected by the advancing interface, as indicated by electron microprobe results. This enrichment of Ni and depletion of Cr in austenite, compared to the composition of ferrite, has also been reported by Lyman[127], David[126] and Cieslak[132] in STEM microanalysis of welds.

In the case of welds with $Creq/Nieq \geq 1.95$ (type C welds), Fig 4.5e, the solidification sequence proposed by Suutala[124] is $L \rightarrow L+\delta \rightarrow \delta$, with $\delta \rightarrow \gamma$ transformation occurring by diffusion-controlled process[124,128,131]. The austenite nucleates at the boundaries of the primary ferrite grains, but

at higher Creq/Nieq it does so inside the grains. The decomposition of ferrite proceeds in the form of an edgewise growth of austenite lath. A distinct orientation relationship lying close to the standard Kurdjumov-Sachs and Nishiyama-Wasserman is found between the austenite and ferrite[124]. Unlike the stainless steels with low Creq/Nieq ratio the solidification structure in these welds is not retained after the solid-state transformation. The relatively large range of temperatures over which the ferrite is stable (Fig 4.7, Region I and II) permits extensive coarsening of the ferrite grains prior to the transformation to austenite, thus explaining the large grain size normally reported in these welds. On the other hand the large grains encourage the Widmanstätten growth of austenite. In its general structure and orientation relationship between austenite and ferrite, the $\delta \rightarrow \gamma$ transformation reported by several authors resembles the decomposition of austenite into Widmanstätten ferrite in low carbon steels.

4.4 Precipitation in Weld Deposits

The complexity of the stainless steel weld microstructure over small areas in the weld deposits, associated with difficulties in obtaining suitable specimens from transmission electron microscopy, has prevented till recent years a full identification and distribution of the various phases precipitating in stainless steel welds.

The precipitation behaviour of austenitic weld deposits, as in wrought austenitic stainless steels (Chapter 2), will depend on the alloy composition - filler metal - and the thermal history of the alloy (weld thermal cycle or post-weld heat treatment). A characteristic feature of the austenitic weld deposits is that they may contain small amounts of ferrite thus avoiding hot cracking during solidification[133-136] by withstanding the stresses imposed by thermal contraction and breaking up the continuity of low melting point films which tend to form between the cells or dendrites (see Section 4.2.3). The presence of δ ferrite, however, may affect the precipitation behaviour of the material, particularly with respect to the formation of intermetallic phases such as σ phase. Small amounts of ferrite are known to accelerate the formation of σ phase[58,59]

and therefore the weld deposit is more likely to contain the brittle intermetallic phase than the fully austenitic parent plate.

The precipitation of σ phase in austenitic stainless steel weld deposits containing δ ferrite has been reported by several workers[137-141]. Usually σ phase is found to precipitate at the γ/δ interfaces (which provide appropriate high energy nucleation sites) during post-weld heat treatment between 500-900°C. However, Wegrzyn et al[138] have detected σ precipitation at the γ/δ interfaces in as-weld conditions, on careful examination of multi-run welding containing areas which have been exposed to the temperature range of σ formation for up to 60 seconds. Working with type 18 wt % Cr 8 wt % Ni weld metals containing, separately, additions of Mo, Nb, V, Si and Cu, Wegrzyn et al have examined the effect of the alloying elements on the formation of σ phase in both manual metal arc multi-run welding and single-run welds heat-treated between 500-850°C up to 200 hours. Their results showed that the greatest rate of ferrite transformation into σ phase occurs at 750°C, and the transformation begins after only 30 seconds in weld metals containing additions of Mo, Nb, V or Si, but at longer times in weld deposits containing Cu. Although elements such as Nb, Si or V are not reported in the composition of σ phase (Table 2.3) as it happens with Mo, it would be expected that these elements will affect the σ formation since all of them are known to be ferrite forming elements. The long term ageing needed for the development of σ phase in fully austenitic stainless steel (Section 2.4.1) is thus shortened by the role of γ/δ interface in enhancing the σ phase precipitation kinetics.

Although the σ phase has been the most reported intermetallic phase in austenitic stainless steel welds because of its adverse effect on mechanical properties, other intermetallic phases such as χ[137,139-142] and R[137,141], and carbides such as $M_{23}C_6$[137,139-142] are found to precipitate in Fe-Cr-Ni-Mo weld deposits on subsequent ageing treatment. In these weld deposits, containing ferrite, no precipitation is found to occur in the austenitic matrix. However, extensive precipitation is observed at the austenitic/ferrite interfaces and within the ferrite. Slattery et al[139] have indicated that the presence of ferrite modifies the precipitation sequence observed by Weiss and Stickler[20] in fully austenitic type 316 stainless steel. Table 4.1 shows the sequence of precipitation obtained

in both full austenitic type 316 stainless steel and duplex deposits type 316 under similar ageing treatment.

Table 4.1 Precipitation behaviour observed under ageing treatment in fully austenitic stainless steel and weld deposits, both of type 316

MATERIAL composition in wt %		VOLUME FRACTION OF FERRITE BEFORE AGEING (%)	AGEING TEMP (°C)	TIME (hours)	PRECIPITATES
Austenitic steel[20] 18Cr 13Ni 3Mo		0	625 850	1000 6	$M_{23}C_6$ + Laves phase $M_{23}C_6$ + χ phase
Weld Deposits 139	18Cr 9Ni 2Mo	6	625 850	1000 6	$M_{23}C_6$ + 4% δ $M_{23}C_6$ + χ + σ phase
	20Cr 10Ni 3Mo	18	625 850	1000 6	χ + σ phase + 6% δ χ + σ phase

In fully austenitic steels the $M_{23}C_6$ usually precedes the intermetallic phases and, as reported in Chapter 2, the formation curves of intermetallic χ and σ phases tend to be at higher temperatures and longer ageing times than those of carbide. In the case of weld deposits containing ferrite, the intermetallic phases σ and χ are formed in preference to $M_{23}C_6$. Slattery et al[139] have shown that $M_{23}C_6$ carbides precipitate in 18Cr 9Ni 2Mo (wt %) weld deposit containing 0.07 wt % C and 6% volume fraction of δ ferrite, but do not precipitate in 20Cr 10Ni 3Mo (wt %) weld deposit containing 0.05 wt % C and 18% volume fraction of δ ferrite. The authors related the absence of $M_{23}C_6$ in the former weld to the relatively low carbon content. However, in weld deposits of similar composition but containing lower carbon content (0.03 wt %) and 4% volume fraction of δ ferrite, $M_{23}C_6$ carbides are found to precipitate[137]. This suggests that the precipitation of $M_{23}C_6$ in the presence of ferrite is related not only to the carbon content but also to the volume fraction of ferrite in the weld deposit. Increasing the amount of ferrite, the σ and χ phase

precipitation kinetics are enhanced and, since the composition range of both phases (Table 2.3) are close to that of δ ferrite, these intermetallic phases form more readily even at lower temperatures. Furthermore, in weld deposits[142] of leaner composition, 16Cr 8Ni 1Mo (wt %) containing 2.0% in volume fraction of ferrite, the only precipitate found to occur at the γ/δ interfaces on subsequent ageing between 650-750°C for up to 10000 hours is the $M_{23}C_6$.

Leitnaker[142] has shown that the transformation of δ ferrite to either χ or σ phase is strongly dependent on the composition of the alloy, as might be expected. In 16Cr 8Ni 2Mo (wt %) weld deposits containing 2.5% volume fraction of ferrite, the only precipitates found to occur during ageing between 650-750°C for 10000 hours were $M_{23}C_6$ and χ phase. The χ phase is found to precipitate when the Mo content of the weld deposit was increased from 1 to 2 wt %. Leitnaker[142] suggested that the σ precipitation has been suppressed by early precipitation of $M_{23}C_6$ which has reduced the chromium content of the ferrite (measured by EMPA), associated with the low volume fraction of ferrite (less γ/δ interface areas). The depletion in chromium, and to a lesser extent in Mo, has left the δ ferrite with a composition closer to the χ phase which is less rich in chromium and contains more Mo than σ phase. This is in agreement with the results reported by Slattery and O'Riordan[140] in 17Cr 11Ni 3Mo (wt %) weld deposits where the $M_{23}C_6$ precipitation observed during multi-run welding is found to be associated with χ phase which precipates on subsequent stress relief treatment at 850°C for 6 hours. Evidence of χ phase growing from $M_{23}C_6$ particles was given by Lai and Haigh[137] in weld deposits aged at 800°C after 100 hours, where χ becomes the dominant phase. Slattery[140] however observed that, at the γ/δ interfaces free of carbides, the σ phase does precipitate.

The precipitation of intermetallic R-phase (hexagonal, a=10.903 Å, c=19.342 Å) has been reported by Lai et al[137] and Keown and Thomas[141] in duplex weld deposits type 316 (18-20 wt % Cr, 10-12 wt % Ni, 2-3 wt % Mo) aged at 538°C for 1000 hours and 600°C for up to 100 hours. R-phase appears to precipitate at γ/δ interfaces and within the ferrite. This phase has been previously reported by Dyson and Keown[143] in a maraging steel 12Cr 6Mo 10Co (wt %) on ageing between 450-700°C for 1 hour. Based

on the experimentally determined crystal structure of R-phase and its relationship with ferrite, Dyson and Keown showed that only small atom movements and lattice strains were required for R-phase to form from ferrite, provided that suitable alloying elements were present. Although the major constitutional elements in R-phase are Fe, Cr and Mo, the amount of molybdenum present is considerably higher (28 wt %) than any intermetallic phase (σ and χ phases) usually found in austenitic stainless steel type 316. Additionally, there are strong views[144] on the effect of Co on the formation of R-phase. Apparently R-phase precipitation from ferrite in austenitic stainless steels type 316 would require more detailed investigation for conclusive assertions.

The precipitation of nitrides or carbides other than $M_{23}C_6$ in austenitic stainless steel weld deposits has received little attention since the beneficial effects obtained with the addition of strong carbide-forming elements such as Nb and Ti described in Chapter 2 can be offset by enhanced precipitation of brittle intermetallic phases such as σ in the presence of ferrite. Nevertheless, the precipitation of carbide or carbonitrides of stabilized elements has been reported to occur in austenitic deposits[145,146] in the same fashion as in fully wrought austenitic stainless steels. In either as weld conditions or during stress relief treatment the Nb(CN)[145] and NbC[146] precipitate only on dislocations in the austenitic matrix, while the δ ferrite is found to decompose to intermetallic σ phase or $M_{23}C_6$ carbides.

4.5 Precipitation in the Heat Affected Zone

Precipitation in the heat affected zone (H.A.Z) of austenitic stainless steel welds has been frequently reported in studies associated with susceptibility to intergranular corrosion attack, known as weld decay, or else related to other corrosive attacks as knife line attack and fissure attack.

The precipitation in the heat affected zone of Fe-Cr-Ni austenitic stainless steels which lead to increased susceptibility to intergranular corrosion attack (weld decay) is found to occur in the narrow region of

the heat affected zone away from the weld deposit, which has been heated within the temperature range 500-900°C for a sufficient length of time during welding. In this region, several authors[147-150] over past years have reported the precipitation of chromium-rich carbides, $M_{23}C_6$, to occur at the austenite grain boundaries during welding by various welding processes. Post-weld heat treatment in the temperature range 500-900°C is also found to cause precipitation of $M_{23}C_6$ over the entire heat affected zone, extending the grain boundary corrosive attack[150]. Although the theory of chromium depletion of the surrounding matrix is generally consistent with the experimentally observed corrosion phenomena, there is evidence indicating that the susceptibility to intergranular corrosion depends on the density[150] and morphology[151,152] of the precipitated grain boundary carbide which is related to time and temperature of heating.

The susceptibility to weld decay can be reduced in a number of ways, as described in Chapter 2. One alternative is to make additions of Nb or Ti in excess of the stoichiometric amount to combine with carbon, as in type 321 and 347 austenitic stainless steels. Although the austenitic stainless steels containing titanium or niobium are more resistant to weld decay, they became susceptible after welding to intergranular attack in a zone adjacent to the weld deposit where very high temperatures (above 1000°C) are encountered in welding operations. Pinnow and Moskowitz[153] presented an approach in which they describe two distinct types of intergranular corrosion in this region of the heat affected zone. The better known one which occurs in a number of environments is called knife attack and is associated with chromium-denuded grain boundaries as in weld decay attack. The other type, which is specific to nitric acid, is best referred to as fissure attack. The former occurs when the carbon content exceeds 0.05 wt % but both are apparently related to the dissolution of TiC or NbC in the heat affected zone.

During the welding thermal cycle, high temperatures are reached in the area close to the fusion line, enabling the dissolution of TiC and NbC. The rapid cooling of this area through the temperature range of TiC or NbC precipitation would not give enough time for these carbides to reprecipitate. On ageing between the temperature range 500-900°C[154] or on multi-run weld[155] (a potentially susceptible zone created by one run may

be sensitized by a subsequent run) the chromium-rich carbide $M_{23}C_6$ is found to precipitate more readily since its precipitation kinetics are faster than those of NbC or TiC (chromium diffuses more rapidly in austenite than does Nb or Ti). Thus, the reduced corrosion resistance observed in this zone which has experienced double heat influence is similar to the weld decay observed in the heat affected zone away from the fusion line in the unstabilized steels. In both cases the intergranular corrosion attack is associated with $M_{23}C_6$ precipitation, though the former is known as knife line attack and is observed in the zone close to the fusion line.

The fissure attack, which is also called knife line attack by some investigators, has received considerable investigation[156-161] in 18Cr 8Ni (wt %) austenitic stainless steel containing additions of Ti or Nb. It appears that fissures occur in nitric acid environment, by preferential attack of titanium and niobium carbides that form at the grain boundaries during welding. These niobium-rich and titanium-rich carbides[160,161] have a dendritic morphology and are found to precipitate in a narrow zone immediately adjacent to the fusion line forming a network at the grain boundaries. The precipitation is found to be enhanced by the presence of ferrite, since these carbides are often observed at γ/δ interfaces. Both niobium-rich and titanium-rich carbides increase the susceptibility of the heat affected zone to intergranular corrosion in nitric acid environment (fissure attack), with titanium carbide showing the strongest tendency[159]. Post-weld heat treatment between the sensitization range (500-900°C) can additionally cause the precipitation of chromium-rich carbides with the formation of depleted regions in the austenite as previously described. Therefore both precipitating processes may contribute to the final corrosion result to a varying extent at different positions within the superheated region of the heat affected zone. However, with respect to niobium and titanium carbides it is the attack on the carbides themselves, facilitated by their branched morphology, that provides the specific corrosion attack in nitric acid environment[162].

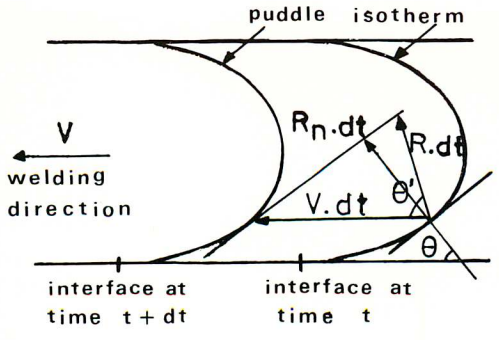

$$R = \frac{V \cos \theta}{\cos(\theta' - \theta)}$$

Fig 4.1 Relationship between welding speed and actual growth rate[105].

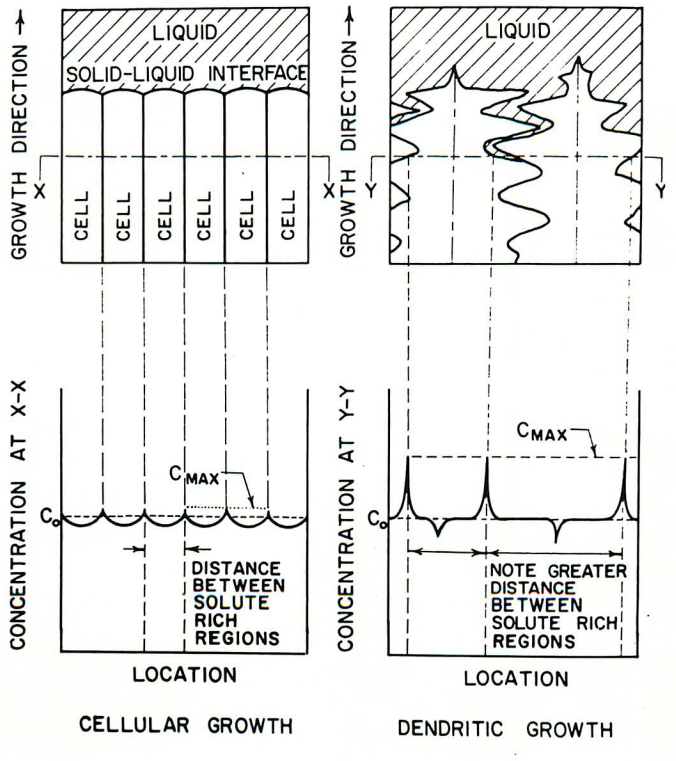

Fig 4.2 Schematic diagram of solute distribution for cellular and dendritic growth patterns[107].

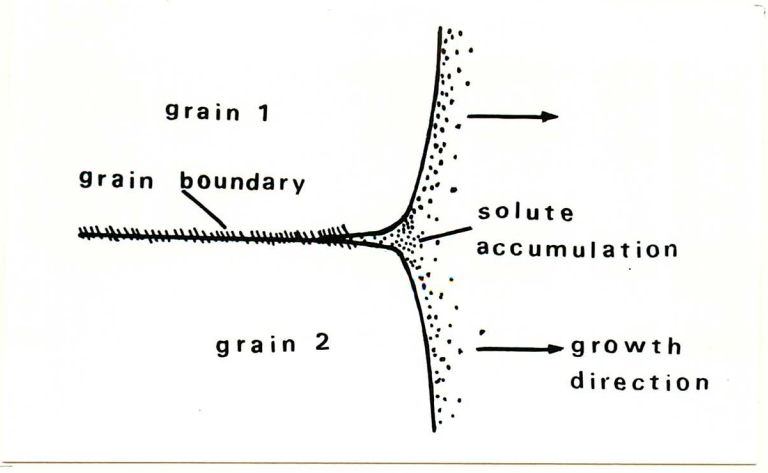

Fig 4.3 Schematic representation of section through a grain boundary groove.

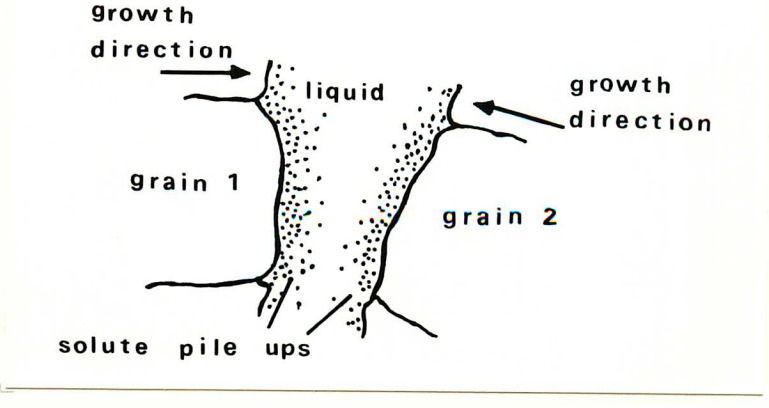

Fig 4.4 Schematic representation of formation of grain boundary by impingement.

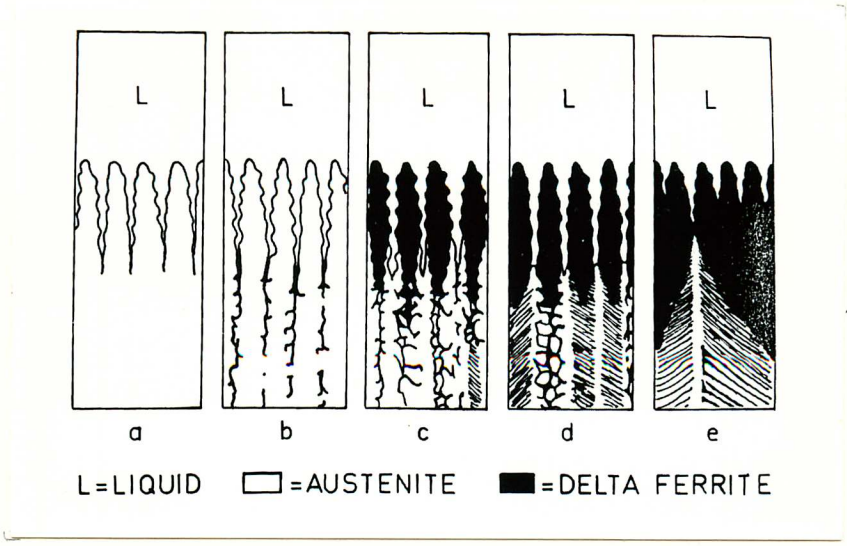

Fig 4.5 Schematic solidification model for austenitic and austenitic-ferritic weld metals[123]: (a) Type A, the weld metal solidifies completely to austenite and no further high temperature transformation takes place; (b) Type A, austenite is the leading phase and δ ferrite solidifies from the rest of the melt; (c) Type B, δ ferrite is the leading phase, austenite solidifies from the rest of the melt and a quick phase transformation $\delta \rightarrow \gamma$ takes place at high temperatures; (d) as (c), but with higher volume fraction of ferrite at room temperature; (e) Type C, the weld metal solidifies completely to δ ferrite and austenite forms through a solid state transformation.

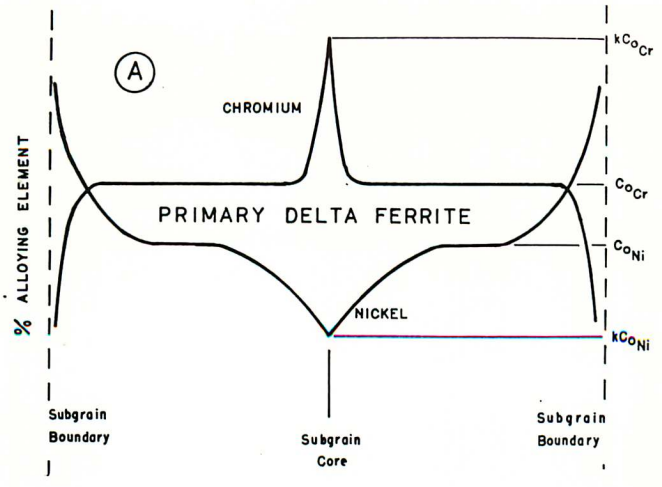

Fig 4.6 Schematic illustration of the chromium and nickel distribution across a subgrain following solidification as primary δ ferrite[128].

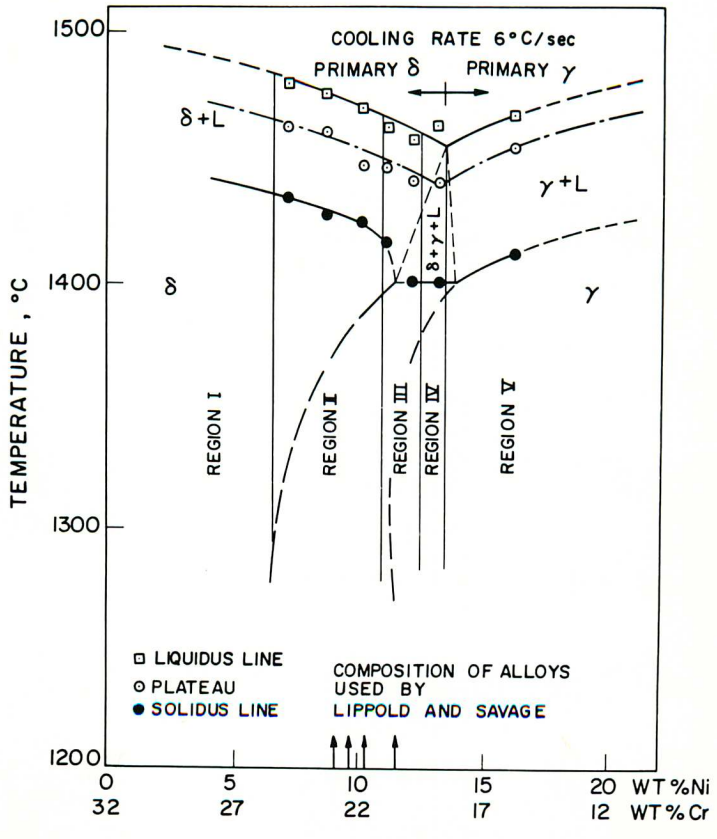

Fig 4.7 Pseudo binary section through the Fe-Cr-Ni phase diagram at 68 wt % Fe, showing the effect of composition on the freezing mode[131].

5. MATERIALS AND EXPERIMENTAL TECHNIQUES

5.1 Introduction

In this chapter the experimental procedures and the welding techniques used in this investigation will be described. Since the aim of this work was to investigate the stability of an austenitic stainless steel (REX 734) with respect to the formation of carbides, nitrides and intermetallic phases, under ageing treatment and welding conditions, the wires and electrodes selected to produce the welds were designed to match the base plate composition. Typical compositions of these materials will be given together with the chemical analysis of the weld deposits. All the welding carried out in this investigation was performed at the Welding Institute.

5.2 Materials

The material used in the ageing experiments was an austenitic stainless steel (REX 734) weld filler wire of 2.4 mm diameter. The wire was chosen because it would represent to a large extent the composition of the welding deposits, and its diameter would be convenient for the preparation of transmission electron microscopy specimens. The wire was provided by the Welding Institute and had the following chemical composition in % wt:

0.058C, 21.3Cr, 9.5Ni, 3.9Mn, 2.6Mo,
0.19Si, 0.28Nb, 0.4N and balance Fe

The materials used in the welding experiments consist of austenitic stainless steel (REX 734) plate, wire (REX 734) and electrodes. Concentrations of the alloying elements in each weld component are given in Table 5.1. The chemical compositions of the weld deposits, obtained

after the welds were made by the Manual Metal Arc (MMA) and Tungsten Inert Gas (TIG) process, are given in Table 5.2.

Table 5.1 Composition of the welding materials (in wt %)

Component	C	Si	Mn	S	P	Cr	Ni	Mo	Nb	N
Plates REX 734	0.044	0.35	3.8	0.015	0.018	21.6	9.6	2.7	0.33	0.42
Wire, Ø1.2mm REX 734	0.038	0.28	4.0	0.004	0.016	21.5	9.4	2.7	0.30	0.38
Electrodes										
Ø3.2mm	0.037	0.13	4.9	0.008	0.019	21.4	9.5	2.7	0.24	0.38
Ø4.0mm	0.035	0.11	5.0	0.005	0.019	21.4	9.1	2.7	0.24	0.39

Table 5.2 Chemical composition of the weld deposits (in wt %)

Weld Metal	C	Si	Mn	S	P	Cr	Ni	Mo	Nb	N
MMA 1	0.045	0.17	4.9	0.010	0.022	21.8	9.2	2.8	0.3	0.42
MMA 2	0.041	0.18	4.9	0.011	0.022	21.8	9.3	2.8	0.3	0.35
TIG 3	0.042	0.20	3.9	0.004	0.019	21.4	9.5	2.7	0.3	0.29

5.3 Heat Treatment of the Alloy

The 2.4mm diameter weld filler wire was cut into specimens about 50mm long, sealed in silica capsules under reduced nitrogen pressure to prevent loss of nitrogen from the specimens, and solution treated at 1300°C for 1 hour before quenching in water (the capsules were broken under the surface of a water bath). After solution treatment the specimens were re-sealed in silica capsules as described above and aged in furnaces at different temperatures. The ageing treatment was carried out at temperatures between 600 -1000°C for up to 1000 hours.

5.4 Welding Technique

Two conventional welding processes, Manual Metal Arc (MMA) and Tungsten Inert Gas (TIG), used in stainless steel welds, were selected for this work. Being well established welding processes they will not be described, but information regarding the welding procedures will be given. All the welds were made using materials in the as-received condition, without heat treatment. The change in welding technique would be expected to lead to variations in the weld deposit composition, particularly nitrogen content, which should produce significant changes in microstructure.

5.4.1 Manual Metal Arc Welding (MMA)

Manual metal arc welding was carried out on 13.5mm thick plates of an austenitic stainless steel (REX 734) using covered electrodes. The chemical composition is shown in Table 5.1. Both electrodes are of similar composition and were specially designed by the Welding Institute for welding REX 734 plates. The difference in diameter is to overcome limitations on current capacity for providing sufficient heat to melt the base plates and the welding electrode, and so gain proper fusion.

The joint preparation used is shown in Fig 5.1. Each panel was 45mm in width and 300mm in length. The plates were kept in position by restraining grips and a copper backing was used to ensure full penetration on the root pass. The standard welding conditions used are summarized in Table 5.3. The composition of the two welds deposited in this manner (MMA1 and MMA2) is given in Table 5.2. The interpass temperature was 150°C.

5.4.2 Tungsten Inert Gas Welding (TIG)

Tungsten inert gas welding was carried out on 13.5mm thick plates using 1.2mm diameter filler wire. Chemical compositions are given in Table 5.1. The joint preparation used is shown in Fig 5.2. The dimensions of the panel and the interpass temperature are the same as those described for the manual metal arc. For completion of the back face assuring full penetration, a groove 3mm in depth was made before the filling pass was

Table 5.3 Welding Parameters

Welding Process	Number of passes	Electrodes or wire diameter, mm	Current A	Voltage V	Travel speed mm/sec	Nominal Heat Input kJ/mm	Location of runs in the weld joint
MMA 1	4	3.2 4.0	110 150	21 21	3 2	0.9 1.6	Root and sealing Middle runs
MMA 2	4	3.2 4.0	120 170	21 21	2.6 1.3	1.0 2.6	Root and sealing Middle runs
TIG 3	14	1.2	140	12	1.2	1.4	All runs

deposited. The standard welding conditions used are summarized in Table 5.3. The composition of the weld deposited in this manner (TIG3) is given in Table 5.2.

5.5 Optical Metallography

For optical metallography, aged specimens were hot mounted in copper powder with a layer of acrylic plastic, Fig 5.3, to give a transverse section. The copper powder provides the necessary conductivity for electropolishing and scanning electron microscopy examination, while the acrylic plastic prevents contamination of the specimen surface by copper during polishing and etching. The weld specimens' transverse section containing the weld deposit and the heat affected zone were big enough to handle without mounting. The surface of the specimens was ground down to 1200 grit size using silicon carbide abrasive paper and they were then mechanically polished using 1μm diamond paste. To eliminate remaining scratches and any deformed surface, the specimens were electropolished in a 70% ethanol, 20% glycerol and 10% perchloric acid bath at room temperature, using an Electropol polisher-etcher machine. Polishing was carried out for 10 seconds at 32 Volts on aged specimens, and 58 Volts on the larger weld specimens. After polishing, the specimens were washed in

cold running water, and then dried with alcohol.

The etchant suitable for all the specimens was 20% sulphuric acid diluted in distilled water. The etching time required depended upon the heat treatment, but was generally between 6 and 90 seconds at 2 Volts. After etching, the specimens were examined under a Carl Zeiss Neophot 2 microscope and photographs taken using an Ilford FP4 35mm film.

5.6 Electron Microscopy

5.6.1 Scanning Electron Microscopy

Scanning electron microscopy was used to study the microstructure of the cross-section of weld specimens. The specimens were prepared as described in the previous section and were examined under an International Scientific Instrument (ISI) 100 scanning electron microscope, operating at 40kV. Generally secondary electron imaging was used. Photographs were taken using Ilford FP4 35mm film.

5.6.2 Transmission Electron Microscopy

Transmission electron microscopy was carried out on either a Phillips 300 or Phillips EM 400 operating at accelerating Voltages of 100 and 120kV respectively. Bright field, centred dark field, selected diffraction area and convergent beam modes were employed.

Thin foils for transmission electron microscopy were prepared by electrochemical thinning. In the case of aged specimens, thin foils were prepared from 2.4mm diameter, 0.25mm thick discs which had been cut out using an oil cooled carborundum slitting wheel. In the case of weld specimens, the discs were obtained through steps which are shown schematically in Fig 5.4. A block containing the whole weld deposit and the heat affected zone was cut longitudinally into about 0.8mm thick slices (Fig 5.4a), using an oil cooled carborundum slitting wheel. The slice was fixed to a steel plate using a Durofix glue then ground down to about 0.25mm thick (Fig 5.4b). The slice was then etched in a solution of

mixed acids (15ml hydrochloric acid, 10ml nitric acid and 10ml acetic acid) to localize the weld deposit. After etching, 3.0mm diameter discs were punched from the centre of the weld deposit (Fig 5.4c).

All discs were ground to a thickness of about 75μm by mechanical grinding. The discs were thinned in a Fischione twin jet polisher using a 15% Perchloric acid in ethanol solution at 32 Volts. The solution was cooled to -40°C to slow down the reactions in order to obtain larger thin areas. After polishing, the specimens were cleaned in a gentle stream of alcohol.

5.7 Microanalysis

5.7.1 Energy Dispersive Analysis of X-Rays

The basis of the analysis is to use a focussed electron probe to impinge on a specimen, causing the emission of characteristic X-rays. The energies of these X-rays indicate which elements are present and the intensities the relative proportions of those elements. The analytical methods used to interpret this information has been considered in this work under application of two techniques.

a) Analysis in Scanning electron microscope (SEM)

To investigate the compositional variations over large areas in the weld deposit substructures, particularly cellular-dendritic austenite and retained δ ferrite, bulk specimens were subjected to microanalysis using an Energy Dispersive System (EDS) linked to ISI 100 scanning electron microscope. EDS analysis was carried out at an accelerating Voltage of 20kV and the specimen was tilted at an angle of 45° to the beam enabling the X-rays to reach the silicon detector. The electron probe beam diameter size was about 1μm, but beam instability can cause a variation in the size of the probe. The main elements in the alloy, except carbon and nitrogen, were analysed and conditions for atomic number effect (Z), absorption (A), and fluorescence (F) were made. Details of the standard ZAF corrections can be found in standard texts[163].

b) Analysis in thin foils (STEM)

The quantitative analysis of individual particles such as carbides, nitrides and intermetallic phases in aged and weld specimens was carried out on a Phillips EM 400 TEM/STEM with a Link 860 microanalysis system, using standard thin foil correction programs to compensate for X-ray detection efficiency and absorption. Due to the limited sensitivity over X-ray techniques for low Z analysis, carbon and nitrogen were not analysed. The specimen was tilted at 35° to the beam enabling the X-rays to reach the silicon-lithium detector, and the electron probe beam diameter used was 100 Å.

5.7.2 Electron Energy Loss Spectroscopy (EELS)

Over the past few years it has been demonstrated experimentally that electron energy-losses caused by inner-shell excitation, and detected in the transmission mode, provided a sensitive method of microanalysis especially for low atomic number elements[164]. Unlike X-ray microanalysis, the energy-loss method can detect elements distributed within the interior of a thin foil specimen, provided the latter is sufficiently thin. X-ray emission techniques measure secondary processes due to the radioactive recombination of an inner core hole with an outer core electron. By contrast, electron energy-loss spectroscopy measures the inner-shell excitation directly through its effect on the transmitted electrons. Therefore, relatively simple equations can be used for quantitative analysis and corrections, for absorption or yield of the secondary process are not required.

Although a large number of fundamental studies which concern the physics of inner-shell losses has been reported, relatively little quantitative work has been done in materials science, per se. The reasons for this, apart from its being a complex technique (for instance elastic-inelastic scattering), lie in the relative accuracy of ± 10% and absolute accuracy of ± 20% obtained in the quantitative results. These limits are fixed by the existing methods of determination of variables such as partial cross-section of excitations to continuum states for the electron shells (K or L, etc) and/or specimen related variables[165]. With regard to

the specimen a critical point is the thickness. The accuracy decreases with increasing thickness since an electron can be multiply scattered. That is to say that having produced a K-shell ionization it can subsequently undergo an elastic scattering, which will deflect it and possibly cause it not to be collected by the spectrometer. Alternatively it can participate in an inelastic collision which will leave it with an additional energy loss and deflection. Detailed information about the principles of electron energy-loss spectroscopy can be found in a text by Joy[166], and its application as a microanalytical technique for materials characterization by Maher[165]. A summary of this technique with an example of the calculations necessary to obtain quantitative results is given in Appendix 1.

In this investigation, the energy-loss microanalysis of carbon and nitrogen in carbides and nitrides particles was carried out on a Phillips EM 400 TEM/STEM operating at 100kV with a Link 860 microanalysis system, using a partial cross-section Egerton's program. The spectrometer was a $\pi/2$ energy-loss spectrometer operated with ~ 18 mrad collection angle, fitted to the electron microscope. Thin foils were cooled to 100°K using liquid nitrogen in a specimen cold holder to avoid contamination.

A practical problem found with the application of the energy-loss microanalysis in this work was in obtaining foils containing particles thin enough to produce quantitative results within the accuracy expected by this technique. To overcome this problem the thin foils prepared for transmission electron microscopy had to be further thinned. The method used for this was ion beam thinning, which was carried out on an Edwards ion beam thinning machine. A schematic diagram of the arrangement in the vacuum chamber is illustrated in Fig 5.5. The thin foil prepared as described in Section 5.6.2 was held between tantalum plates in the holder and was bombarded either from both sides or one side, as the case may be, by argon ion beams. The specimen holder was rotated, so that the beam bombards a non-stationary surface giving a smooth thin area. The grazing angle could be varied. An angle of 15° would give a suitable smooth surface at a reasonable thinning rate. Usually the thinning rate was slow. At 4kV and 40μA beam current, thinning rate was about 1μm per hour. The specimen was left to thin for about 10 minutes since a longer time

would tend to break off the thin area obtained previously by twin jet polishing. This technique gave good results but was not successful in all cases. Thus, the quantitative analysis is given only when the accuracy falls within ± 20% expected by the energy-loss microanalysis technique. When out of this range, the results are used only for qualitative assessments.

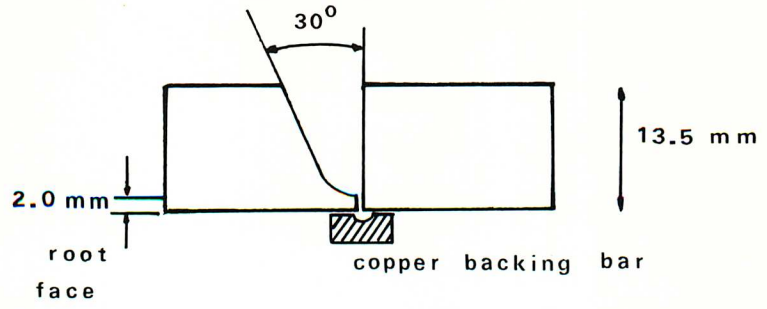

Fig 5.1 Joint preparation for manual metal arc welding process (MMA).

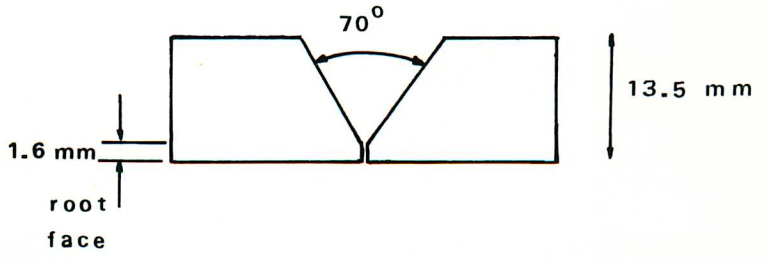

Fig 5.2 Joint preparation for tungsten inert gas welding process (TIG).

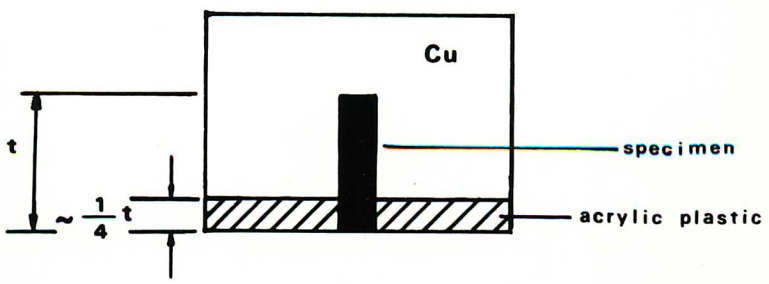

Fig 5.3 Schematic representation of the hot mounting used for optical metallography on aged specimens.

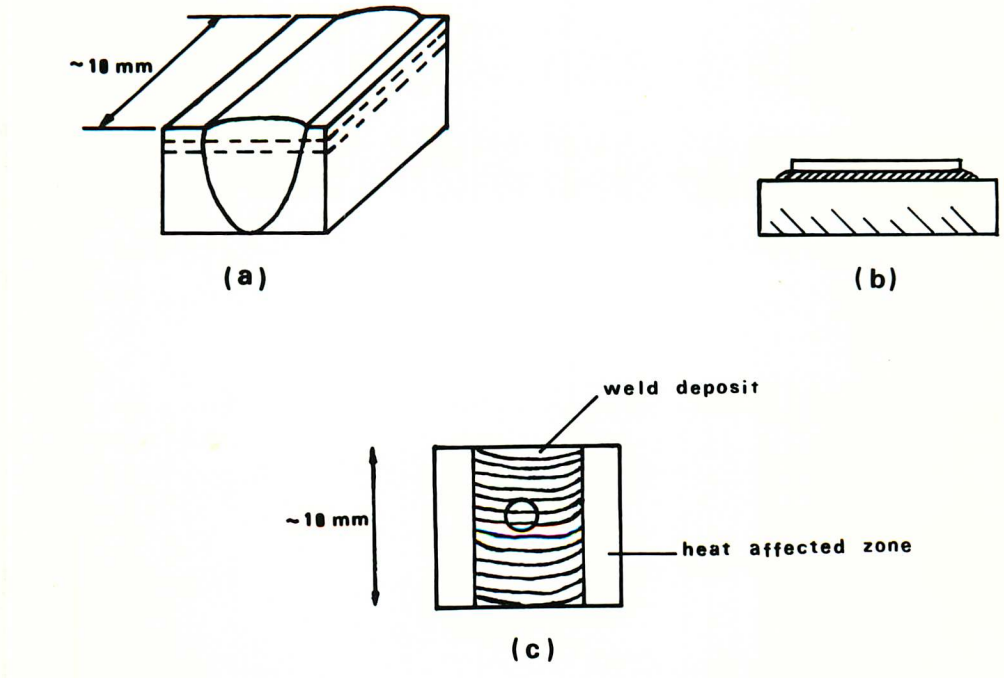

Fig 5.4 Schematic representation of the steps used in the preparation of thin foil from weld specimens.
a) longitudinal cuts in the weld specimens of ~ 0.8mm thick slices.
b) mechanical grinding to 0.25mm thick slices.
c) 3.0mm diameter disc punched from the 0.25mm thick slice containing the weld deposit.

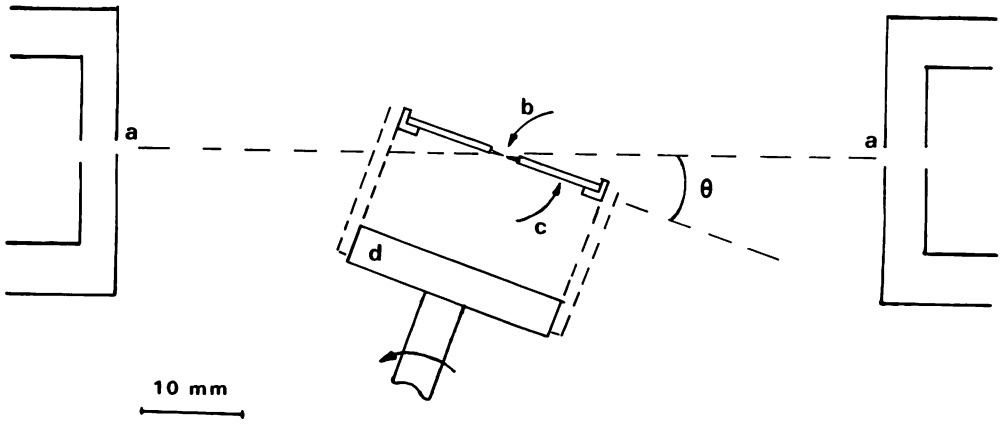

Fig 5.5 Schematic diagram of the arrangement in the vacuum chamber of ion beam thinning machine.

a) Ion beam
b) specimen
c) tantalum plates
d) specimen holder
θ = grazing angle

6. AGEING BEHAVIOUR OF REX 734

6.1 Introduction

The ageing behaviour of REX 734 was studied in a weld filler wire of 2.4mm diameter, after solution-treatment at 1300°C for one hour. The microstructural changes observed during ageing treatment between 600-1000°C for up to 1000 hours will be described in this chapter. The techniques by which the various phases present in REX 734 were identified have been described in Chapter 5. The precipitation behaviour of this alloy proved to be complex and, in order to present the results as clearly as possible, the microstructural changes observed at each temperature will be presented with brief reference to Z phase precipitation reaction. This phase will be treated in more detail in a separate chapter with regard to its crystallography, chemical composition and occurrence. Other phases such as $M_{23}C_6$, χ phase, Cr_2N and σ phase will be described only in the present chapter.

6.2 The Structure After Solution Treatment

The grain size after solution treatment at 1300°C was relatively coarse with the mean grain diameter being approximately 0.3mm. The coarse grained fully austenitic structure frequently showed annealing twins and a small number of undissolved particles which were identified by X-ray microanalysis in thin foils. Spectra from those particles showed three varieties of inclusions where the most common one was rounded, and contained a large proportion of aluminium and iron with some chromium and nickel, Fig 6.1. The microanalysis spectra of the other two types of inclusions observed in the solution-treated specimens are shown in Fig 6.2 which indicate, in both cases, the presence of iron in large quantities followed by Cu and Cr or K and Ca. All the spectra obtained from

inclusions suggest that those particles are complex oxides, with three or more elements being present.

The microstructural characterization of the solution-treated material showed that no precipitation was evident and that no significant levels of deformation were present in the matrix, see Figs 6.3 and 6.4. Stacking faults were occasionally observed in association with undissolved particles, Figs 6.1 and 6.4. This suggests that the dislocation which dissociates to form a stacking fault is one which has been generated during quenching as a result of differences in thermal-expansion coefficient between the undissolved particle and the austenite matrix.

6.3 Structures After Ageing at 600°C

6.3.1 Grain Boundary Precipitation Reaction

When the alloy was aged at 600°C, precipitation was evident only after 1000 hours at that temperature. At grain boundaries faceted particles precipitated and were identified to be $M_{23}C_6$. The particles show a cube on cube orientation relationship with one of the austenite grains constituting the boundary. The parallel orientation relationship between the carbide and austenite is well documented and has been established by workers such as Lewis and Hattersley[27] and Singhal and Martin[33]. In Fig 6.5, a grain boundary is shown where some carbide precipitates were in parallel orientation with one austenite grain and some with the other grain. Carbide particles B in Fig 6.5 are in parallel orientation to grain 2 (γ_2) and particles A are parallel to grain 1 (γ_1). The growth of the particles has caused the $\gamma/M_{23}C_6$ boundary to migrate; the grain boundary fringe contrast is seen at the A particle showing this effect, and although migration in the opposite direction has in fact taken place at the B particles the boundary fringes are not in contrast. The intergranular precipitation of the new phase and the resultant simultaneous migration of the grain boundary is usually described as a type of discontinuous precipitation.

A number of small particles in Fig 6.5 (indicated by arrow) may be seen to be delineating the previous austenite grain boundary. These particles were too small in size to be solved by electron diffraction pattern but, from its appearance, it is believed to be Z phase (NbCrN) as we shall see later. The Z phase precipitation occurred at an earlier stage in the precipitation sequence so that, on subsequent $M_{23}C_6$ carbide precipitation at the same boundary, the carbide grew adjacent to the Z phase particles.

The $M_{23}C_6$ particles observed had a face-centred cubic crystal structure with lattice parameter a=10.65 A. The unit cell size of $M_{23}C_6$ obtained in the present investigation is relatively smaller than that reported by some authors[24,25,26] and within the range given by Weiss and Stickler[20] (Table 2.1). Small changes in stoichiometry of $M_{23}C_6$ would produce a change in its lattice parameter as reported by Gullberg[167] and Andersson and Lundberg[168]. According to Gullberg[167] a linear relationship exists between the amount of chromium and iron in a $(FeCr)_{23}C_6$ carbide and the lattice parameter. He showed that in a 14 wt % Cr ferritic stainless steel the carbide may have a chromium content between 60-67 wt % with a corresponding lattice parameter ranging from 10.60 to 10.61 A. Furthermore, Andersson and Lundberg[168] have shown that increasing amounts of molybdenum in the $M_{23}C_6$ carbide cause a significant expansion of lattice and observed that the lattice increases linearly with increasing Mo content of the carbide (e.g. 0-11 wt % Mo caused a change in the lattice parameter from 10.64 to 10.71 A). The metal composition of $M_{23}C_6$ carbide in the present work and its lattice parameter is in good agreement with the work of Gullberg[167] and Andersson and Lundberg[168].

In Fig 6.6 a spectrum obtained from $M_{23}C_6$ particle at the grain boundary in Fig 6.5, is shown with the corresponding composition in wt % of the metal elements present in the phase (determined using standard thin foil program to compensate for X-ray efficiency and absorption). The carbide composition can then be written as $(Cr_{16}Fe_{4.5}Mo_{1.5}Ni)C_6$. The presence of carbon in the carbide was confirmed by electron energy-loss microanalysis of $M_{23}C_6$ particles. No nitrogen was detected in these particles. A typical spectrum, Fig 6.7, was recorded for a grain boundary particle at the edge of a foil cooled to 100°K to reduce surface diffusion

of contaminants. The quantity of a particular element contributing to the measured intensity (number of atoms per cm^2 of surface within the incident electron beam) is obtained by integrating the carbon K edge and chromium L edge over a window after background subtraction and correction for the effect of convergence, and comparing with partial cross-section calculated according to Egerton's programmes (Appendix 1). The results shown in the right-hand corner of Fig 6.7 give a Cr/C ratio of 3. This is an encouraging result on the potential quantification of EELS data considering that the ratio of chromium to carbon in the $(Cr_{16}Fe_{4.5}Mo_{1.5}Ni)C_6$ carbide is 2.7.

6.3.2 Intragranular Precipitation Reaction

Matrix precipitation was also detected at 600°C. The state of precipitation after ageing for 1000 hours at 600°C is illustrated in Figs 6.5 and 6.8, where disc-shaped precipitates can be observed in the matrix showing lobe contrast (Fig 6.8). The particles identified as $M_{23}C_6$, Fig 6.9, were not found to be associated with dislocations.

Precipitation of $M_{23}C_6$ on dislocations which form during the quench, or are generated by the prismatic punching mechanism around growing particles, has been reported by Lewis and Hattersley[27] and Beckitt and Clark[32]. The resultant dislocation nucleated precipitates were reported by the authors to be angular in shape and growing from corner to corner, or face to face on the dislocation line, resulting in stringers of particles. Singhal and Martin[34] reported the random matrix dot particles which grow rapidly on ageing along <110> austenite directions acquiring the shape of thin laths forming a Widmanstätten pattern.

In the present investigation, the intragranular carbide morphology is related to discrete disc-shaped particles which appear to have nucleated independently of any feature. Occasionally zones free of precipitation were observed near the grain boundary, Fig 6.10 (indicated by arrow). The precipitate-free regions in the present work have a non-uniform distribution and are believed to arise due to solute depletion by growth of $M_{23}C_6$ intergranular particles. At 600°C ageing temperature the dominant precipitate is $M_{23}C_6$.

6.3.3 Summary

a) The intergranular precipitation reaction was only observed after 1000 hours. The precipitates were found to be Z phase and $M_{23}C_6$ carbides.
b) The Z phase precipitation reaction preceded that of $M_{23}C_6$ carbide.
c) The intragranular precipitation reaction was only observed after 1000 hours and the particles were identified to be $M_{23}C_6$.

6.4 Structures After Ageing at 700°C

6.4.1 Grain Boundary Precipitation Reaction

The first precipitation reaction at this temperature was the small equiaxed Z phase which has a tetragonal unit cell a=3.01 A c=7.28 A. Detailed information about the crystallography and microanalysis of Z phase will be given in Chapter 7. After 1 hour of ageing, the Z phase precipitation was evident at grain boundaries, Fig 6.11 where particles are showing strain contrast. At high magnification, Fig 6.12, the Z particles can be seen within the grain boundary. The first sign of twin boundary precipitation of Z phase was detected after 10 hours ageing, Fig 6.13 (twin boundaries in the present investigation were identified by selected area diffraction patterns). Further ageing at 700°C did not produce extensive grain boundary Z phase precipitation nor did these particles grow significantly large. These were indicated by the presence of other phases competing for the same nucleation site.

At 700°C the rate of $M_{23}C_6$ precipitation was faster than at 600°C. Initially the carbide was seen to precipitate intergranularly, such that after 10 hours discrete faceted particles would be of the order of 0.1 μm occasionally showing fringe contrast, Fig 6.14. Continued ageing at this temperature resulted in fast growth of the particles, Fig 6.15, and in the carbide being present to some degree in all nucleation sites after 1000 hours. In Fig 6.16 large $M_{23}C_6$ particles of about 1 μm in size can be seen in a twin boundary. In the vicinity of large intergranular $M_{23}C_6$ particles there appeared to be a localized high density of dislocations, Figs 6.15 and 6.16 which will nucleate Z phase as will be seen later in

Chapter 7. These dislocations are generated to relieve stresses arising from the differential thermal expansion of the particle and matrix.

$M_{23}C_6$ carbides were slower to nucleate than Z phase, and whenever Z phase was present at a boundary, the $M_{23}C_6$ formed around it. Frequently, $M_{23}C_6$ was seen to have grown and engulfed the small equiaxed Z particles which were delineating the austenite grain boundary.

6.4.2 Intragranular Precipitation Reaction

Z phase

The precipitation reaction in the matrix at 700°C was observed after ageing for one hour. The small equiaxed particles observed in association with dislocation after 1 hr of ageing were identified to be Z-phase. Precipitation of this phase on dislocations was particularly noticeable in regions around the undissolved particles, Fig 6.17, where a high density of dislocations was generated during quenching as a result of differences in thermal-expansion coefficient between the undissolved particle and the austenite matrix. It was observed that the dislocation nucleated precipitate also formed as a 'string' of particles along the length of the dislocation, and it appeared that the dislocations were punched away from the particles after the latter had grown to certain critical size. This can result in further nucleation on the freed dislocation, and the precipitation and growth cycle can be repeated. Fig 6.18 shows dislocations which have given rise to several 'rows' of precipitate particles. The driving force for this phenomenon is the need by the growing particles for vacancies which are supplied by the climbing process[44]. The intragranular precipitation of Z phase was prolific, and on further ageing the small equiaxed particles started to develop into small cuboids which on growing had often joined or overlapped so that irregular slabs of Z phase, Fig 6.19, were produced, and always had dislocations associated with them. Occasional interaction of dislocations had occurred to produce nodes as at point A.

The material had a very low density of stacking faults, and no precipitation was associated with it, Fig 6.20. In the present work, the faults were not seen in the early stage of ageing but at later times and in

association with existing particles. As mentioned before, in the early stage of ageing REX 734 at 700°C, the undissociated dislocations appear to be involved in the climb-precipitation reaction of Z phase, originating rows of precipitate. Borland[80] has suggested that stacking fault precipitation is likely to occur only when dislocations dissociate before precipitation occurs on them. It is possible that in the present investigation the stacking fault has an indirect role on the precipitation as proposed by Silcock[40], who considers that the dislocation which dissociates to form a stacking fault is one which has been generated by precipitation on a pre-existing dislocation. On the other hand, it may be that a part of the original dislocation assumes an orientation in which it may dissociate in the appropriate way.

The precipitation of Z phase, a mixed niobium-chromium nitride, has been reported to occur in Nb-N austenitic steels by a number of authors[80,95,96,102]. More recently, Colclough[35] has given detailed information about the Z phase precipitation reaction in a commercial austenitic stainless steel type Nitronic 50 (21Cr 12Ni 2Mo 5Mn (wt %)). He detected the precipitation of Z phase at grain boundaries, twin boundaries and within the matrix. Colclough observed that at grain boundaries the Z phase precipitation was well established at 700°C only after 18 hours of ageing, and that the intragranular precipitation at this temperature was limited even after 1008 hours. He also pointed out that the precipitation at twin boundaries was rare at this temperature and attributed the limited appearance of Z phase at twin boundaries to the predominance there of $M_{23}C_6$.

In the present investigation, the faster precipitation reaction of Z phase is thought to be due to the higher content of nitrogen and niobium in REX 734 austenitic stainless steel (0.4 wt % N, 0.3 wt % Nb) in comparison to Nitronic 50 (0.24 wt % N, 0.2 wt % Nb) studied by Colclough[35]. This has permitted the precipitation of Z phase at grain boundaries even at 600°C which was not detected by Colclough. At low temperatures, in Cr-Ni stainless steels stabilized by the addition of niobium or titanium, $M_{23}C_6$ carbides are normally expected to precede other precipitation reactions due to the more rapid diffusion of chromium in austenite than Nb or Ti[169]. The high content of nitrogen in the present investigation had

delayed the precipitation of $M_{23}C_6$ which was not observed before 10 hours of ageing at 700°C and 1000 hours of ageing at 600°C. The effect of nitrogen in retarding the $M_{23}C_6$ is in agreement with the observations of Thier et al[170], in austenitic steels 17Cr 13Ni 5Mo (wt %) containing nitrogen between 0.04-0.3 wt % N. They found that, as the nitrogen content increases, the precipitation curve of $M_{23}C_6$ is shifted to long ageing times (e.g. at 600°C ageing temperature an increase in nitrogen content from 0.04 wt % to 0.15 wt % has delayed the $M_{23}C_6$ precipitation reaction from 10 hours to 500 hours respectively). It seems that the delay in the $M_{23}C_6$ precipitation is related to the fact that no isostructural nitrides occur and it appears that nitrogen is not soluble in the carbide as shown by EELS microanalysis in the previous section. This is perhaps due to the position of the carbon atoms in the structure. In $M_{23}C_6$ each carbon atom is at the centre of a square anti-prism of metal atoms. Normally carbides can dissolve large amounts of nitrogen and can eventually be replaced when the interstitial atoms are in octahedral holes since the nitrogen is also octahedrally coordinated. However, nitrogen does not dissolve in structures where each carbon atom is surrounded by a trigonal prism of metal atoms (e.g. Cr_7C_3)[77].

$M_{23}C_6$

At 700°C the intragranular precipitation of $M_{23}C_6$ is observed in the austenite matrix, often associated with oxide inclusions. In Fig 6.21 a carbide particle (indicated by arrow) showing fringe contrast is seen to have nucleated at an undissolved particle within the austenite grain. The selected area diffraction pattern in Fig 6.21b indicates a cube on cube orientation relationship with the matrix. On further ageing, this form of precipitation continues to grow until the particle reaches a size of about 0.3μm after 1000 hours ageing. In Fig 6.22, a typical $M_{23}C_6$ particle with four bounding surfaces is shown in which the interfaces exhibit an array of dislocations in the image. The array of dislocation is believed to be generated in order to accommodate the precipitate/matrix interface misfit. Consequently the precipitate is not fully coherent.

χ phase

At 700°C a new phase is found to precipitate in the matrix. After 1000 hours of ageing, the intragranular precipitation of χ phase is detected, Fig 6.23. The particles are usually massive, showing more than four bounding surfaces as in Fig 6.23, and often, on growing, engulf Z particles in the austenite matrix, Fig 6.24. The χ phase observed in the present work has a body centred cube crystal structure with lattice parameters a=8.81 A. The unit cell size differs slightly from that reported in the literature[24,49,50] (Table 2.3), but small changes in the stoichiometry of χ phase might be expected to produce this change as can be seen from the electron energy dispersive microanalysis results obtained by scanning transmission electron microscopy. The spectrum in Fig 6.25 and the corresponding composition in wt % of the elements present in the phase (determined using standard thin foil correction programs to compensate for X-ray detection efficiency and absorption) shows a high content of Fe, Cr and Mo in agreement with the results reported by other authors[24,49]. However the actual percentage of each element differs from those in Table 2.3 and from that obtained by Weiss and Stickler[20] (22 wt % Mo, 21 wt % Cr, 52 wt % Fe, 5 wt % Ni). This indicates that χ phase can vary appreciably in composition with a high tolerance for metal interchange and may explain the variations observed in lattice parameters by various workers. The crystallographic relationship of χ phase particles and austenite matrix in the present investigation (Fig 6.24) agrees with that reported in the literature[74]:

$$\{111\}\ \gamma\ //\ \{110\}\ \chi$$
$$\langle 01\bar{1}\rangle\ \gamma\ //\ \langle \bar{1}10\rangle\ \chi$$

In REX 734 stainless steel, $M_{23}C_6$ carbide precipitation preceded χ phase precipitation at all temperatures. Similar observations have been reported by Weiss and Stickler[20], who additionally suggested that $M_{23}C_6$ carbide may act as a nucleation site for χ and σ phases particularly at grain boundaries. They have also shown that, in low carbon steels, χ phase formation precedes that of σ, but the formation curves tended to be at higher temperatures and longer times than those for the carbide phase. In the present investigation no σ phase was detected at temperature below

900°C as will be seen later, and the χ phase precipitation reaction occurs within the temperature range of $M_{23}C_6$ but at a longer ageing time. At 700°C ageing no association is found between $M_{23}C_6$ and χ phase particles. However, at higher temperatures χ particles are frequently observed at grain boundaries in close contact with remnants of $M_{23}C_6$ particles (see next section). At low temperatures (600-700°C) in REX 734, large $M_{23}C_6$ particles dominate the boundaries and are found to be stable up to 1000 hours.

6.4.3 Summary

a) Intergranular reactions

$$\text{Z phase} \xrightarrow[700°C]{10\text{hrs}} M_{23}C_6$$

b) Intragranular reactions

$$\text{Z phase} \xrightarrow[700°C]{100\text{hrs}} M_{23}C_6 \xrightarrow[700°C]{1000\text{hrs}} \chi \text{ phase}$$

6.5 Structures After Ageing at 800°C

At 800°C the precipitation reactions at short ageing times (up to 10 hours) were similar to 700°C with respect to phase occurrence, though differences in nucleation and growth rates were observed.

6.5.1 Grain Boundary Precipitation Reaction

Following the general trend established at 700°C the first type of precipitate to occur at grain boundaries was the small equiaxed Z phase particle. This mode of precipitation was established after 1 hour and always preceded the nucleation of any other phase on the grain boundaries. Further ageing at 800°C produced only a limited number of intergranular particles, since other phases were competing for the same nucleation site. The Z phase precipitation reaction at grain boundary was quickly followed by the nucleation and growth of $M_{23}C_6$ around Z phase particles. As mentioned before, $M_{23}C_6$ particles were seen to have grown and engulfed the

small equiaxed Z phase particles, which marked the position of the original grain boundary. An example of this effect is shown in Fig 6.26.

The twin boundary precipitation reaction of Z phase was also faster than that at 700°C, and is well established at coherent twin boundaries after 100 hours, Fig 6.27. By this stage of the ageing reaction, the grain boundaries $M_{23}C_6$ particles had become unstable transforming to χ phase. Evidence of this transformation is shown in Fig 6.28. Particles X in Fig 6.28 are χ phase, particles N are Cr_2N and C are $M_{23}C_6$. A convergent beam diffraction pattern of those particles is shown in Fig 6.29. Particle T in Fig 6.28 and the corresponding convergent beam in Fig 6.29d shows undoubtedly a body-centred cubic structure (the b.c.c $[\bar{1}12]$ zone axis is markedly different in angle and interplanar distance ratio from the f.c.c $[\bar{1}12]$ for example). This indicates that particle T is not a $M_{23}C_6$ (face-centred cubic). The lattice parameter of this phase (designated in the present work as χ' phase) is a=10.18 Å which is larger than χ phase detected in REX 734 (a=8.81 Å). However, the chemical analysis of the phase shows a composition relatively close to the $M_{23}C_6$. Utilizing the microanalysis attachment on the scanning transmission electron microscope the state of the precipitate reaction could be quantified. In Fig 6.30 a STEM image, of the same boundary at Fig 6.28, indicates the location of the microanalysis in each particle at the grain boundary. The spectrum obtained for each particle is given in Fig 6.31 with the corresponding quantitative results. It can be seen from Fig 6.31g that the microanalysis of the b.c.c particle T (χ' phase) is relatively close to that of the $M_{23}C_6$ particle in Fig 6.31h, although richer in Fe and Mo, and depleted in Cr. This suggests that $M_{23}C_6$, in the process of dissolving, reaches a chromium composition compatible with the formation of χ phase. The Fe and Mo content needed to stabilize the χ phase would then be provided by the matrix. The neighbouring area replenished in chromium and depleted in Mo and Fe would then form, with the nitrogen available, the Cr_2N phase, which tends to be a favourable precipitation reaction at high temperatures in high nitrogen stainless steels.

After 1000 hours of ageing at 800°C no $M_{23}C_6$ is detected at the grain boundaries, but particles of χ phase and Cr_2N can be seen instead, in alternating disposition along the grain boundaries. An example of this is

shown in Fig 6.32.

In agreement with Weiss and Stickler[20], in the present steel, $M_{23}C_6$ acts as nucleation sites for χ phase. The instability of $M_{23}C_6$ at high temperature and long ageing time has been reported by several authors[37,62,63], some of whom have observed the replacement of this carbide by others more stable such as NbC, TiC or intermetallic phases such as σ and χ. The nucleation of either σ or χ phase strongly depends on the composition of the alloy and ageing treatment. However, in the presence of $M_{23}C_6$ another suitable site for the precipitation of χ phase and σ is provided since the carbide, during the process of dissolving, would, to a large extent, contribute to the basic elements needed for the formation of those phases. In the present investigation the high content of Mo as well as the ability of χ phase to dissolve carbon as postulated by Goldschmidt[25], is thought to have encouraged the formation of χ phase rather than σ.

The Cr_2N observed at the grain boundaries after 100 hours ageing at 800°C has a hexagonal structure with lattice parameter a=2.77 A c=4.45 A, c/a=1.60. Small variations in lattice parameter were observed when the chromium content of the precipitate is low (~ 68 wt %), spectrum in Fig 6.31e. A typical composition of Cr_2N in REX 734 is shown in Fig 6.31b and 6.31d where the chromium content is about 88 wt %. Electron energy-loss microanalysis of Cr_2N precipitates confirm the presence of nitrogen. A typical spectrum, Fig 6.33, was recorded for a grain boundary chromium nitride particle at the edge of a foil cooled to 100°K to reduce surface diffusion of contaminants. The quantity of a particular element contributing to the measured intensity (number of atoms per cm^2 of surface within the incident electron beam) is obtained in the same way as described for carbon (section 6.3.1 and example in Appendix 1). The results shown in the right-hand corner of Fig 6.33 give a Cr/N ratio of 2.5. This is a quite good result on the quantification of EELS data considering that the accuracy usually obtained is about 20%, and the actual ratio of chromium to nitrogen is 2.

The Cr_2N particles in REX 734 austenitic stainless steel were massive and precipitate only at grain boundaries in close association with χ phase

during the dissolution of $M_{23}C_6$. However, no carbon was detected in Cr_2N particles by EELS analysis, which suggests that some carbon may have dissolved in χ phase as proposed by Goldschmidt[25]. This could not be confirmed by EELS since no particle of χ phase sufficiently thin could be obtained. Although attempts were made, no fixed orientation relationship could be found between χ phase and Cr_2N.

The precipitation reaction of χ phase and Cr_2N observed at grain boundaries after 100 hours of ageing at 800°C seems to continue, so that after 1000 hours it can be seen at twin boundaries in optical micrographs, Fig 6.34.

6.5.2 Intragranular Precipitation Reaction

At 800°C, the intragranular precipitation reaction followed that observed at 700°C, showing small equiaxed Z particles on dislocation. The growth rate is faster with the equiaxed particles quickly developing into small cuboids such that after 100 hours these cuboids were about 550 Å, and frequently generated dislocations around themselves. At this stage of ageing it was observed that stringers of Z particles led to the development of secondary branches. The secondary stringers precipitation involves Z phase cuboids radiating from primary stringers, and such an arrangement is clearly shown in Fig 6.35. The creation of dislocations which act as nuclei for the stringers of precipitates forming the branches will be discussed in Chapter 7 where evidence is given for the formation of dislocation loops around growing Z phase cuboids.

At 800°C in REX 734, the matrix precipitation of Z phase is followed by $M_{23}C_6$ and χ phase precipitation. After 100 hours ageing both $M_{23}C_6$ and χ phase had nucleated in the matrix and had grown to a large size. Continued ageing did not necessarily lead to further precipitation of the carbide; however, in the case of χ phase the reaction had advanced to the stage where χ phase was predominant over $M_{23}C_6$. The χ phase morphology observed at this temperature was the same as that at 700°C. In the optical microscope, the matrix χ particles can be seen as rods and faceted particles, Fig 6.36, depending on the orientation in relation to the surface of the specimens. The low aspect ratio suggests that the

morphology of χ phase is that of a faceted rod shape. Thin foil transmission electron microscope images in Figs 6.37 and 6.38 show typical χ phase particles detected after 100 hours and 1000 hours of ageing respectively. In Fig 6.38 the matrix/particle orientation relationship is confirmed, and dislocation can be observed emerging from the χ particle. These dislocations are thought to relieve the stresses generated by the growing particle. Detailed crystallographic work would be necessary in order to determine the orientation of the χ particle facets and the preferred growth directions.

6.5.3 Summary

a) Intergranular reactions

$$\text{Z phase} \xrightarrow[800^{\circ}C]{10hrs} M_{23}C_6 \xrightarrow[800^{\circ}C]{100hrs} \chi \text{ phase} + Cr_2N$$

b) At grain boundaries after 1000 hrs $M_{23}C_6$ carbides are replaced by χ phase and Cr_2N.

c) Intragranular reactions

$$\text{Z phase} \xrightarrow[800^{\circ}C]{100hrs} M_{23}C_6 + \chi \text{ phase}$$

6.6 Structures After Ageing at 900°C

6.6.1 Grain Boundary Precipitation

At 900°C the precipitation at short ageing times followed the general trend observed at lower temperatures with Z phase particles occurring as the first precipitate at grain boundaries. The precipitation reaction appears to be faster at 900°C than at lower temperatures, with small cuboids being detected after one hour. On further ageing, other phases such as χ phase, Cr_2N and σ phase competed with Z phase for the same nucleation sites, and were seen to grow and surround Z phase particles which delineated the original austenite grain boundary. At the boundary

regions containing only Z phase, this grew into large cuboids, some of them reaching a size of about 2000 Å after 1000 hours ageing. No $M_{23}C_6$ carbides could be detected at this temperature.

After 100 hours at 900°C not only χ phase and Cr_2N were observed at grain bounderies, as at lower temperatures, but another phase, the intermetallic σ phase, could also be detected. Although χ phase and Cr_2N were dominant over σ phase, the latter were seen to occur either close to Cr_2N particles, Fig 6.39, or more often as isolated particles, Fig 6.40 (contamination spots from EDS analysis are seen over the particle and matrix). The massive σ particles (about 1μm in size) generate dislocations during growth to accommodate the strains produced by the difference in volume between the precipitate and matrix, and some of the dislocations dissociated to produce stacking faults as seen in Fig 6.40. At twin boundaries the σ phase, although massive in appearance, takes a more "globular" shape, as seen in Fig 6.41. The particle in Fig 6.41 can be seen to have grown on either side of the nucleating twin boundary which is delineated by pre-existing Z phase precipitate.

The σ phase particles were unambiguously identified by selected area diffraction patterns, as shown in Fig 6.42, where different zone axes from σ particle in Fig 6.40 were obtained by tilting the specimen. The lattice parameter of σ phase in the present investigation was found to be a=8.86 Å and c=4.6 Å, which is close to σ phase observed by other workers, as will be seen later. The phase was also identified by its characteristic spectra obtained using STEM dispersive analysis. This is not to say that the spectra from particles of the same phase were identical; for example, a spectrum obtained from σ phase particle in Fig 6.39 is shown in Fig 6.43, where the FeKα and CrKα peaks are almost equal. The other elements detected in the phase in small quantities were nickel and molybdenum. Fig 6.44 shows a spectrum from σ phase in Fig 6.40. This spectrum is more characteristic of σ phase which forms either in the matrix or as an isolated particle at the grain boundaries. The composition of σ phase obtained using standard thin foil correction programs to compensate for X-ray detection efficiency and absorption is 51Fe 31Cr 9Mo 4Ni (wt %) as indicated at the right-hand corner of Fig 6.44. It should be pointed out that care was taken to ensure that the variations in the spectra from the

same phase could not be attributed to factors such as accelerating voltage of the electron beam and the detector/specimen geometry since these were always constant. The variations were related to features such a closeness to other phases and particle size, but were not so great as to create any ambiguity.

Andersson and Lundberg[168] reported a series of σ phase compositions and unit cell dimensions for σ phase precipitation in a 25Cr 20Ni (wt %) steel which contained varying levels of molybdenum. The chemical analysis of the present material showed that 2.6 wt % Mo is present in the steel. In Andersson and Lundberg's steels, over a similar molybdenum content, the precipitating σ phase had a composition in the range 39-36Cr, 43Fe, 9Ni, 3-7Mo (wt %) which showed that, as the molybdenum content of the σ phase increased, the chromium levels correspondingly decreased to accommodate the additions. The lattice parameters of the σ phase in this compositional range were a=8.825-8.845 A and c=4.575-4.597 A, i.e. as the molybenum level increased, the lattice parameters increased accordingly though the c/a ration remained constant. An equivalent σ phase precipitate from Andersson and Lundberg's study with 9 wt % Mo had unit cell dimensions a=8.855 A c=4.596 A, which compares with the σ phase seen in the present material, REX 734, of a=8.86 A c=4.6 A. Weiss and Stickler's[20] σ phase in their AISI type 316 alloy had unit cell dimensions a=8.832 A c=4.599 A and an approximate composition 29Cr, 11Mo, 5Ni, 55Fe (wt %).

In the present investigation, ageing after 1000 hours did not produce a significant change in the precipitation reaction at grain boundaries except for the particle size, with σ phase ranging between 2-5μm in size.

An important aspect of the nucleation and growth reaction of phases such as $M_{23}C_6$, Cr_2N, χ phase and σ phase throughout the ageing treatment of REX 734 steel was their lack of interaction with previous precipitated Z phase during its formation and growth. Many examples of this were seen, as shown in Figs 6.26, 6.32 and 6.41, where large grain boundary particles of $M_{23}C_6$, Cr_2N, χ and σ phases grew to engulf Z phase particles. The Z phase particles clearly delineate the position of the original grain boundary.

6.6.2 Intragranular Precipitation Reaction

As also happens at lower temperatures, the Z phase was the first precipitate to occur at 900°C on dislocations in the matrix. As a result of the faster precipitation kinetics at this temperature, the stringer precipitation of Z phase cuboids was established after 10 hours, and after 100 hours these cuboids were about double the size of those observed at 800°C (500 A). The Z phase precipitation reaction in the matrix did not seem to have been completed even after 1000 hours, when some cuboids reached a size of about 1600 A, Fig 6.45. Evidence of this will be given in the following section.

Following the intragranular precipitation of Z phase, χ phase is found to precipitate in the austenite matrix after 100 hours, having the same morphology, e.g. faceted rod shape (Fig 6.46) or massive (Fig 6.47) as described at lower temperatures. On further ageing the χ particles grow to about 5μm long as seen in Fig 6.48.

Long ageing time at 900°C led to the precipitation of a new intermetallic phase in the matrix, not observed at lower temperatures. This intermetallic phase was identified as σ phase. The particles were massive, as seen in Fig 6.49, and quite often had faults. A number of dislocations were always seen around these large particles (about 4μm in size after 1000 hours) as described at grain boundaries. Although it was not possible to obtain thin foil specimens containing σ phase after 100 hours, it is believed that the precipitation of the phase may have occurred around that time since the size of the intragranular particles at 1000 hours were about the same as those observed at the grain boundary at 1000 hours, and it has already been shown that σ phase is detected at these sites after 100 hours.

A specific orientation relationship could not be found between σ phase and austenite, although some particles would be consistent with the following parallelism between planes as indicated in the diffraction pattern in Fig 6.49.

$$(110)\gamma \;//\; (001)\sigma$$

Lewis[64] has claimed that all the intragranular acicular σ precipitates he analysed supported an orientation relationship first proposed by Nenno et al[49] which was

$$(111)\gamma \;//\; (001)\sigma$$
$$[0\bar{1}1]\gamma \;//\; [140]\sigma$$

Duhaj et al[55], on the other hand, could not find a specific orientation relationship which would satisfy all the precipitates analysed but proposed that the precipitation reaction was almost always consistent with one of three parallelisms between planes:

$$(111)\gamma \;//\; (100)\sigma$$
$$(110)\gamma \;//\; (001)\sigma$$
$$(112)\gamma \;//\; (100)\sigma$$

The first relationship was the most common.

In the present investigation the results seem to agree with the second relationship above, proposed by Duhaj[35]; however further analysis of the crystallography of σ phase in REX 734 would be needed to confirm the orientation relationship between σ and austenite.

6.6.3 Summary

a) Intragranular reactions

$$\text{Z phase} \xrightarrow[900°C]{100\text{hrs}} \chi \text{ phase} + Cr_2N + \sigma \text{ Phase}$$

b) Intragranular reactions

$$\text{Z phase} \xrightarrow[900°C]{100\text{hrs}} \chi \text{ phase} + \sigma \text{ phase}$$

6.7 Structure After Ageing at 1000°C

6.7.1 Grain Boundary Precipitation Reaction

The precipitation reaction at 1000°C was markedly different from that at lower temperatures. The ageing of REX 734 at this temperature resulted in a dominant precipitation of Z phase at all nucleation sites. The precipitation reaction of Z phase was faster at 1000°C than at lower temperatures, but the density of precipitate was lower. After one hour of ageing the Z phase was observed at grain boundaries, and the morphology of the particles was cuboid. On further ageing, the grain boundary particles continue to coarsen to about 450nm, Fig 6.50. The precipitation reaction at grain boundaries appeared to be complete after 100 hours. At this stage, a crystalline structure was detected around Z phase particles, Fig 6.51. This phase, designated in the present work as ϕ phase, has a face-centred cubic structure with lattice parameter a=8.3 Å, and is stable after 1000 hours.

The face-centred cubic ϕ phase was identified by thin foil electron diffraction and convergent beam patterns, Fig 6.52, where $[\bar{1}12]$ zone axis is unmistakably of a f.c.c structure. No phase with such a lattice parameter has been reported to occur in stainless steels. Further characteristics of the phase would require microprobe analysis and perhaps ageing treatment at higher temperature in order to establish whether the phase was formed by instability of Z phase or as a result of depletion in solute atoms at neighbouring areas of Z particles as those reach their optimum volume fraction in equilibrium with austenite.

The twin boundary reaction followed a similar trend to the grain boundary reaction, and Z phase precipitation was well established after one hour. The particles were of similar size to the grain boundary precipitates and had the same morphology, Fig 6.53, but the particle density at this site was less than at grain boundaries.

6.7.2 Intragranular Precipitation Reaction

After one hour at 1000°C, a few isolated particles of about 300nm size were observed in the austenitic matrix, Fig 6.54. The Z phase particles quite frequently had dislocations or faults associated with them (arrowed in Fig 6.54) which it is believed are generated in order to relieve stresses during growth. After 100 hours the intragranular precipitation of Z phase appears to be complete, with most of the particles being of the order of 450nm. As observed at grain boundaries at the same ageing time, the ϕ phase could be seen around Z phase particles, Figs 6.55 and 6.56. Electron diffraction patterns obtained from both particles confirm the f.c.c structure for ϕ phase with lattice parameter a=8.3 A. After 1000 hours of ageing, no significant change of intragranular precipitation reaction was detected nor did the ϕ phase around the Z particles grow significantly larger.

6.7.3 Summary

Intergranular and intragranular reactions

$$\text{Z phase} \xrightarrow[1000^{\circ}C]{100hrs} \phi \text{ phase}$$

6.8 General Summary

a) $M_{23}C_6$

$M_{23}C_6$ carbide has been shown to precipitate in REX 734 over the temperature range 600-800°C. The carbide precipitates at grain boundaries, twin boundaries and in the matrix. At 800°C after 100 hrs the carbide became unstable leading to the formation of χ phase and Cr_2N at grain boundaries. The $M_{23}C_6$ has a unit cell size a=10.65 A and its composition is $(Cr_{16}Fe_{4.5}Mo_{1.5}Ni)C_6$. The $M_{23}C_6$ particles were seen to precipitate with a cube-cube orientation relationship with austenite at intergranular and intragranular sites. Intragranularly the carbides were observed on two morphologies, disc-shaped particle and faceted particle.

$M_{23}C_6$ precipitation was particularly dominant at 700°C.

b) Z phase

Z phase precipitates in REX 734 over the temperature range 600-1000°C. Z phase occurs at grain boundaries throughout the temperature range, at twin boundaries, and as intergranular particles precipitate on dislocation. This phase is found to co-exist with $M_{23}C_6$, χ phase, Cr_2N, σ phase and φ phase at their characteristic temperature range. The Z phase precipitation reaction precedes any other precipitation reaction in REX 734 in all nucleation sites between 700°C and 1000°C.

c) χ phase

χ phase precipitates in REX 734 over the temperature range 700-900°C. The phase occurs at intergranular sites and in the matrix. χ phase has a b.c.c structure with lattice parameter a=8.81 A and has a simple orientation relationship with the austenitic matrix. Intragranularly the χ phase has a faceted rod shape morphology. The phase composition is about 48 wt % Fe, 27 wt % Cr, 18 wt % Mo and 5 wt % Ni.

d) σ phase

σ phase precipitates in REX 734 only at 900°C. The particles are massive and are observed at intergranular sites and in the matrix. The phase has a tetragonal structure with unit cell size a=8.86 A c=4.6 A. The phase composition is about 51 wt % Fe, 31 wt % Cr, 9 wt % Mo, 4 wt % Ni.

e) Cr_2N

Cr_2N nitride has been shown to precipitate in the present investigation over the temperature range 800-900°C. The phase is observed to precipitate only at grain boundaries. Cr_2N has a hexagonal structure with lattice parameter a=2.77 A c=4.45 A.

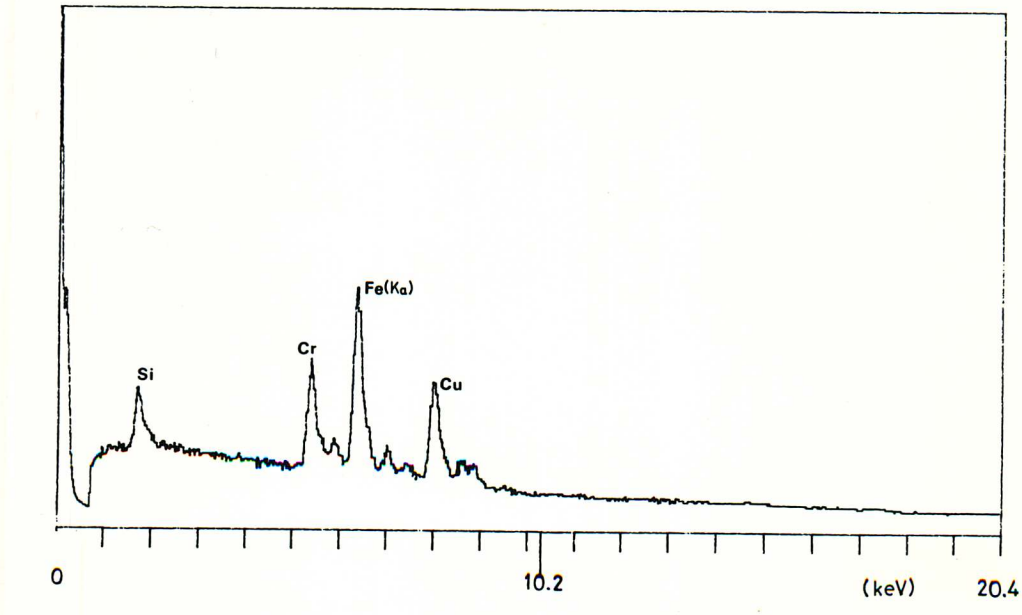

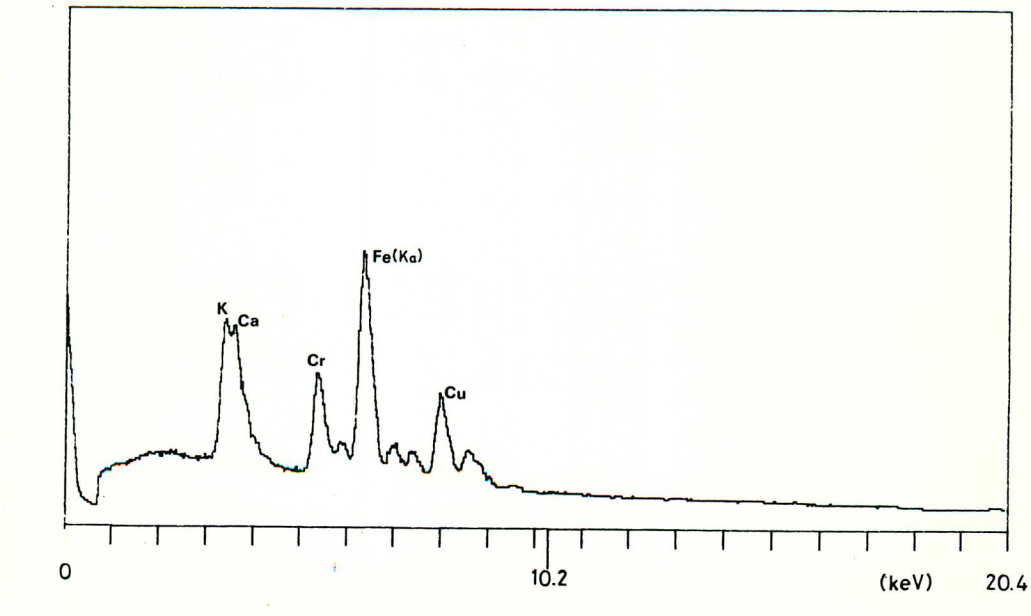

Fig 6.2 Scanning transmission electron microscope microanalysis from other types of inclusions in the austenitic matrix after solution treatment at 1300°C for 1 hr.

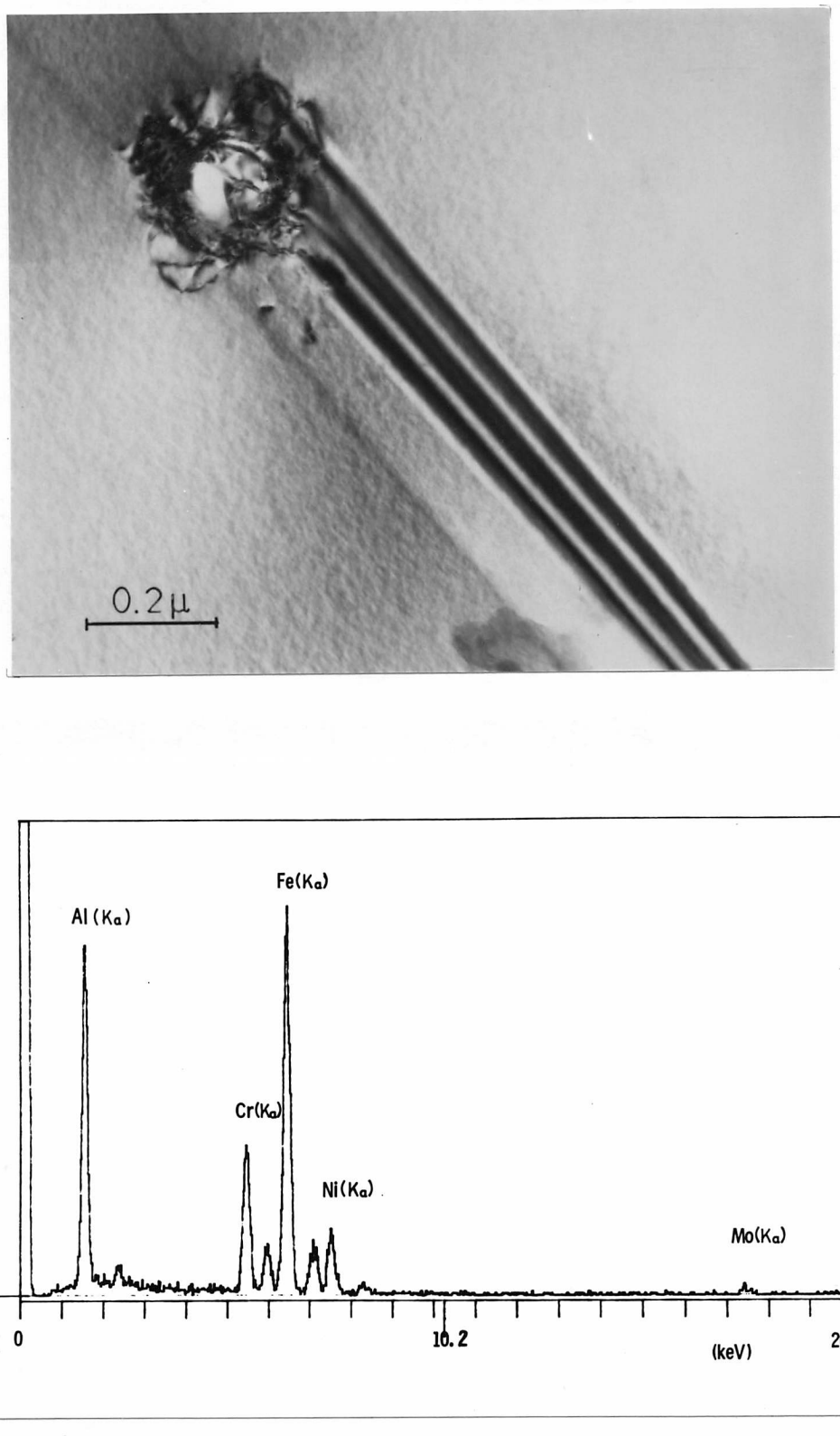

Fig 6.1 Inclusion in the austenitic matrix after solution treatment at 1300°C for 1hr. a) Bright field TEM image; b) Scanning transmission electron microscope microanalysis spectrum from the particle.

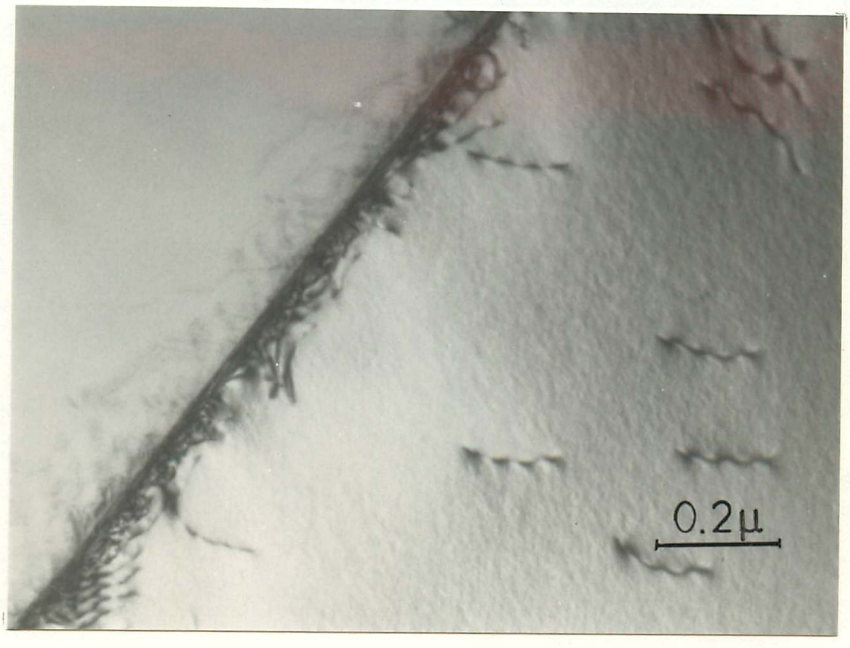

Fig 6.3 Bright field TEM image of a grain boundary free of precipitate after solution treatment at 1300° for 1 hour.

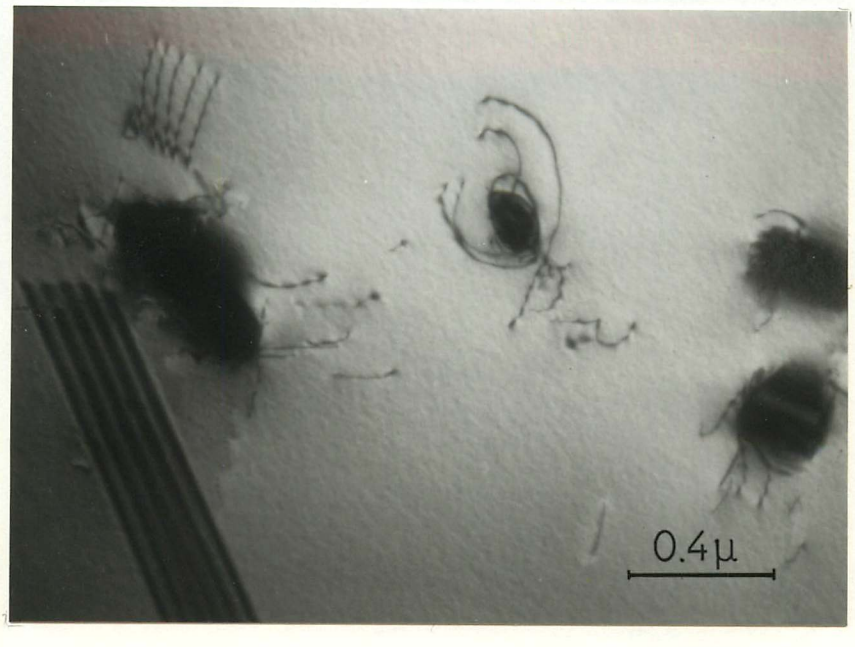

Fig 6.4 Bright field TEM image of dislocations free of precipitate around undissolved particles in the austenitic matrix. Solution treatment at 1300° for 1 hour.

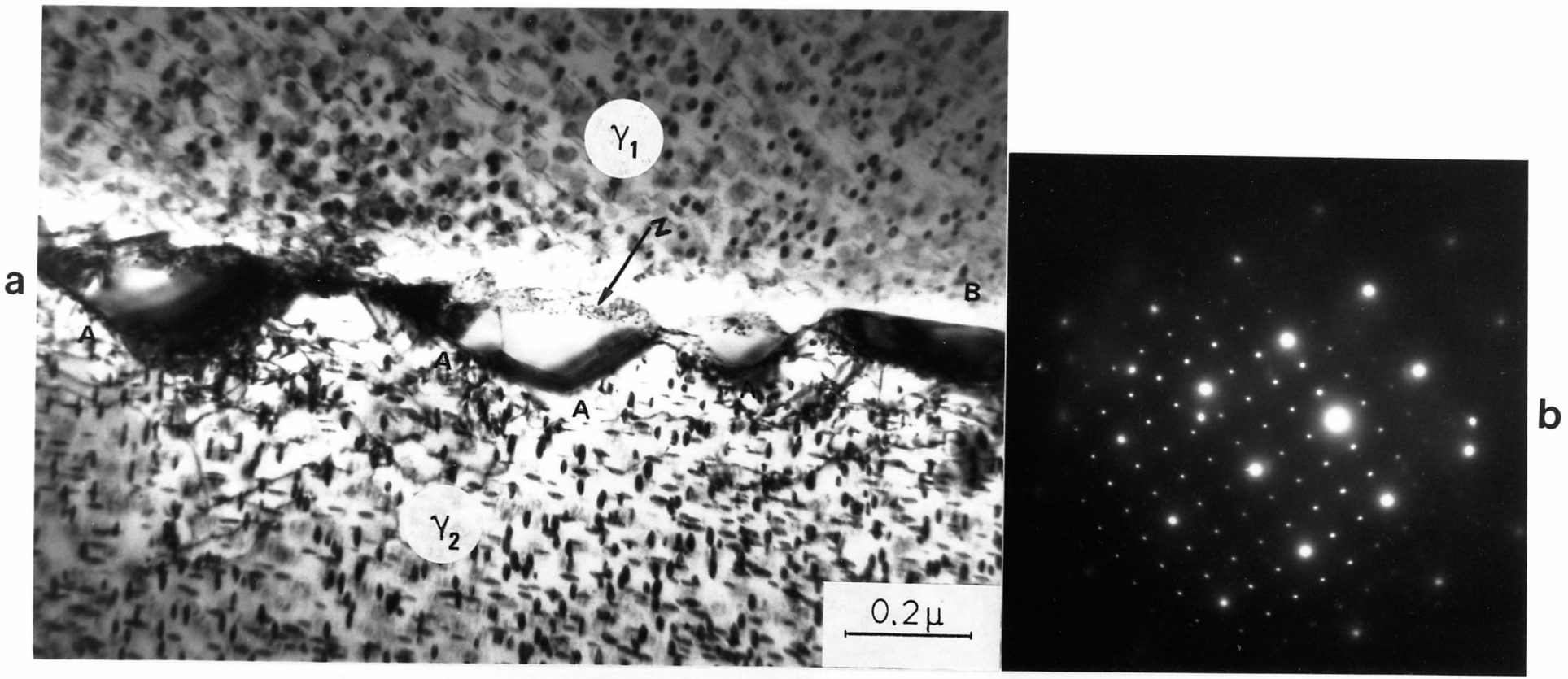

Fig. 6.5 a) Bright field TEM image showing Z phase precipitate (arrowed) and $M_{23}C_6$ precipitate (particles A and B) on grain boundary. γ_1 and γ_2 show matrix precipitation of $M_{23}C_6$. Aged at 600 °C for 1000 hrs.

b) Selected area diffraction pattern of the $M_{23}C_6$ in austenite. Zone axis [001]γ, [001]$M_{23}C_6$.

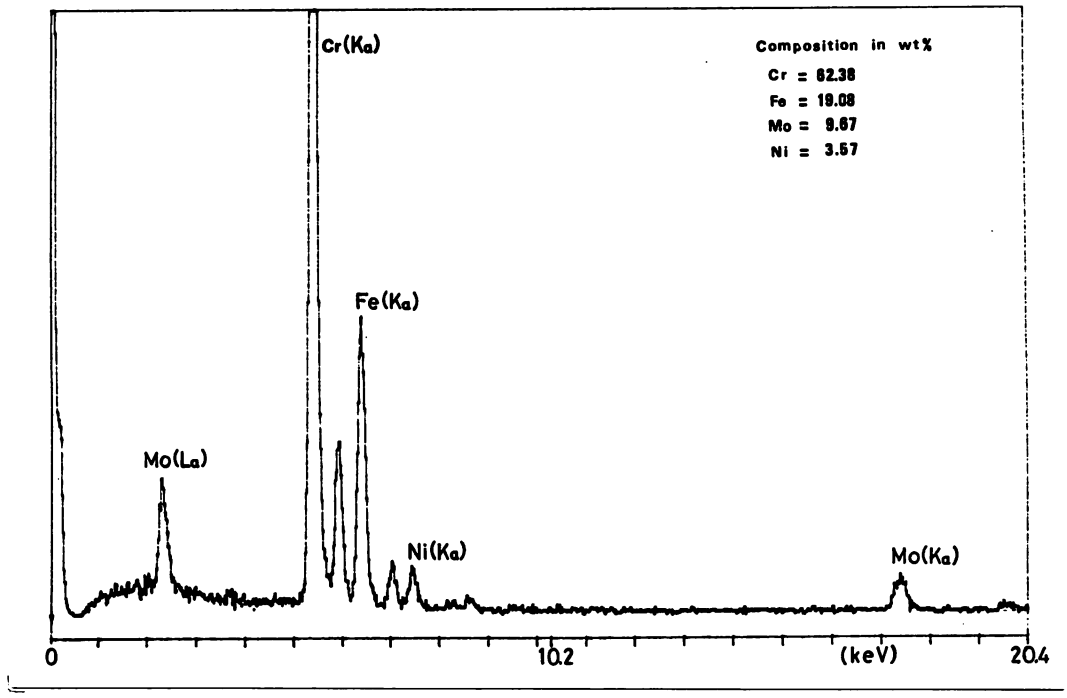

Fig 6.6 Electron energy dispersive spectrum of $M_{23}C_6$ in thin foil specimen.

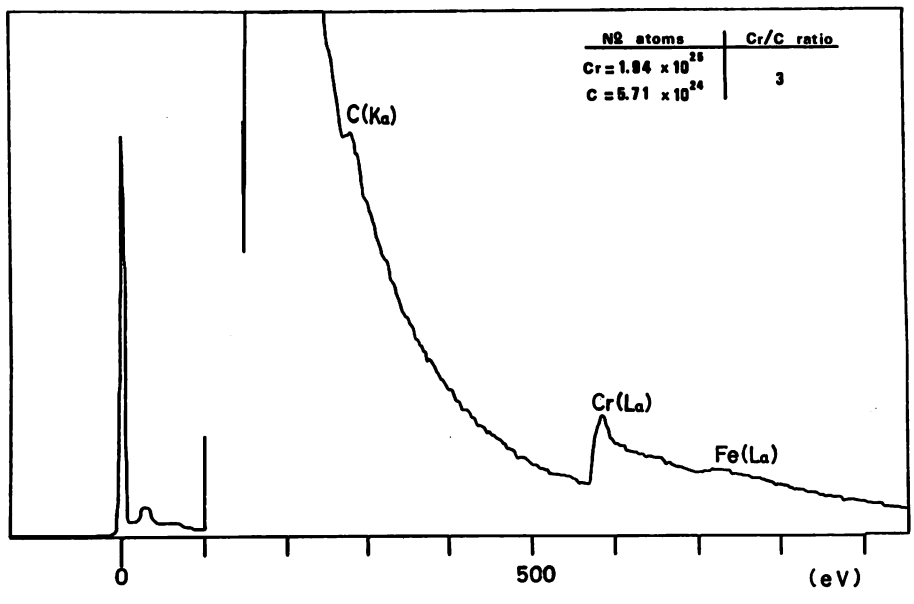

Fig 6.7 Electron energy loss spectrum of $M_{23}C_6$ particle measured with 100kV incident electrons and 18 mrad collection angle, β.

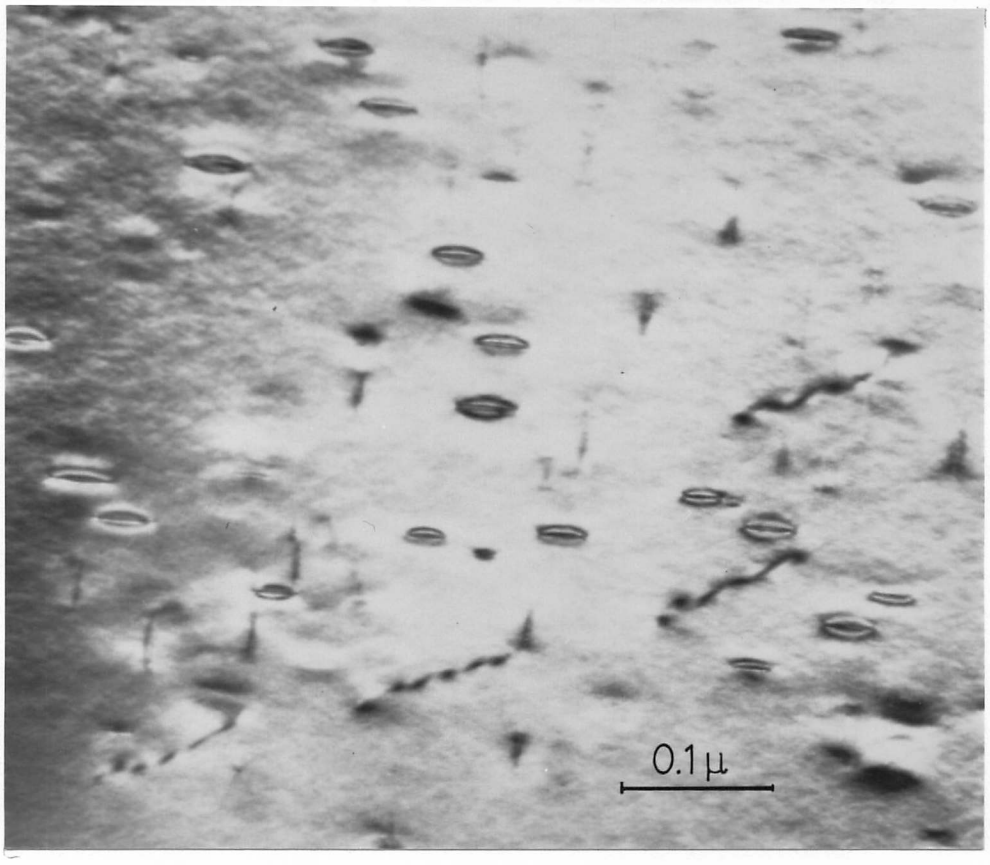

Fig 6.8 Bright field image of $M_{23}C_6$ disc-shaped precipitates in the austenitic matrix showing lobe contrast. Aged at 600°C for 1000 hrs.

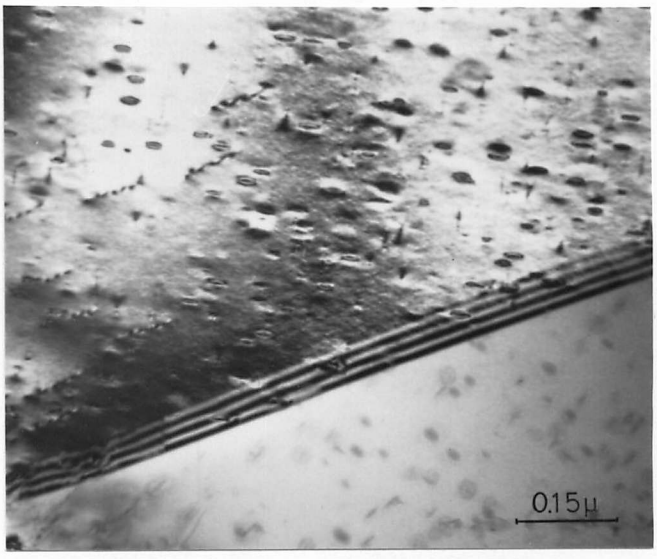

a

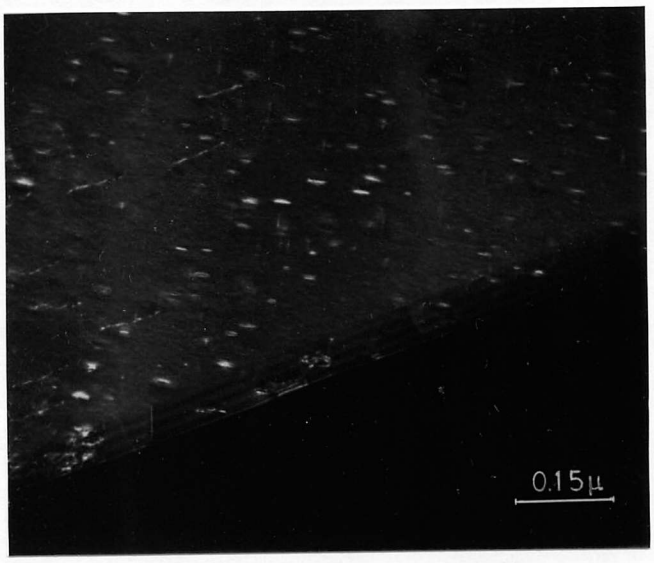

b

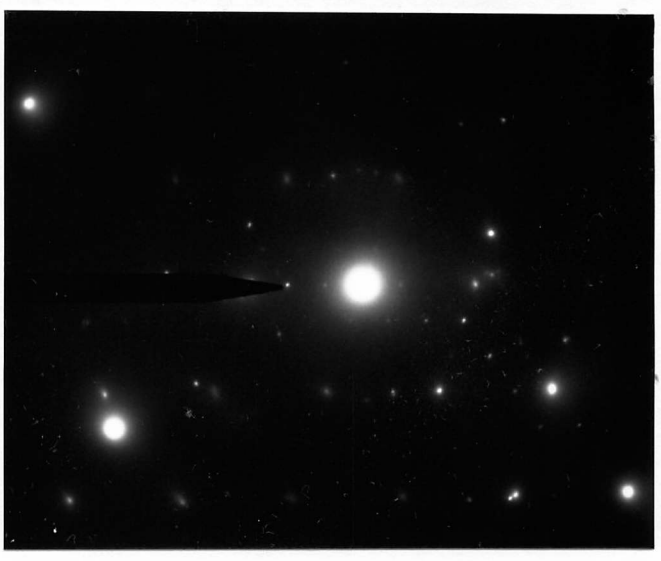

c

Fig 6.9 a) Bright field TEM image showing $M_{23}C_6$ precipitation in the austenite matrix. Aged at 600°C for 1000 hrs.
b) Dark field image
c) Centred dark field diffraction pattern of $M_{23}C_6$. Zone axis [011] $M_{23}C_6$.

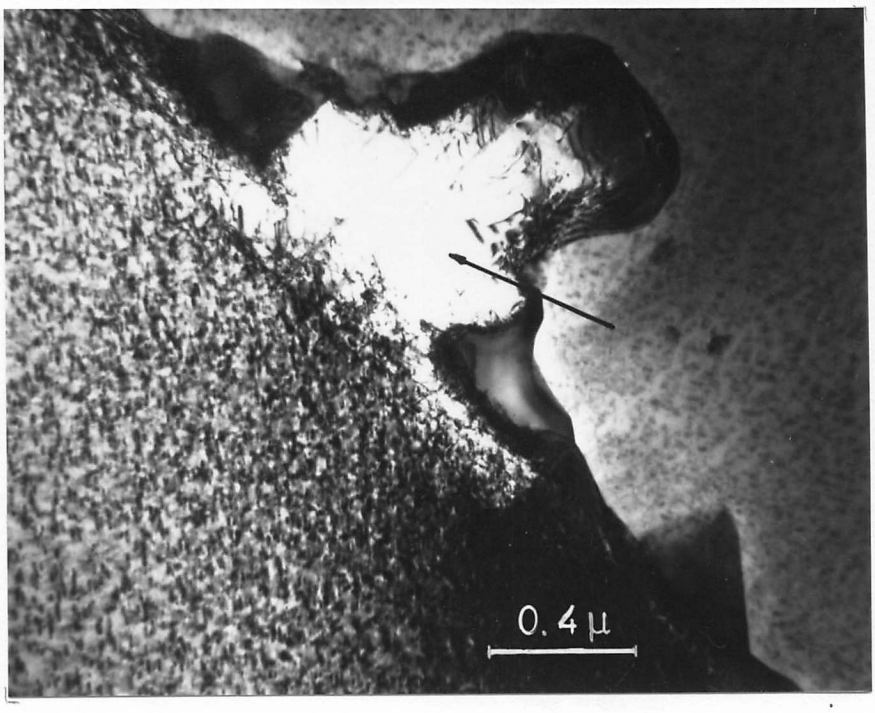

Fig 6.10 Bright field TEM image showing zone free of precipitation (arrowed), and precipitation of $M_{23}C_6$ at grain boundary and matrix. Aged at 600° for 1000 hrs.

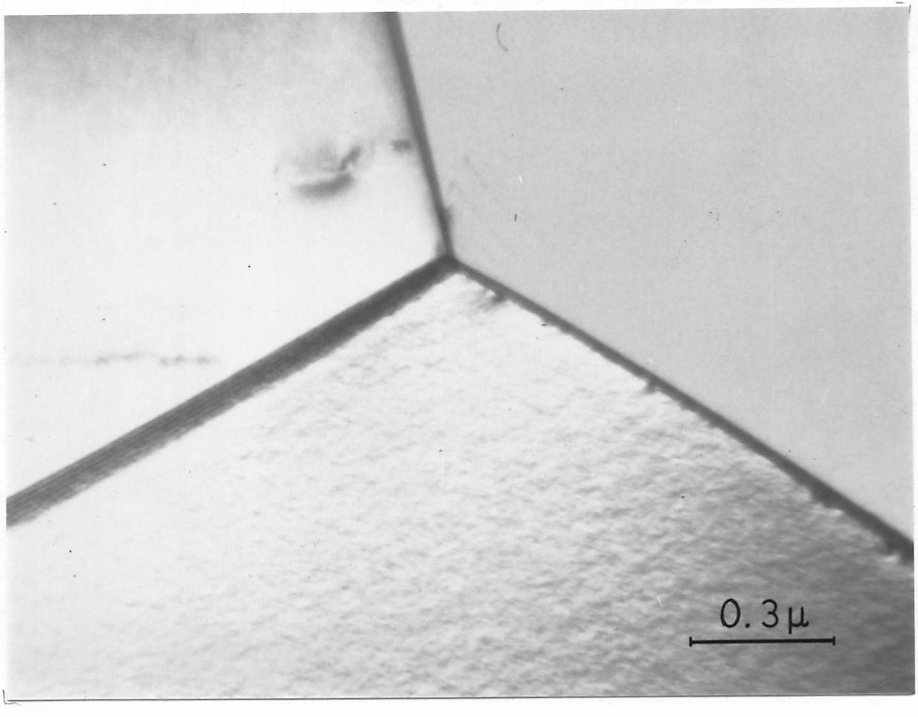

Fig 6.11 Z phase precipitate particles showing strain contrast at grain boundaries. Aged at 700° for 1 hr.

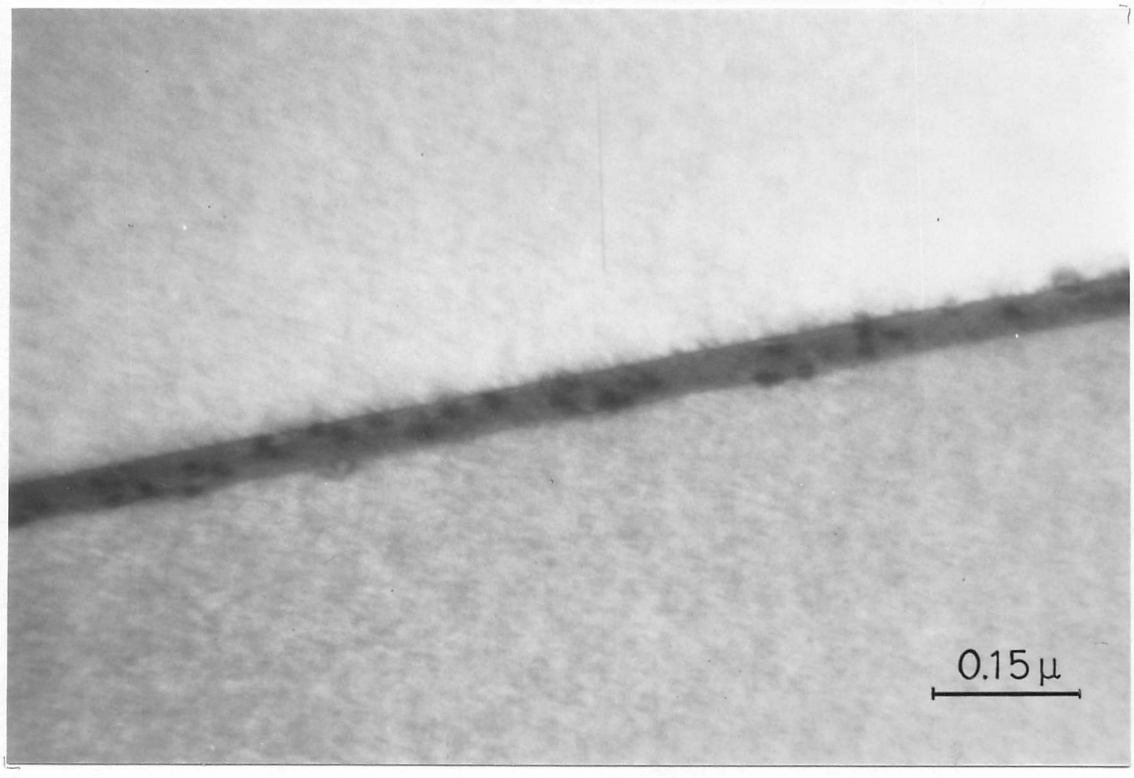

Fig 6.12 Bright field image showing Z phase precipitation at grain boundary. Aged at 700°C for 1 hr.

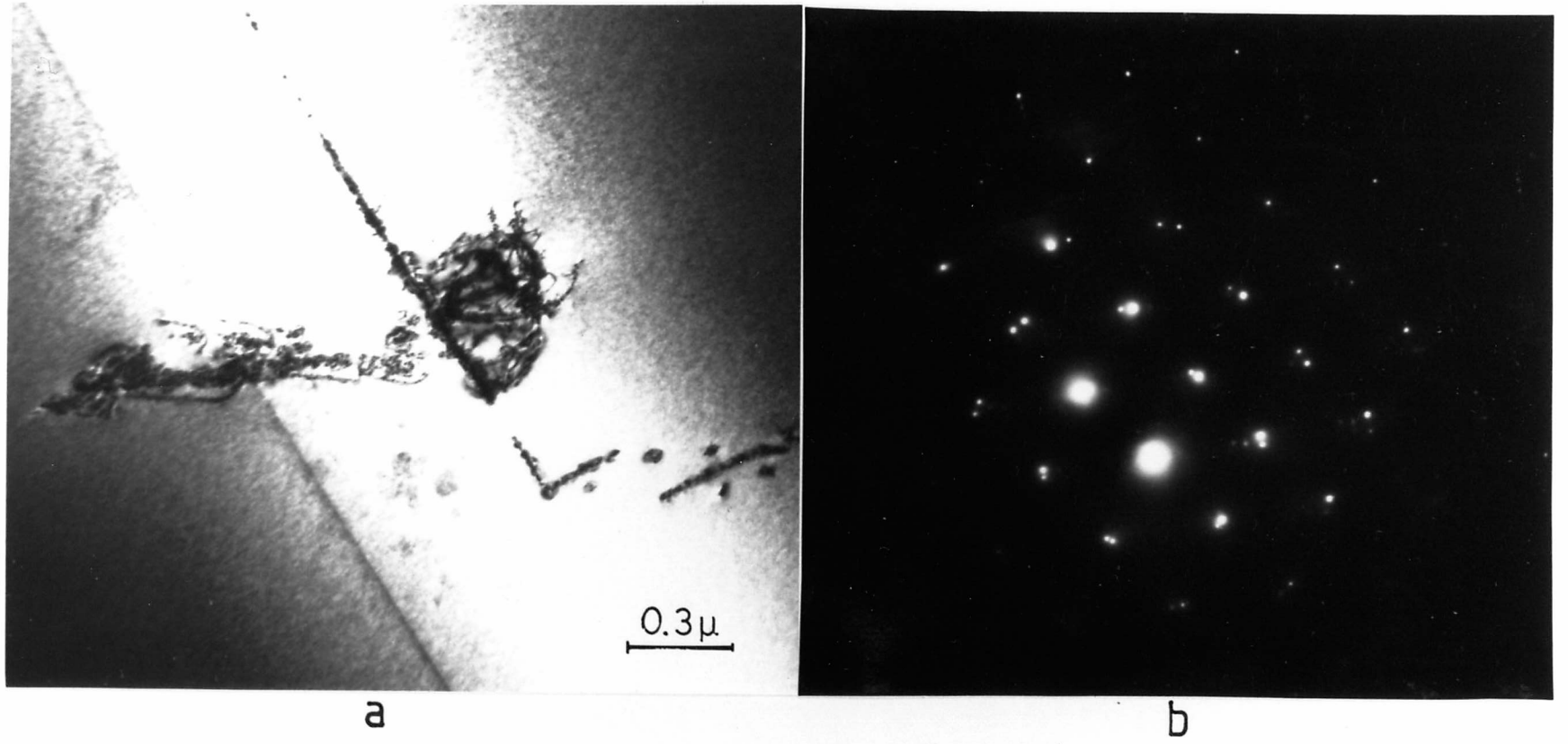

Fig. 6.13 Twin boundary precipitation of Z phase. Aged at 700 °C for 10 hrs. a) Bright field TEM image; b) Selected area diffraction pattern, $[\bar{1}01]Y$, $[\bar{1}\bar{1}0]Z$.

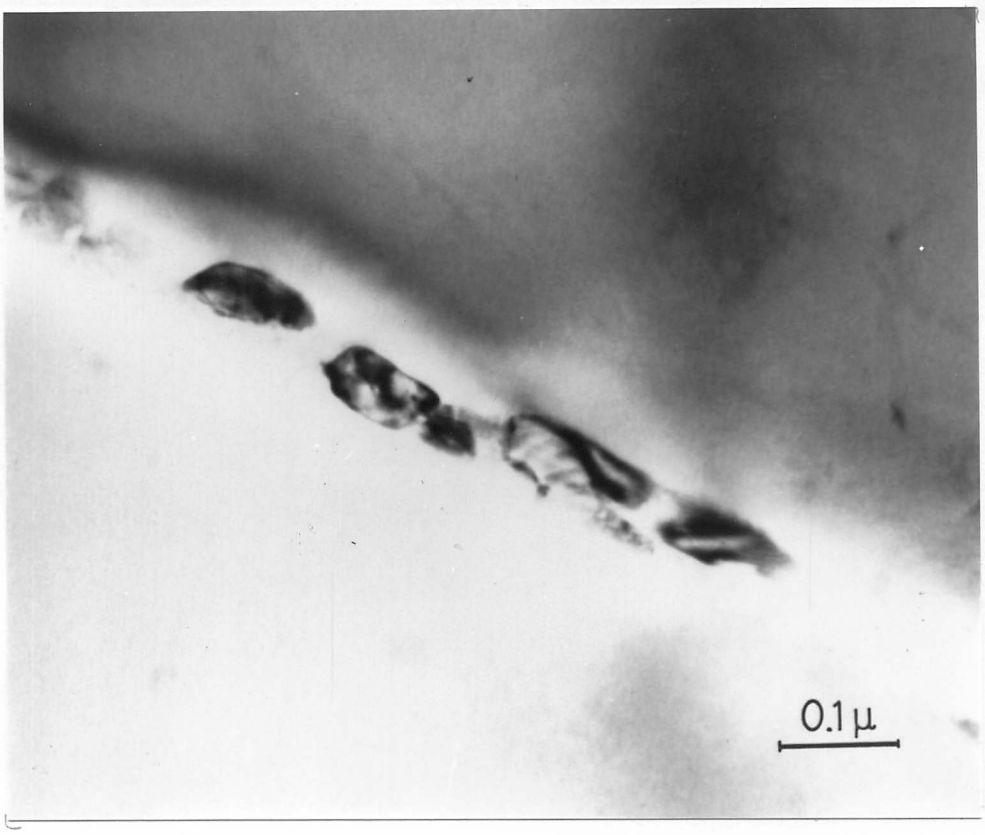

Fig 6.14 Bright field TEM image showing $M_{23}C_6$ at grain boundary. Aged at 700°C for 10 hrs.

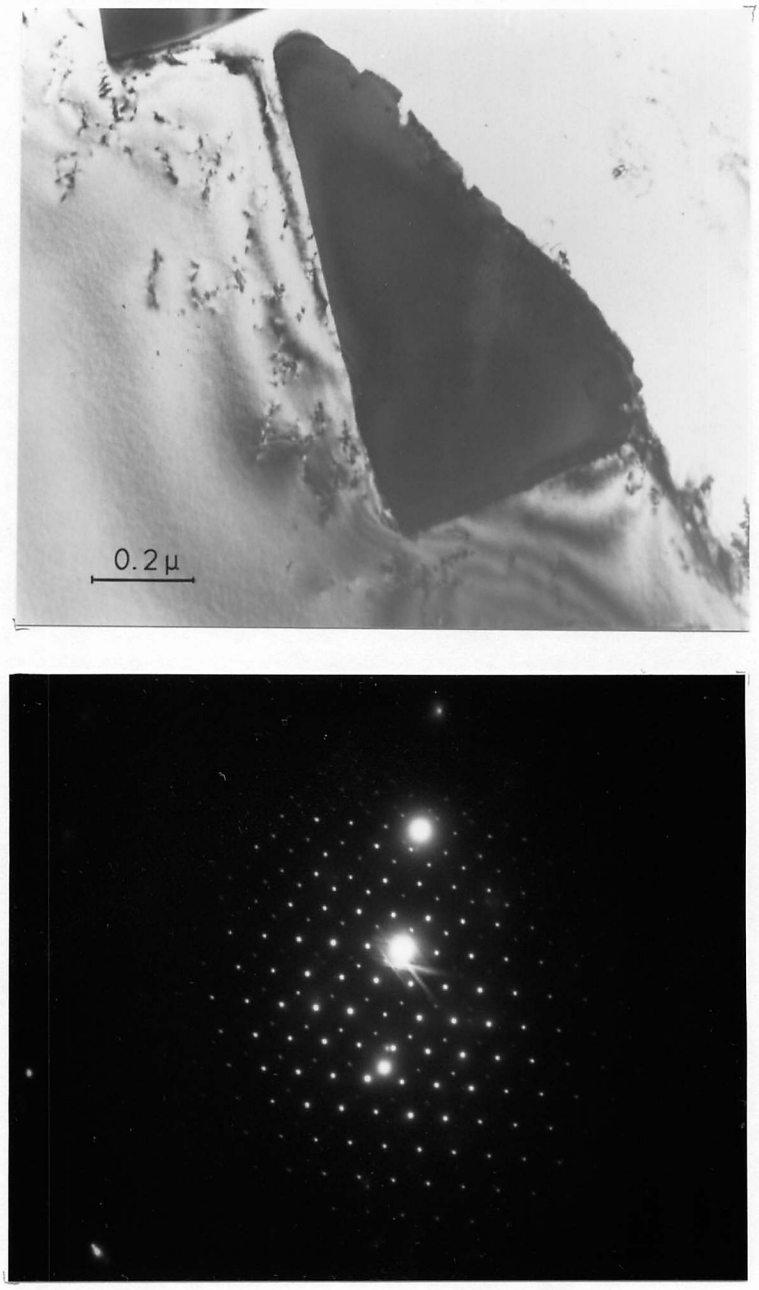

Fig 6.15 $M_{23}C_6$ precipitation at grain boundary after 100 hrs at 700°C. a) Bright field TEM image; b) SADP, zone axis: $[0\bar{1}1]_\gamma$, $[011]_{M_{23}C_6}$.

Fig 6.16 $M_{23}C_6$ precipitation at twin boundary. Aged at 700°C for 1000 hrs. a) Bright field TEM image; b) Dark field image; c) SADP, zone axis: [011]γ, [011]$M_{23}C_6$.

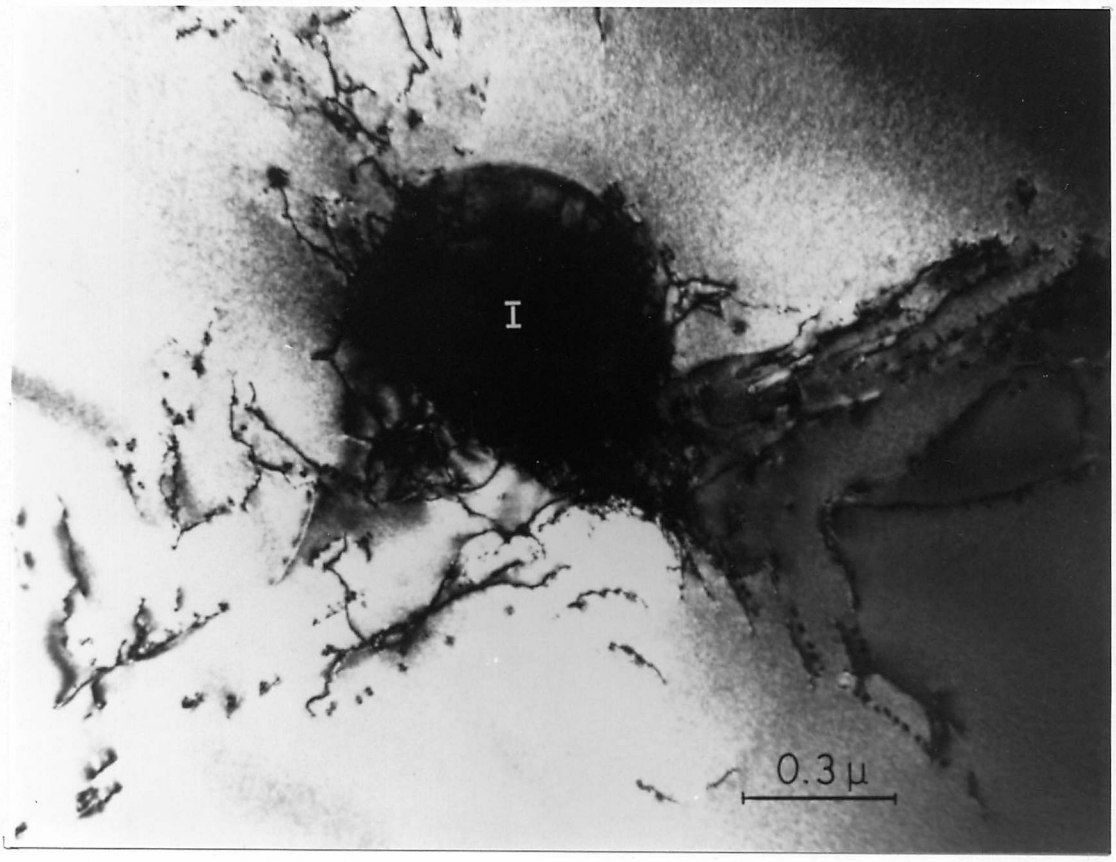

Fig 6.17 Bright field TEM image showing Z phase precipitation on dislocations around undissolved particle (I) in the austenitic matrix. Aged at 700°C for 1 hr.

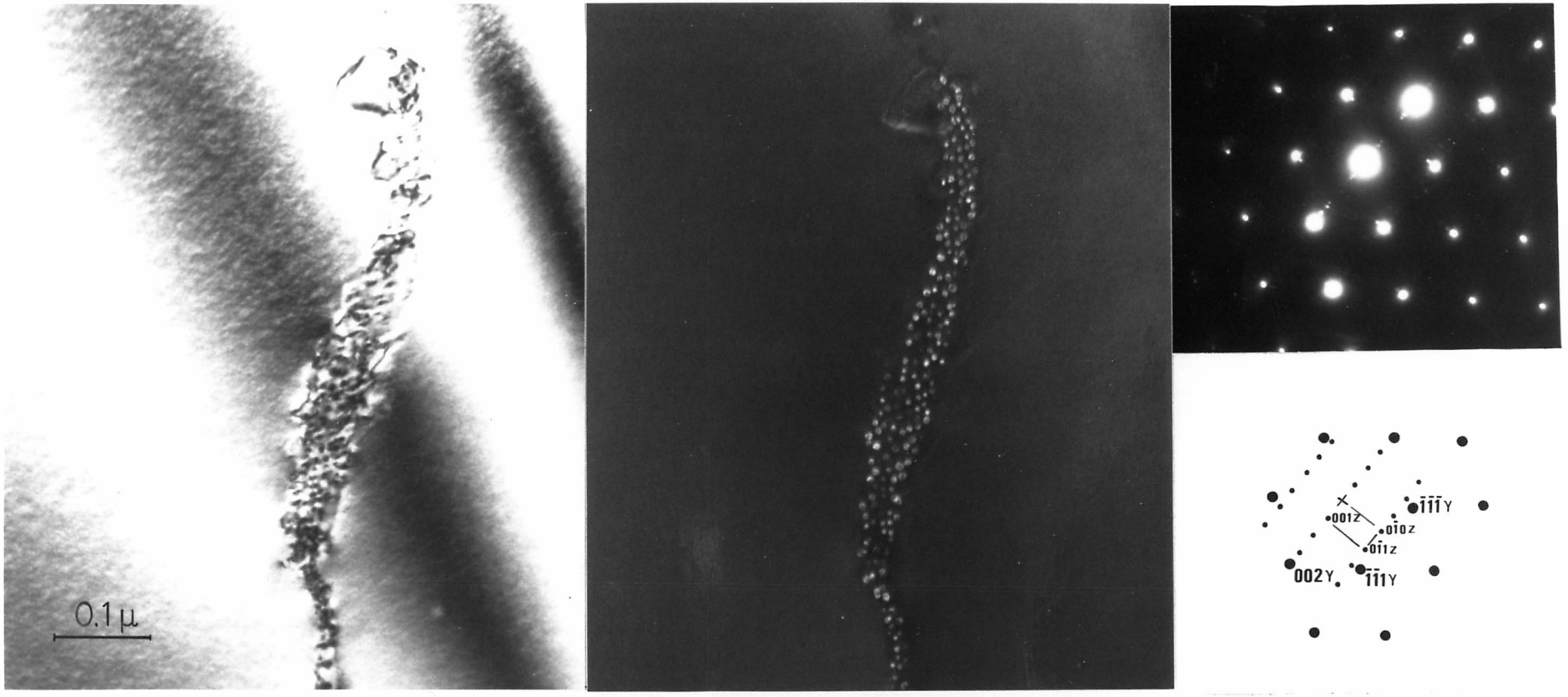

Fig. 6.18 TEM images showing precipitation of Z phase on dislocations after 1 hr at 700 °C.
a) bright field; b) dark field; c) selected area diffraction pattern, zone axis [$\bar{1}$10]Y, [$\bar{1}$00]Z

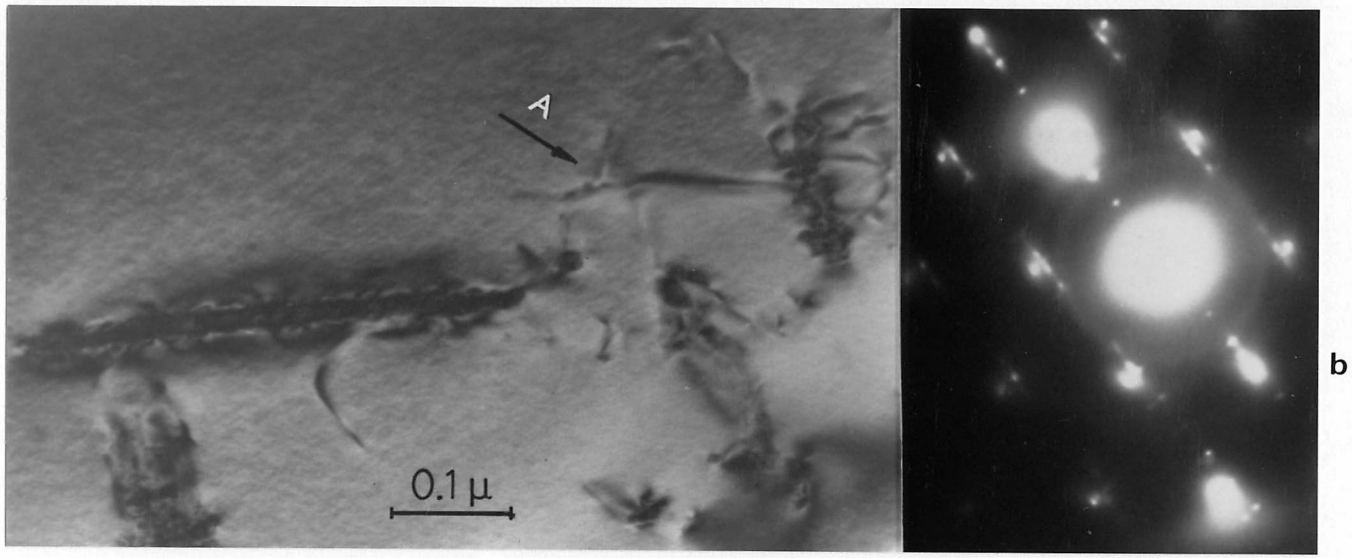

Fig 6.19 Formation of Z phase slabs in the matrix. Interaction of dislocation (arrowed, A). Aged at 700°C for 1000 hrs. a) Bright field; b) SADP, zone axis: $[\bar{1}10]\gamma$, $[\bar{1}00]Z$.

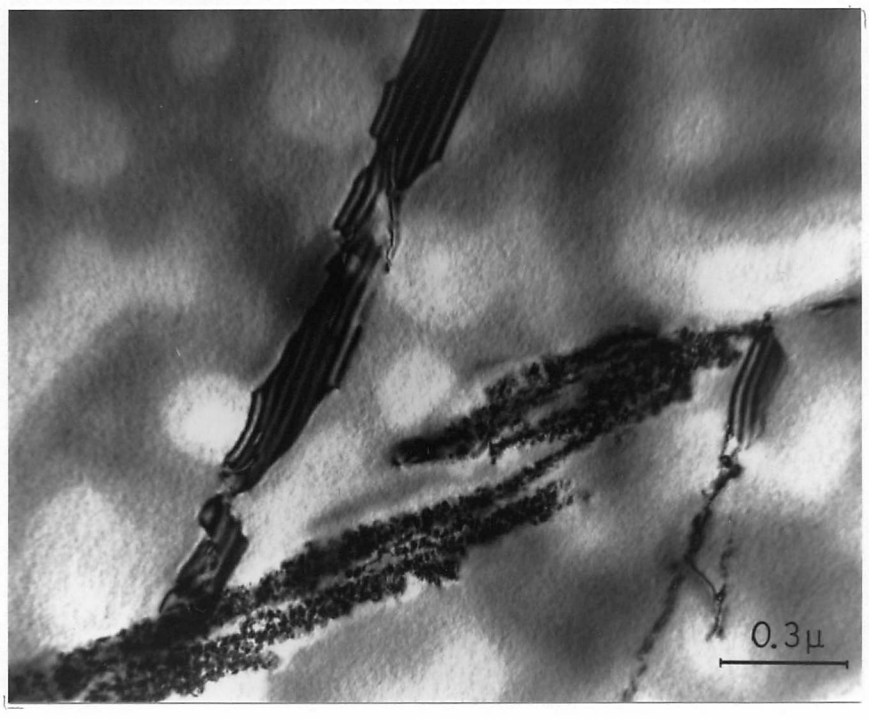

Fig 6.20 Bright field TEM image showing stacking faults free of precipitates.

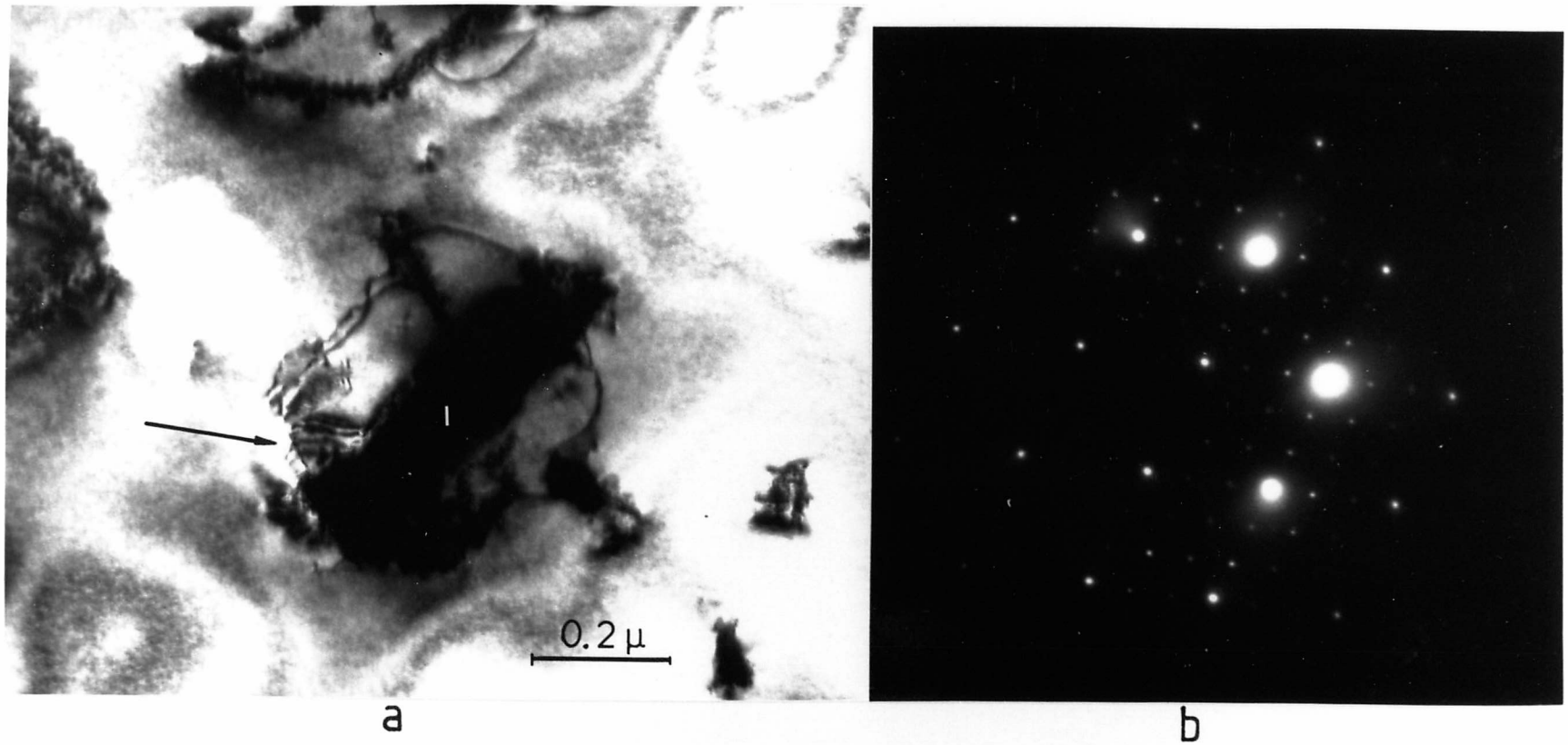

Fig. 6.21 Matrix precipitation of $M_{23}C_6$ (arrowed) showing Moiré fringes is growing from inclusion (I). Aged at 700 °C for 100 hrs. a) Bright field TEM image ; b) Selected area diffraction pattern, [011]γ , [011] $M_{23}C_6$.

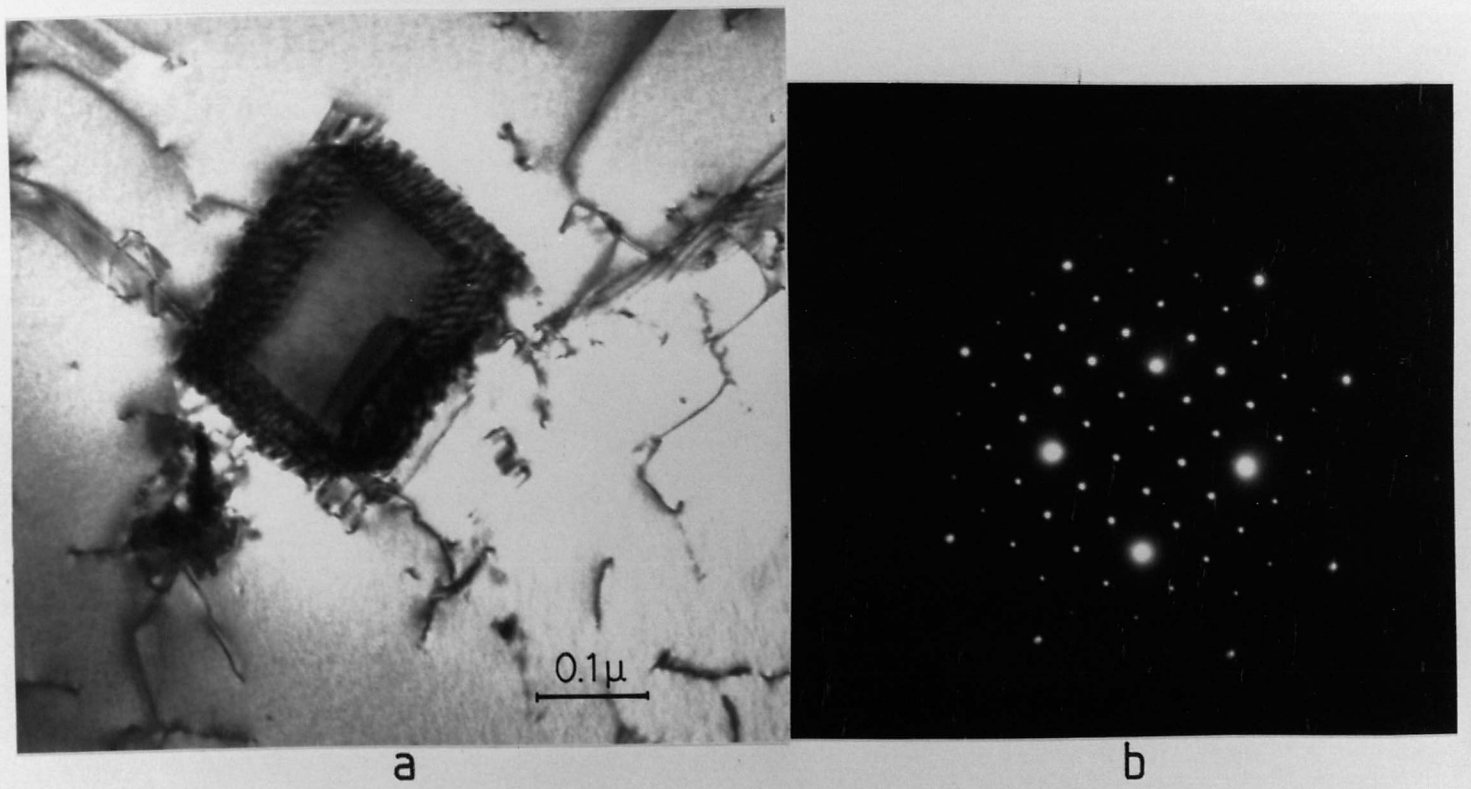

Fig. 6.22 Faceted $M_{23}C_6$ particle in the matrix after 1000 hrs at 700 °C.
a) Bright field TEM image; b) Selected area diffraction pattern.
$(100)\gamma \;//\; (100)M_{23}C_6$, $[010]\gamma \;//\; [010]M_{23}C_6$.

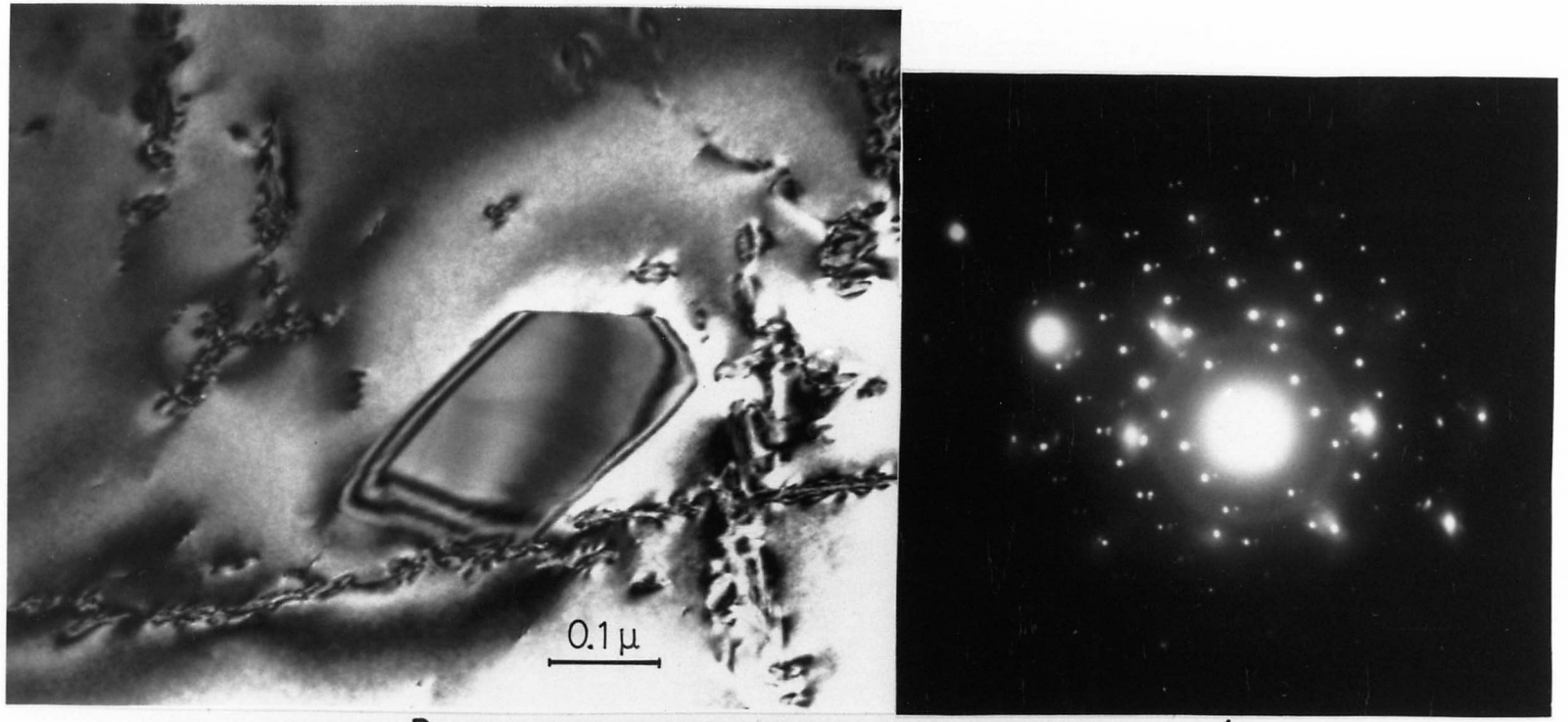

Fig. 6.23 Massive X phase precipitate in the matrix after 1000 hrs at 700 °C. a) Bright field TEM image; b) Selected area diffraction pattern, [011] Y , [$\bar{1}$13] X phase.

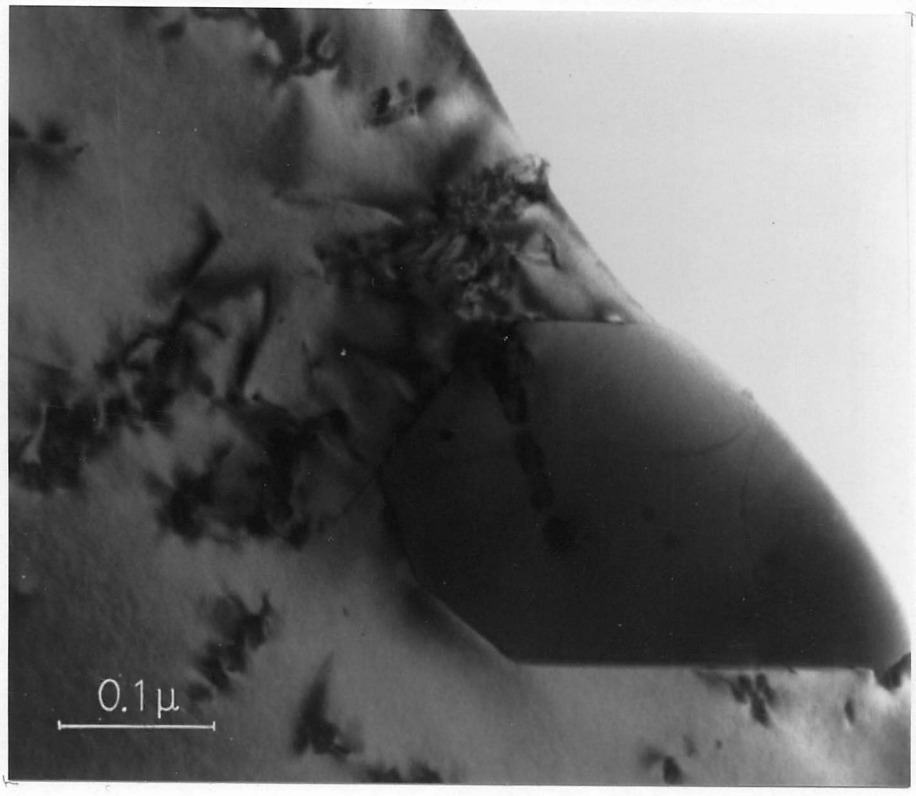

a

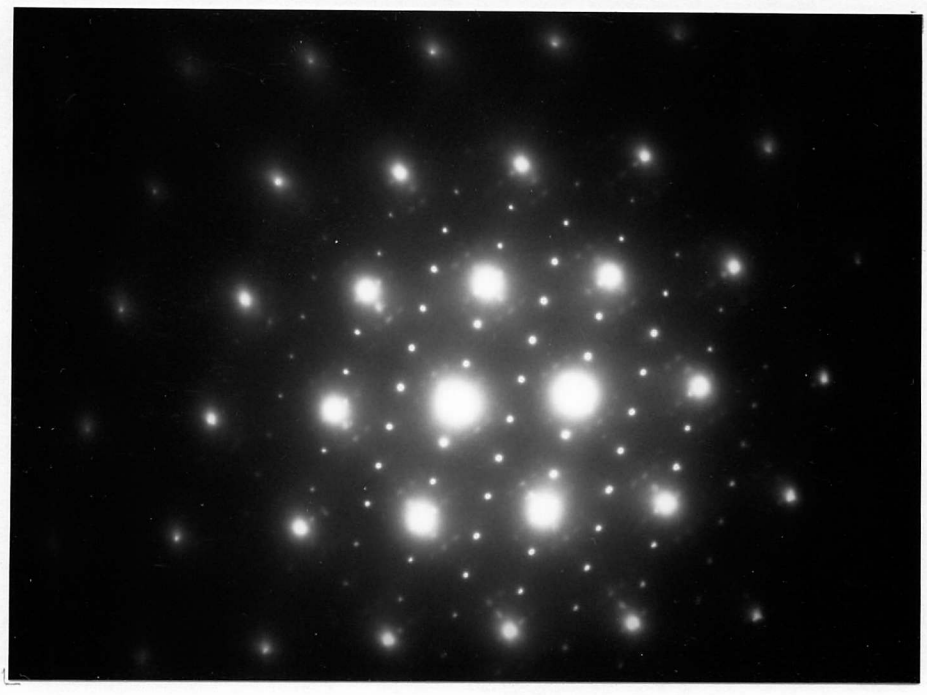

b

Fig 6.24 χ phase precipitation in the matrix, engulfing Z phase precipitates. Aged at 700° for 1000 hrs. a) Bright field TEM image; b) SADP, $[01\bar{1}]\gamma$ // $[\bar{1}10]\chi$, $(111)\gamma$ // $(110)\chi$.

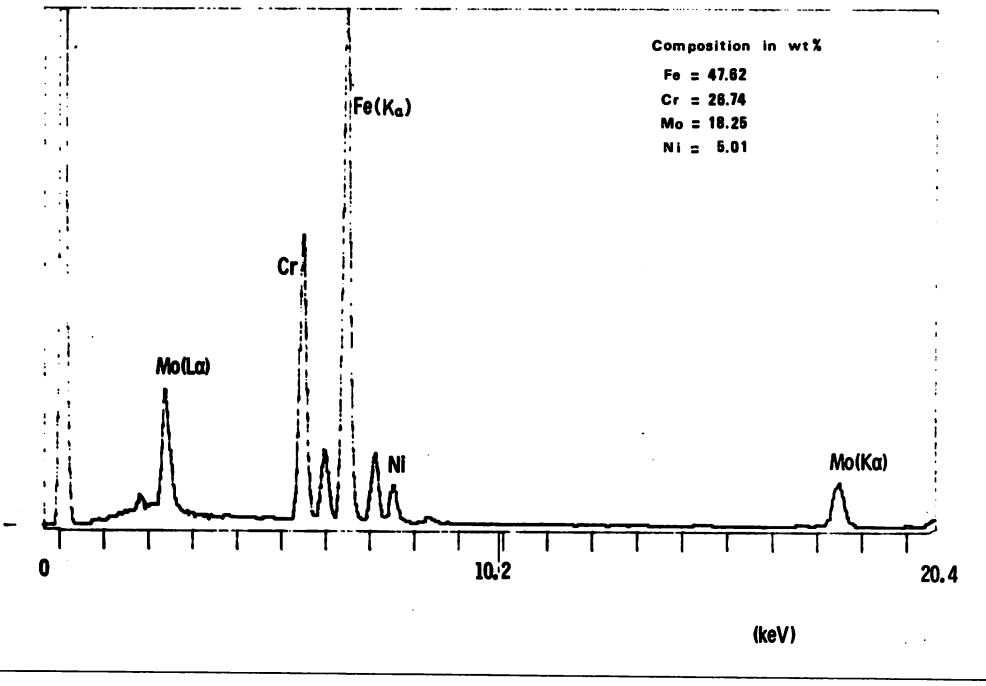

Fig 6.25 Electron energy dispersive spectrum of χ phase in thin foil specimen.

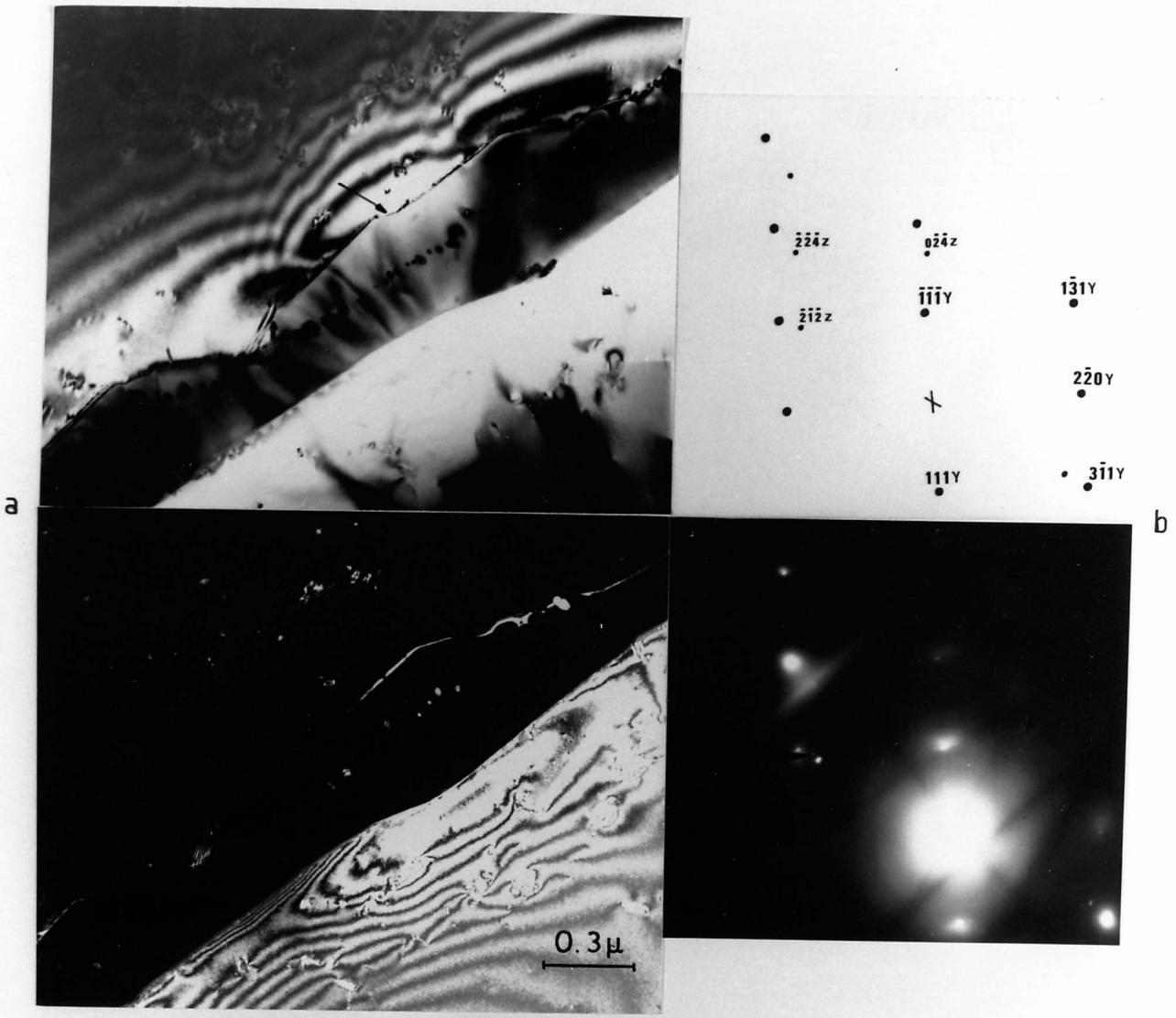

Fig. 6.26 a) Bright and dark field TEM images showing Z phase precipitates at grain boundary. $M_{23}C_6$ particles (arrowed) followed Z phase precipitation. Aged at 800 °C for 100 hrs. b) Selected area diffraction pattern of Z phase precipitates. $[\bar{1}\bar{1}2]Y$, $[0\bar{2}1]Z$ phase.

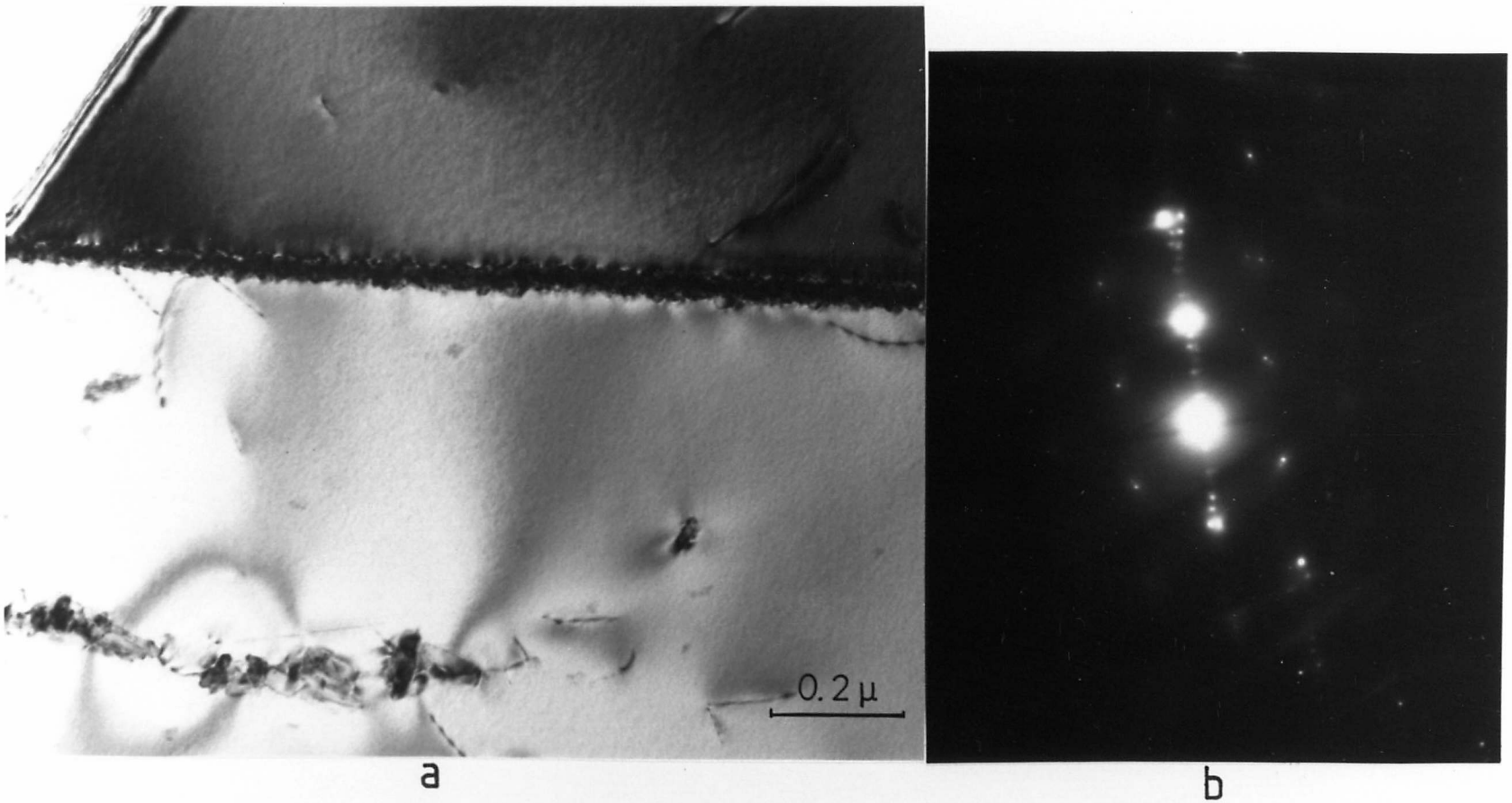

Fig. 6.27 a) Bright field TEM image showing Zphase precipitates on a coherent twin boundary. Aged at 800 °C for 100 hrs. b) Selected area diffraction pattern of the Zphase precipitates. Zone axis $[\bar{1}10]\gamma$; $[\bar{1}00]Z$.

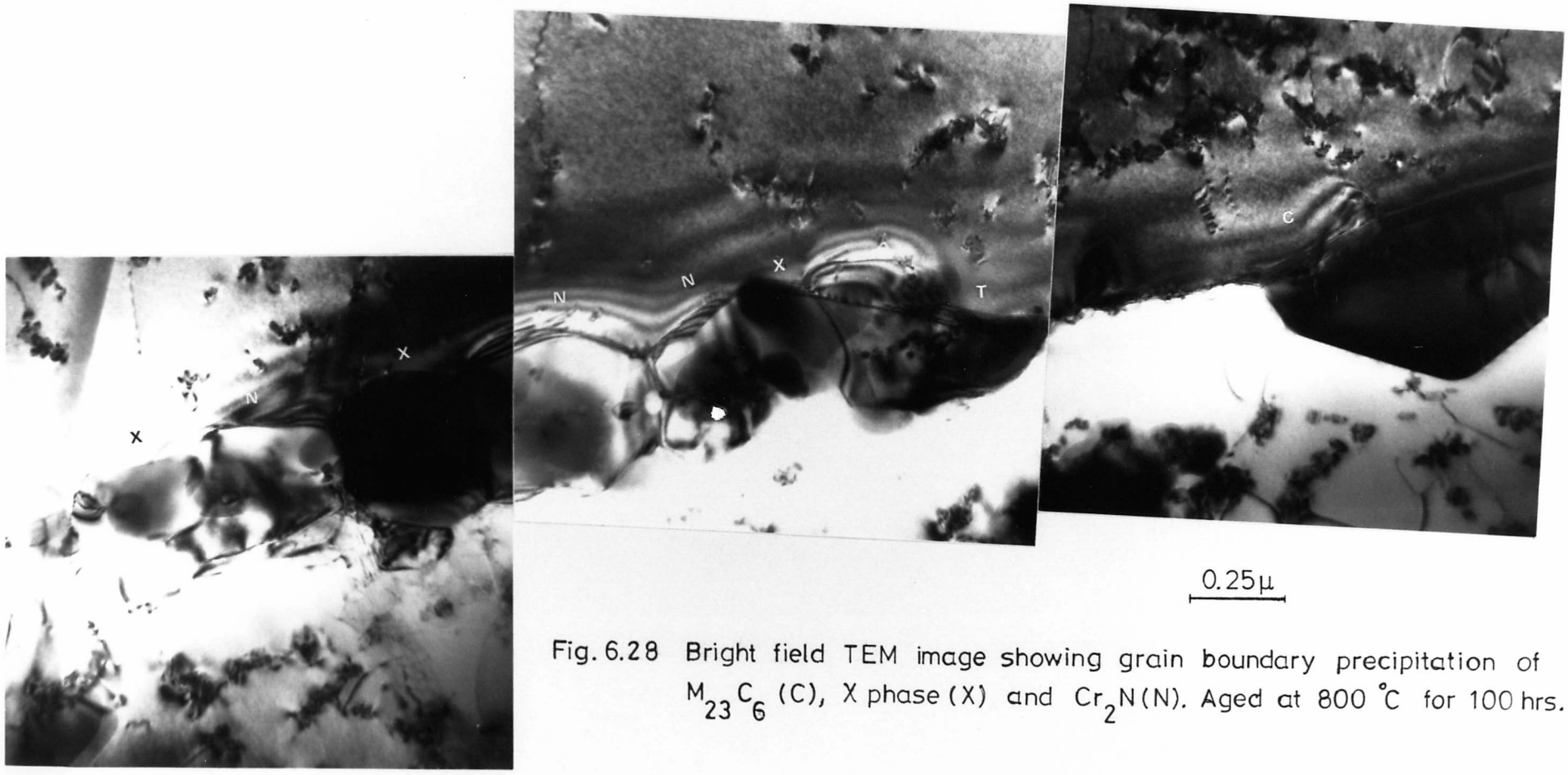

Fig. 6.28 Bright field TEM image showing grain boundary precipitation of $M_{23}C_6$ (C), X phase (X) and Cr_2N (N). Aged at 800 °C for 100 hrs.

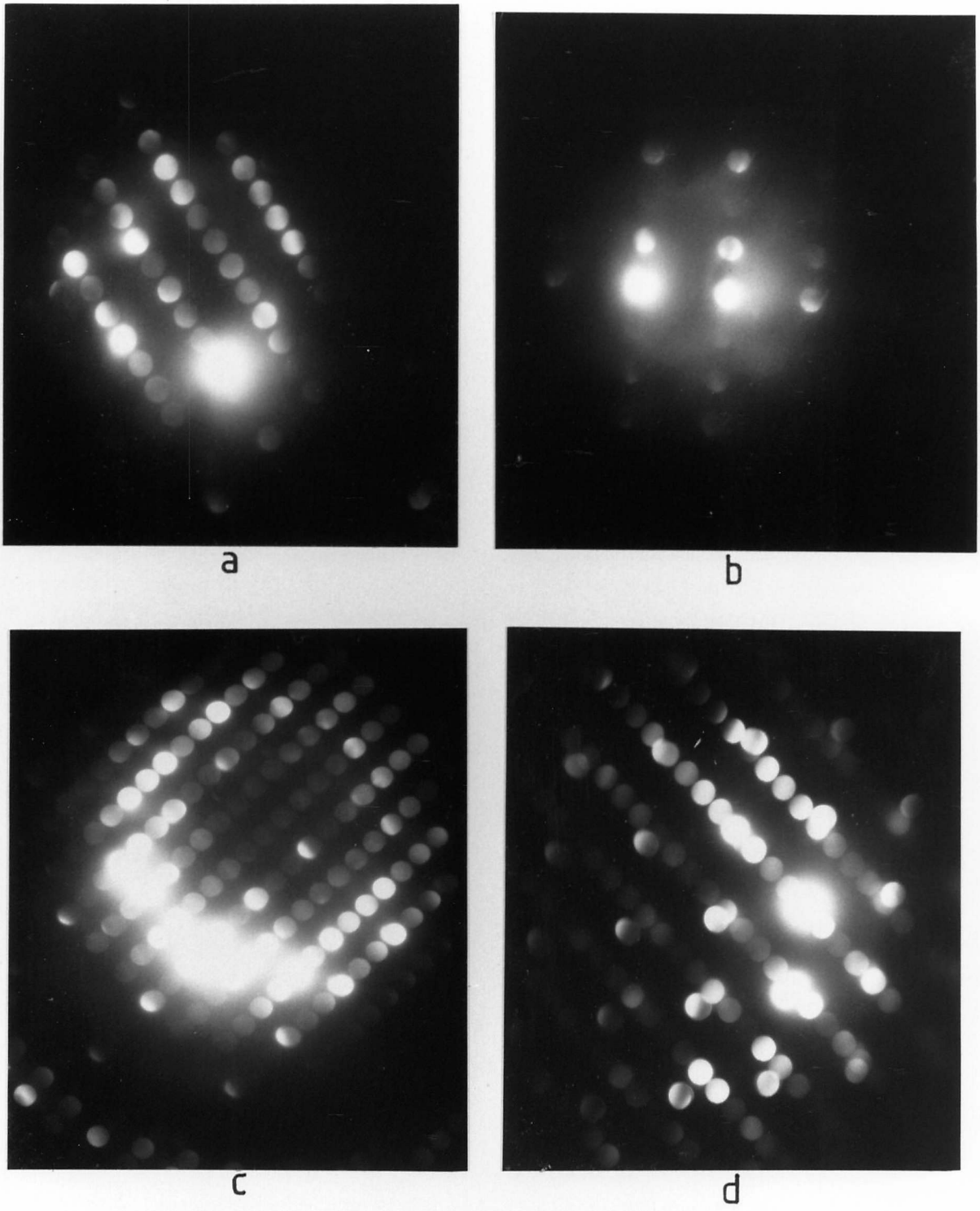

Fig.6.29 Convergent beam electron diffraction patterns from precipitates at grain boundary in Fig.6.28.

a) X phase, zone axis $[\bar{1}33]$, particle X

b) Cr_2N, zone axis $[\bar{1}2\bar{1}6]$, particle N

c) $M_{23}C_6$, zone axis $[\bar{1}12]$, particle C

d) precipitate $[\bar{1}12]$ bcc, $[011]\gamma$, particle T.

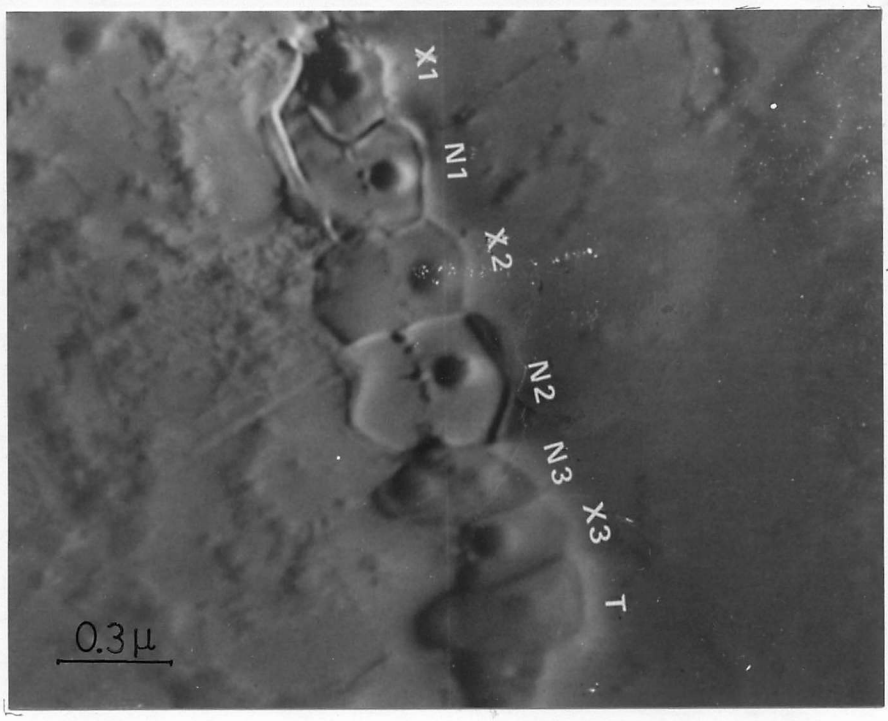

Fig 6.30 Scanning transmission electron microscope image showing the location of the beam for EDS analysis at grain boundary precipitates in Fig 6.28.

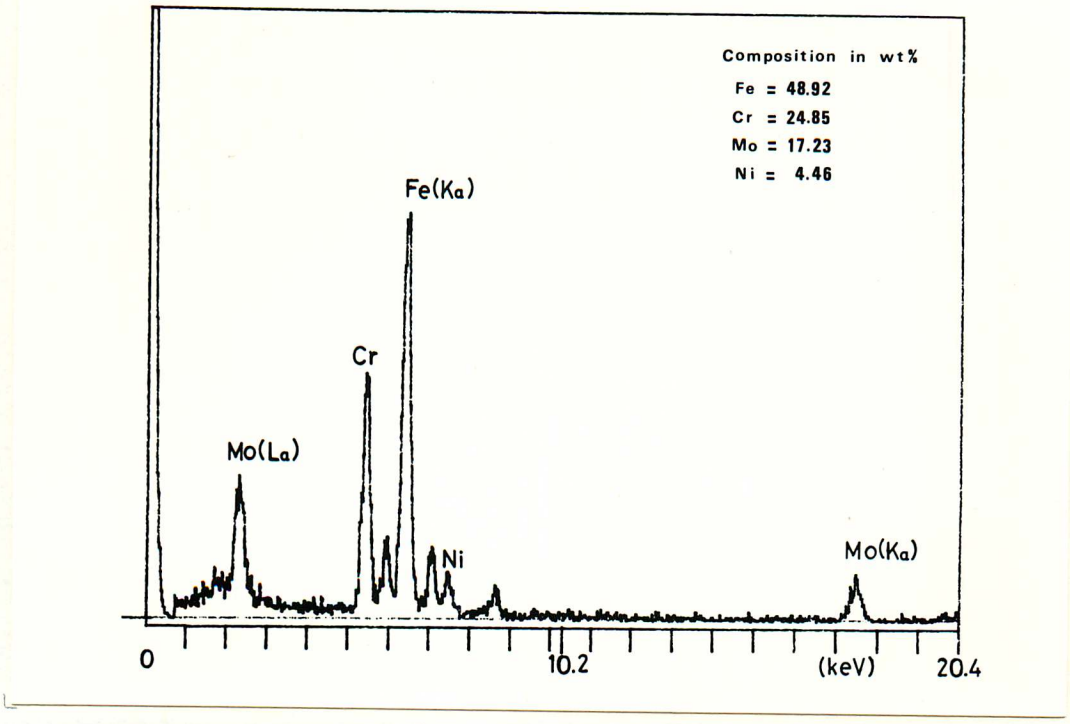

a

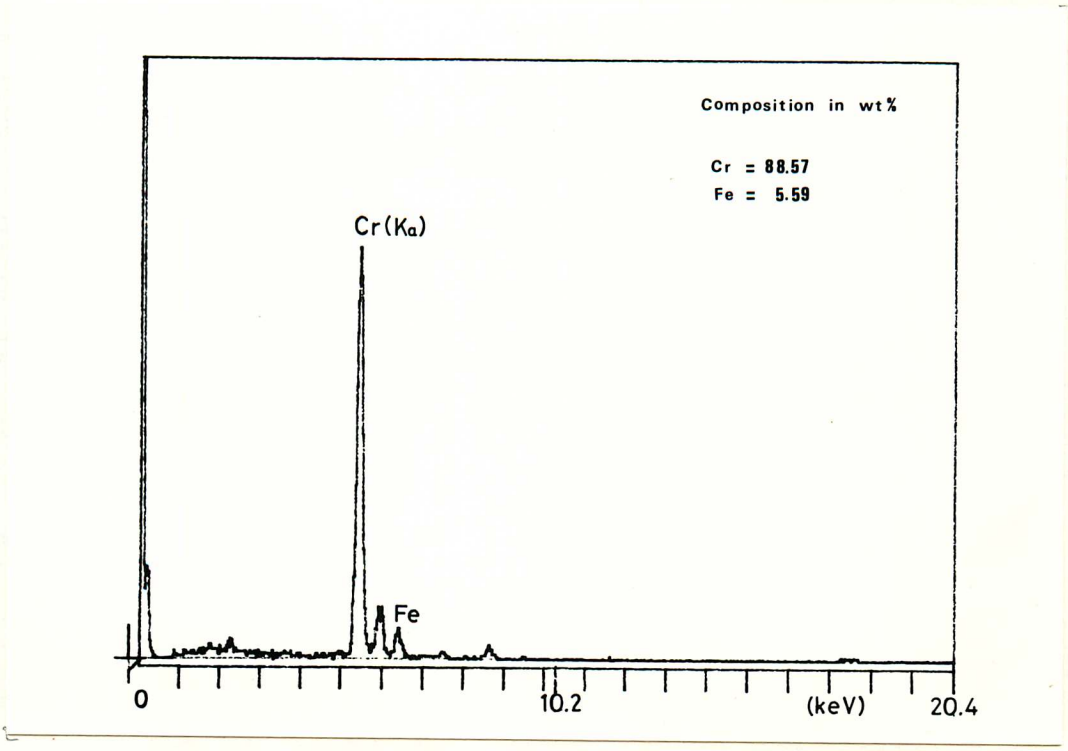

b

Fig 6.31 Electron energy dispersive microanalysis of precipitates at grain boundary in Fig 6.30.
a) beam located at X(1), χ phase
b) beam located at N(1), Cr_2N

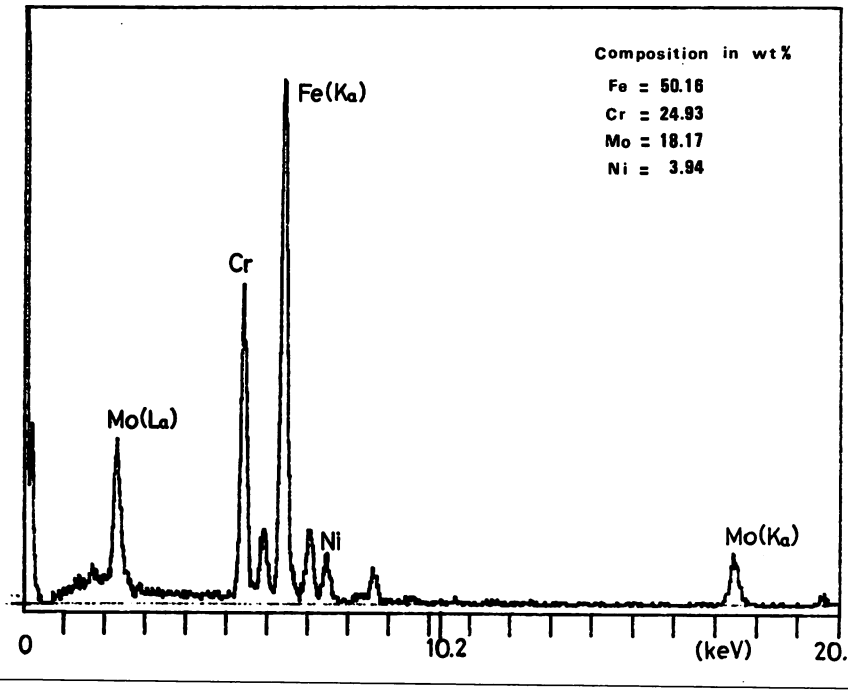

c

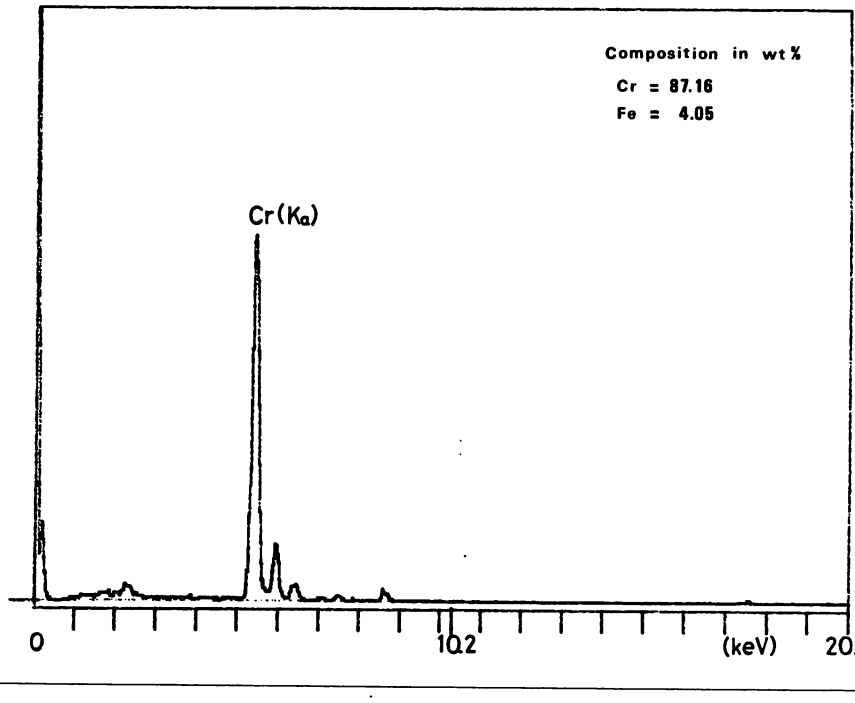

d

cont. Fig 6.31

c) beam located at X(2), χ phase

d) beam located at N(2), Cr_2N

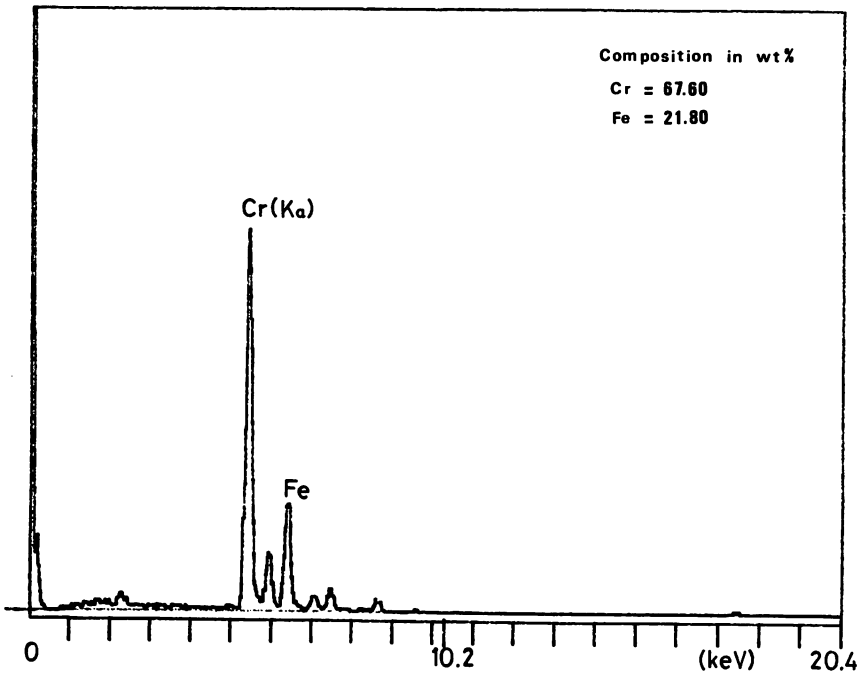

e

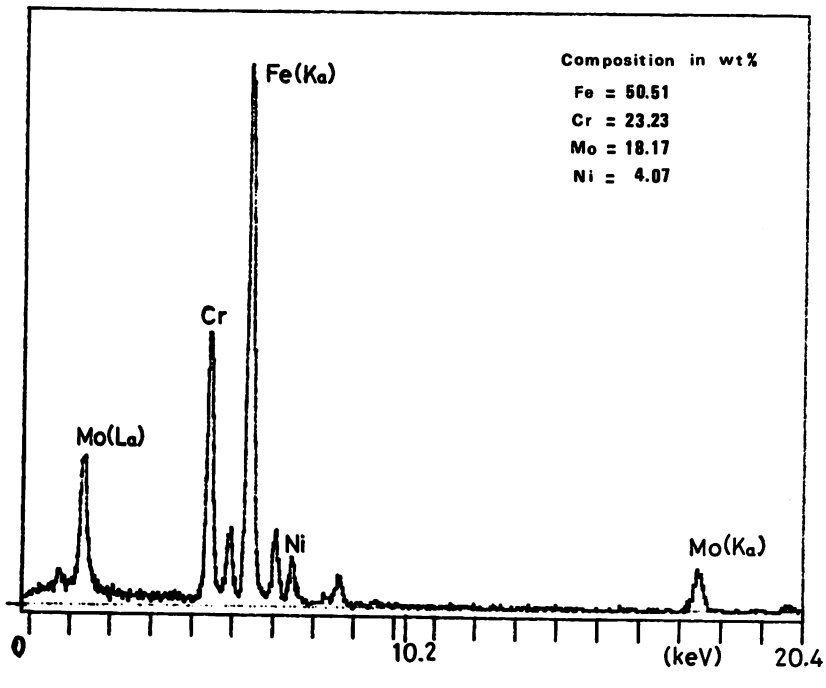

f

cont. Fig 6.31

e) beam located at N(3), Cr_2N

f) beam located at X(3), χ phase

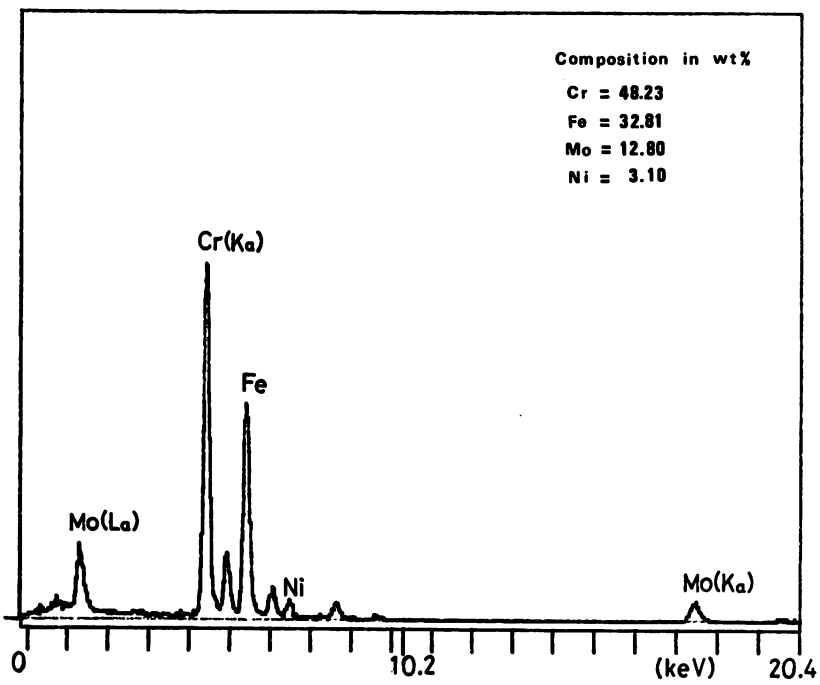

g

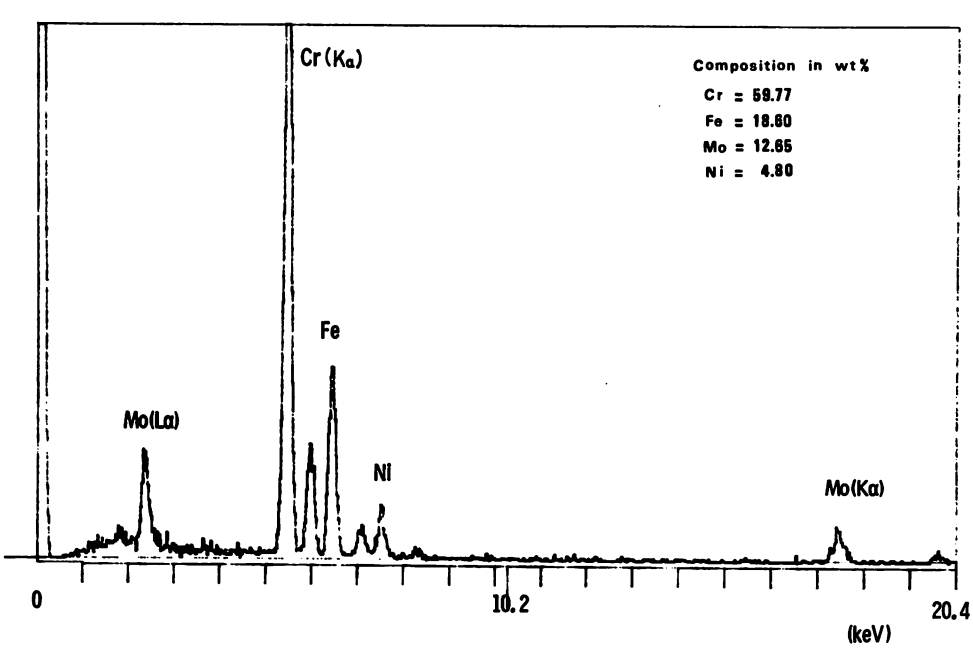

h

cont. Fig 6.31

g) beam located at T, χ' phase

h) spectrum of $M_{23}C_6$ particle C in Fig 6.28

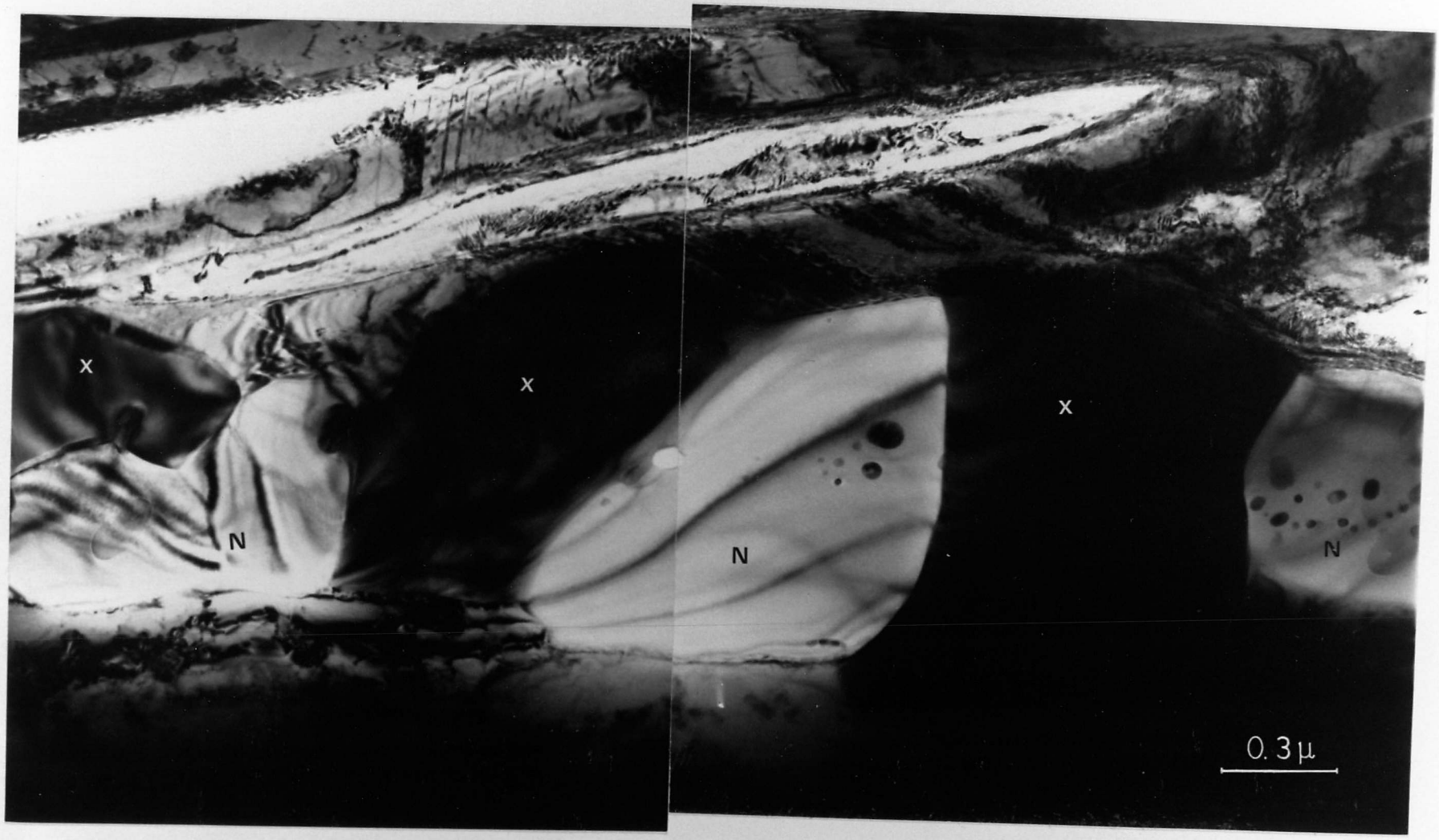

Fig. 6.32a Bright field TEM image showing grain boundary precipitation of X phase (X) and Cr_2N (N) after ageing at 800 °C for 1000 hrs.

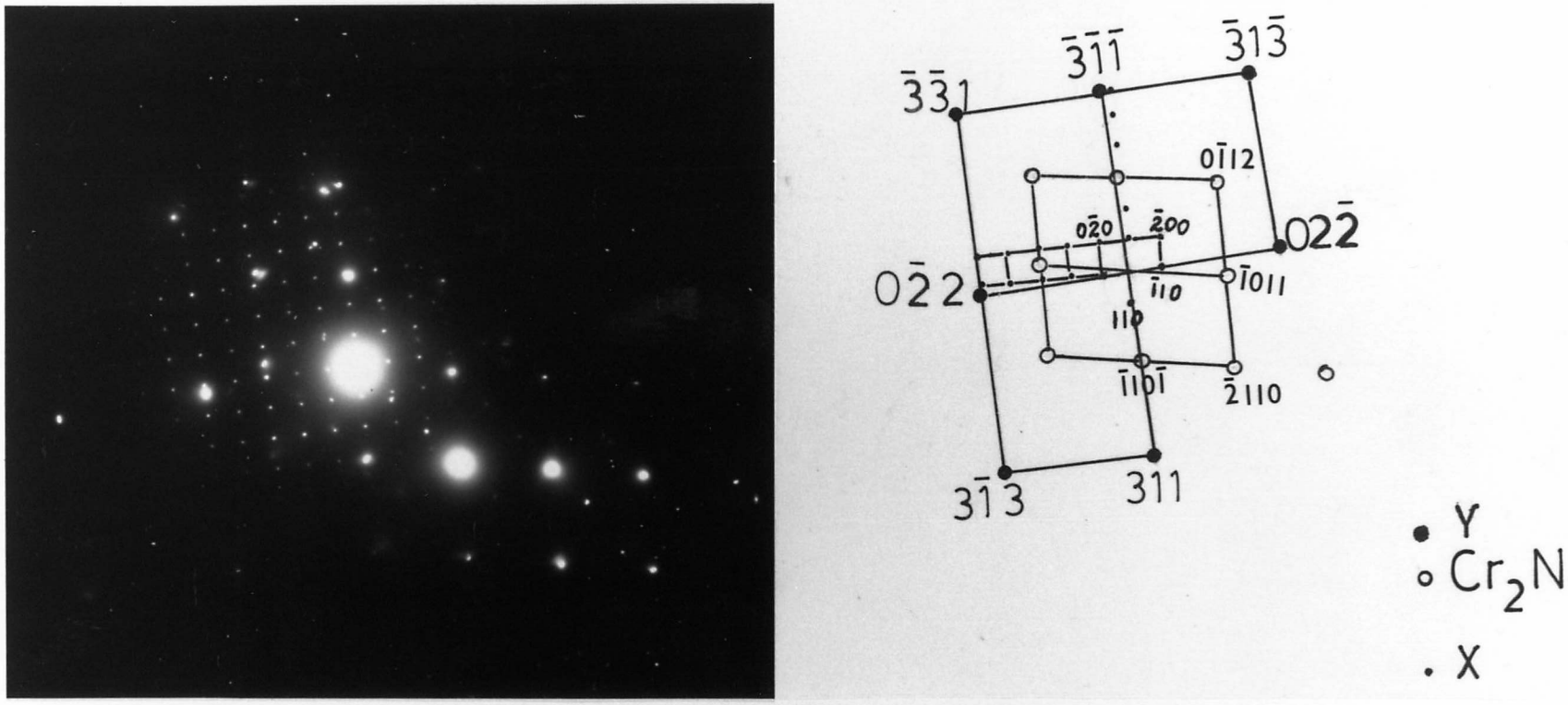

Fig. 6.32b Selected area electron diffraction of the precipitates, Cr_2N and X phase on grain boundary. Zone axis : $[\bar{2}33]$Y ; [001]X ; $[01\bar{1}1]$ Cr_2N .

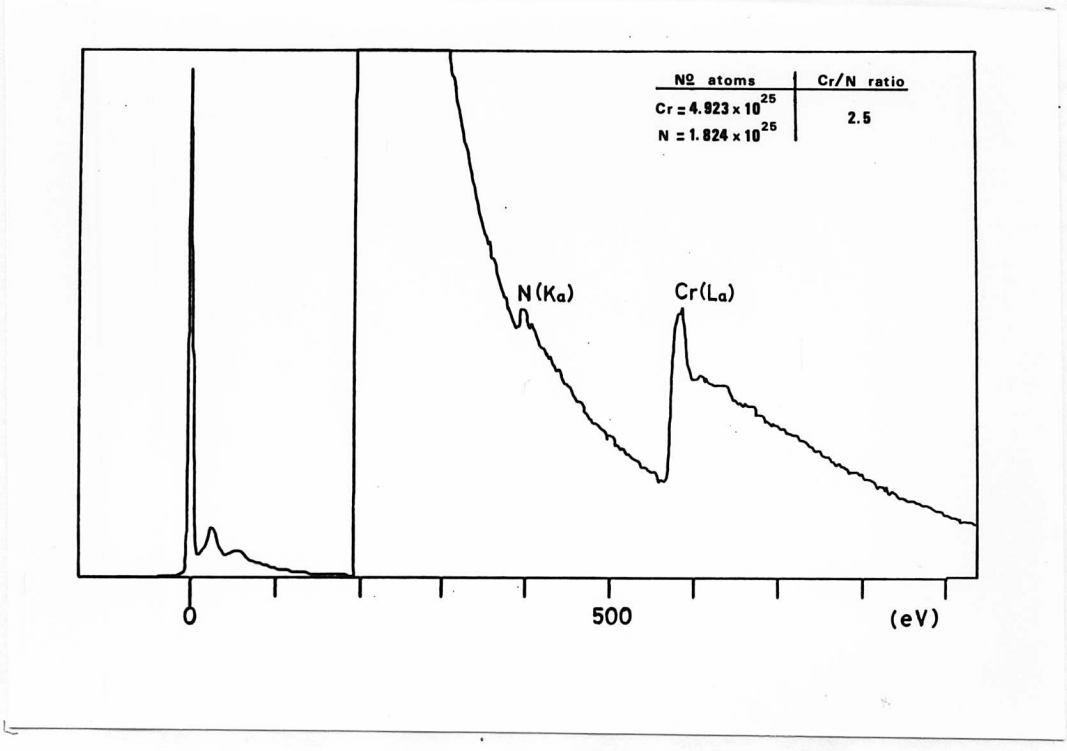

Fig 6.33 Electron energy loss spectrum of Cr_2N particle measured with 100 kV incident eletrons and 18 mrad collection angle, β.

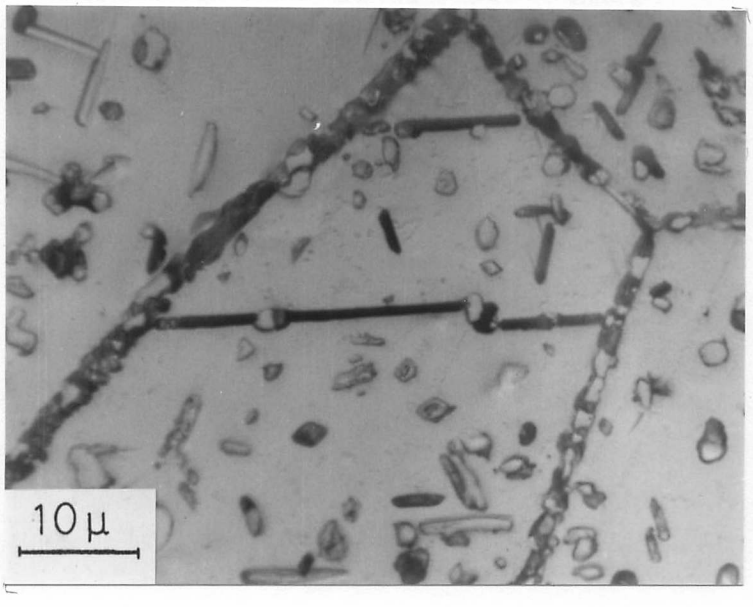

Fig 6.34 Optical micrograph showing grain boundaries and twin boundaries precipitation reaction after 1000 hrs at 800°C.

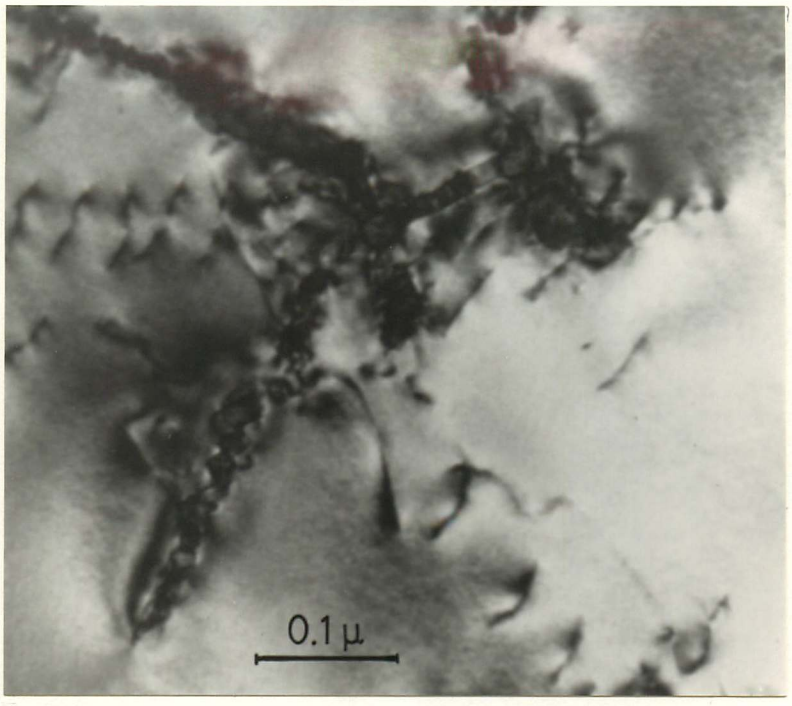

Fig 6.35 Bright field transmission electron microscope image showing growth of secondary stringers of Z phase particles. Aged at 800°C for 100 hrs.

Fig 6.36 Optical micrograph showing matrix precipitation of faceted rod shape χ phase. Aged at 800°C for 1000 hrs.

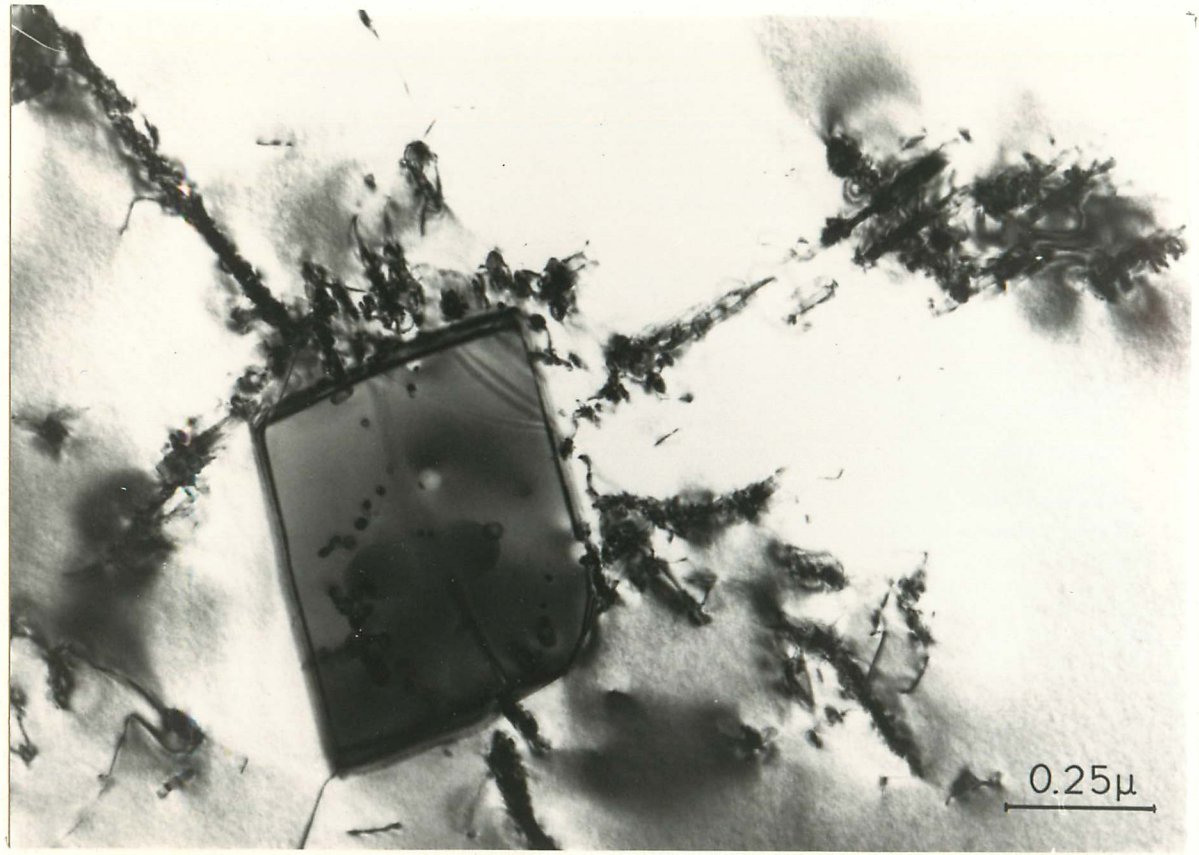

Fig 6.37 Bright field TEM image showing faceted χ phase in the austenitic matrix. Aged at 800°C for 100 hrs.

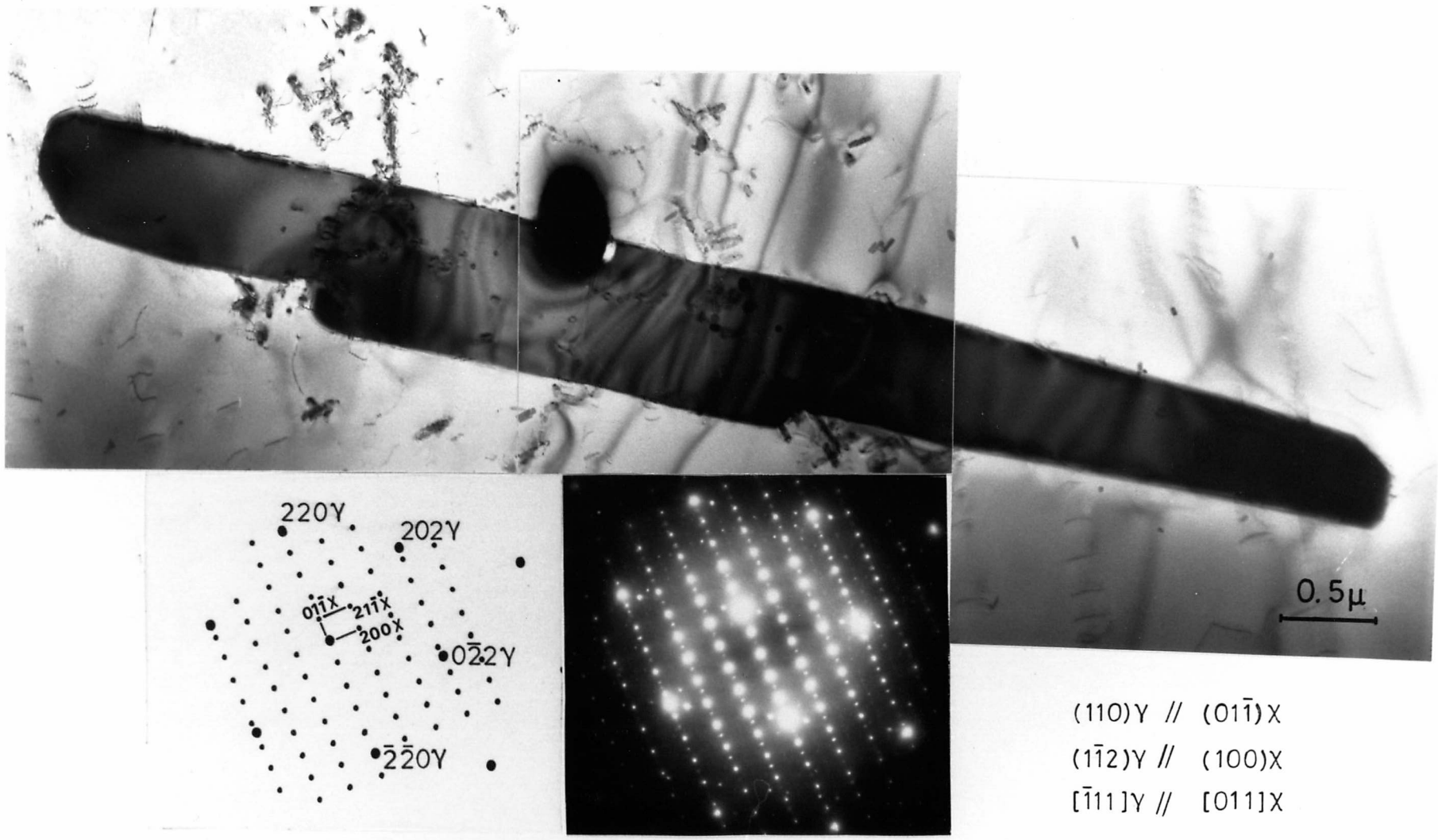

Fig. 6.38 Bright field TEM image showing χ phase in the austenitic matrix. Aged at 800 °C for 1000 hrs.

Fig 6.39 Precipitation of σ phase (σ) particle close to Cr_2N(N) at grain boundary. Z phase (arrowed) precipitates earlier in the same boundary. Aged at 900°C for 100 hrs.

Fig 6.40 Isolated σ phase particle at grain boundary (contamination spots from EDS analysis are over the particle and matrix (S)). Aged at 900°C for 100 hrs.

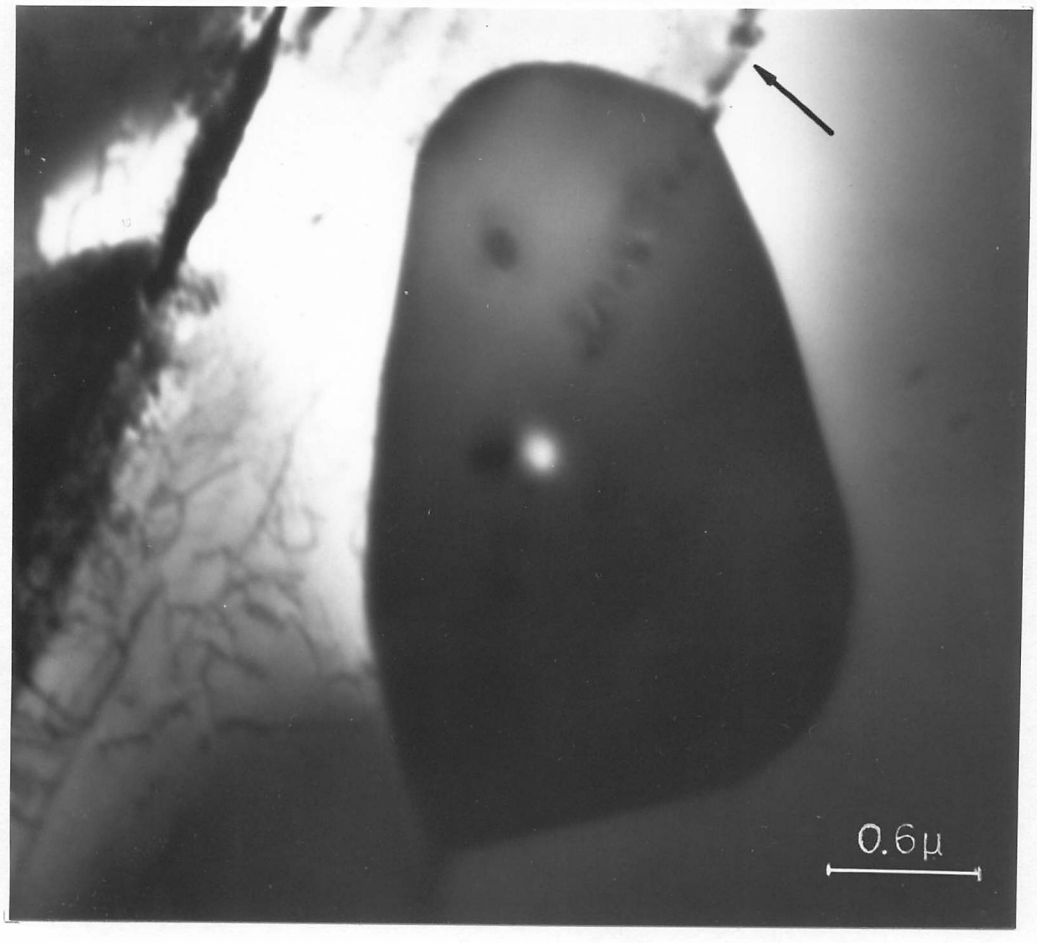

Fig 6.41 σ phase precipitate at twin boundary delineated by Z phase (arrowed). Aged at 900°C for 1000 hrs.

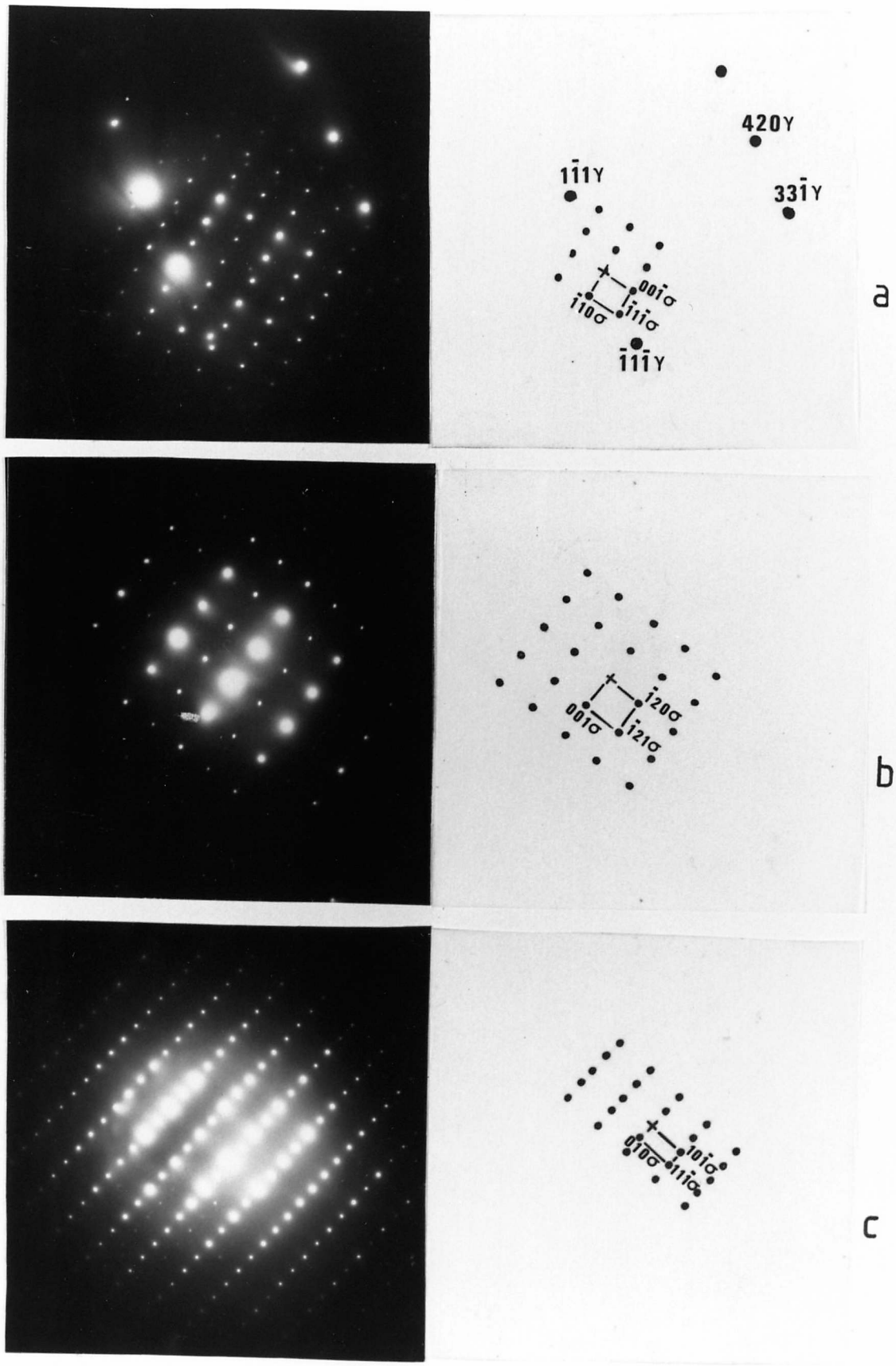

Fig. 6.42 Selected area diffraction patterns from σ phase in Fig.6.40.
a) zone axis [1̄23]γ ; [110]σ
b) zone axis [210]σ, tilted 18° clockwise from [110]σ
c) zone axis [101]σ, tilted 50° clockwise from [110]σ.

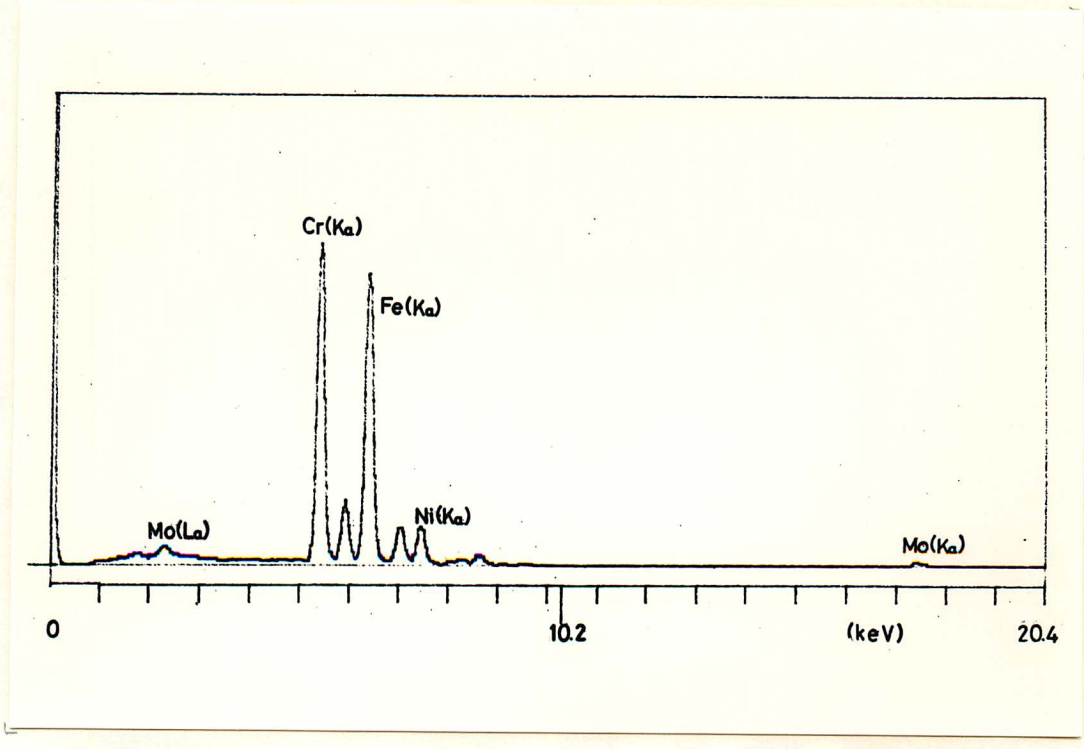

Fig 6.43 Electron energy dispersive spectrum obtained from σ phase particle in Fig 6.39.

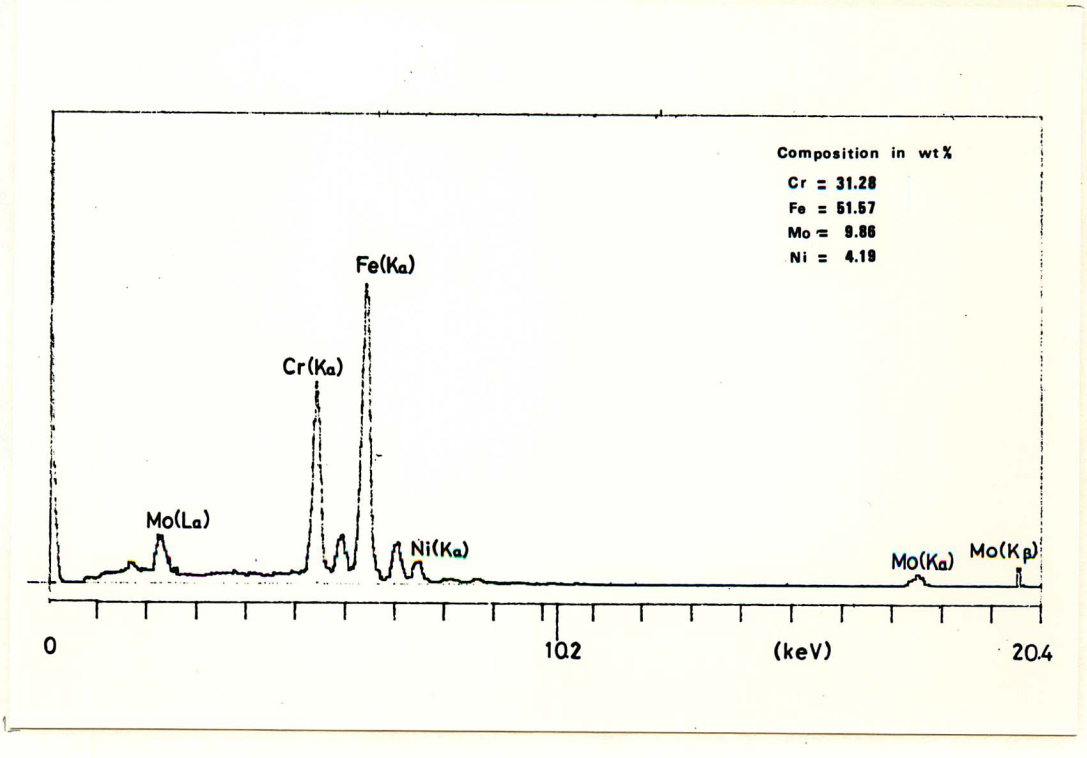

Fig 6.44 Electron energy dispersive spectrum obtained from σ phase particle in Fig 6.40.

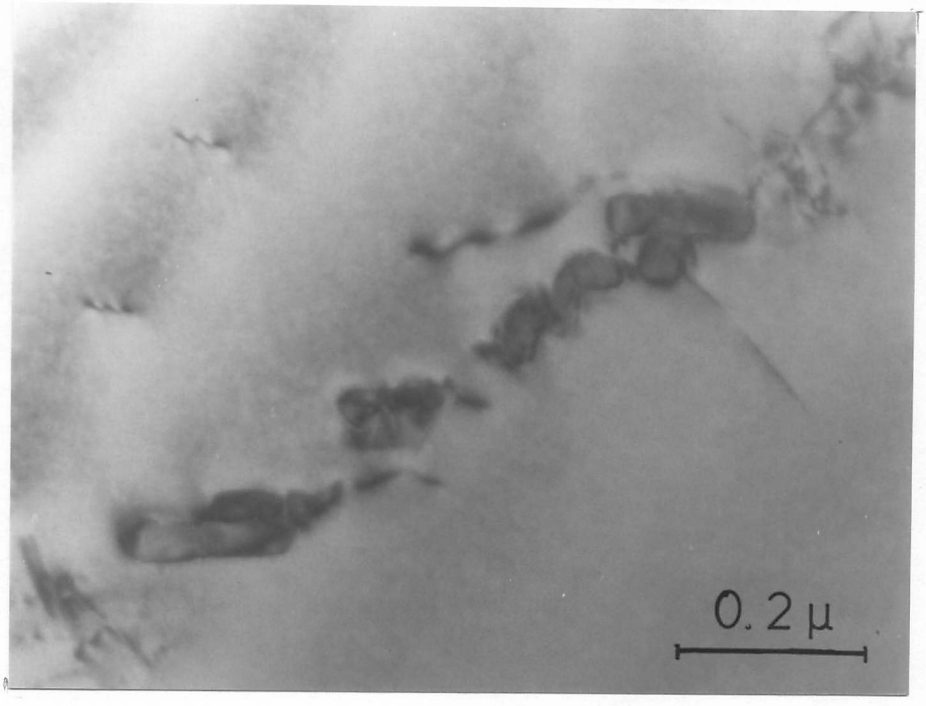

Fig 6.45 Matrix precipitation of Z phase cuboids. Aged at 900°C for 1000 hrs.

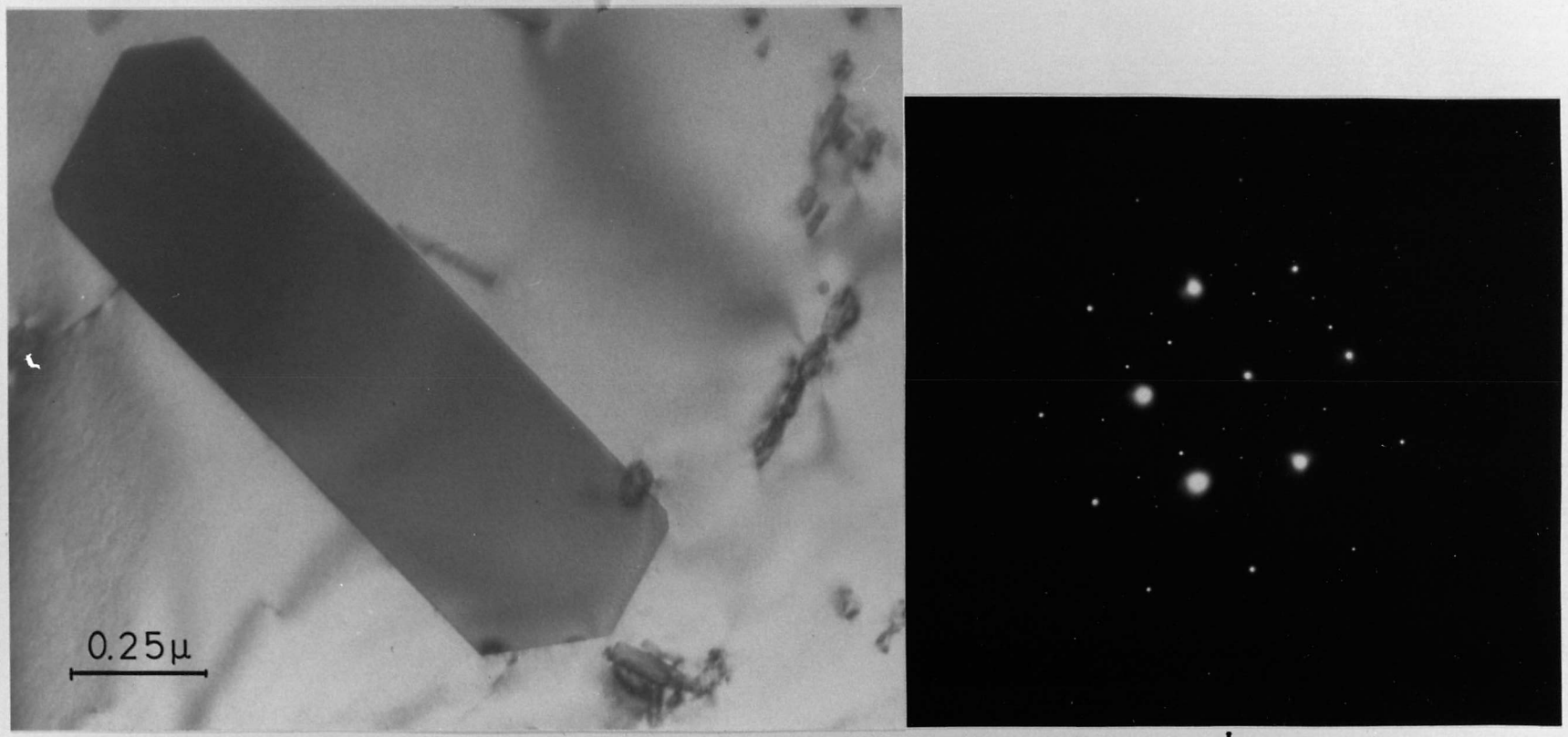

Fig. 6.46 Faceted rod shape X phase particle in the austenite matrix after 100 hrs at 900 °C. a) Bright field TEM image. b) Selected area diffraction pattern ; $[01\bar{1}]\gamma$ // $[\bar{1}10]X$, $(111)\gamma$ // $(110)X$, $(100)\gamma$ // $(11\bar{2})X$.

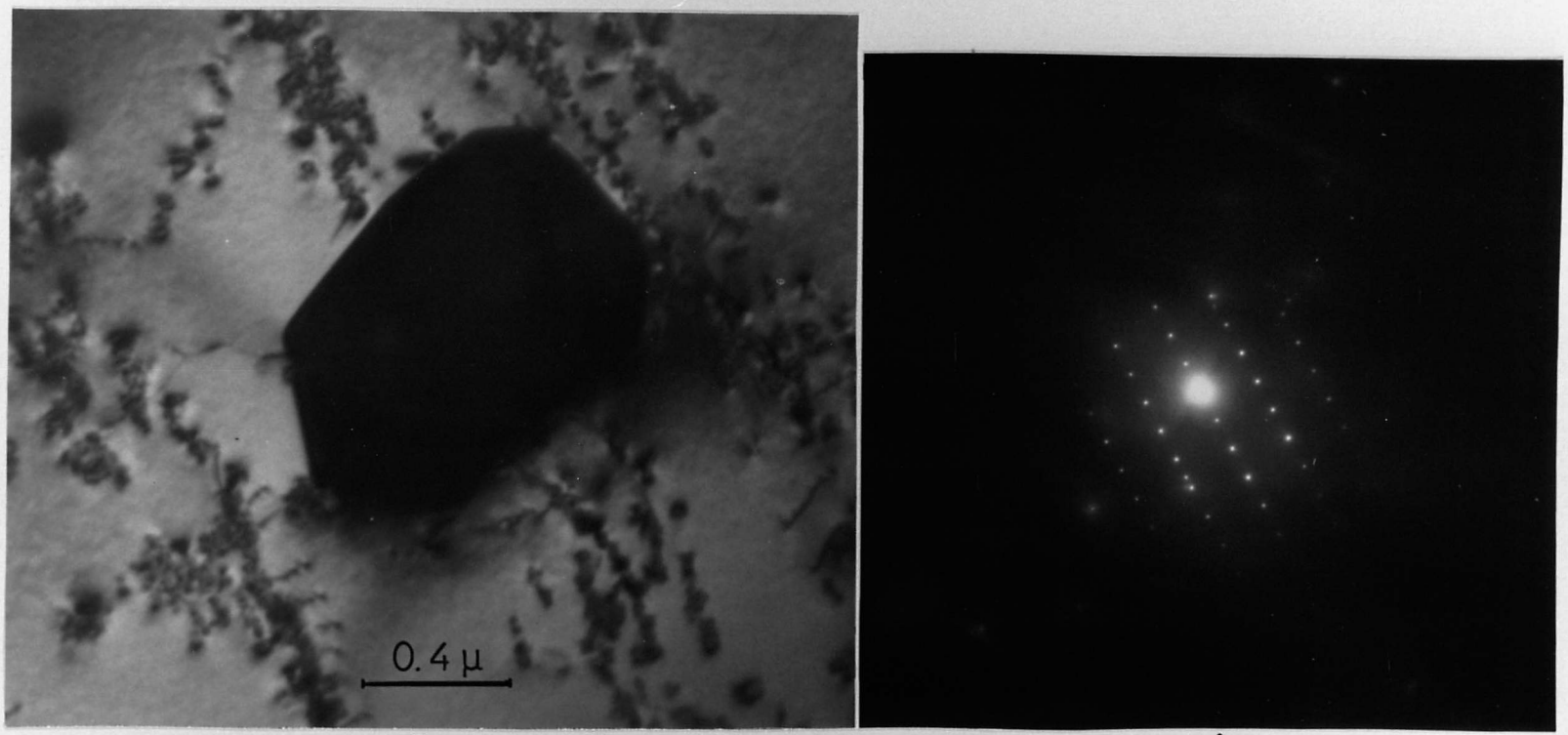

Fig. 6.47 Massive X phase particle in the matrix, surround by stringer precipitation of Z phase cuboids. Aged at 900 °C for 100 hrs. a) Bright field TEM image; b) Selected area diffraction pattern from X phase. Zone axis $[\bar{1}13]X$.

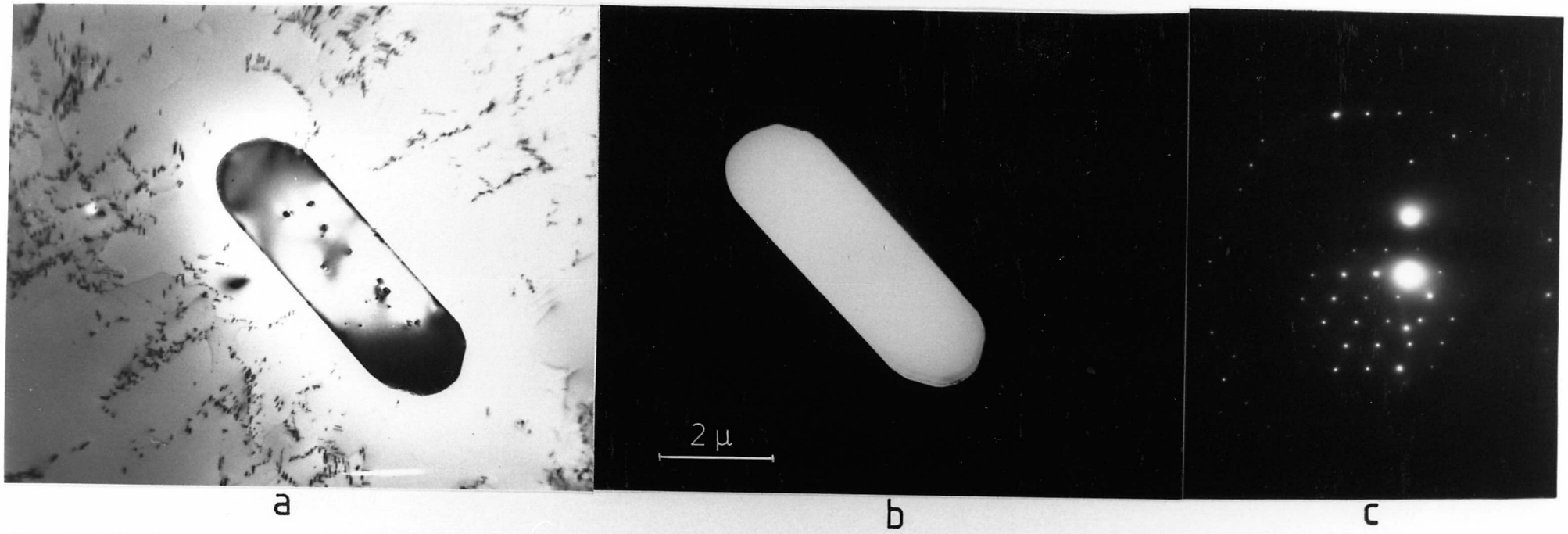

Fig. 6.48 Faceted rod shape X phase precipitate in the matrix, surround by Z phase precipitates on dislocations. Aged at 900 °C for 1000 hrs. a) Bright field TEM image; b) Centred dark field image of X phase; SADP, zone axis [012] X .

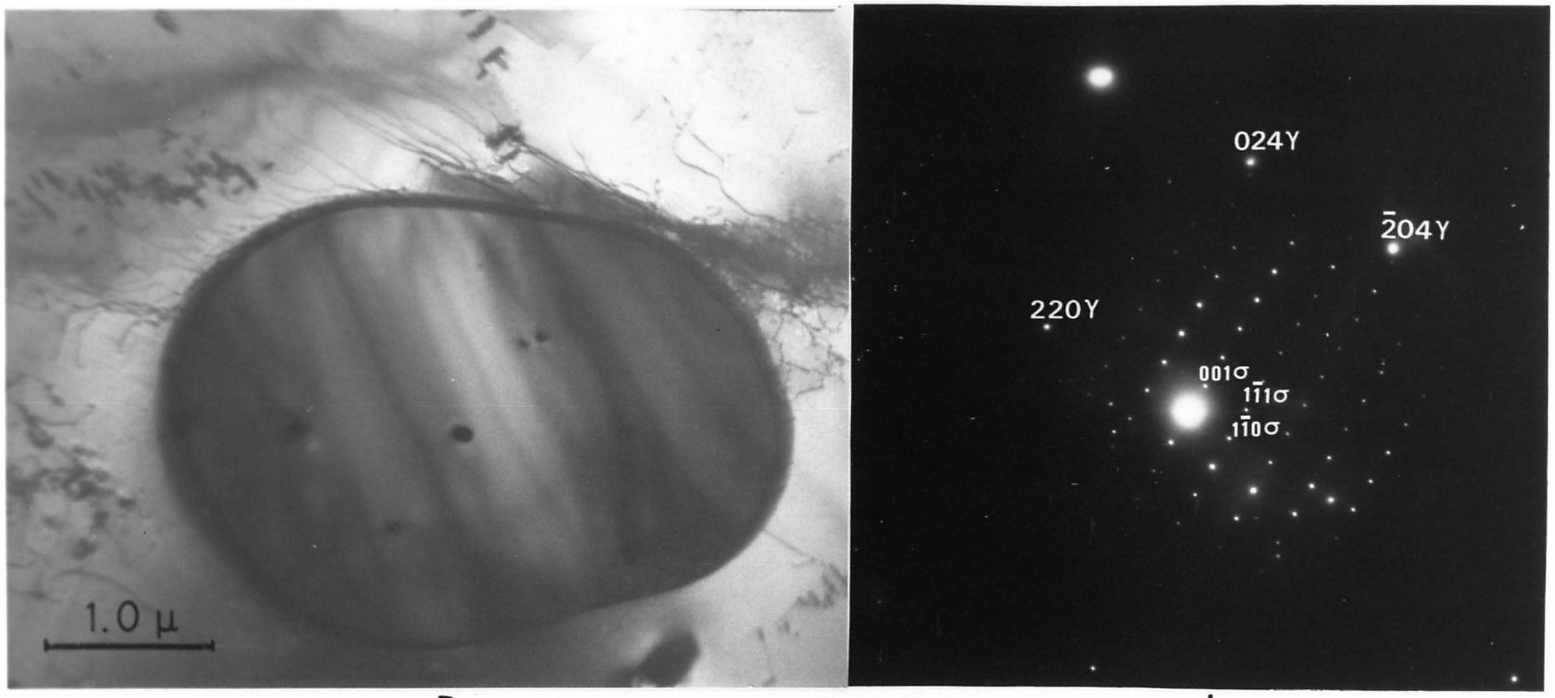

Fig. 6.49 Massive σ phase precipitate in the matrix after 1000 hrs at 900 °C. a) Bright field TEM image ; b) SADP, $[2\bar{2}1]\gamma$, $[110]\sigma$; $(110)\gamma$ // $(001)\sigma$.

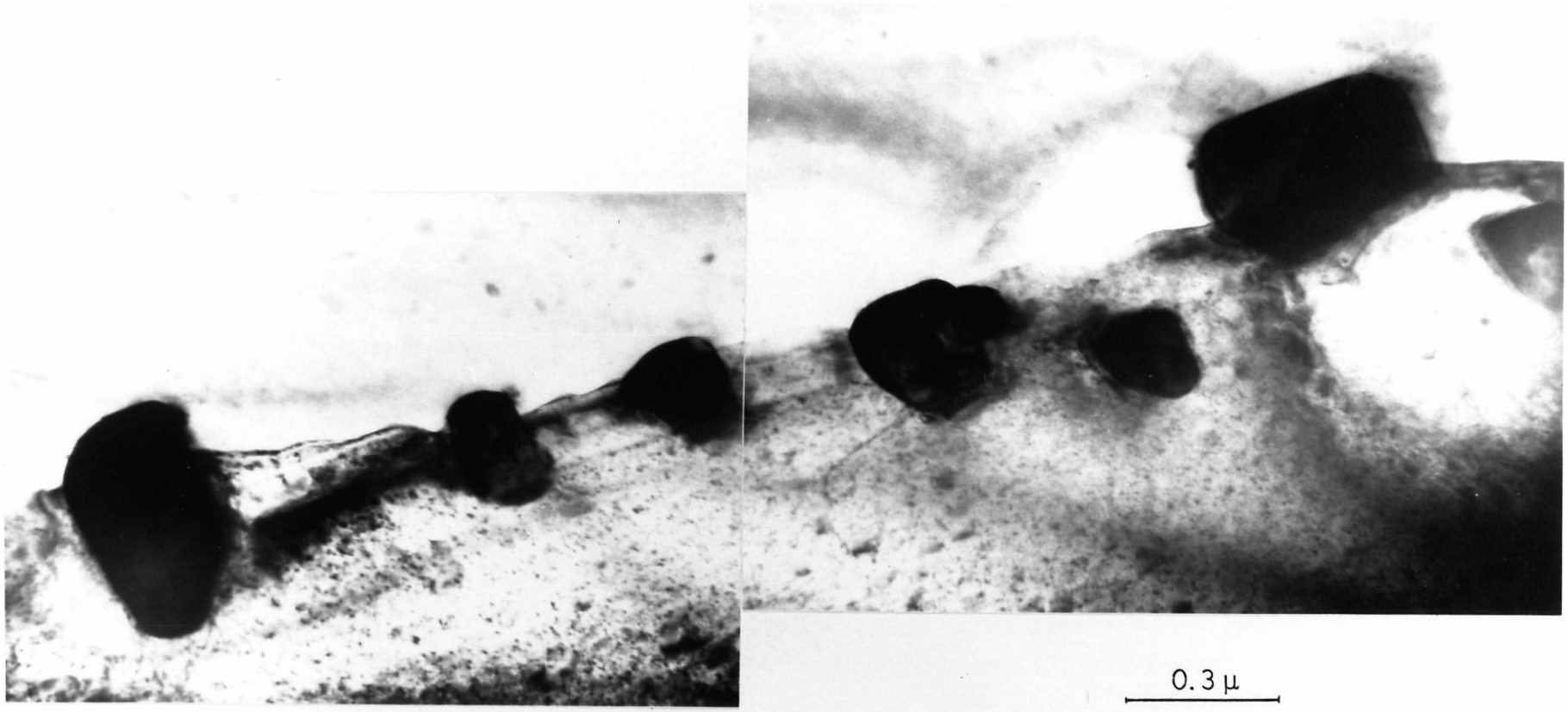

Fig. 6.50 Bright field TEM image showing grain boundary precipitation of Z phase. Aged for 100 hrs at 1000 ^{o}C

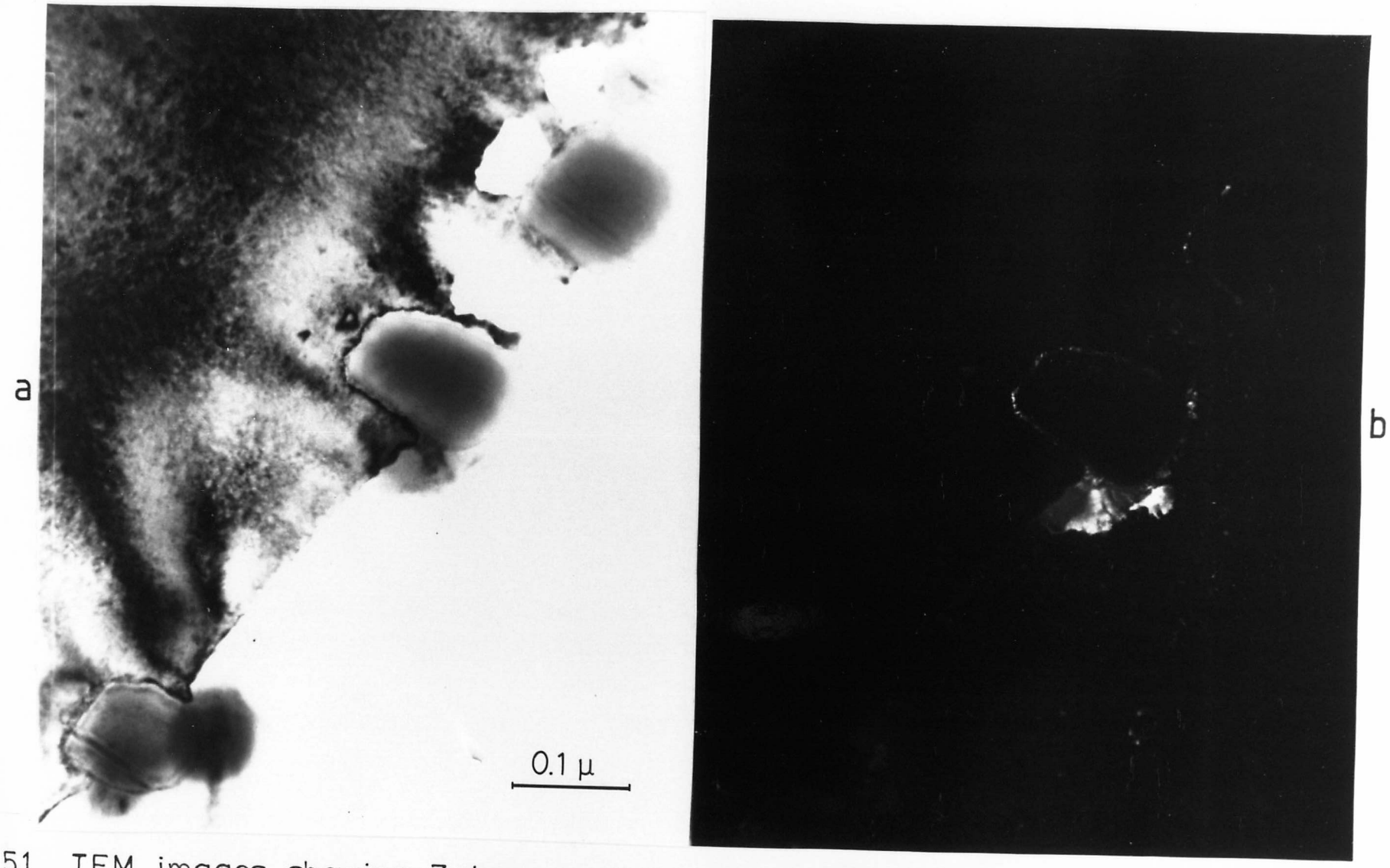

Fig. 6.51 TEM images showing Z phase particles surrounded by a crystalline f.c.c phase at grain boundary. Aged at 1000 °C for 100 hrs. a) Bright field image; b) Dark field image.

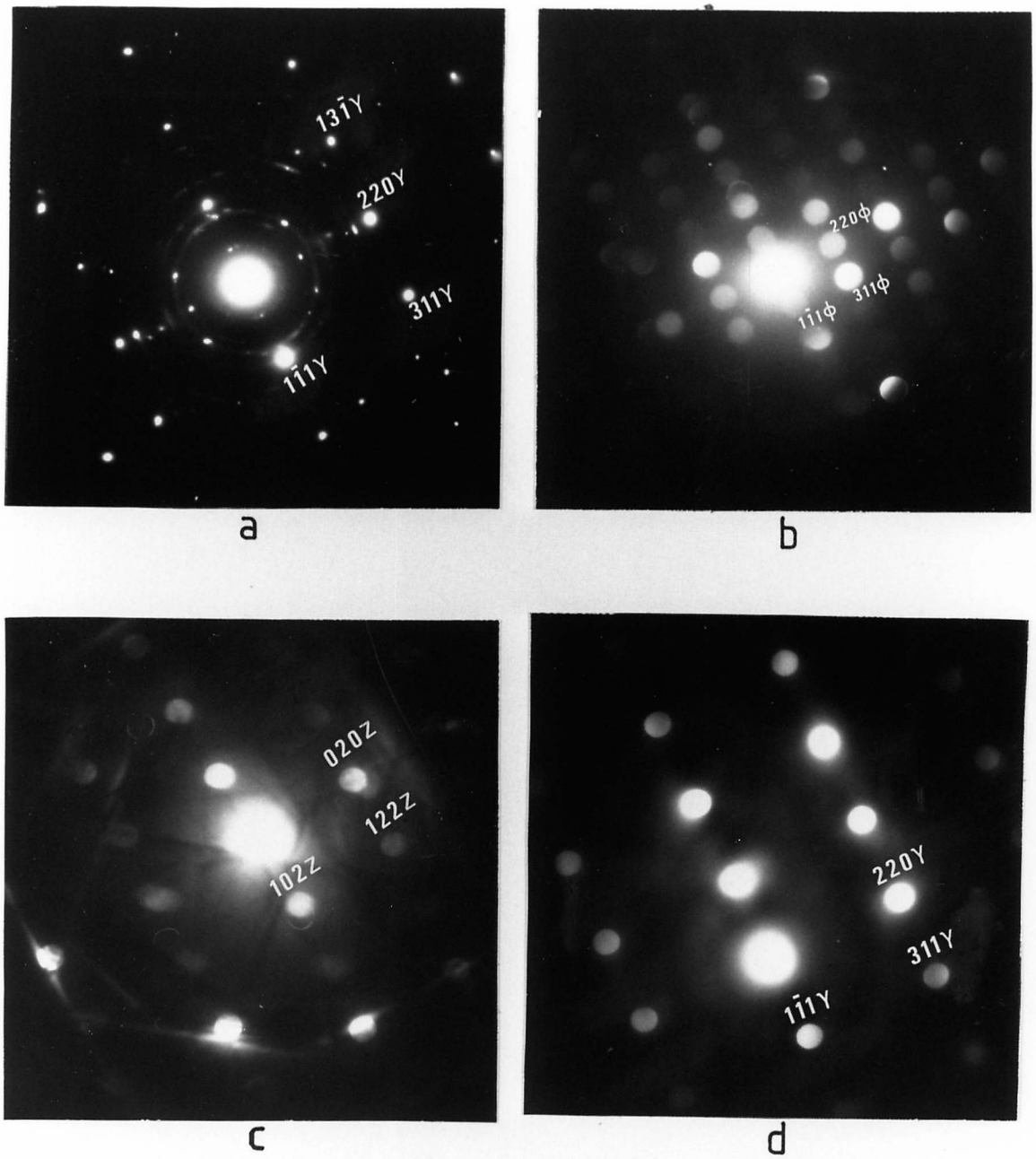

Fig. 6.52 Electron diffraction and convergent beam patterns from bright field image in Fig. 6.51.

a) SADP, zone axis: $[\bar{1}12]\gamma$; $[\bar{1}12]$ ϕ phase; $[\bar{2}01]$ Z phase

b) CBDP of ϕ phase (ϕ) around Z particle; zone axis $[\bar{1}12]\phi$

c) CBDP of Z phase; zone axis $[\bar{2}01]$Z

d) CBDP of matrix; zone axis $[\bar{1}12]\gamma$.

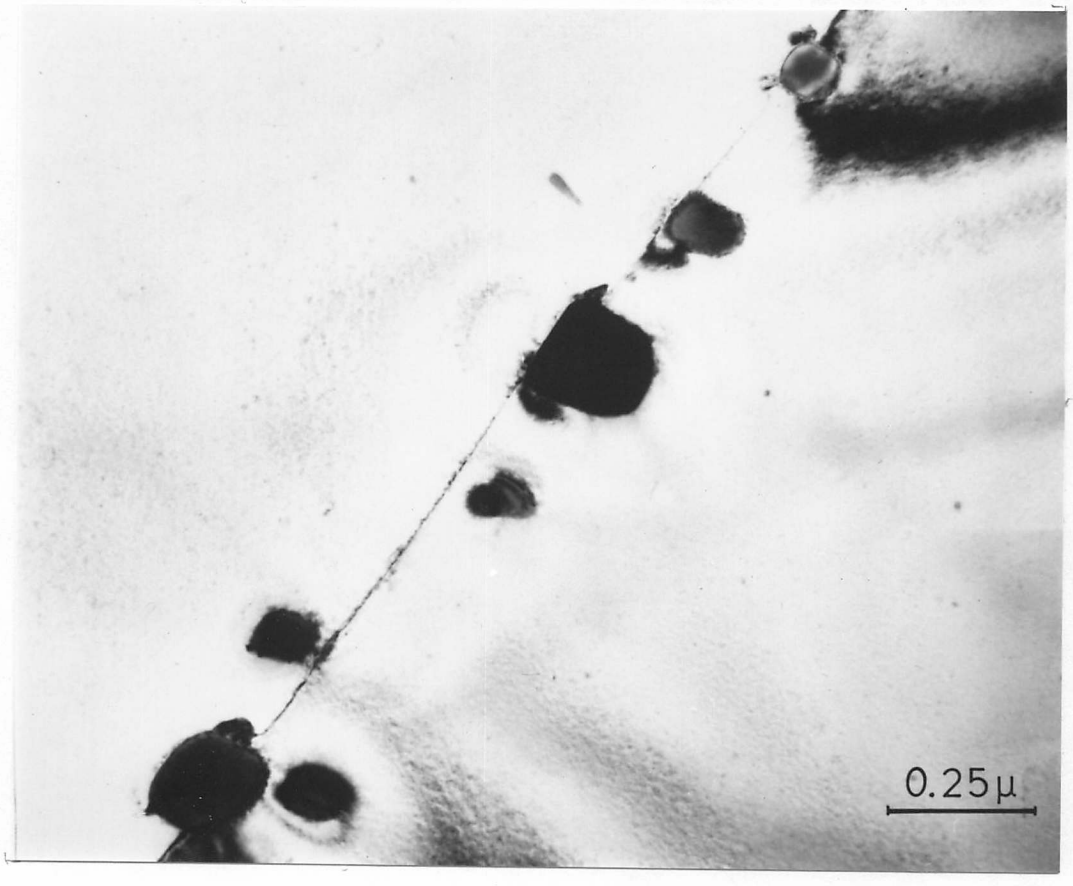

Fig 6.53 Bright field TEM image showing Z phase precipitation at twin boundary. Aged at 1000°C for 100 hrs.

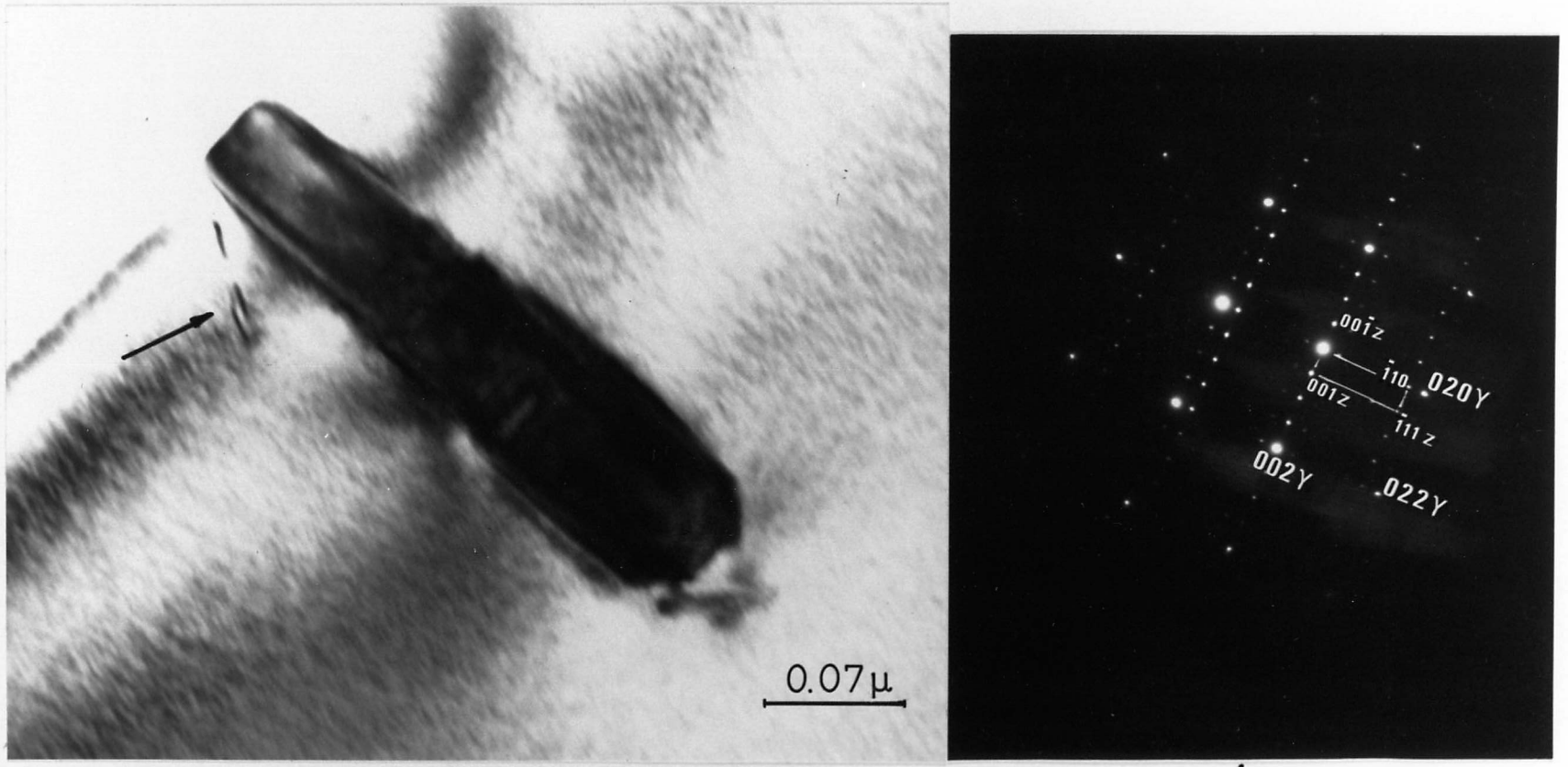

Fig.6.54 TEM images showing precipitation of Z phase. Aged at 1000 °C for one hour.
a) Bright field image; b) SADP, [100]γ // [110]Z, (001)γ // (001)Z.

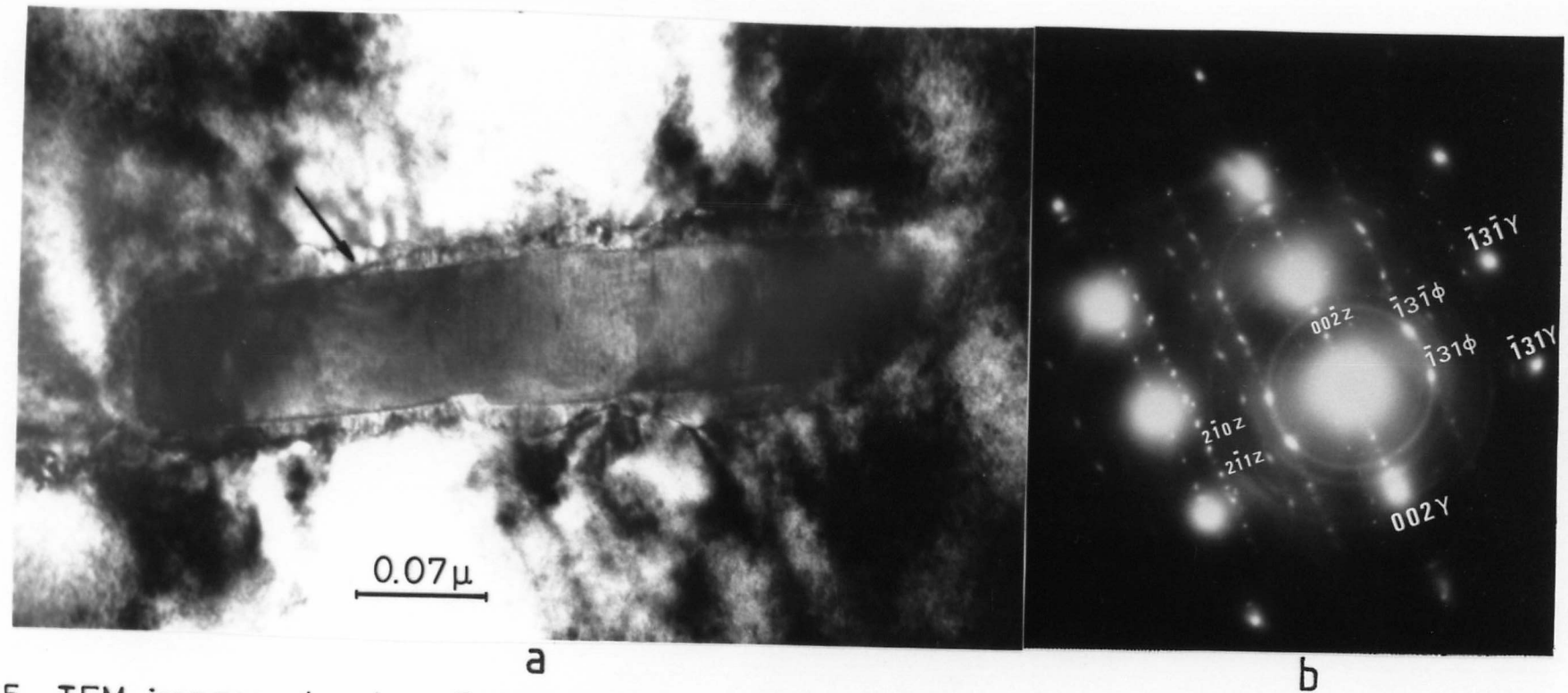

Fig. 6.55 TEM images showing Z phase particle surround by a crystalline fcc phase (arrowed) in the austenitic matrix. Aged at 1000 °C for 100 hrs. a) Bright field ; b) SADP, zone axis : [310]Y, [120]Z , [310] Φ phase .

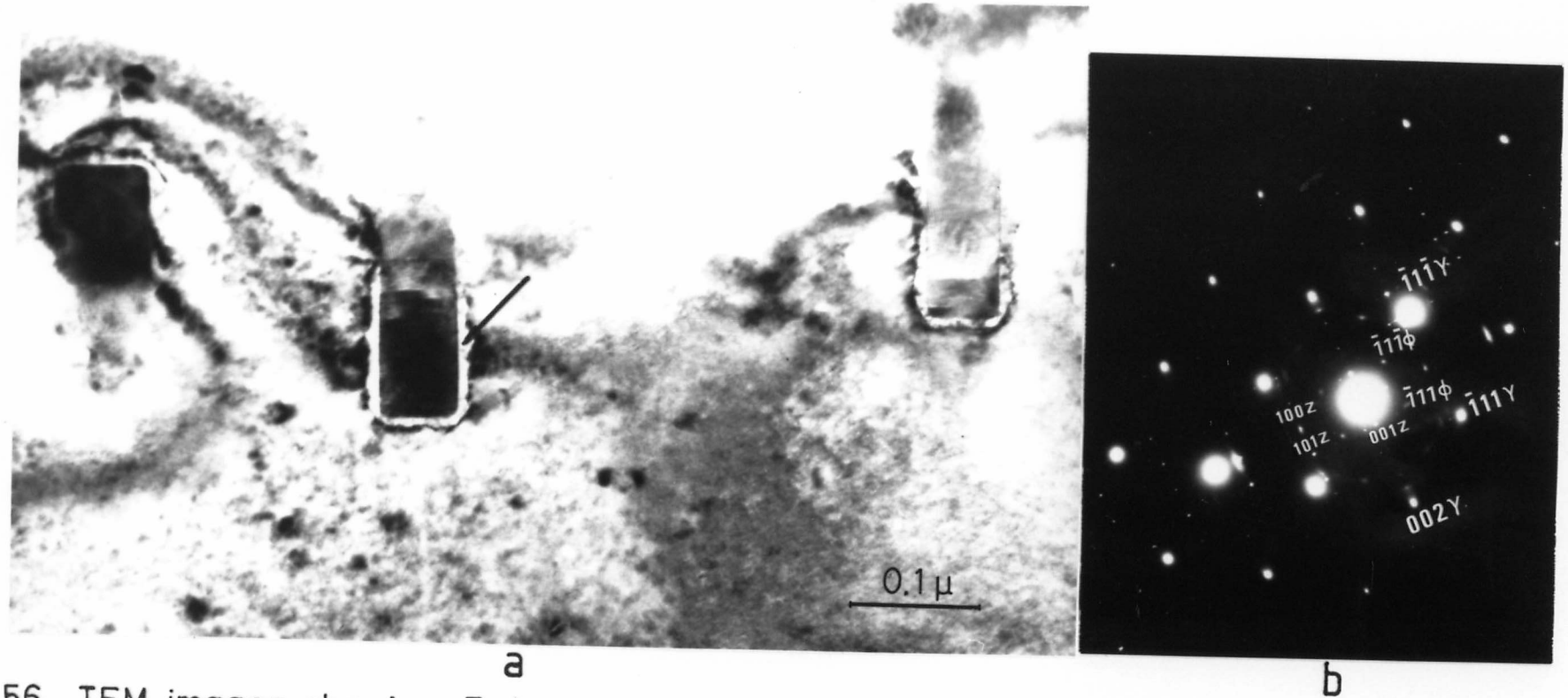

Fig. 6.56 TEM images showing Z phase particles surround by a crystalline fcc phase (arrowed) in the austenitic matrix. Aged at 1000 °C for 100 hrs. a) Bright field ; b) SADP, zone axis: [110]Y, [010]Z , [110] Φ phase .

7. MORPHOLOGY AND CRYSTALLOGRAPHY OF Z PHASE

7.1 Introduction

In Chapter 6, which outlined the general behaviour of REX 734 austenitic stainless steel, Z phase (Nb rich nitride) has been referred to, amongst other phases occurring in the temperature range 600-1000°C. The degree of precipitation and the precipitation rate of Z phase were a function of the ageing temperature, while the phase nucleated at grain boundaries and on dislocations. In order to understand better the precipitation reaction of Z phase in the present material, this chapter will give further consideration to the occurrence of this phase, with particular attention to its crystallography. Information on the composition of Z phase will also be presented.

7.2 Occurrence of Z Phase

The Z phase precipitated in REX 734 austenitic stainless steel over a wide temperature range 700-1000°C at all nucleation sites and always preceded the nucleation of any other phase. At 600°C the precipitation of Z phase is observed only at grain boundaries and is clearly in evidence after 1000 hours (Fig 6.5), however the $M_{23}C_6$ particles subsequently nucleate and grow adjacent to the Z phase particles. At this temperature however, the first sign of Z phase intergranular precipitation is observed after 100 hours, Fig 7.1, where small individual particles, sometimes showing strain contrast, can be seen within the boundary. The dislocations piling up at the boundary are free of precipitate, indicating that the reaction on matrix dislocations occurs more slowly at the boundary, as the latter is energetically a more favourable site for nucleation and growth. The dominant precipitate at 600°C is $M_{23}C_6$ which probably arises as a result of the more rapid diffusion of chromium vis-a-

vis niobium in austenite at low ageing temperatures. In the temperature range 700-1000°C the precipitation reaction of Z phase is faster and was detected after 1 hour at grain boundaries.

The morphology of Z phase precipitate at boundaries was equiaxed particles. On subsequent ageing the particles did not grow significantly large because the growing process was interrupted by the precipitation of other phases such as $M_{23}C_6$, χ phase, σ phase and Cr_2N which often competed for the same nucleation sites. In boundary areas free of other phases the small equiaxed Z particles grew to small cuboid particles about 400 A in size, Fig 7.2 (indicated by arrow).

The precipitation of Z phase in the matrix was associated with dislocations in the temperature range 700-1000°C. Precipitation of small equiaxed particles on dislocations was observed after 1 hour of ageing at 700°C. Occasionally a line of particles was observed without any accompanying dislocation. It was noted that dislocations can climb the precipitates and move a short distance. An example of this is shown in Fig 7.3 where the dislocations have moved away from the string of particles. As shown in Chapter 2, the free dislocations would provide a new site for subsequent precipitation of Z phase, occasionally forming rows of precipitates, Fig 6.18. A further precipitation effect was apparent in the temperature range 700-800°C. In the vicinity of large intergranular $M_{23}C_6$ particles there appeared to be a localized high density of dislocations, generated by growth of the $M_{23}C_6$ particles, on both sides of the grain boundary. These dislocations also nucleated Z phase, see Fig 7.4. Similar precipitation effects were not seen close to large χ phase and Cr_2N particles, even though on growing the intermetallic and chromium nitride did generate dislocations. The reason for the difference in this precipitation behaviour is believed to result not from any fundamental differences in the resultant matrix deformation following precipitation but rather to the precipitation sequence of the REX 734 austenitic stainless steel.

With increasing time and/or temperature of ageing, the equiaxed Z particles on dislocations were observed to grow into cuboids, and frequently had dislocations or dislocation loops around them (indicated

by arrow in Fig 7.5). Quite often, at this stage, the cuboids had joined or overlapped so that irregular slabs of Z phase were produced. At the temperature range 800-900°C the growing rates were faster and more frequently the stringer of Z particles led to the development of secondary branches as in Fig 6.35. The creation of dislocations which act as nuclei for the strings of precipitates forming the branches has been discussed by Lewis and Hattersley[27] and later confirmed by Beckitt and Clark[32] for $M_{23}C_6$ precipitation. More recently similar observations have been reported by Colclough [35] for Z phase precipitation which the author referred to as Z phase "propeller". The mechanism suggested by Lewis and Hattersley seems to agree with the present work where the origin of this distribution is due to dislocations generated by the "prismatic punching" mechanism, around growing particles. There is evidence that dislocation loops are formed around growing particles, Fig 7.5, and that these loops are capable of gliding, offering an opportunity for further precipitation, Fig 7.6. The force which drives the loop out is the repulsion between consecutive loops created by the growing particles, and the loops will only continue to be created as long as the precipitates continue to grow.

At 1000 °C the density of precipitate in the matrix was low and dislocations were observed in the matrix in association with the particles which show a plate-like morphology. At this temperature, the Z phase particles have nearly reached their optimum volume fraction after one hour of ageing. As the rate of precipitation is faster, it would be expected that the stringer precipitation would form more quickly than at lower temperatures, however such stringer precipitation was never detected at 1000°C. The reason for this is thought to be related to the solubility of the Z phase. Although the solubility curve of Z phase in austenite is not known, in the present investigation no Z phase (undissolved particles) could be detected in the as-received material after solution treatment at 1200°C for one hour. Furthermore, on ageing REX 734 at 1000°C, a new phase, designated as ϕ phase (see section 6.7), is detected around Z phase particles after 100 hours. The formation of ϕ phase appears to be related either to the dissolving process of Z phase or the depletion in solute in the neighbouring areas.

The Z phase precipitation reaction observed in the present investigation is quite different from that reported by Colclough[35] in a 21Cr 12Ni (wt %) austenitic stainless steel containing 0.18 wt % Nb and 0.24 wt % N. The author indicated that, at the early stages of the precipitation reaction, Z phase particles were not associated with any type of imperfection, though later in the ageing sequence dislocations did appear to be associated with the growing Z phase. The author also observed that Z phase particles alone could be detected on ageing at 1000°C and in the as-received material after solution treatment at 1200°C for 1/2 hour.

In the present work, the intragranular precipitation reaction of Z phase was seen to be associated with dislocations formed by quenching stresses during quenching from the solution heat-treatment temperature. The precipitation of Z phase on dislocations led to high precipitate densities because of the autocatalytic process operating. The discrete small equiaxed particles nucleated on existing dislocations and it seems that they grow partially coherent with the matrix. In order to accommodate the strains resulting from the difference in atomic volume between the two lattices, loops of dislocation are "punched" out by the growing particle into the matrix. These punched loops then act as sites for further precipitation of Z phase, resulting in the formation of stringers observed after long ageing times at low temperatures and short times at high temperatures, with the exception of 1000°C where this feature was not observed.

7.3 Crystallography

While simple carbides and nitrides invariably have an orientation relationship with austenite, there is very little published data regarding the crystallography of Z phase precipitation in austenite. The tetragonal Z phase structure as described by Jack and Jack[102] is in effect two body-centred cells, one on top of the other, and in fact the atomic arrangement may have a simple relationship with austenite. In the present work, according to various diffraction patterns taken from Z phase equiaxed particles and cuboids at different zone axes, an invariable orientation

relationship with the austenite matrix is observed in agreement with Colclough[35]:

(001) Z phase // (001)γ
[100] Z phase // [110]γ

The relationship between the two cells is shown in Fig 7.7 where the diffraction pattern arises from the Z phase particle which precipitated during ageing treatment at 1000°C. From the solution of the diffraction pattern in Fig 7.7, it is clear that the incident beam is parallel to the [110] γ direction and that the solution of Z phase diffraction pattern corresponds to the [100] Z phase. Based on this relationship the unit cells can be drawn as in Fig 7.8. Taking the austenite lattice parameter as a=3.63 Å while the unit dimensions for the Z phase are a=3.01 Å and 7.28 Å; the atomic arrangement in the (001) austenite plane, in agreement with that suggested by Colclough[35], is shown in Fig 7.9 where, from the position of the austenite atoms, it can be seen that the (001) Z phase plane would fit closely. From this arrangement a good atomic match is clear for the niobium and chromium atoms in the Z phase but in addition the nitrogen atom in the (001) Z phase plane would fit into the interstitial site, as shown. The degree of misfit between the Z phase and austenite lattice would be

$$\frac{3.01 - 2.56}{\frac{(3.01 + 2.56)}{2}} = 16\%$$

The match for the planes perpendicular to this section can be checked from the resultant atomic arrangement which arises from the configuration presented in Fig 7.9. In the <001> austenite direction the arrangement is that shown in Fig 7.10. Again, this atomic arrangement results in a close match between the two structures, and the nitrogen atoms in the Z phase conveniently fit into the interstitial sites in the austenite. The degree of misfit would be:

$$\frac{2(7.28 - 7.26)}{7.26 + 7.28} = 0.3\%$$

A stereogram depicting the orientation relationship between the two phases is shown in Fig. 7.11. Using this stereogram it is possible to solve and predict electron diffraction patterns for a given beam direction for the austenite and Z phase. Examples of this is given in Figs 7.12 and 7.13. In Fig 7.12, a bright field, dark field and selected area diffraction pattern is presented from Z phase intragranular precipitates. The arbitrarily indexed matrix reflections show that the beam direction with respect to the austenite matrix is $B_\gamma=[\bar{1}03]$. Using the stereogram for the orientation relationship between the two phases, it is found that this direction corresponds with the solution of the diffraction pattern based on interplanar distance and interplanar angle measurements in Fig 7.12.

A further diffraction pattern, bright field and dark field images from Z phase intragranular precipitates, is presented in Fig 7.13. In Fig 7.13b it is apparent that two sets of precipitate contribute to this diffraction pattern. A solution to one of the diffraction patterns is presented in Fig 7.13c, and on the basis of the arbitrarily designated matrix indices the beam direction, with respect to the austenite matrix, is $B_\gamma=[\bar{1}10]$. For this beam direction there is another possible variant, $B_\gamma=[\bar{1}01]$. Utilizing this variant the expected diffracting zone is shown in Fig 7.13d. From the solution of each diffraction pattern it is apparent that the orientation relationship is confirmed.

7.4 Chemical Microanalysis

In the present investigation, Z phase cuboids in thin foil specimens could be identified by their characteristic X-ray chemical microanalysis. Jack and Jack[102] showed from X-ray diffraction data that Z phase was ideally a niobium-chromium nitride of composition $Nb_2Cr_2N_2$ and Colclough[35] has shown through microanalysis results that this phase is primarily composed of niobium and chromium.

Throughout the temperature range in which Z phase formed in REX 734, two types of electron energy-dispersive spectra were obtained by scanning transmission electron microscopy. The first example is shown in Fig 7.14 where it can be seen that the Z phase is basically composed of niobium and

chromium, with small amounts of iron, nickel and molybdenum being present. The height of the Nb Lα peak is relatively greater than that of chromium Kα. Fig 7.15 shows the spectrum from a different particle where the heights of the niobium Lα and chromium Kα peaks are relatively closer, but there is more iron. Such variations between particles were common, suggesting that there is some tolerance for metal interchange with retention of high concentration of niobium and chromium.

In order to obtain a quantitative result for Z phase chemical composition, attempts were made to determine the nitrogen content of the phase, however no successful specimen could be obtained for electron energy-loss analysis. Therefore, the results presented in this section are only those obtained with electron energy-dispersive analysis, but without quantification of each element being present in the Z phase.

7.5 Summary

a) In the temperature range 600-900°C Z phase precipitates in REX 734 as equiaxed particles at boundaries and on dislocations in the matrix. At later stages of ageing between 700-900°C the equiaxed particles grow into cuboids.

b) At 1000°C the Z phase particle shows a plate-like morphology.

c) The Z phase has a tetragonal structure with lattice parameter a=3.01 Å, c=7.28 Å, and has an orientation relationship with austenite as follows:

$$(001)\ Z\ \text{phase}\ //\ (001)\ \gamma$$
$$[100]\ Z\ \text{phase}\ //\ [110]\ \gamma$$

d) Z phase is primarily composed of niobium and chromium but some iron may be present.

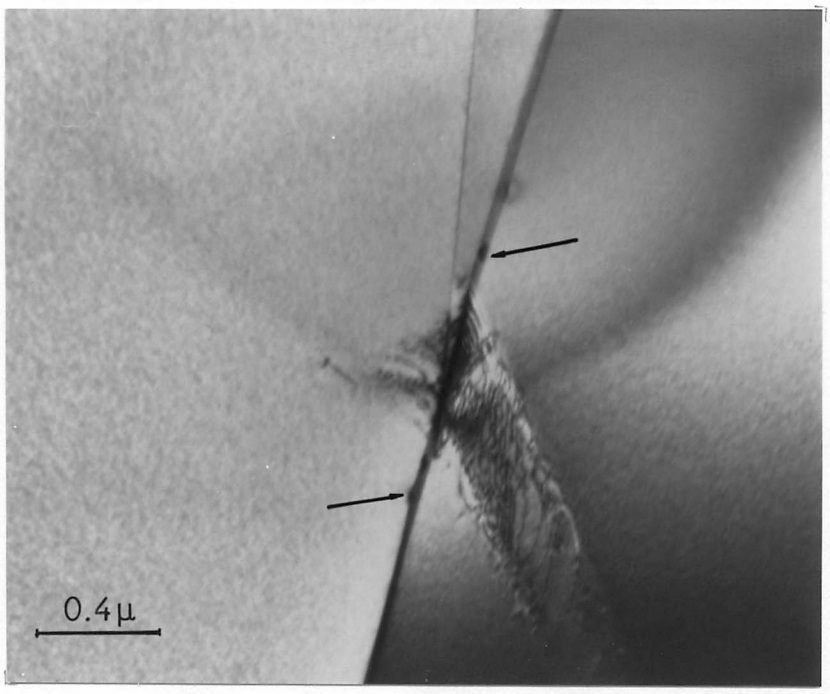

Fig 7.1 Bright field TEM image showing Z phase precipitation at grain boundary. Aged at 600°C for 100 hrs.

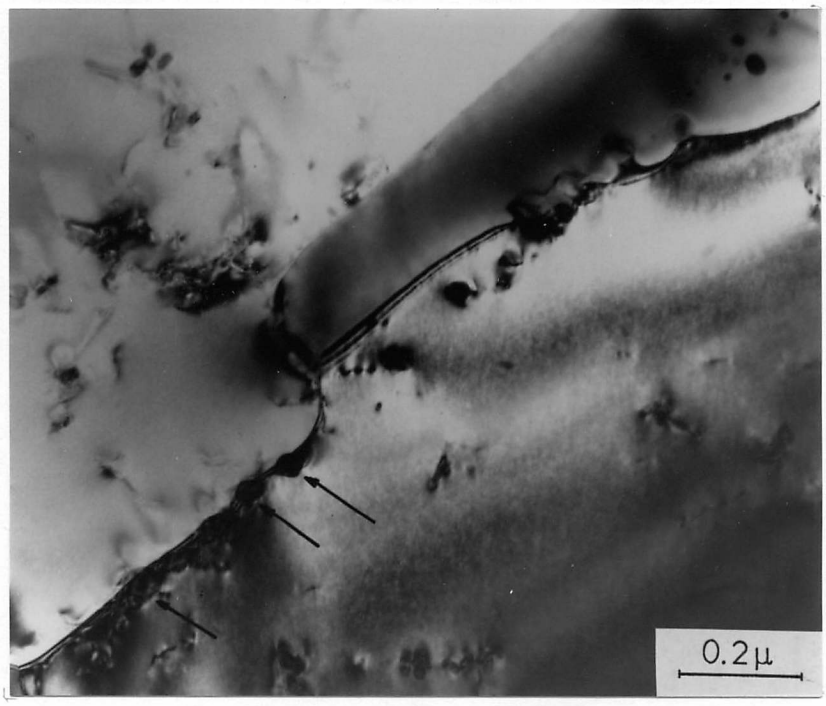

Fig 7.2 Bright field TEM image showing Z phase cuboids (arrowed) at grain boundary. Aged at 800°C for 100 hrs.

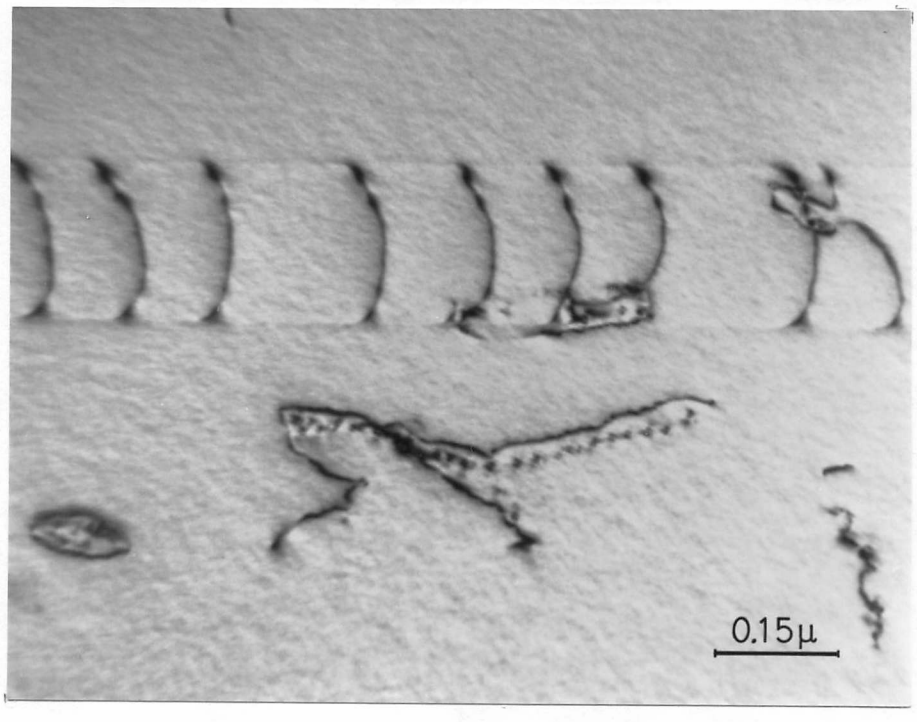

Fig 7.3 Bright field TEM image showing Z phase precipitation on dislocations in the matrix. Aged at 700°C for 1 hr.

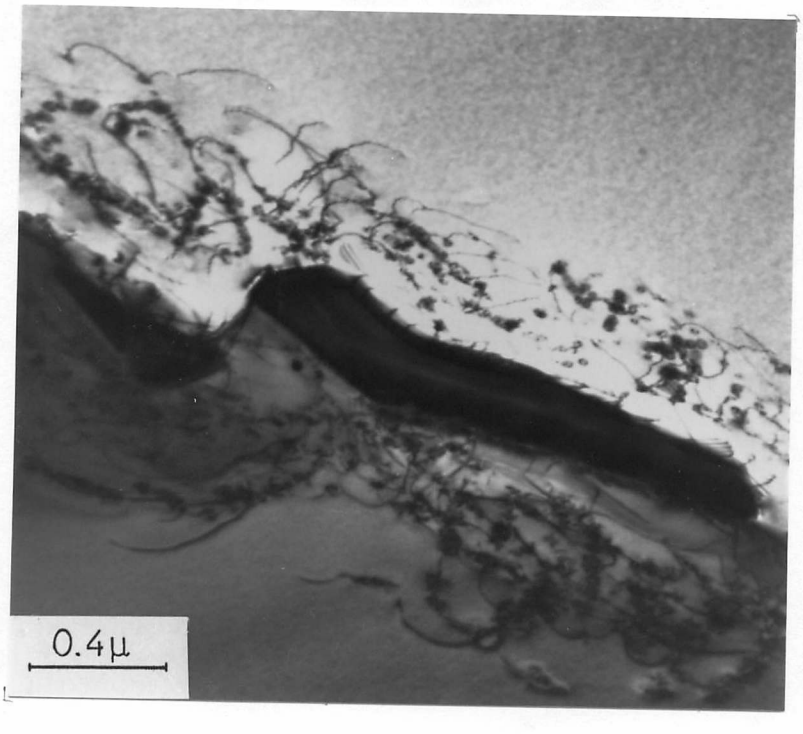

Fig 7.4 Bright field TEM image showing Z phase precipitation on dislocations generated around $M_{23}C_6$ particles. Aged at 800°C for 10 hrs.

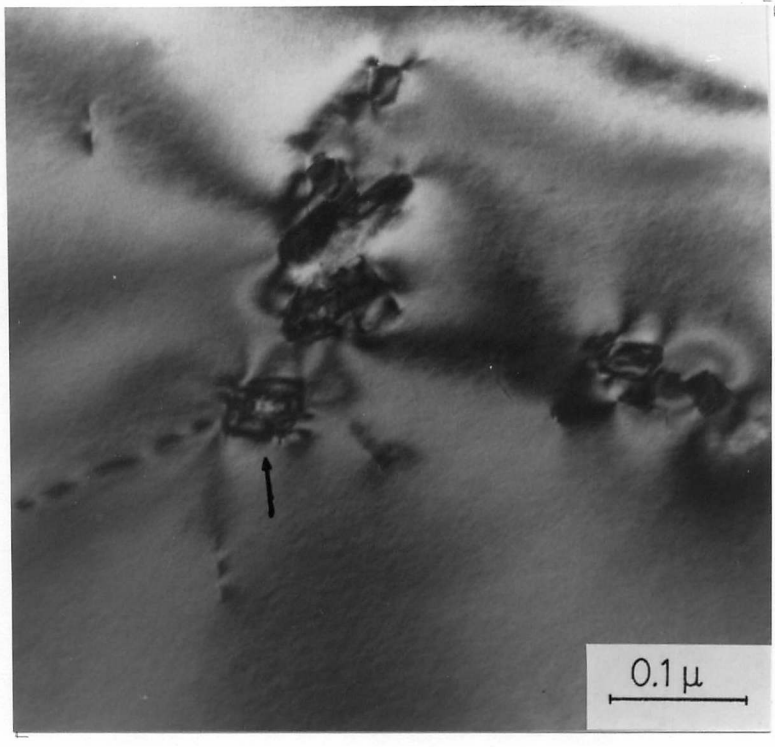

Fig 7.5 Dislocation loops (arrowed) emerging from a Z phase cuboid precipitate particle. Aged at 800°C for 100 hrs.

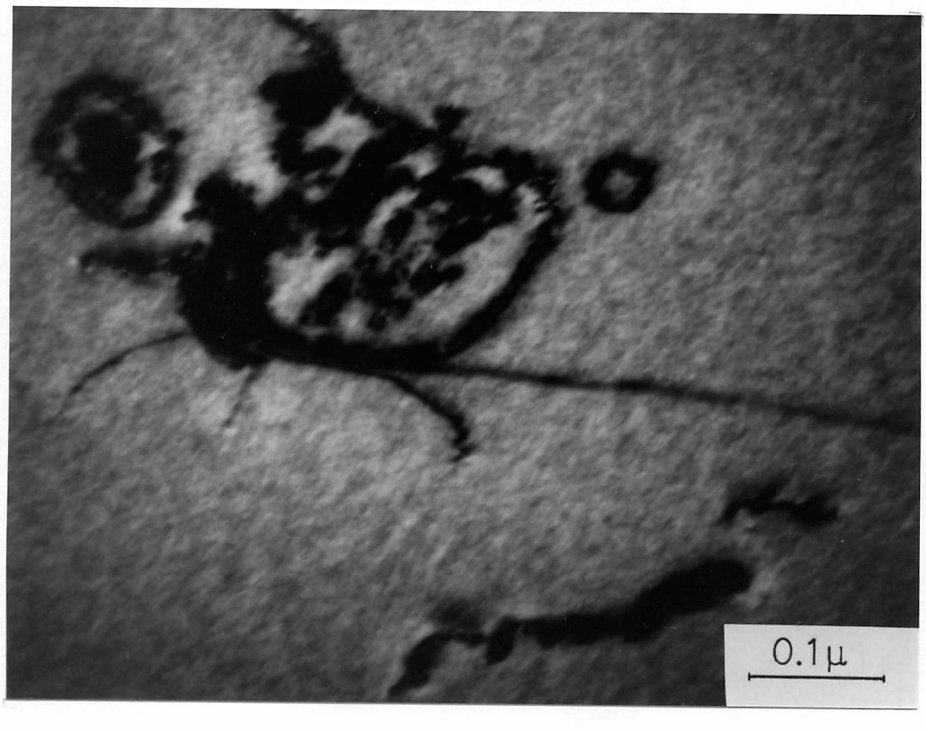

Fig 7.6 Dislocation loops around a matrix precipitation cluster decorated with small particles on subsequent precipitation of Z phase.

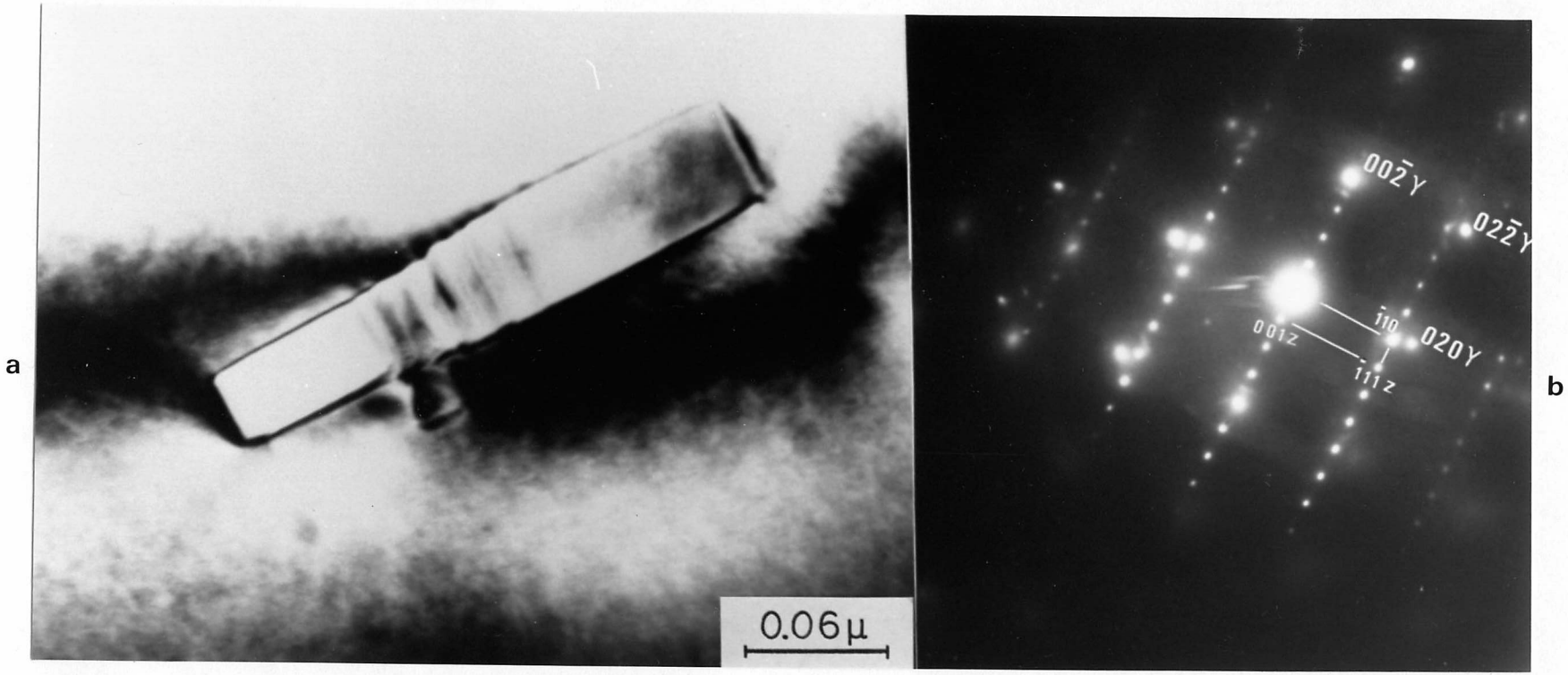

Fig 7.7 a) Bright field TEM image showing Z phase particle in the matrix. Aged at 1000°C for 1 hr.
b) Selected area diffraction pattern of Z phase. [100] γ // [110] Z; (001) γ // (001) Z.

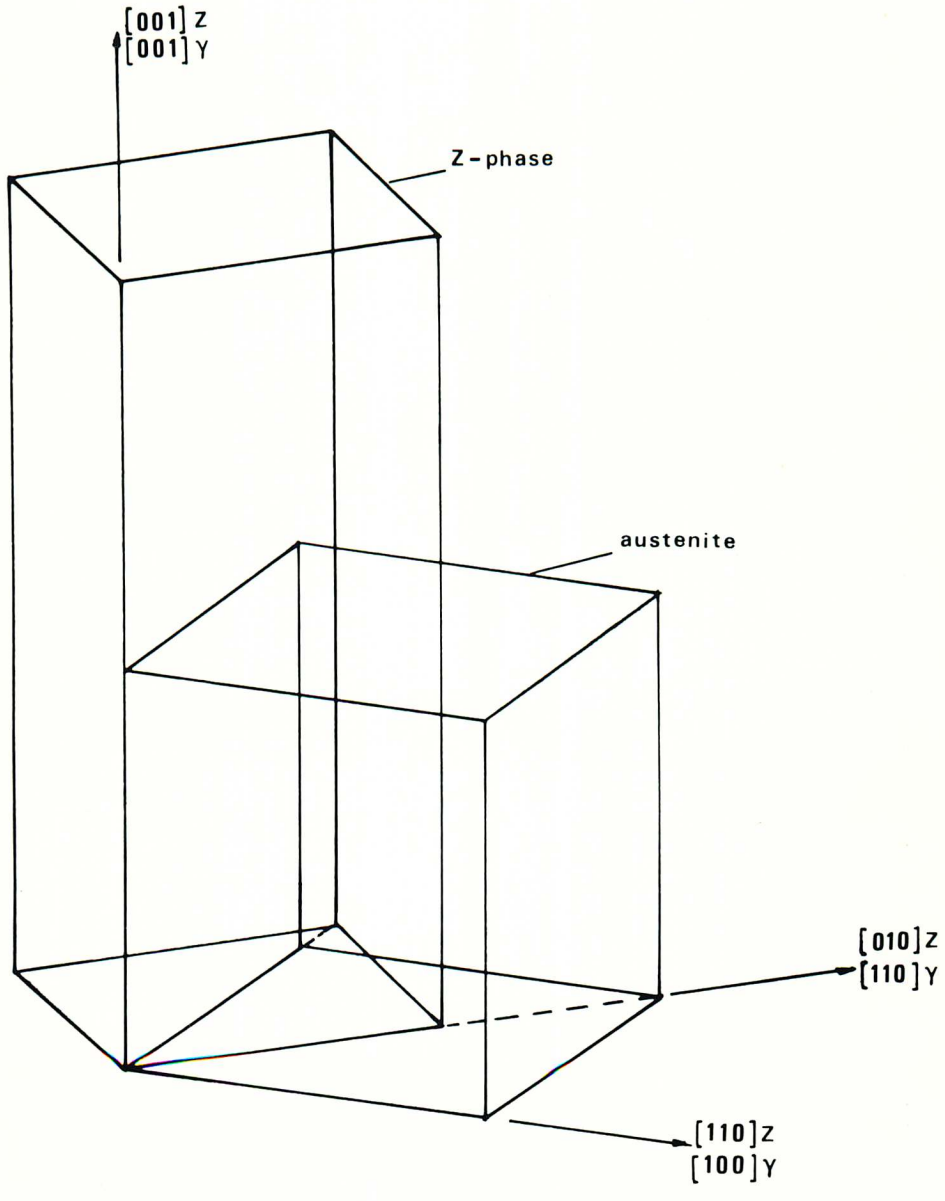

Fig 7.8 Schematic representation of observed orientation relationship between austenite and Z phase.

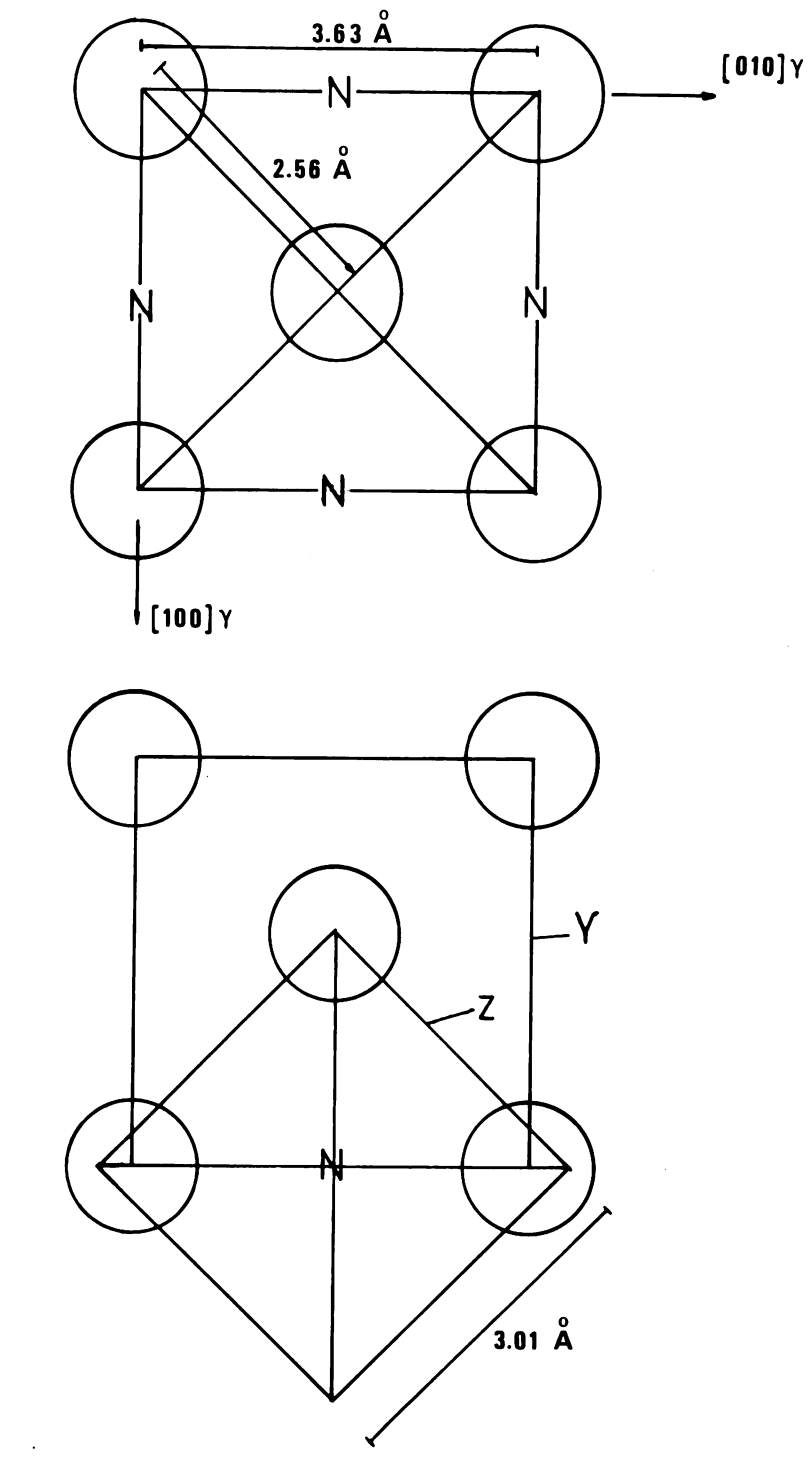

Fig 7.9 Atomic arrangement of austenite and Z phase in the [001]γ direction for the orientation relationship between the two phases.

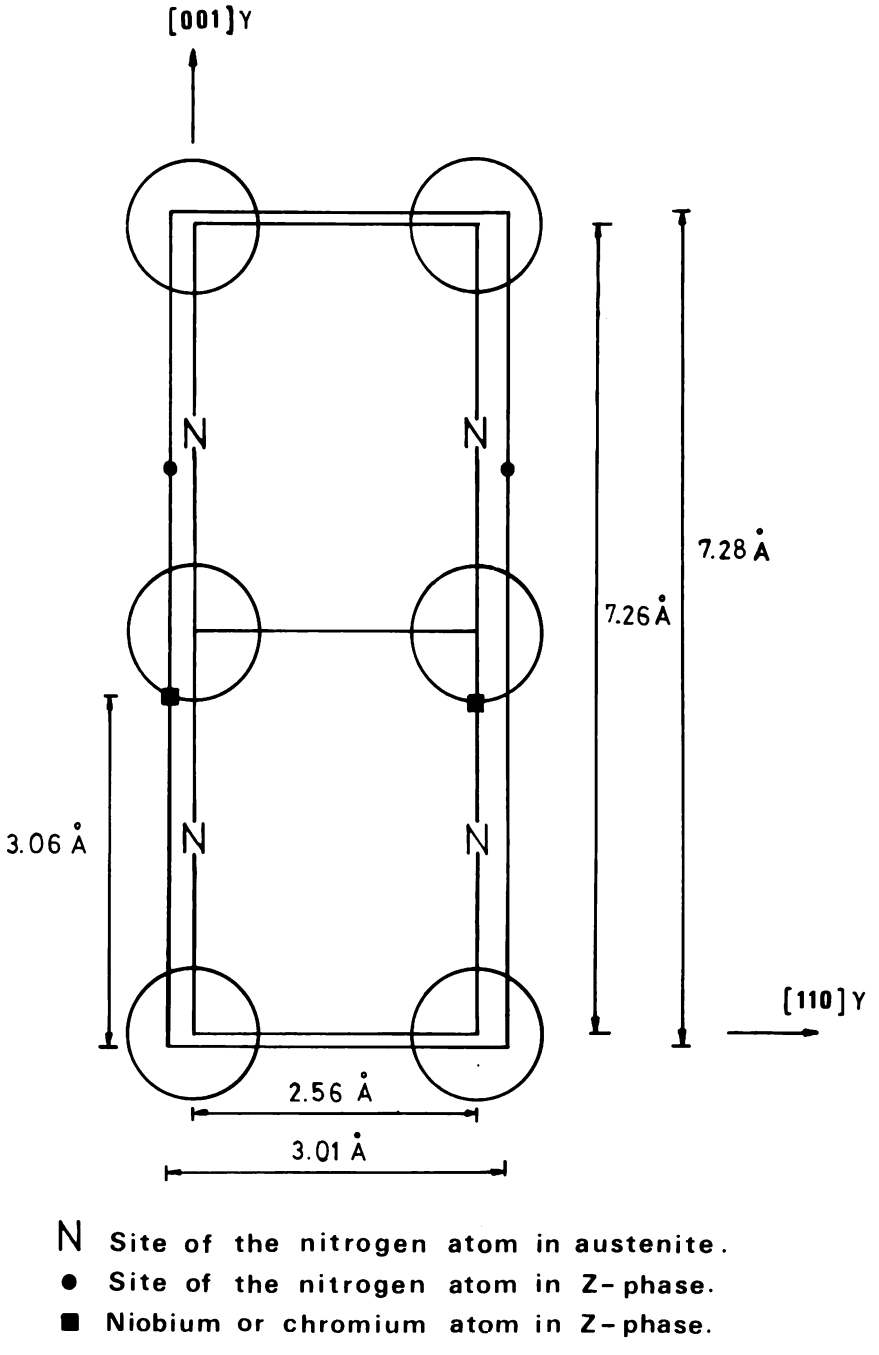

Fig 7.10 Atomic arrangement of austenite and Z phase in the $[1\bar{1}0]\gamma$ direction for the orientation relationship between the two phases.

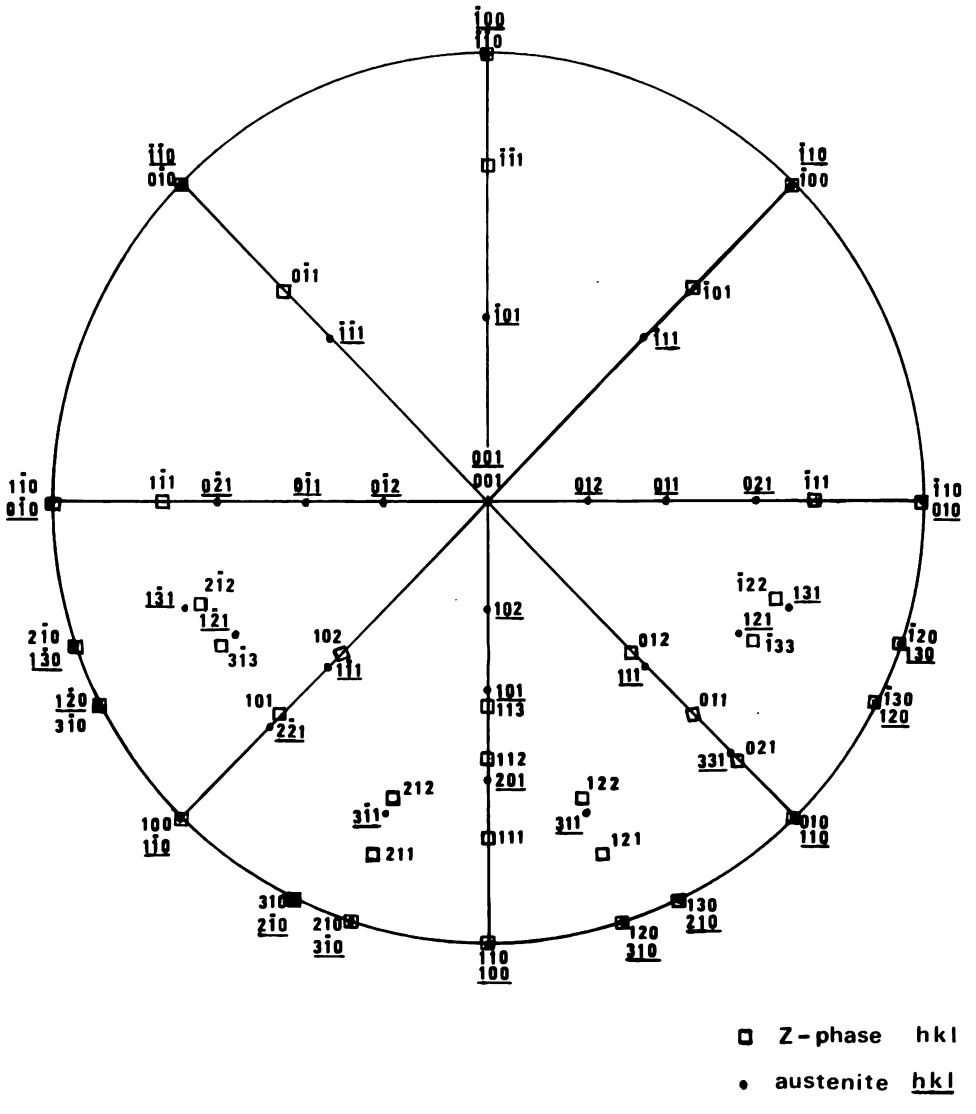

Fig 7.11 Stereographic projection for Z phase and austenite, based on the orientation relationship observed: (001)γ // (001)Z; [100]γ // [110]Z.

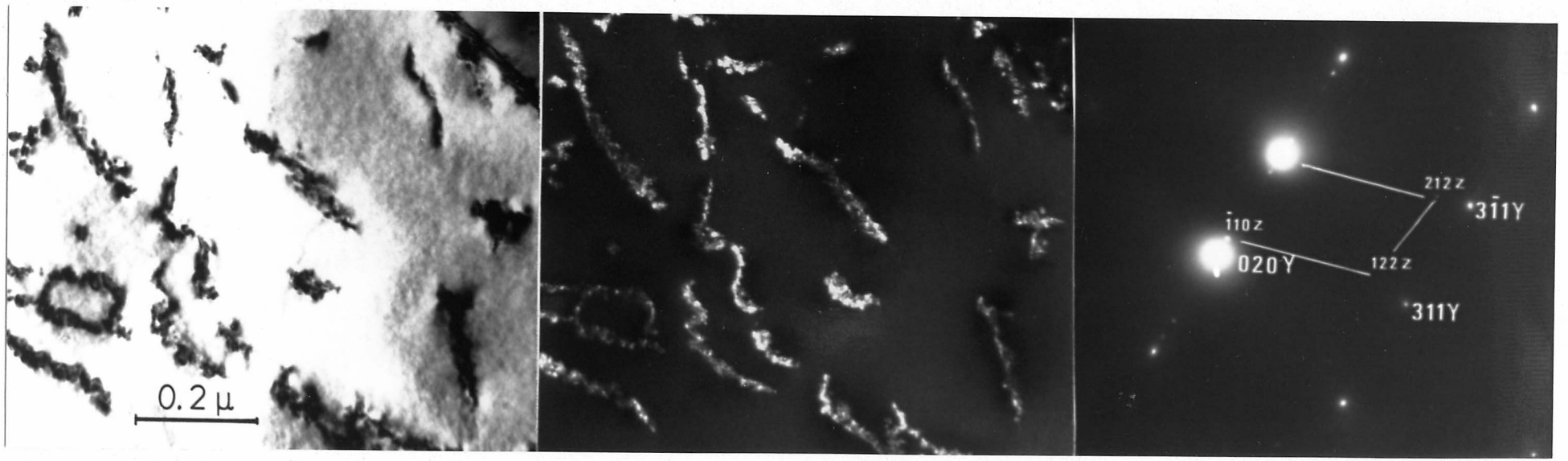

Fig 7.12 Bright field, dark field and selected area diffraction pattern of intragranular precipitation of Z phase. Aged at 700°C for 100 hrs. Zone axis $[\bar{1}03]$ γ, $[\bar{1}\bar{1}1]$ Z phase.

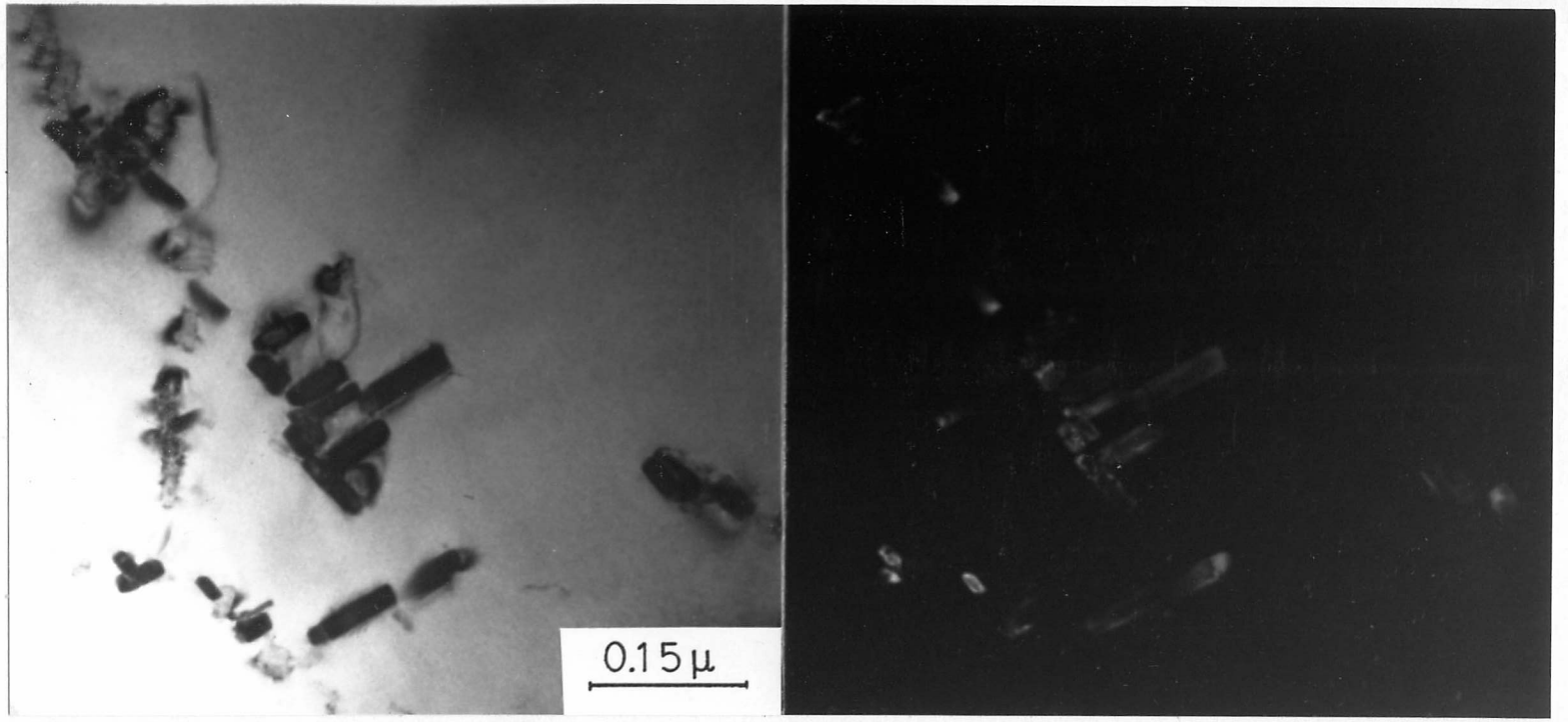

a

Fig 7.13 a) Bright and dark field images showing two sets of intragranular Z phase precipitates. Aged at 800°C for 100 hrs.

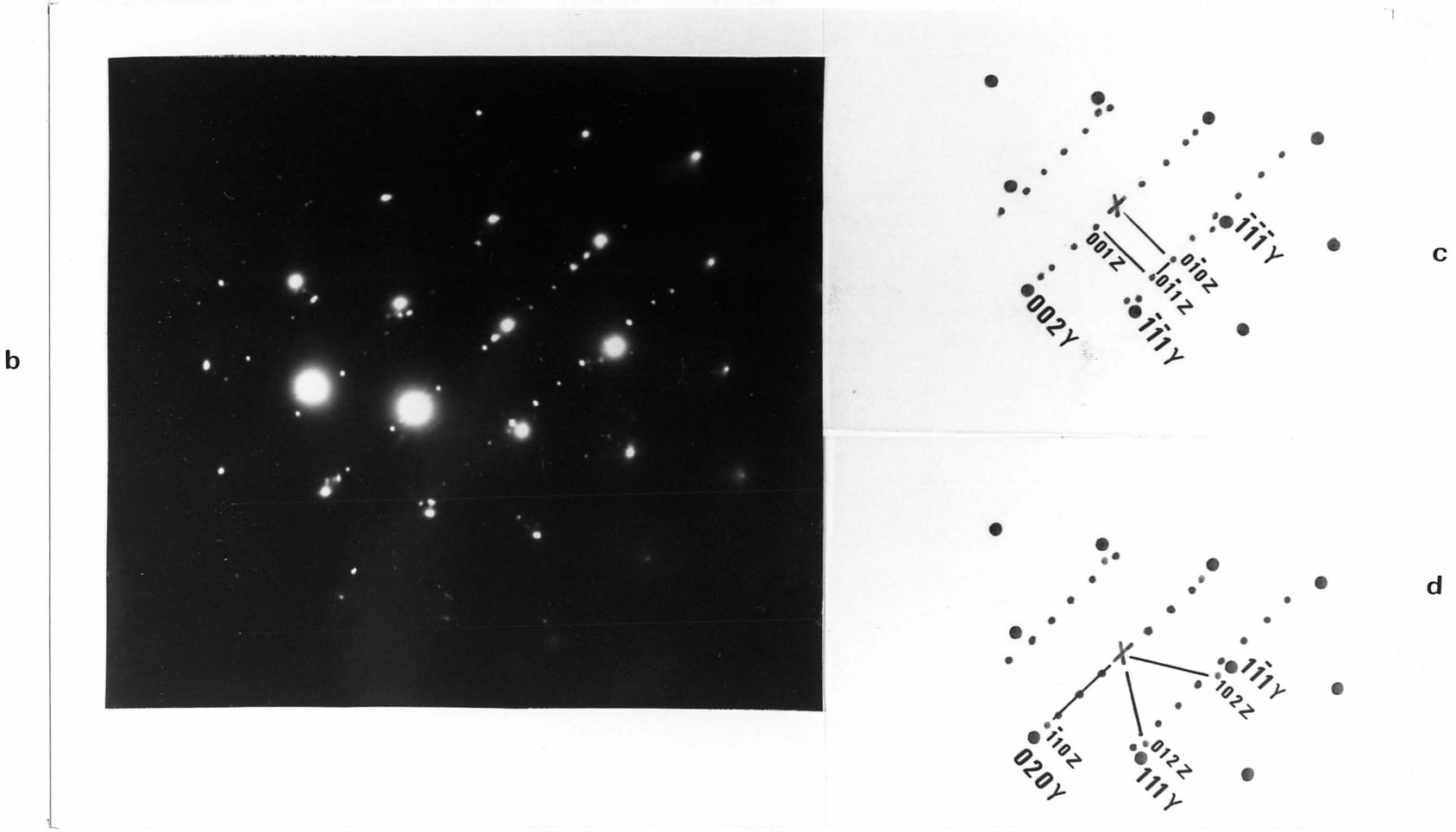

Fig 7.13 b) Selected area diffraction pattern from two sets of intragranular Z phase precipitates. c) Solution to the diffraction pattern of one set of Z phase precipitates in Fig 7.13b. $[\bar{1}10]\gamma$ // $[\bar{1}00]z$. d) Solution to the diffraction pattern of other set of Z phase precipitates in Fig 7.13b. $[\bar{1}01]\ \gamma$ // $[\bar{1}\bar{1}0]z$.

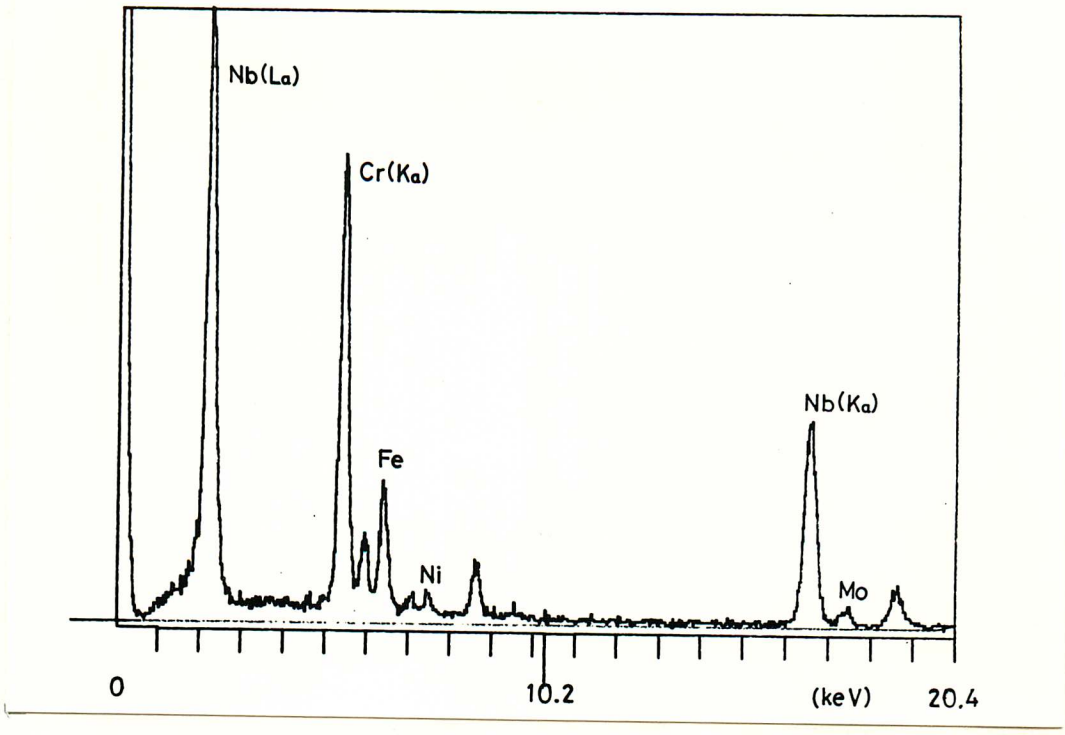

Fig 7.14 Electron energy-dispersive spectrum of a Z phase particle in thin foil specimen.

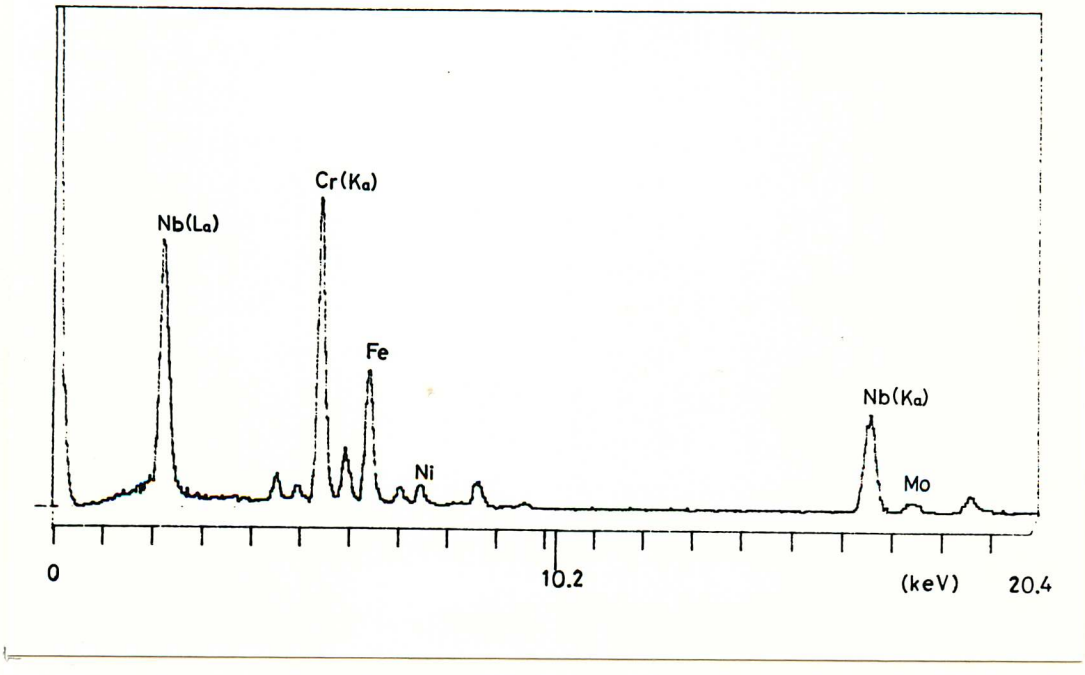

Fig 7.15 Electron energy-dispersive spectrum of a Z phase particle in thin foil specimen. This Z phase variant contains more iron and chromium.

8. STRUCTURES DEVELOPED IN WELDING

8.1 Introduction

The structures developed in REX 734 austenitic steel weld joints were studied using optical microscopy, scanning electron microscopy, transmission electron mocroscopy and related techniques such as electron energy-dispersive X-ray analysis. These techniques and the preparation of specimens have been described in Chapter 5. The results obtained with these various techniques were found to be complementary, giving an overall picture of the transformations that have occurred in welding.

One important characteristic in welding which differs from the ageing treatment of REX 734 previously studied is the presence of δ ferrite in the weld deposits. The appearance of δ ferrite is strongly dependent on the composition of the weld deposits, and in the present investigation it was found that nitrogen had a significant influence on the amount of δ ferrite observed in the fusion zones at room temperature. This will be the subject of the next section in this chapter. In the other two sections the general precipitation behaviour of the welds will be described together with the identification of the various phases present in the fusion zone. Although the type of precipitating phases present in welding such as Z phase, χ phase and σ phase has been previously identified under normal ageing treatment conditions (Chapter 6), the general structure of the welds was more complex and it was difficult to obtain specimens from selected regions.

8.2 Effect of N on the δ Ferrite Transformation

The room temperature microstructure of weld deposits in the present investigation exhibited a duplex (δ + γ) microstructure with relatively low content of ferrite measured by magnetic permeability using a EL Cometer Inspector gauge calibrated against magnetic gauge instrument [1]. The Ferrite Number (FN), which is approximately the percentage of ferrite, obtained for each welding joint is indicated below:

WELDING PROCESS	FN (Ferrite Number)
MMA1	2.5
MMA2	2.0
TIG3	6.5

A significant variation in the content of ferrite can be seen between the two welding processes (MMA and TIG). A number of factors such as composition, ferrite morphology, ferrite dissolution and/or transformation, and cooling rate may influence the amount of ferrite present in the weld deposits. Here we should also mention changes in the nitrogen content during welding, which could contribute significantly to variations in ferrite content. The nitrogen content on the TIG weld deposit was for example about half of that obtained in MMA1 weld deposit, see Table 5.2.

The ferrite content expected from the Schaeffler diagram in Fig 2.6, for the chemical composition of the weld deposits is much higher (between 10% and 20%) than that actually measured. The main reason is the non-inclusion of nitrogen on the nickel equivalent used to determine that diagram. Nitrogen is well known as a strong austenite stabilizer as has been discussed in Chapter 2. Taking for instance the effect of nitrogen and reviewing the effect of other elements, Schneider[171] has modified the Schaeffler diagram. Using the Schneider's modified Schaeffler diagram the predicted content of ferrite would fit more closely to the results obtained in the present investigation, see Fig 8.1.

---

[1] The ferrite number (FN) was measured by The Welding Institute in accordance with AWS A 4.2-74 specification.

The effect of nitrogen on δ ferrite in weld deposits has been discussed by other authors[132,172,173]. Cieslak et al[132] for instance observed that increasing the nitrogen content of the weld deposits by adding nitrogen to the shielding gas caused a decrease in Ferrite Number as can be seen in Fig 8.2. The observed decrease in FN with increasing nitrogen content of the shielding gas is consistent with previous work[172,173]. Furthermore, Cieslak pointed out that increasing nitrogen content, the weld deposit changes the solidification mode from one of primary delta ferrite to one of primary austenite which is accompanied by an increase in the hot-cracking susceptibility. In the present investigation hot-cracking was not observed in the weld deposits but the soldification mode seems to have changed with the reduction of nitrogen, in agreement with Cieslak as will be seen later.

Fig 8.3 shows a typical solidification structure from weld deposit MMA1. It can be seen that an austenitic columnar structure has developed containing some ferrite between cellular dendritic interstices (arrowed). In some areas a ferrite network is formed as indicated by A in Fig 8.3 and seen in Fig 8.4. The ferrite in this case seems to be located mainly at the cores of the original cellular dendrites, and originates from the last liquid to solidify.

No significant change in the amount and location of ferrite was observed in MMA2 weld deposit in relation to MMA1 as can be seen from Fig 8.5. This is in reasonable agreement with the FN measurements presented before. However, the effect of nitrogen is not revealed unambiguously. A reduction on the nitrogen content of 0.07 wt % N could be detected in the case of MMA2 weld deposit, however, contrary to what would be expected, a reduction in nitrogen content of the MMA2 weld deposit was accompanied by a small decrease in the ferrite number of 0.5. The decrease in ferrite content could perhaps be associated with differences between location of the FN measurements in the MMA2 weld deposit and the actual content of nitrogen in the corresponding area. The nitrogen content obtained by chemical analysis is representative of the whole weld deposit while the FN is a measure of the weld deposit centre. Variations in the ferrite content are expected to occur within the weld deposit as will be discussed later.

On the other hand, it may be possible that the decrease in FN observed in this case is also related to the decomposition of ferrite during cooling to room temperatures. In the MMA2 weld deposit the weld heat input is higher than that in MMA1 (Table 5.3), and the cooling would then be expected to be slower, thus providing more opportunity for ferrite to decompose during cooling to room temperature. In fact looking at higher magnification, the ferrite network observed at both weld deposits at room temperature, Figs 8.6 and 8.7, does show some difference in appearance. In the case of MMA2, Fig 8.7, it appears that there is a greater tendency of ferrite to decompose, to form austenite and precipitates which could account for the discrepancy in the FN measurement.

In the case of TIG weld deposit, the variation in ferrite content was quite clear and the reduction of nitrogen content (Table 5.3) is accompanied by an increase in FN. The location of ferrite was in most of the areas at the core of the cellular austenite dendrites as seen in Fig 8.8. Although there was a tendency for ferrite to decompose, this did not occur extensively, Fig 8.9, as that observed in the MMA weld deposits.

Analysing the results obtained on the basis of the solidification mode proposed by Suutala[123] (Chapter 4), it appears that the MMA1 amd MMA2 weld deposits solidify as primary austenite and the delta ferrite solidifies from the last of the melt. The Creq/Nieq (Schneider's Creq and Nieq) ratio for MMA1 and MMA2 is 1.4 and 1.23 respectively, which approximate to the value given by Suutala, Creq/Nieq $\leq$ 1.48, for a solidification mode having austenite as the primary or leading phase, and with δ ferrite solidifying from the last melt between the cells or cellular dendrites of the austenite.

In the case of the TIG weld deposit, the Creq/Nieq ratio is 1.32, which is also within the range of solidification mode having austenite as the leading phase. However, the location of the δ ferrite is in most of the areas at the core of the cellular dendrites, indicating a solidification mode with δ ferrite as leading phase and austenite solidifying from the last of the melt. Except for the location of δ ferrite no further examiniation was made to confirm that the solidification mode had changed from primary austenite to primary ferrite,

although a possible change of the solidification mode would be consistent with the decrease in nitrogen content of the TIG weld deposit.

Although several authors[125,130,132] have found that the location of δ ferrite in the final weld deposit microstructure is consistent with the solidification mode (e.g. primary austenite solidification mode shows δ ferrite at cellular dendrite interstices and primary ferrite solidification mode shows ferrite at the core of the cellular dendrites), in the present work it was thought that more experiments on solidification and careful microanalysis on ferrite/austenite interfaces would be needed to make conclusive assertions.

It should be mentioned that the FN results presented in this section for both welding processes were representative of measurements of ferrite content at the weld deposits centre. A variation of +1 is found for measurements of ferrite at the top (sealing run) of the weld deposits, and -1 for root runs made by manual metal arc welding process (MMA1, MMA2). In the case of the TIG weld deposit a variation of +1.5 for both top and root runs is obtained.

Variations in ferrite content within the weld were also reported by David[174]. The author has related this fact to the weld metal composition, ferrite morphology, and dissolution of ferrite resulting from the effect of thermal cycles during subsequent weld passes. In the present investigation no significant change in ferrite morphology has been observed, but a tendency to increase the instability of ferrite was observed when a weld pass was subjected to thermal treatment by subsequent passes. Additionally, variations on metal dilution may have occurred leading to changes in local chemical composition since, in practice, the extent of dilution depends on the welding process and procedure variables such as current, travel speed, welding techniques, joint design and material thickness. In fact, except for the material thickness the other parameters changed as can be seen from Table 5.3 and Figs 5.1 and 5.2.

Although such variation in FN from location to location within the weld deposit may influence its mechanical and chemical behaviour, from the viewpoint of microstructure analysis this would not affect the results and

discussion presented before. These variations are well within the ferrite number range observed between the two welding processes (MMA,TIG), and will not be considered separately.

8.3 Precipitation in the Weld Fusion Zone

8.3.1 Manual Metal Arc Weld Deposits

The weld fusion zones obtained by the manual metal arc welding process have shown a significant difference in precipitation behaviour between areas that have been subjected to welding thermal cycles by the multipass technique, and those free of it (e.g. sealing runs). In the latter, the austenite and δ ferrite are seen to be free of precipitates as shown by scanning electron microscope image in Fig 8.10. This result was confirmed by examination of thin foils obtained from sealing runs of the weld fusion zones. An example of an austenite/austenite interface and austenite/δ ferrite interface is given in Figs 8.11 and 8.12 respectively. In both cases no precipitation was detected. The heavily deformed austenite matrix quite often would show slip bands and a high density of dislocations as shown in Fig 8.13, but again no indication of precipitation was found.

In the case of areas which have been subjected to thermal cycles by subsequent passes (e.g. weld runs below the sealing run), precipitation could be detected in areas which seemed to have been previously γ/δ interfaces. An example of this is shown in Fig 8.14 where some of the particles could be identified by their characteristic spectra, utilizing the microanalysis attachment on the ISI scanning electron microscope. From the spectra obtained these particles were identified as χ phase and σ phase. The particles were analysed for Fe, Ni, Mo, Cr, Si, Mn and the phases were identified by the Weiss et al[175] intensity peak technique, where the particles are grouped according to their characteristic Mo/Cr and Fe/Cr X-ray intensity ratios, Figs 8.14b and 8.14c. This technique gives results within a 95% confidence limit since effects such as variation in electron beam intensity, surface topography, particle shape and particle

orientation which affect considerably the absolute X-ray intensities, are minimized. However, since the spatial resolution for analysis is degraded significantly compared with the incident beam diameter, as a result of electron scatter beneath the specimen surface, this method is more suitable for the relatively large particles, ideally 1μm and above, if an X-ray contribution from the matrix is to be avoided. This was a quite serious limitation found in the present investigation since the largest particles in the weld fusion zones were about 2.8μm in size, but a large number of particles were smaller than 1μm in size. Nevertheless, the results could be used as a guide for thin foil examination.

Thin foil specimens obtained from weld passes that had undergone heat treatment by subsequent welding passes indicate extensive precipitation of intermetallic phases, σ and χ phase, in regions that appear to contain originally γ/δ interfaces, indicated by the presence of ferrite occasionally at one side of the particles. An example of this precipitation in the weld fusion zone of MMA1 is shown in Fig 8.15, where the precipitating particles, austenite and areas containing δ ferrite are indicated. It is interesting to note that in certain areas, for instance, on the left-hand side of the Fig 8.15 δ ferrite is surrounded by χ phase, σ phase and austenite, while in other areas such as those arrowed are dominated by σ phase, where the matrix on both sides of the particle is austenite. It appears that the intermetallic σ phase on growing has consumed the δ ferrite. Selected area diffraction patterns obtained from those particles (indicated by circles A and B in Fig 8.15) are shown in Fig 8.16.

Another example of precipitation of intermetallic phases in the weld fusion zone is shown in Fig 8.17 (thin foil prepared from weld run below the sealing run in MMA2). The structure is quite complex and not all features could be fully explained, however the identification of the precipitating phases could be unambiguously obtained by selected area diffraction patterns, convergent beam patterns, and electron energy-dispersive analysis utilizing the scanning transmission electron microscope and microanalysis unit attached to the microscope. The particles identified along the γ/δ interface are indicated in Fig 8.17, together with austenite and ferrite areas detected. Moire fringes (A)

between σ and δ ferrite matrix were sometimes observed as in Fig 8.17. The precise position of γ/δ interface was not always clearly visible since both χ and σ phase particles can precipitate and grow without revealing the presence of ferrite. However, in some areas (Fig 8.17) boundary fringes (B) which "climb" the sides of the particle illustrate the new position of the interface, now between the particle and δ ferrite. This suggests that the particles grow more readily into the δ ferrite. Although χ phase and σ phase particles could be seen in alternating disposition along some of the γ/δ interfaces this is not a general tendency. It does seem, however, that χ phase is a dominant precipitate over σ phase in these weld fusion zones. This is thought to be related to the presence of Mo and to the high content of interstitials (C and N) in the material as will be discussed in the next chapter.

The lattice parameter of the tetragonal σ phase observed in the weld fusion zone was a=8.64 Å and c=4.49 Å, and that of χ phase was a=8.69 Å. The lattice parameter of both phases were smaller than those observed for the same phases under ageing treatment (σ phase a=8.86 Å, c=4.6 Å; χ phase a=8.81 Å). These variations are thought to be related to the reduction of molybdenum in the composition of the phases as indicated by energy-dispersive X-ray analysis. In Table 8.1 the composition of σ phase and χ phase detected in the weld fusion zones is showed, together with the average composition of austenite and δ ferrite obtained after several measurements using the scanning transmission electron microscope (microprobe size about 100 Å).

Table 8.1 Composition of phases observed in weld fusion zones of REX 734

PHASE	COMPOSITION IN wt %
χ phase	51Fe 28Cr 5Ni 11Mo
σ phase	52Fe 32Cr 4Ni 6Mo
γ phase (austenite)	61Fe 21.5 Cr 9.2 Ni 1.5 Mo 4.9Mn
δ phase (ferrite)	60Fe 26.2Cr 4.6Ni 4.5Mo 4.5Mn

The composition of the σ phase in REX 734 after ageing treatment showed in Chapter 6 was 51Fe 31Cr 9Mo 4Ni (wt %), and for χ phase was 47Fe 27Cr 18Mo 5Ni (wt %). It can be seen from Table 8.1 that a significant reduction is obtained in the Mo content of the intermetallic phase as a result of welding as compared with aged alloys. The reduction in molybdenum content is accompanied by a decrease in the lattice parameter of those phases in agreement with observations of other authors[24,48,168] (though the c/a ratio in the case of σ phase remained constant).

Another interesting aspect is that the composition of the intermetallic phases are closer to δ ferrite than to austenite. The ferrite, being richer in chromium, could be preferentially absorbed during the growth of σ and χ phase. In fact a reduction in Cr and Mo of 3 wt % and 1.7 wt % respectively was particularly observed in the ferrite surrounding the intermetallic particles. In agreement with several workers[58,59,139] the presence of δ ferrite is found to accelerate the formation of σ and χ phase which were only observed in REX 734 after long ageing times. The presence of Mo may have contributed to further acceleration of σ and χ phase formation as reported by Beattie et al[60] and Wegrzyn et al[138].

The χ phase and σ phase were not the only precipitates observed in the weld fusion zones exposed to further thermal cycles by subsequent weld passes. Precipitation of Z phase on dislocations was also detected in the austenitic matrix. In Fig 8.18 an example of this precipitation can be seen from bright field and dark field transmission electron microscope images, together with the corresponding selected area diffraction pattern of austenite and Z phase particles. The Z phase observed in these weld fusion zones (Fig 8.19) appears to precipitate only on dislocations in the austenitic matrix in the same fashion as that observed during ageing treatment, while the δ ferrite is found to decompose to intermetallic σ and χ phase. Similar behaviour has been reported for Nb(CN) and NbC by Klemetti et al[145] and Iwamoto et al[146]. In either as weld conditions or during stress relief treatment the authors found that the Nb(CN) and NbC precipitate only on dislocations in the austenite matrix, while the δ ferrite decompose to σ phase or $M_{23}C_6$ carbides. In the present investigation no $M_{23}C_6$ carbide was detected.

In fully austenitic steels the $M_{23}C_6$ usually precedes the intermetallic phase as reported in Chapter 2. This sequence was observed in the present work during ageing treatments of REX 734 (Chapter 6), when the formation of intermetallic χ and σ phases tend to be at higher temperatures and longer ageing times than that of carbide. However, in the case of weld deposits containing ferrite the σ and χ phase are formed in preference to $M_{23}C_6$. As mentioned before the precipitation kinetics of these intermetallic phases can be enhanced by the presence of ferrite, which is rich in chromium, and since the composition ranges of both phases are close to that of δ ferrite, these intermetallic phases form more easily even after short times.

8.3.2 TIG Weld Deposit

Unlike the MMA fusion zones little evidence for precipitation was found in TIG weld fusion zones. The optical micrographs did not show clearly the precipitation reaction at the δ ferrite/austenite interfaces, nor did the scanning electron micrographs. However, indication that some precipitation had occurred in weld areas exposed to thermal cycles by subsequent weld passes could be obtained and is shown in Fig 8.20 (particles arrowed). The particles were smaller than 1μm which made their identification difficult by energy-dispersive analysis using scanning electron microscope (incident beam diameter about 1μm).

Thin foils examination on TEM did show a very low density of precipitate at the δ/γ interfaces. The particles were mainly individual particles of about 0.35μm in size as shown in Fig 8.21. Convergent beam diffraction patterns obtained from those particles were solved indicating that they were χ phase (Figs 8.21b and 8.21c). The convergent beam diffraction patterns in Fig 8.21c and the selected area diffraction pattern in Fig 8.16b suggest that χ phase may have a simple cube/cube orientation relationship with δ ferrite however, to confirm this further analysis should be done.

Another example of χ phase particles at γ/δ interfaces is shown in Fig 8.22 (particles arrowed) at low magnification. The δ ferrite surrounded by a heavily deformed austenite matrix is occasionally pinned

by inclusions (I) rich in manganese and sulphur which are quite common in these weld deposits. The shape of the retained ferrite is clear, showing quite often planar and curved interface with large areas free of precipitates (Fig 8.23). Occasionally steps were seen on the γ/δ interface, Fig 8.24, suggesting that a diffusion-controlled growth process had occurred during solid-solid transformation after the solidification.

Although χ phase was the only precipitate found in the TIG weld fusion zone the occurrence of σ phase cannot be ruled out, since the areas observed in thin foils were relatively small in comparison to the actual size of the weld deposit. Furthermore σ phase does precipitate in REX 734 MMA weld fusion zones in the presence of ferrite as seen in the previous section, and during ageing treatment at 900°C after 100 hours (Chapter 6).

No precipitation on dislocations was seen in the austenite matrix, Fig 8.25, as observed before in MMA fusion zones. The reason for this is probably related to changes in the arc energy during welding (Table 5.3). For the same material thickness the reduction in the arc energy obtained in TIG weld process may have caused an increase in the cooling rate, thus affecting the length of time in which the weld fusion zone has been held at the temperature range that Z phase precipitates.

Although the amount of retained ferrite is greater in the TIG weld deposits the density of precipitates at the γ/δ interfaces seems to be less than that observed for MMA weld deposits. Similar observations were made by Cieslak et al[132] in type 304L austenitic stainless steel weld deposits where nitrogen additions were made to the weld through the shielding gas. The authors observed that additions of nitrogen had changed the solidification mode from primary δ ferrite to primary austenite with accompanying reduction in the ferrite content of the weld fusion zone. They pointed out that there is an increased tendency for precipitates to form at the austenite/eutectic-ferrite interfaces (solidification mode as primary austenite), while the austenite/ferrite interfaces (solidification mode as primary δ ferrite) are almost free of precipitates. Cieslak et al[132] suggested that the large number of precipitates at the austenite/eutectic-ferrite interfaces is probably caused by the supersaturation of the eutectic-ferrite with elements

rejected ahead of the moving austenite/liquid interface during solidification. These elements later nucleate precipitates which grow during the decomposition of the eutectic-ferrite.

In section 8.2 it was suggested that a possible change in the solidification mode may have occurred from leading austenite (MMA welding process) to leading ferrite (TIG welding process) as the nitrogen content in the weld deposit was reduced. The ferrite content is observed to increase with reducing nitrogen and the retained ferrite is mainly located at the core of the cellular dendrites. The composition of δ ferrite in the weld TIG deposit was found to be 58.5Fe, 23Cr, 7.6Ni, 3Mo, 4.9Mn (wt %) which is slightly depleted in Cr and Mo and enriched in Ni in comparison with δ ferrite in MMA weld deposits (Table 8.1). Although these variations were not significantly large it may have affected the precipitation reaction. Another possibility to be considered here is that the welding parameters have varied as the weld process has changed, and this may lead to change in the cooling rate, affecting the precipitation reaction as previously mentioned.

8.4 Summary

a) A decrease in nitrogen content observed in TIG weld deposit is followed by an increase in the amount of δ ferrite at room temperature in the weld zone.

b) No precipitation was detected in the weld fusion zones (MMA and TIG) free of subsequent welding thermal cycles by multipass technique.

c) Precipitation of χ phase and σ phase at the γ/δ interfaces was observed in the weld fusion zones subjected to welding thermal cycles by multipass technique. This precipitation appears to be more extensive in MMA than in TIG weld deposits. In the case of MMA weld fusion zones Z phase was found to occur on dislocations in the austenite matrix.

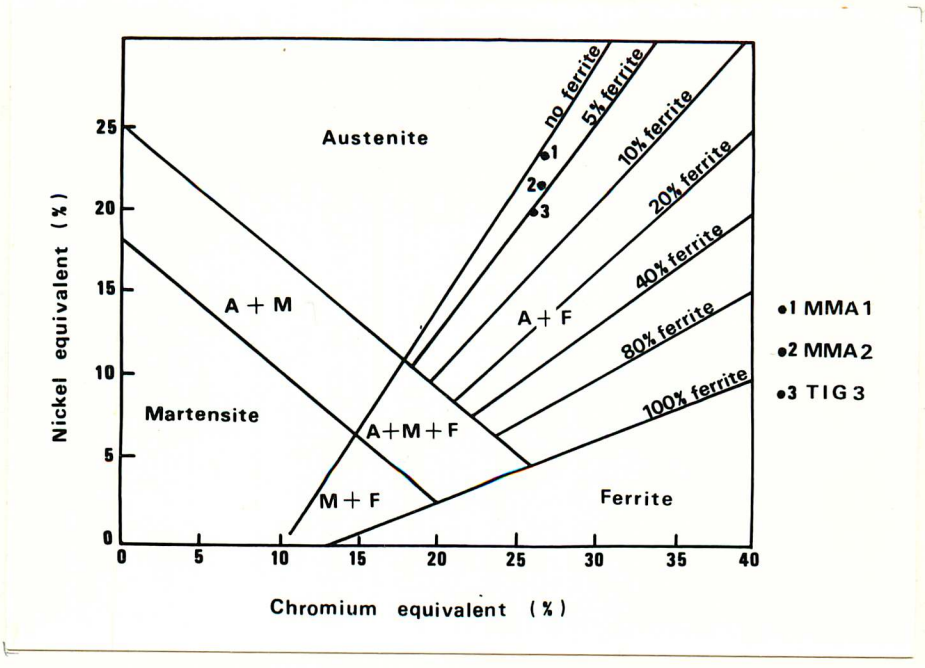

Fig 8.1 Ferrite content in the weld fusion zones REX 734 according to Schneider's modified Schaeffler diagram. Creq = Cr + 2Si + 1.5Mo + 5V + 5.5Al + 1.75Nb + 1.5Ti + 0.75W; Nieq = Ni + Co + 0.5Mn + 0.3Cu + 30C + 25N (all in wt %).

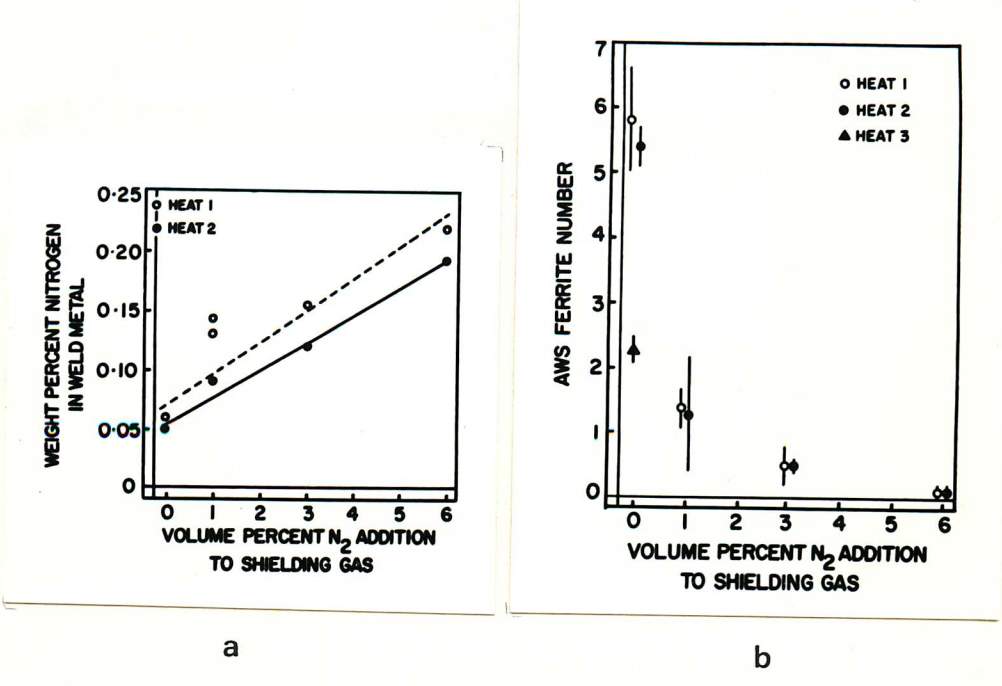

a b

Fig 8.2 a) Nitrogen content of weld metal as a function of N content of the GTA shielding gas.
b) Ferrite content of weld metals as a function of nitrogen content of the GTA shielding gas[132].

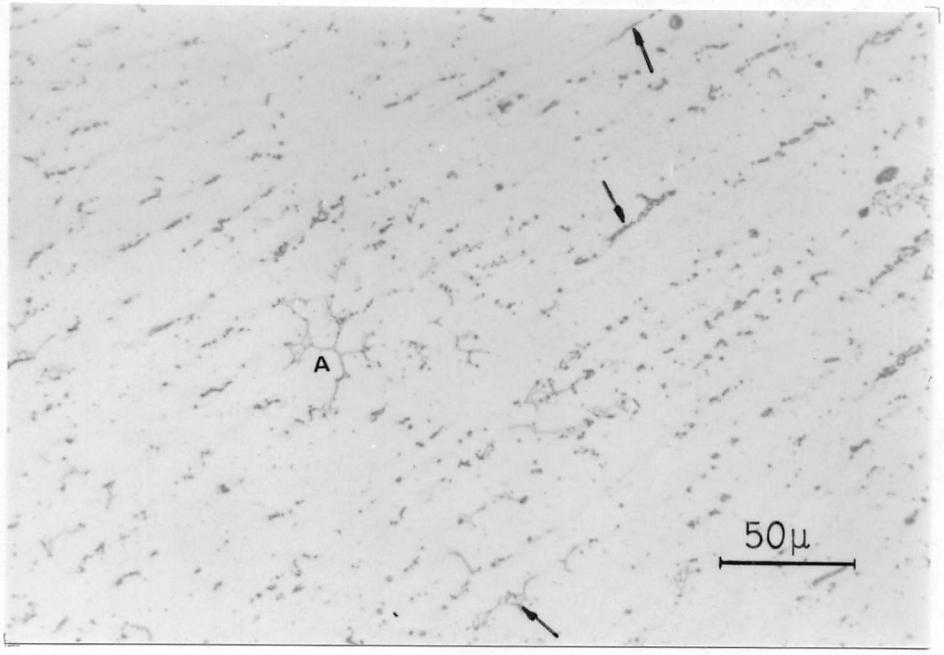

Fig 8.3 Optical micrograph showing the solidification structure of MMA1 weld fusion zone. δ ferrite at the cellular dendrite interstices (arrowed) and at the core of cellular dendrites (A).

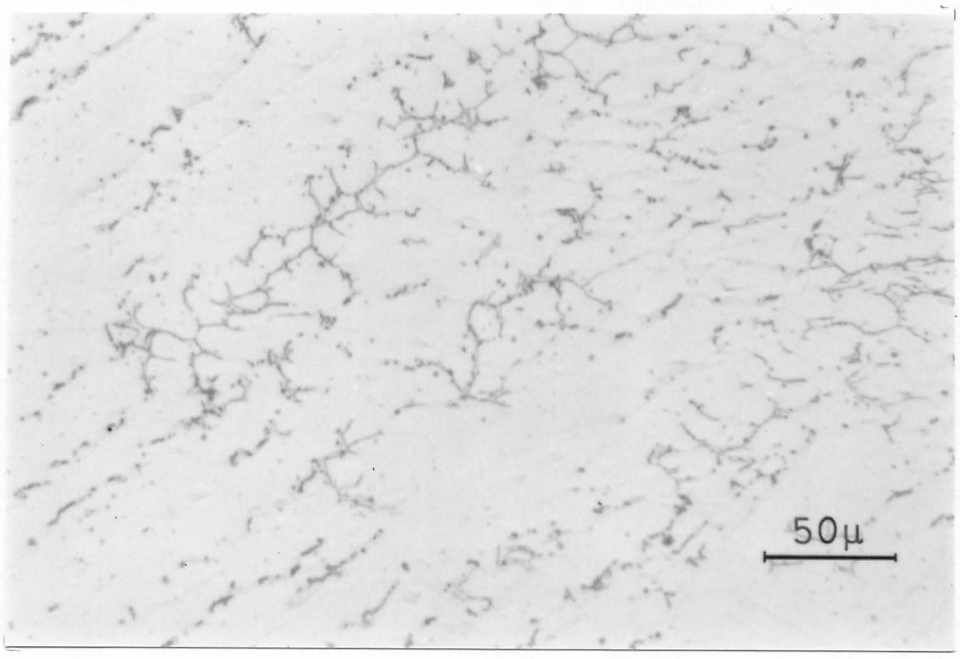

Fig 8.4 Optical micrograph showing ferrite at the core of cellular dendrite austenite. MMA1 weld fusion zone.

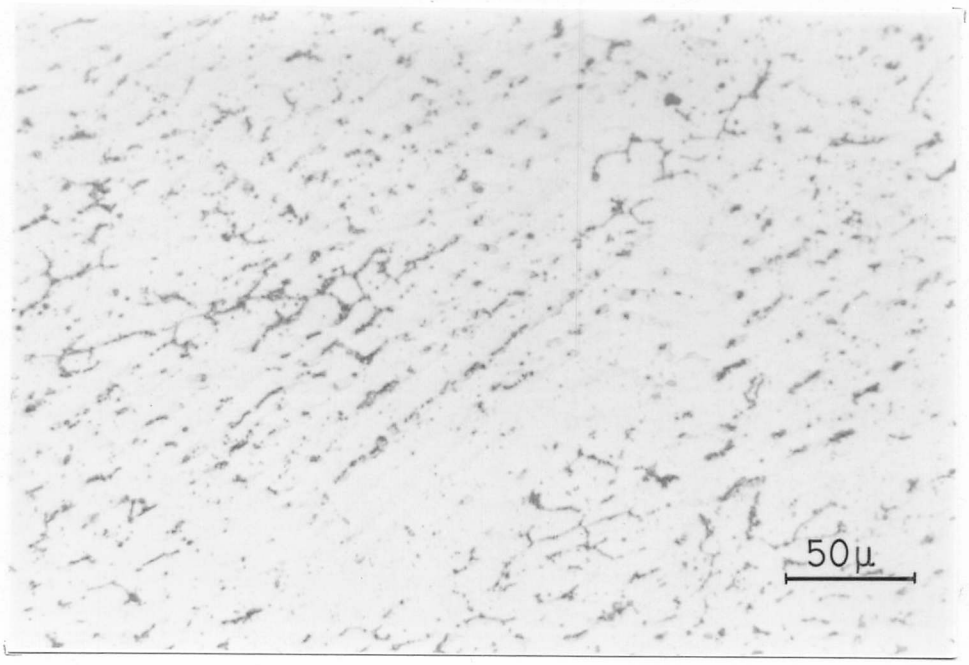

Fig 8.5 Optical micrograph showing the solidification structure of MMA2 weld fusion zone.

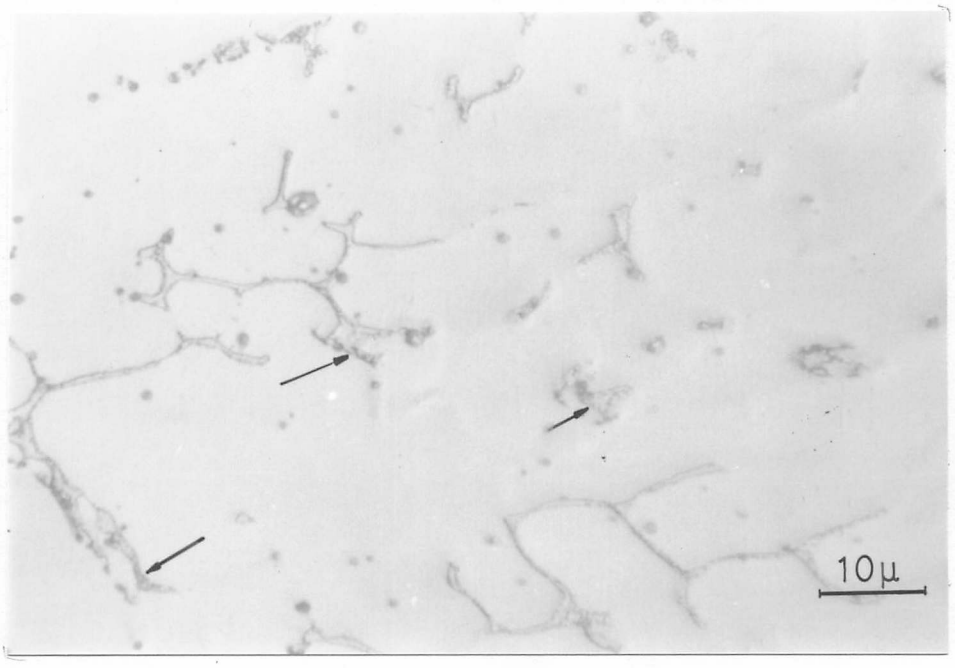

Fig 8.6 Optical micrograph showing decomposition of δ ferrite in MMA1 weld fusion zone (arrowed).

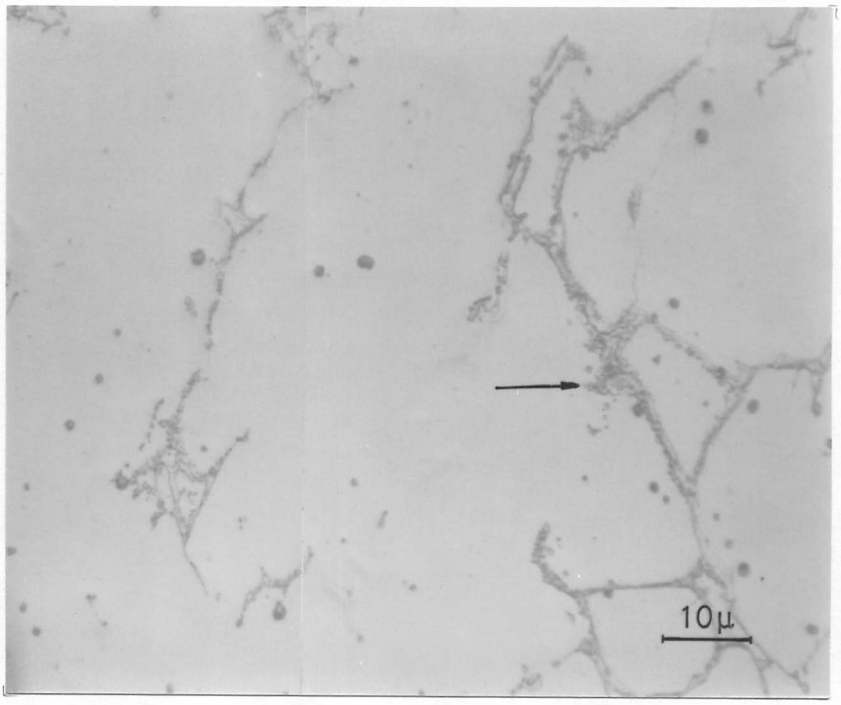

Fig 8.7 Optical micrograph showing extensive decomposition of ferrite in MMA2 weld fusion zone (arrowed).

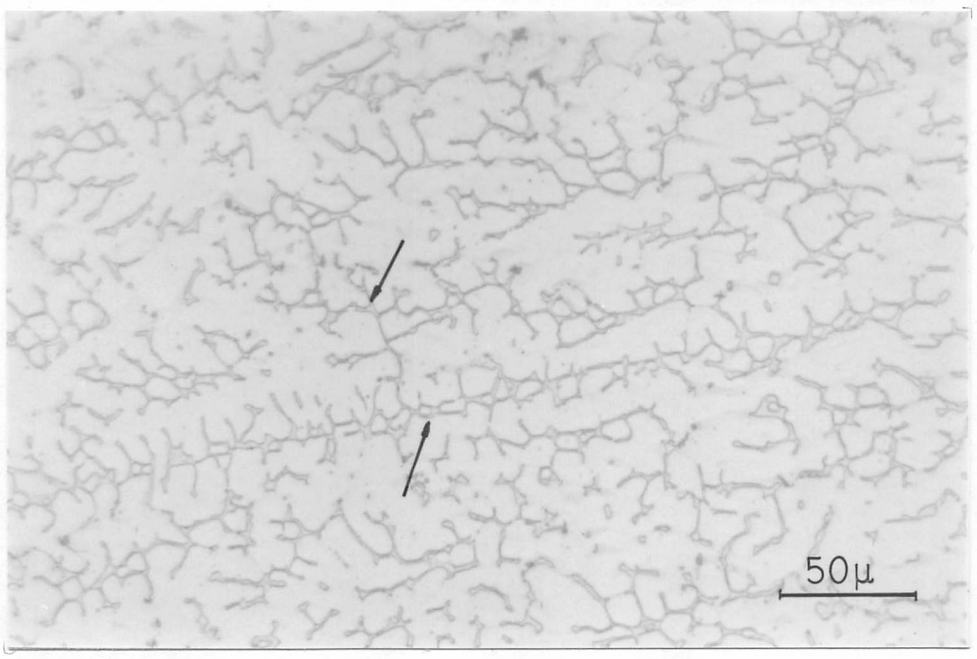

Fig 8.8 Optical micrograph showing the solidification structure of TIG 3 weld fusion zone. Ferrite at the core of cellular dendrites (arrowed).

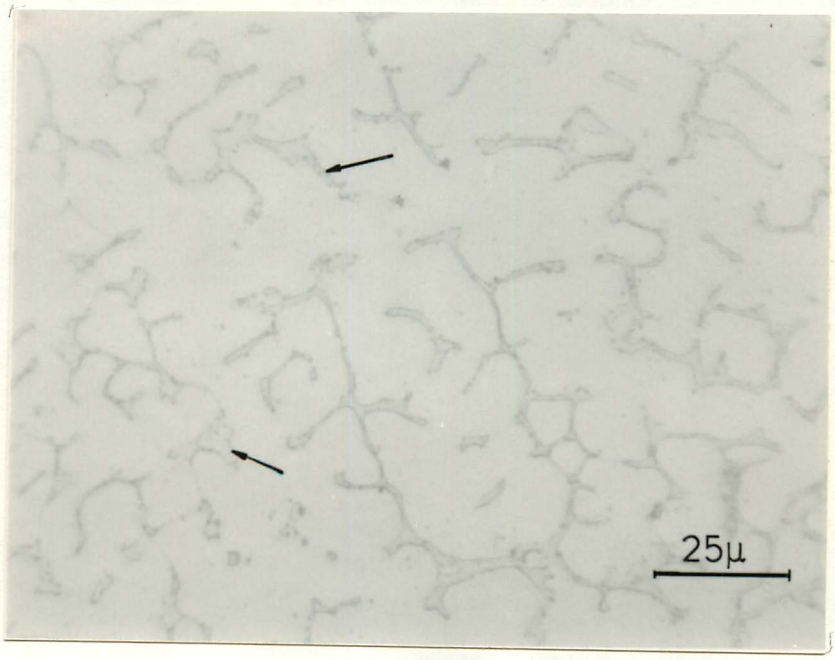

Fig 8.9 Optical micrograph showing decomposition of ferrite in TIG 3 weld fusion zone (arrowed).

Fig 8.10 Scanning electron microscope image showing δ ferrite/austenite interfaces free of precipitates.

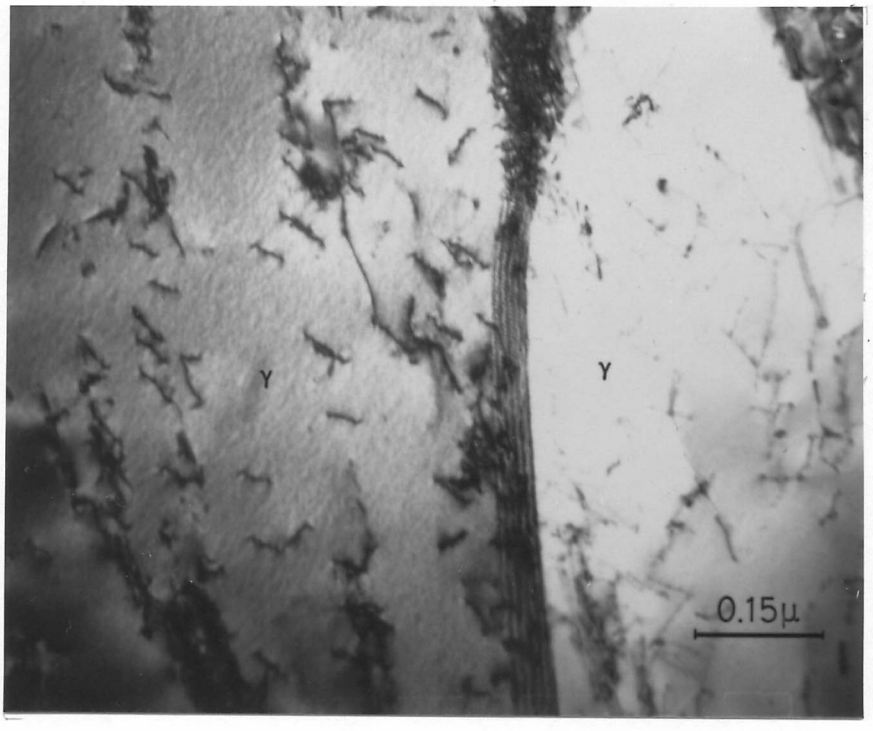

Fig 8.11 Bright field transmission electron microscope image showing a γ/γ interface.

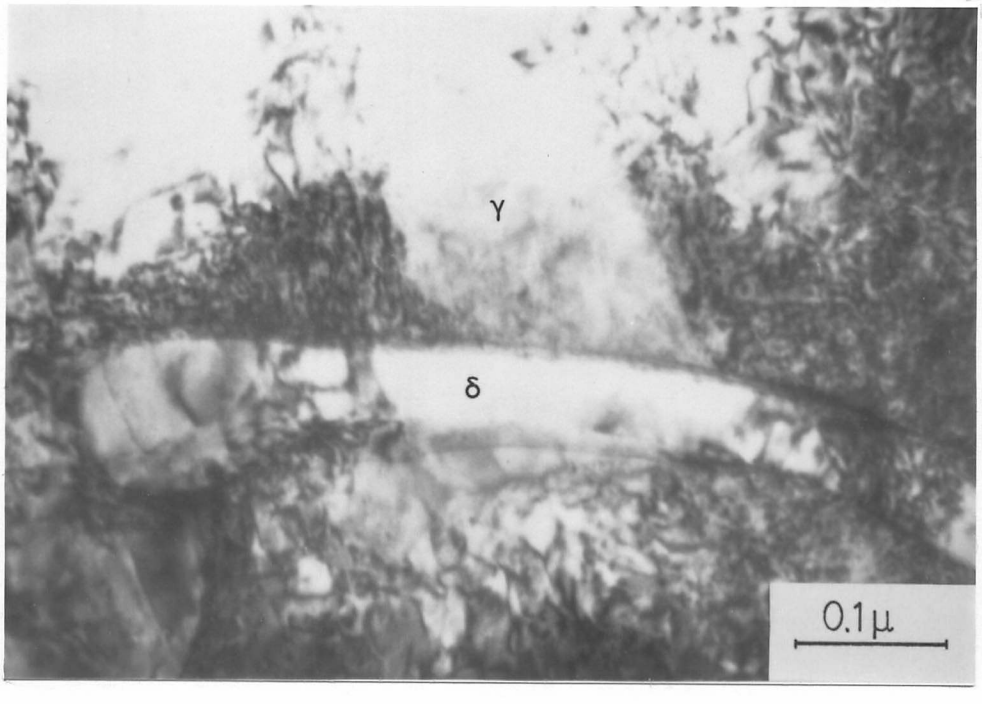

Fig 8.12 Bright field transmission electron microscope image showing δ ferrite.

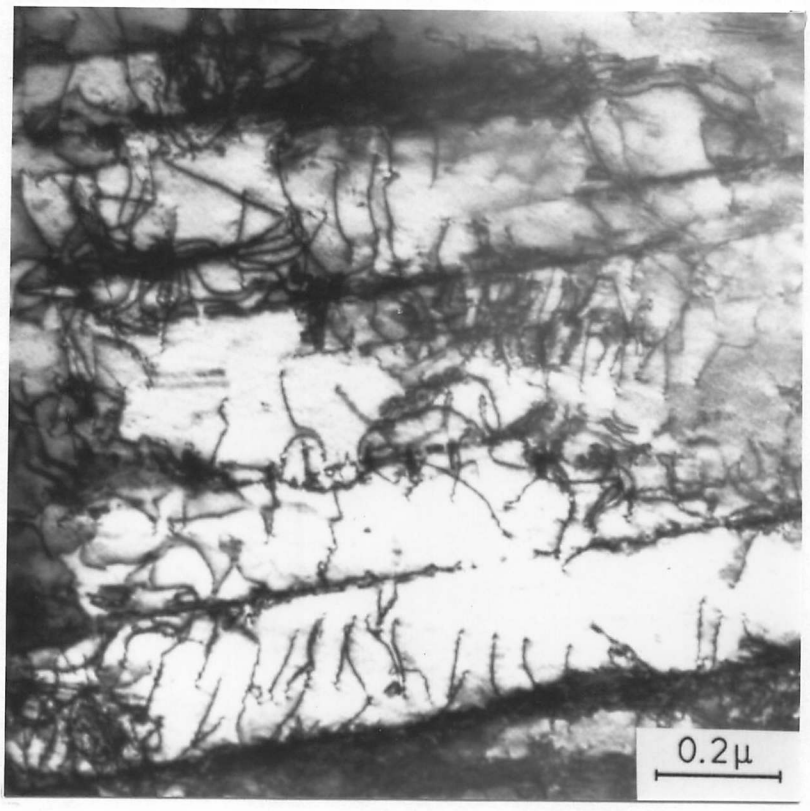

Fig 8.13 Bright field TEM image showing dislocations free of precipitates, and slip bands in the austenitic matrix.

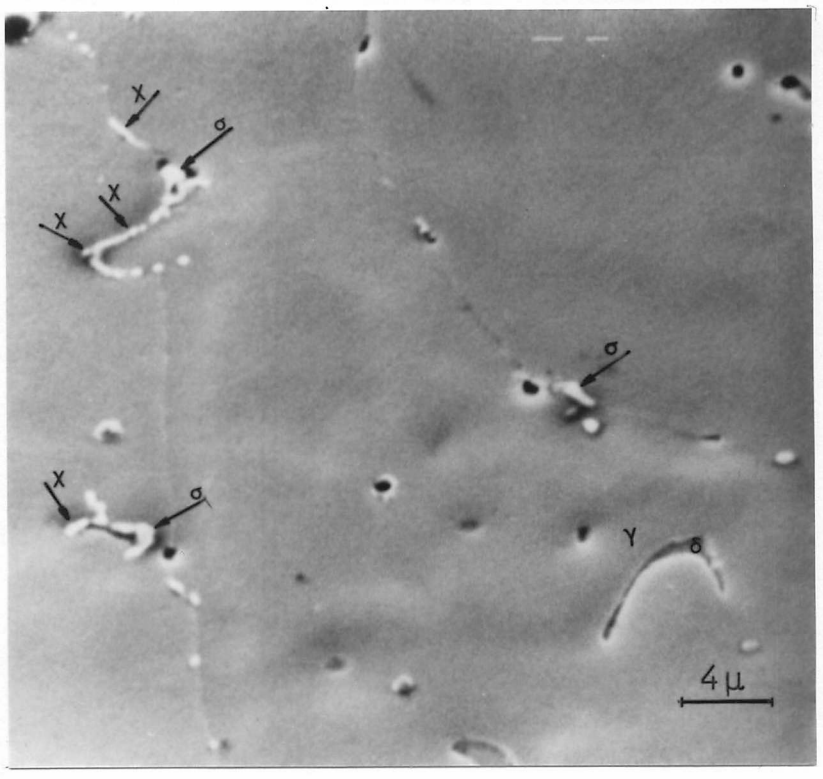

a

Fig 8.14 Interface precipitation of χ and σ phase in MMA weld fusion zone.
a) Scanning electron microscope image.

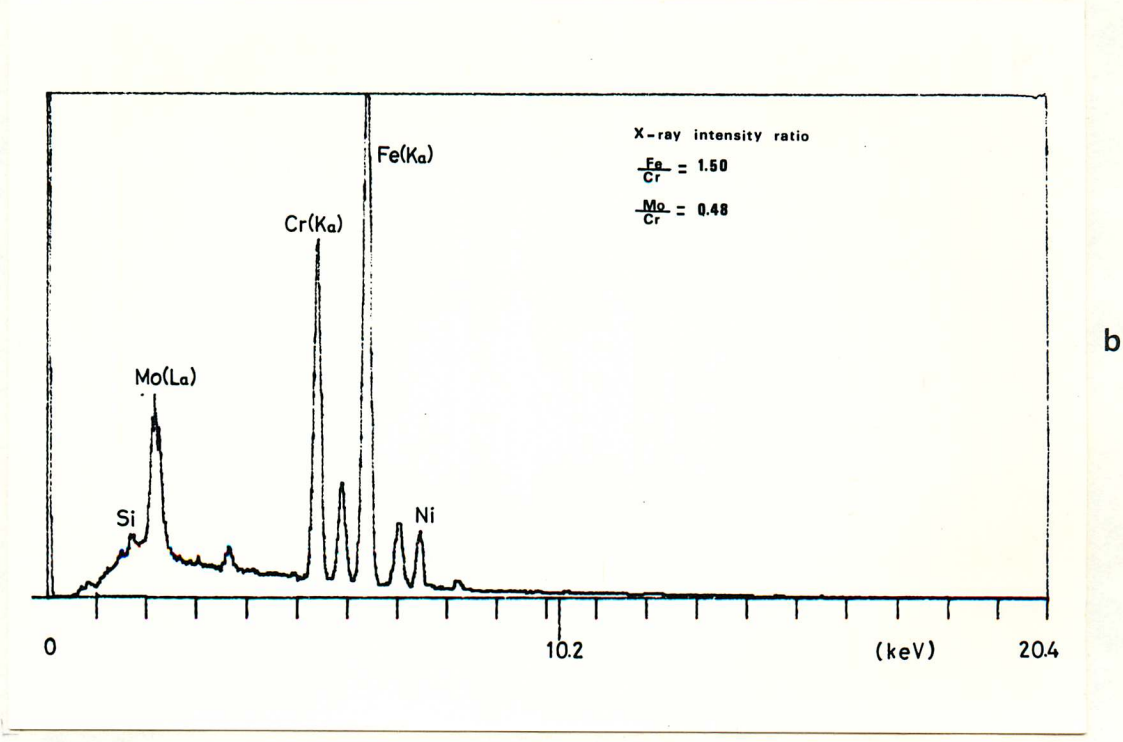

b

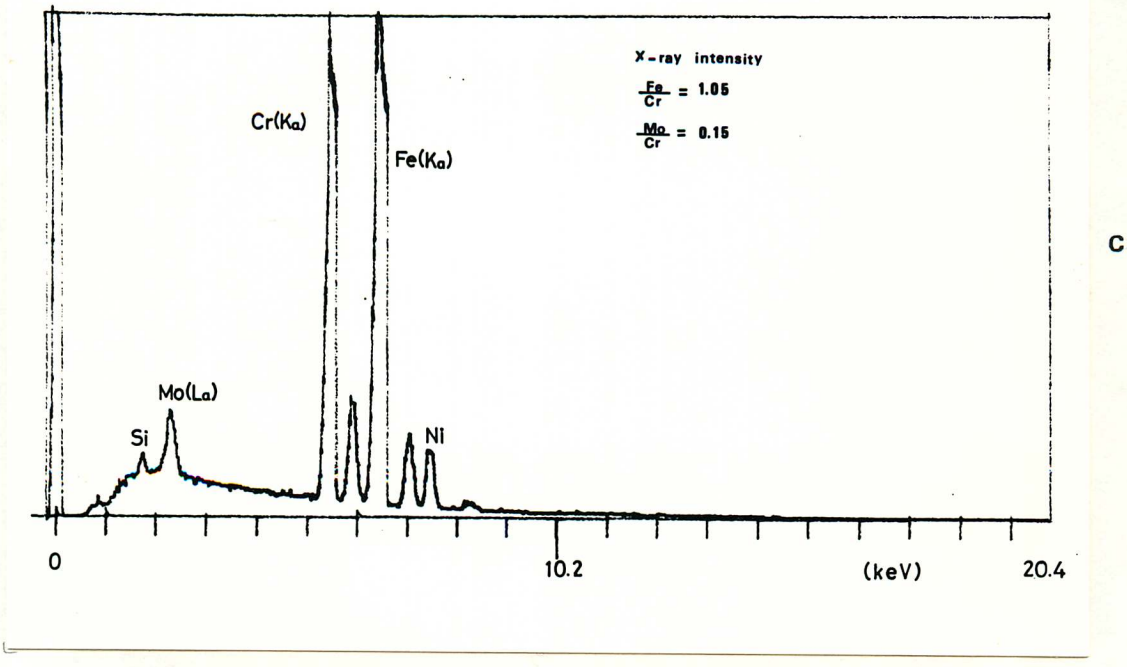

c

Fig 8.14 b) Characteristic spectrum obtained from χ phase particles in Fig 8.14a.
c) Characteristic spectrum obtained from σ phase particles in Fig 8.14a.

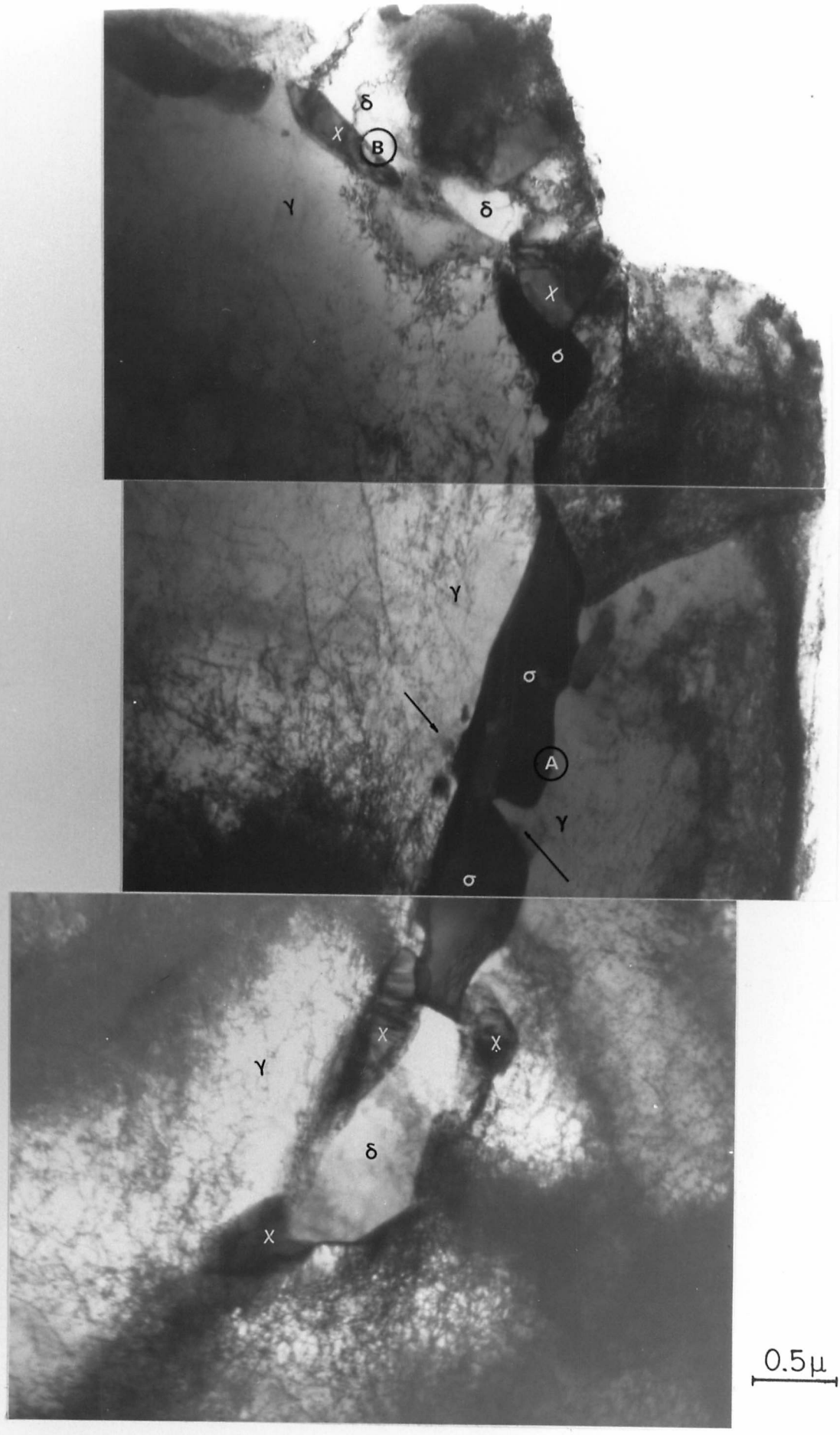

Fig. 8.15 Precipitation of χ and σ phase at γ/δ interface in MMA 1. Bright field TEM image.

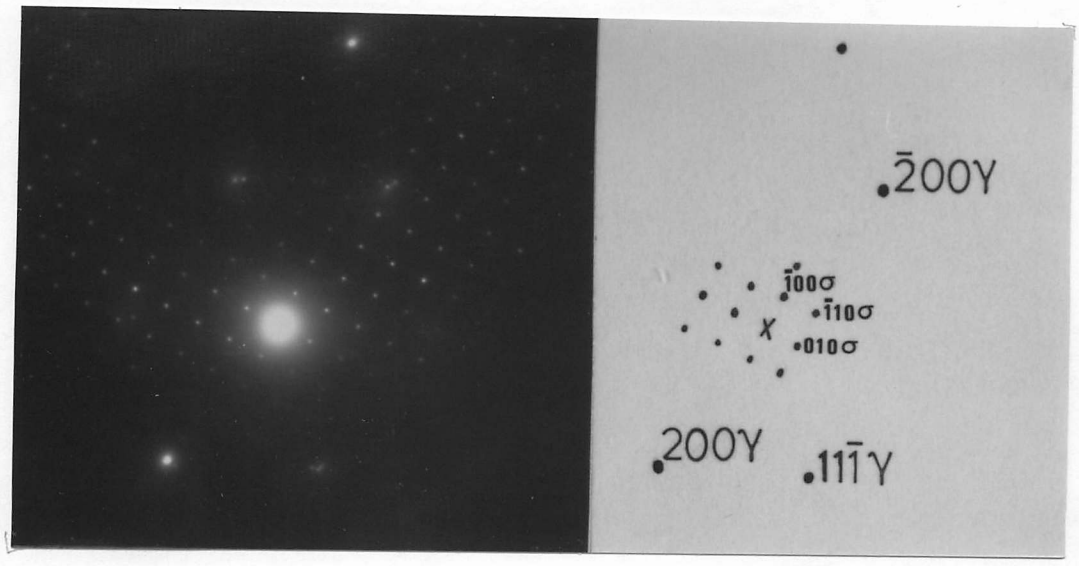

a

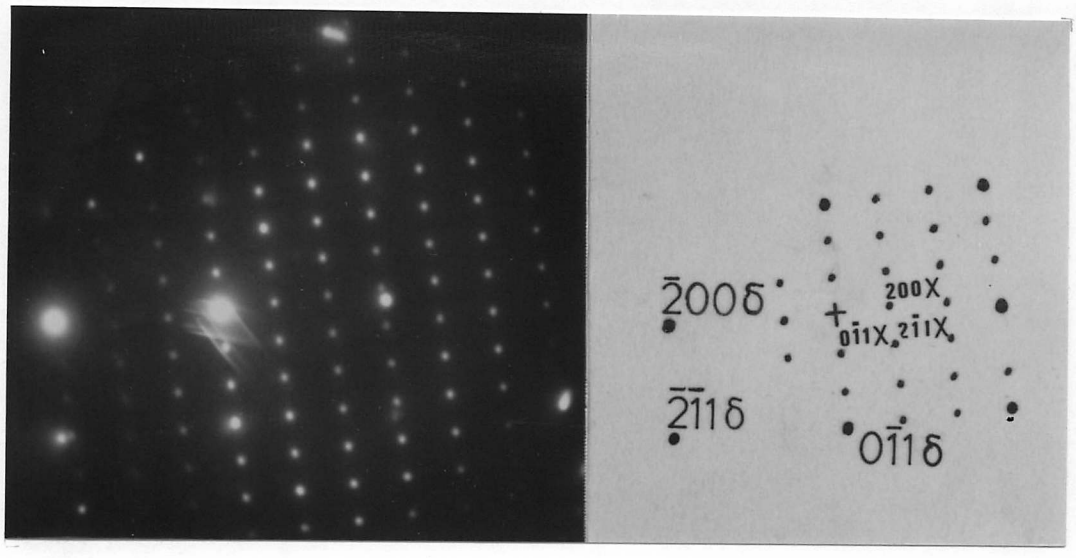

b

Fig 8.16 Selected area diffraction patterns from particles in Fig 8.15.
a) particle (A), zone axis $[011]\gamma$, $[00\bar{1}]\sigma$ phase;
b) particle (B), zone axis $[011]\delta$, $[011]\chi$ phase.

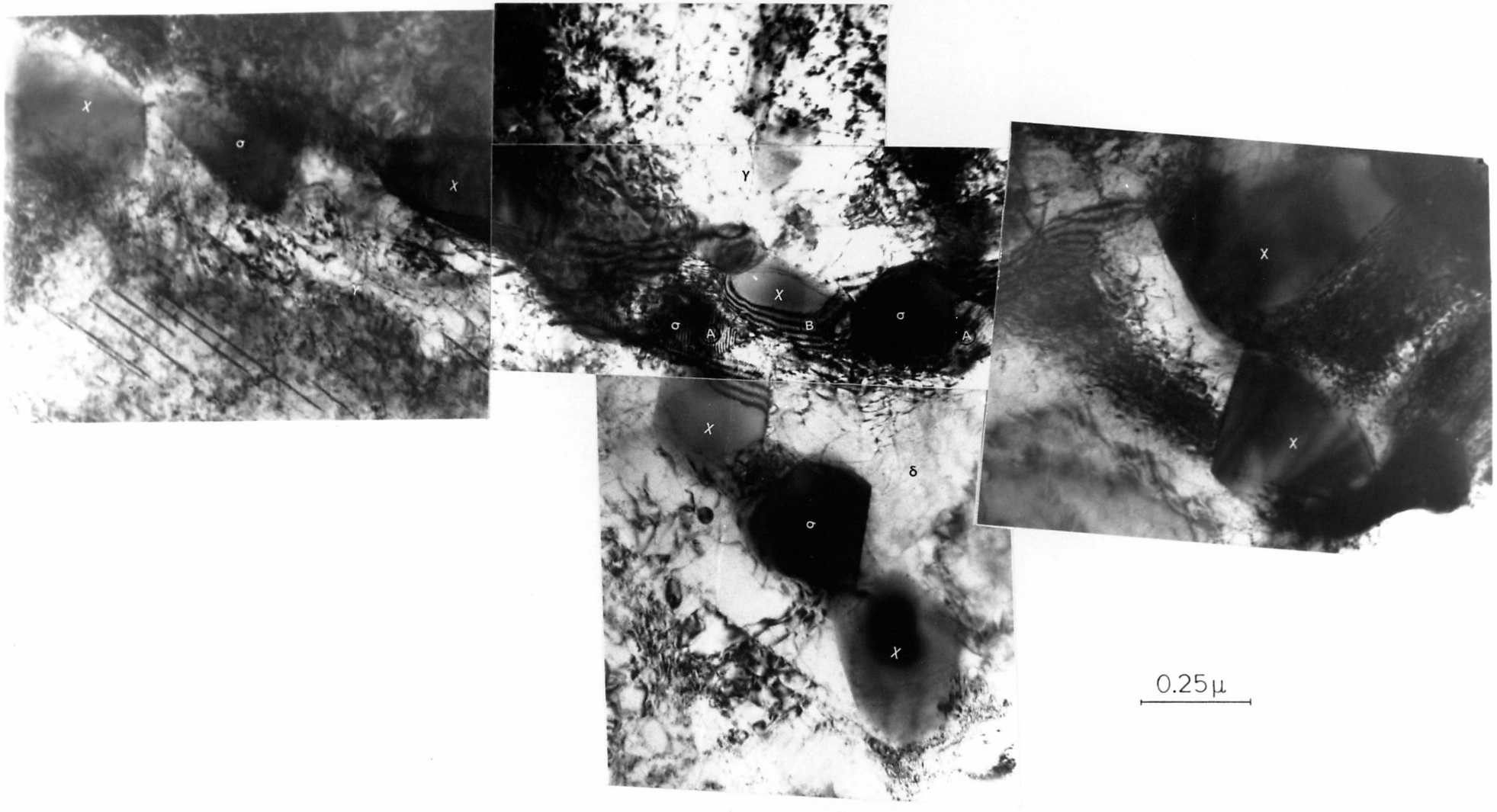

Fig.8.17 Bright field TEM image showing precipitation at the γ/δ interface in an MMA2 weld fusion zone. X phase (X), σ phase(σ), austenite(γ), ferrite (δ).

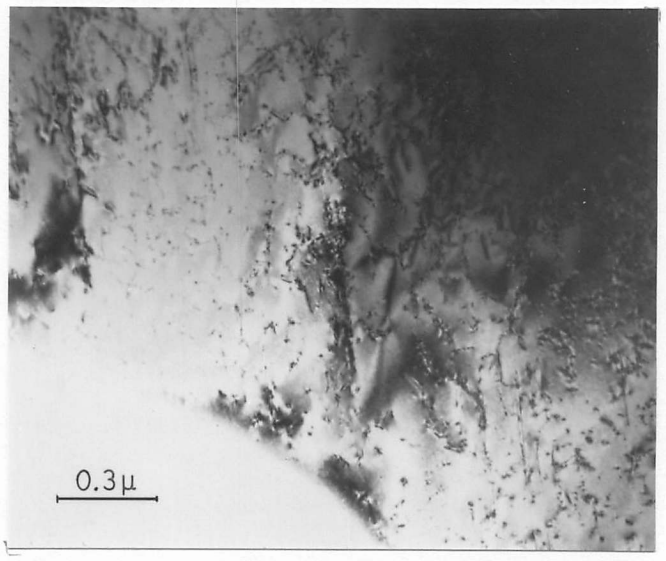

a

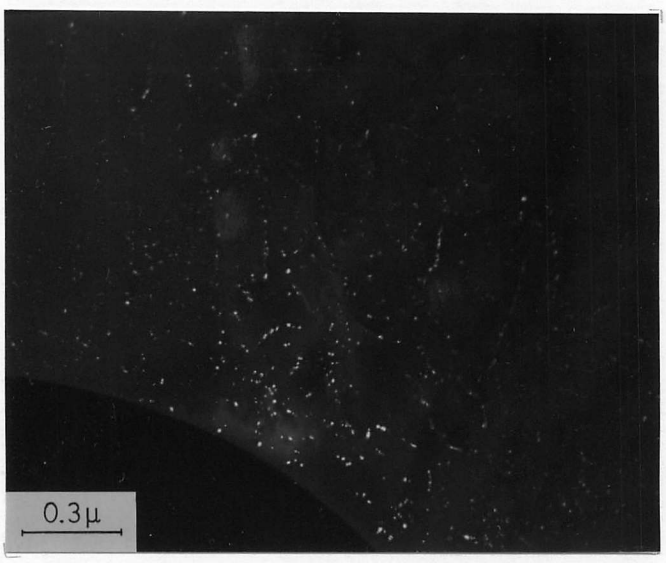

b

c

Fig 8.18 Precipitation of Z phase on dislocations in the austenitic matrix. MMA weld fusion zone. a) Bright field TEM. b) Centred dark field. c) Selected area diffraction pattern. Zone axis $[\bar{1}10]\gamma$, $[\bar{1}00]$ Z phase.

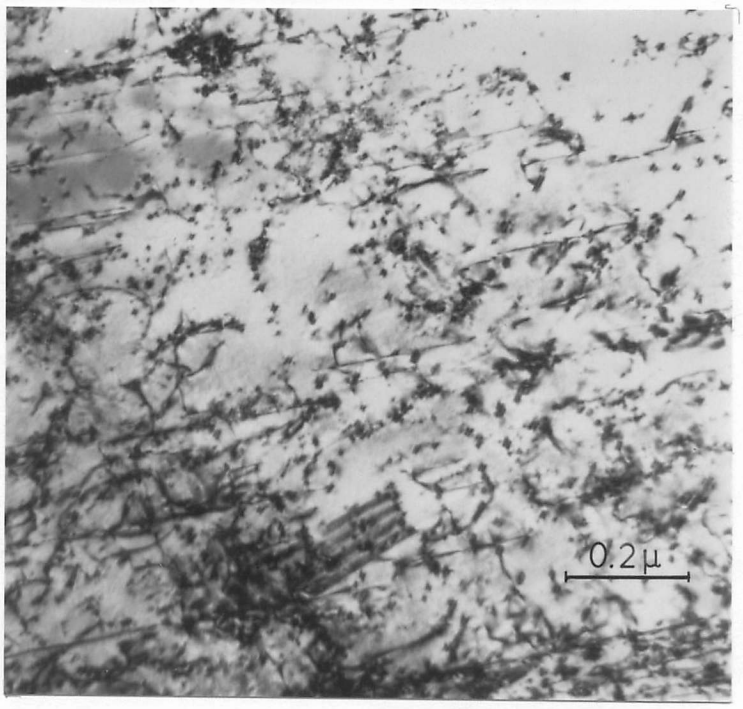

Fig 8.19 Bright field TEM image showing Z phase precipitates on dislocation in the austenitic matrix. MMA weld fusion zone.

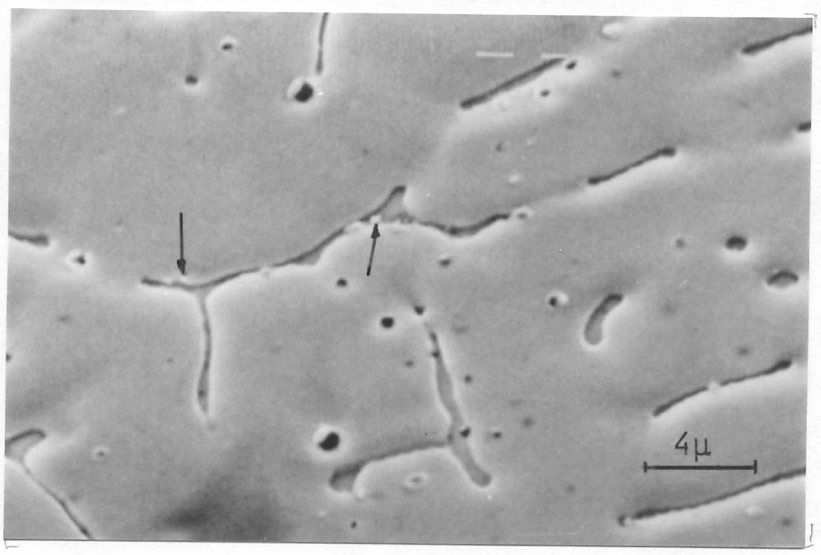

Fig 8.20 Scanning electron microscope image showing precipitates along γ/δ interface. TIG 3 weld fusion zone.

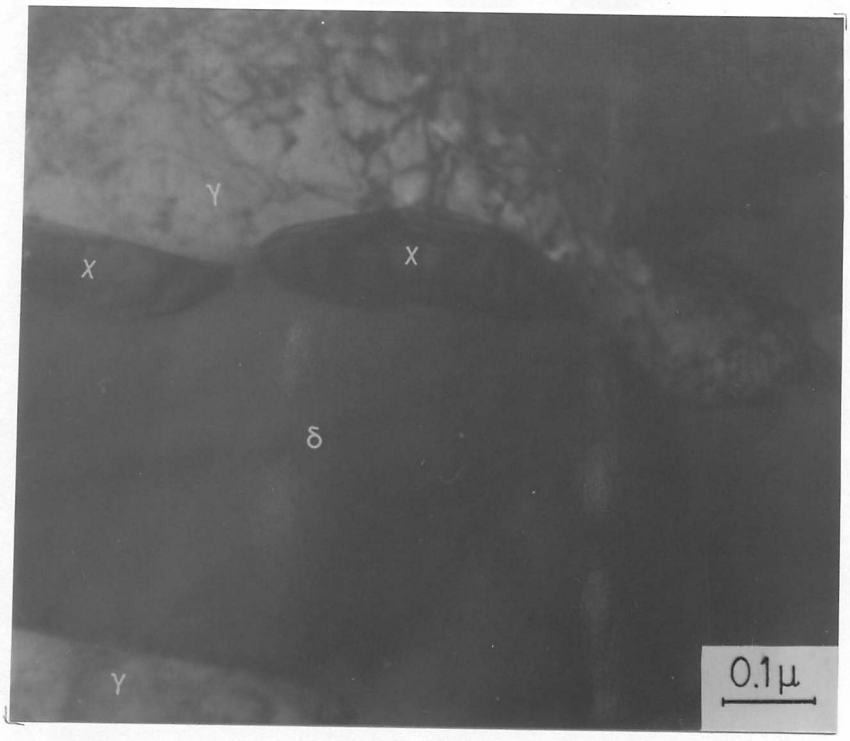

a

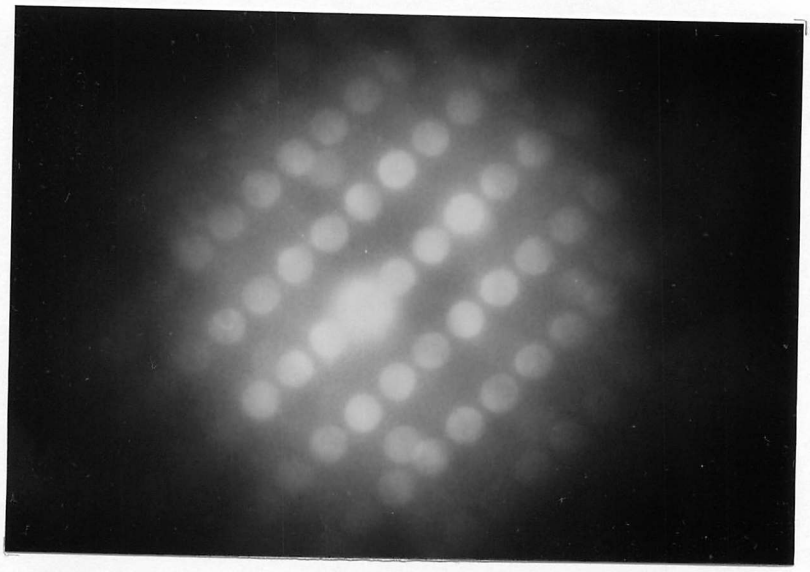

b

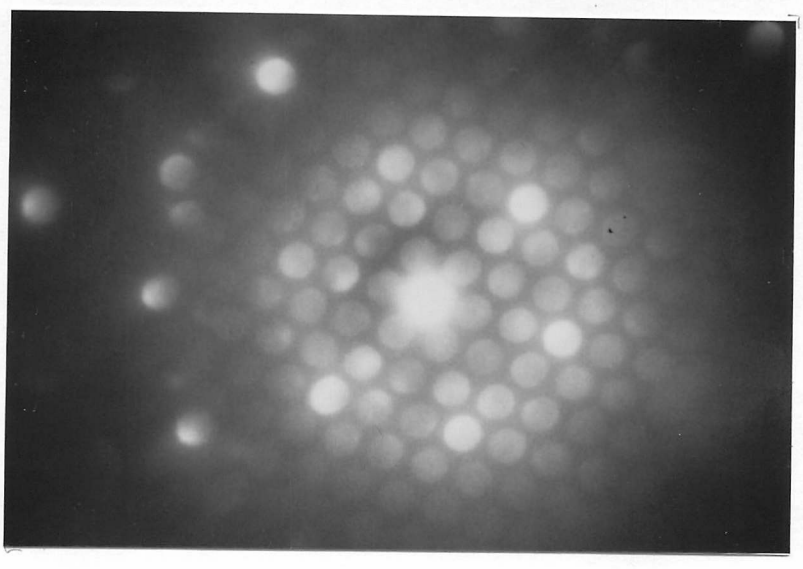

c

Fig 8.21 χ phase precipitation at δ/γ interface. TIG 3 weld fusion zone. a) Bright field TEM image; b) Convergent beam diffraction pattern, zone axis $[\bar{1}13]\chi$ phase; c) Zone axis $[\bar{1}11]\delta$, $[\bar{1}11]\chi$ phase.

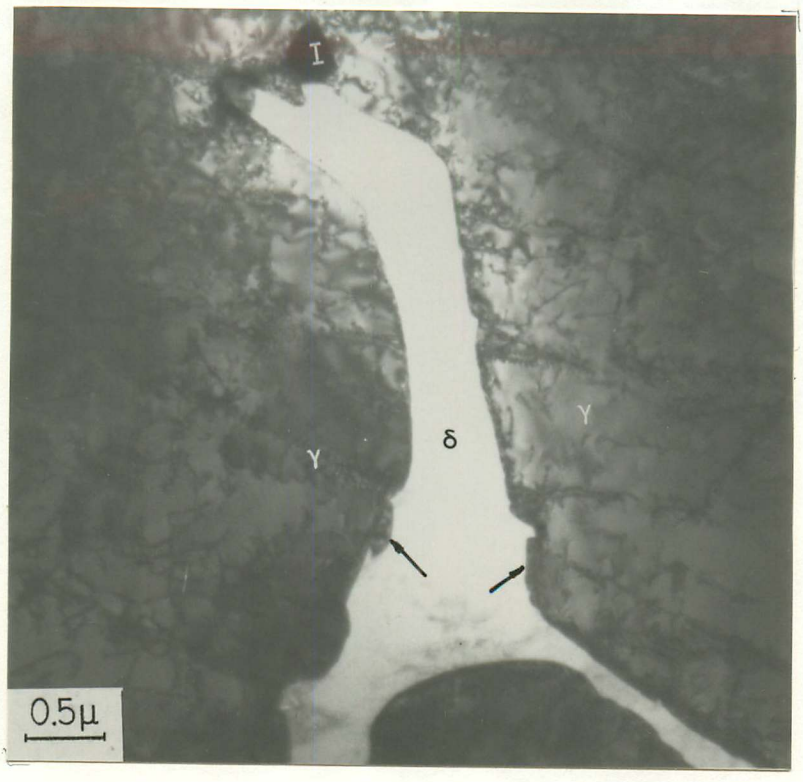

Fig 8.22 χ phase particles (arrowed) at γ/δ interface. TIG 3 weld fusion zone.

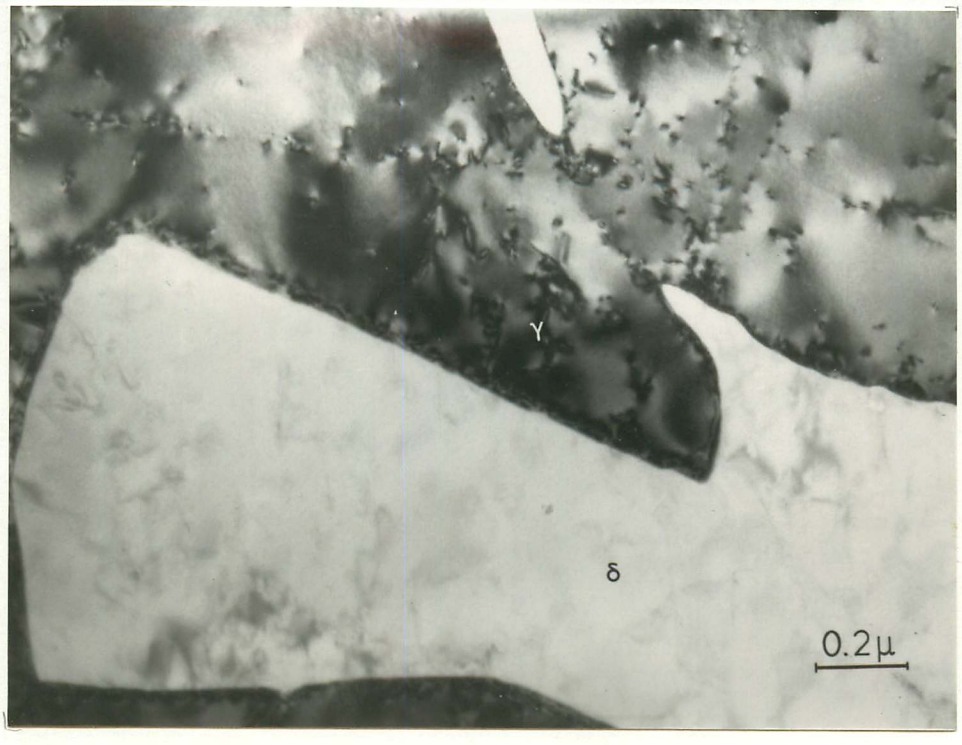

Fig 8.23 Planar and curved austenite/δ ferrite interfaces free of precipitates. TIG 3 weld fusion zone.

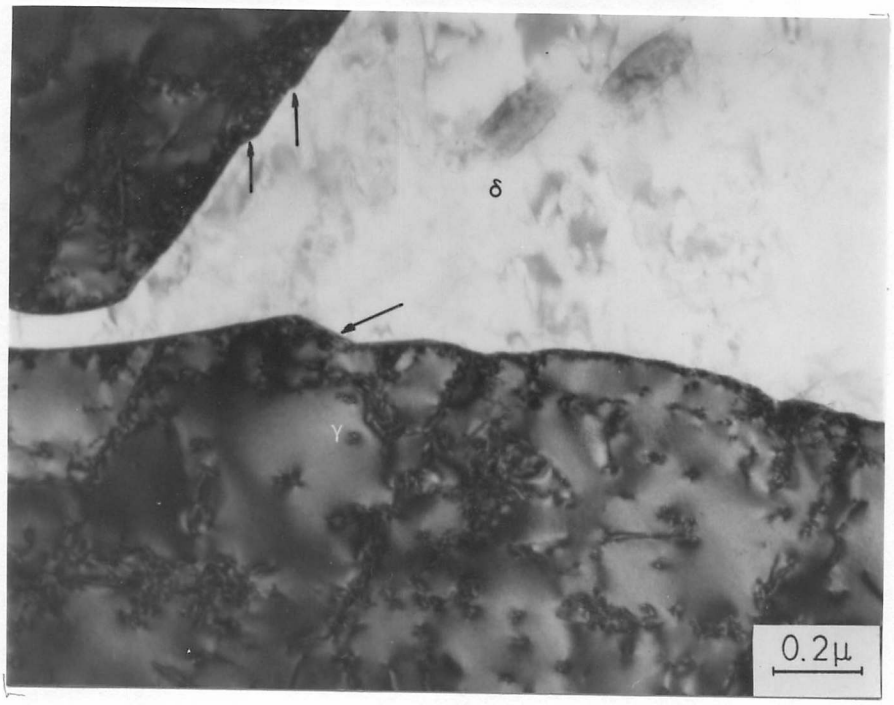

Fig 8.24 Planar and stepped interfaces in TIG 3 weld fusion zone.

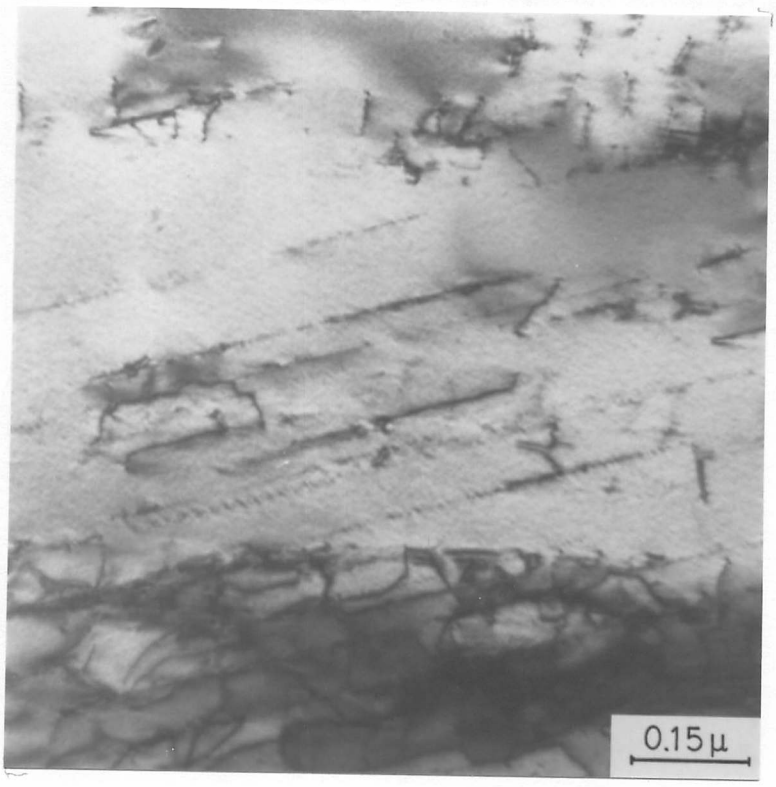

Fig 8.25 Dislocations free of precipitates in the austenitic matrix. TIG weld fusion zone.

9. DISCUSSION

9.1 General

The high nitrogen austenitic stainless steel REX 734 was developed through the need to improve the strength and corrosion properties of the common austenitic stainless steel types, such as the AISI 300 series. The starting point for the development of a strong, highly corrosion resistant steel was the well-known chromium-nickel-molybdenum type 316 S16[5]. Solid solution strengthening is achieved by increasing chromium and nitrogen contents and supplemented by a small addition of niobium. This alloying process also serves to improve corrosion resistance. The corrosion behaviour of the nitrogen containing austenitic stainless steels has been studied by Osozawa and Okamoto[176] who claimed that the nitrogen in solution in the austenite dissolves in the corrosive medium and reduces the number of protons. This reduces the pH of the solution in the immediate vicinity of the corrosion site and thereby reduces the susceptibility of the alloy to corrosion. Sakamoto et al[177] pointed out that this mechanism relies on the nitrogen in the steel being dissolved in the matrix and not involved in any precipitation.

In high nitrogen content austenitic stainless steels there are usually strong carbide and nitride-forming elements such as Cr, Nb or Ti. The latter two are stabilizing-elements which help to prevent intragranular corrosion which usually accompanies the precipitation of chromium-rich carbides or nitrides at grain boundaries. Since the enhanced properties of this class of steel are dependent on the nitrogen being present in interstitial solid solution, it is relevant to ask what effect precipitation will have on the mechanical and corrosion properties of such steel, and what precipitation characteristics will be exhibited during heat treatment or under welding conditions. Consequently the present general discussion will deal mainly with the precipitation

characteristics of REX 734, and, where appropriate, a brief discussion of the possible effect of precipitation reactions on the mechanical properties and corrosion resistance of the material will be presented.

The microstructural behaviour of high nitrogen austenitic stainless steels has not received much attention[3,35,80,170], consequently the full range of precipitation which can occur and the sequences of precipitation have not been worked out. Irvine et al[3] and Thier et al[170] reported Cr_2N precipitation in this type of steel while Borland[80] reported the precipitation of NbN and M_6N, and Colclough[35] reported the precipitation of Z phase, which is a niobium-chromium rich nitride. These results indicate that high nitrogen austenitic stainless steels are susceptible to nitride formation.

In the present work, the high nitrogen austenitic stainless steel, REX 734, exhibited several types of precipitation involving nitrides, carbides and intermetallic phases. Z phase, $M_{23}C_6$, χ phase, σ phase, Cr_2N and ϕ phase have all been shown to form in this steel during ageing treatments, defined in Fig 9.1. In the duplex (γ + δ) weld deposits, χ phase, σ and Z phase were observed. The precipitation of the nitrogen-rich phases is a cause for some concern since their effects both on corrosion and mechanical properties are uncertain.

9.2 Precipitation of $M_{23}C_6$

The extensive precipitation of $M_{23}C_6$, particularly dominant at 700°C, is of great concern since this precipitation will have a deleterious effect on the corrosion resistance of the material, and may promote room temperature embrittlement. Gooch[150] has shown that the susceptibility to intergranular corrosion caused by $M_{23}C_6$ precipitation depends on the density and morphology of the precipitated grain boundary carbide, which is related to time and temperature of heating. Susceptibility to intercrystalline attack arises when sufficient grain boundary carbide precipitation has taken place for there to be a virtually continuous chromium-depleted region along the grain boundaries. Therefore, in the early stages of ageing, it is possible to have carbides present at

austenite grain boundaries, causing modified anodic polarization curves, without the material being susceptible to intercrystalline attack.

The stability of REX 734 to $M_{23}C_6$ precipitation can be estimated roughly from the chemical composition of the steel given that niobium carbide, NbC[40,45], may precipitate in austenitic stainless steel. The carbon and niobium contents of the steel REX 734 are 0.058 wt % and 0.28 wt % respectively. If all the niobium were to precipitate as carbide then 0.035 wt % C could be removed from the solid solution. Clearly there is not enough niobium present in the matrix to prevent $M_{23}C_6$ formation. Furthermore, the presence of nitrogen leads to the formation of nitrides, as the present work demonstrates. In particular, niobium combines more strongly with nitrogen than carbon, thus reducing the amount of Nb available to form carbide. This will therefore leave the REX 734 more susceptible to $M_{23}C_6$ formation. However, Thier et al[170] showed that, in 17Cr, 13Ni (wt %) alloy with no other strong carbide-forming element, the increasing level of nitrogen in the matrix from 0.04 - 0.15 wt % delayed the appearance of the $M_{23}C_6$ from 10 hours to 500 hours at 600°C and from 0.03 to 0.4 hours between 800-900°C respectively.

In the present work, $M_{23}C_6$ carbide was first seen on the grain boundaries of REX 734 after 10 hours between 700-800°C and after 1000 hours at 600°C. Weiss and stickler[20] reported $M_{23}C_6$ formation in their AISI type 316L alloy after 0.1 hr between 650-900°C. In a higher carbon content variant, the AISI type 316 alloy, White and Le May[36] found $M_{23}C_6$ after 15 hours at 600°C. Singhal and Martin[33] reported $M_{23}C_6$ precipitation in their 26Cr, 24Ni, 0.3Ti (wt %) alloy after 0.5 hours at 750°C. In a 22Cr, 13Ni wt % containing 0.04 wt % C and 0.24 wt % N, Colclough[35] observed intergranular $M_{23}C_6$ precipitation after 8 hours between 800-900°C.

Comparison of the kinetics of the $M_{23}C_6$ precipitation reaction seen in REX 734 with the above results suggests that the $M_{23}C_6$ precipitation reaction in REX 734 occurs slowly. The rate determining factor in $M_{23}C_6$ precipitation is clearly the nucleation of $M_{23}C_6$ since the precipitate, once formed, grows rapidly. The effect of nitrogen in delaying the $M_{23}C_6$ precipitation is thought to be related to the fact that no isostructural

nitride occurs, and it appears that nitrogen is not soluble in the carbide. This has been confirmed by the EELS microanalysis in the present investigation where no nitrogen was detected in the $M_{23}C_6$ particles analysed.

Thier et al[170] showed that the slowing down of the $M_{23}C_6$ reaction in their high nitrogen content alloy was accompanied by an enhancement of the M_6C reaction, consequently they suggested that their M_6C may contain nitrogen. Borland[80] claimed that M_6N precipitated at the expense of NbN in his 18Cr 12Ni 1.2Nb (wt %) alloy. Borland, during his investigation into this steel, containing various niobium (0.62 - 1.68 wt %) and nitrogen (0.02 - 0.09 wt %) additions, reported that NbN, M_6N and Z phase all precipitated in such alloys. He always observed the concurrent precipitation of NbN and Z phase in the temperature range 700-800°C. The results of Borland[80] and Thier et al [170] suggest that in niobium-nitrogen containing austenitic stainless steels, M_6N, NbN and Z phase should be the predominant phases and that the $M_{23}C_6$ reaction may be retarded. While a sluggish $M_{23}C_6$ precipitation reaction was seen in REX 734 and extensive Z phase precipitation, NbN and M_6N or $M_6(CN)$ were never seen in the temperature range 600-1000°C for times between 1-1000 hours, due presumably to the lower Nb content of REX 734.

In the case of weld deposits of steels AISI type 316, Slattery et al[139] suggested that the absence of $M_{23}C_6$ is associated with the relatively low carbon content (0.05 wt %). However the high volume fraction of δ ferrite (18%) must have enhanced the precipitation of intermetallic phases such as σ and χ, which were the only phases observed by the author after the weld had been aged at 625 and 850°C. In fact, Lai et al[137] observed $M_{23}C_6$ precipitation at lower carbon content (0.03 wt %) and in the presence of 2 to 4% volume fraction of δ ferrite in weld deposits. The results obtained in these studies suggest that not only will the carbon content of the weld deposit affect the precipitation of $M_{23}C_6$ but also the volume fraction of δ ferrite, the presence of which encourages the formation of σ and χ precipitation.

In REX 734 weld deposits no $M_{23}C_6$ precipitation was observed in the as-welded condition, despite the level of carbon (0.04 wt %). The reason

for this is thought to be associated with the presence of nitrogen (0.3 - 0.4 wt %) which will delay the $M_{23}C_6$ precipitation, as previously discussed, and the presence of δ ferrite, which, though in relatively low volume fraction (2 - 6%), will enhance the precipitation of σ and χ phases. From the corrosion-resistance viewpoint the absence of $M_{23}C_6$ in the weld deposits in a high nitrogen content steel does seem to present an advantage which is not possessed by the aged specimens.

9.3 Precipitation of Z phase

Jack and Jack[102] identified niobium-chromium nitride, NbCrN, which is known as Z phase. The phase has been observed on many occasions in a variety of stainless steels, Table 9.1, though in a number of instances it has not been recognised as Z phase[177-179]. The phase has been reported to precipitate in austenitic stainless steels with a diverse range of niobium-nitrogen levels over a wide temperature range, however none of these workers has thoroughly charted the precipitation characteristics of the phase. More recently Colclough[35] reported that, over the temperature range 700-1000°C in a 22Cr 13Ni (wt %) steel containing 0.18 wt % Nb, 0.04 wt % C and 0.24 wt % N, Z phase precipitates at grain boundaries, twin boundaries and in the austenitic matrix in association with dislocations.

Table 9.1 The occurrence of Z phase in various heat treated alloys

Workers	Alloy (wt %)	Ageing Temp. Range
E.A. Jenkinson et al[179]	18Cr, 12Ni, 1Nb, 0.04N	635-750°C
D.W. Borland[80]	18Cr, 12Ni, 0.62-1.68Nb, 0.02-0.09N	700-800°C
H. Hughes[96]	18Cr, 12Ni, 0.73-1Nb, 0.024-0.2N	950-1050°C
J.M. Silcock et al[180]	20Cr, 25Ni, 0.14-0.2Nb, 0.7-1.1N	750-950°C

He observed that the precipitation reaction of Z phase was relatively slow in the temperature range 700-900°C with the particles being detected after 18 hrs at grain boundaries and matrix. At 1000°C, Colclough observed that the phase forms quickly and is well developed after 1/4 hour at all nucleation sites.

In the present work, Z phase has been shown to precipitate in REX 734 over a wide temperature range, 600-1000°C, frequently exhibiting a well-defined orientation relationship with the austenite matrix. The particles were equiaxed at an early stage of precipitation, but, on growing, developed into cuboids and tended to coarsen further, showing a plate-like morphology when approaching their optimum volume after 1 hour at 1000°C. The phase is rich in niobium and chromium but may contain Fe, as indicated in Figs 7.14 and 7.15. The precipitation reaction of Z phase in REX 734 was found to be rapid, being detected after one hour between 700-900°C at grain boundaries and on dislocations in the matrix. At 1000°C the reaction was faster with plate-like Z phase particles already being formed after 1 hr. On further ageing at this temperature the particle size tended to equilibrate (about 450nm) with the development of a new f.c.c phase (designated as ϕ phase) growing around the Z phase particles.

The Z phase precipitation reaction observed in the present investigation is faster than that observed by Colclough[35], due presumably to the higher nitrogen and niobium content in REX 734. The Z phase precipitation could be seen even in MMA weld deposits where the time for which those zones had been exposed to the temperature range of Z phase precipitation was expected to be much shorter than that used normally in isothermal heat treatment. In the weld deposits Z phase precipitates quickly on dislocations in the heavily deformed austenitic matrix. Although these Z phase nucleated on dislocations could favourably influence creep behaviour, the relatively rapid growth of Z phase at higher temperatures might have a deleterious effect.

Another aspect of Z phase precipitation is whether the enhanced mechanical properties of the interstitially solid solution strengthened austenitic stainless steel could be jeopardised by significant quantities of nitrogen being removed from solution. If all the niobium were to be used up in precipitating Z phase then the maximum amount of nitrogen which could be removed from the matrix would be approximately 0.05 wt % N. When compared to the original nitrogen content of the alloy, 0.4 wt % N, it can be seen that the amount which is capable of being removed through precipitation is small. This would suggest that Z phase precipitation may not significantly affect the solid solution strengthening effect of

nitrogen. Similarly, the nitrogen removed from solid solution by Z phase precipitation may not affect the pitting corrosion. However this type of precipitation may contribute to the precipitation hardening effect, thus changing the mechanical properties.

It should be pointed out that the mechanical properties and corrosion resistance of REX 734 would also depend on the other precipitating phases found during ageing treatment, and that the effect of nitrogen as a solid solution strengthening element can be affected by Cr_2N precipitation and perhaps to a lesser extent by χ phase precipitation if, as suggested by Thier et al[170], some nitrogen may dissolve in χ phase. Therefore it is difficult to predict the precipitation effect on the mechanical properties and corrosion resistance of the material during ageing treatment.

9.4 Precipitation of χ and σ Phases

The precipitation of χ phase in REX 734 during ageing treatment is found to occur at about the same time as that reported by other workers[20,74] in austenitic stainless steel AISI type 316, over the temperature range 700-900°C. In the present investigation χ phase was evident after 1000 hours at 700°C and after 100 hours in the temperature range 800-900°C, and was always preceded by $M_{23}C_6$ precipitation (Fig 9.1). The χ phase precipitation appears to be related to $M_{23}C_6$ precipitation. At long ageing times (after 100 hrs) at high temperatures χ phase is found to replace $M_{23}C_6$ carbides through an intermediate compound designated as χ' phase, which has a body-centred cubic structure with lattice parameter a=10.18 A and composition 32Fe, 48Cr, 13Mo, 3Ni (wt %), Fig 6.31g. On continued ageing the equilibrium composition of χ phase is reached and found to be 48Fe, 27Cr, 18Mo, 5Ni (wt %) with a lattice parameter a=8.81 A, while the face-centred cubic $M_{23}C_6$ carbide had an equilibrium composition with 19Fe, 62Cr, 10Mo, 3 .5Ni (wt %) with lattice parameter a=10.65 A. The χ phase is thought to dissolve some carbon since no other carbide followed the χ phase precipitation but instead a Cr_2N was found to precipitate side by side with χ phase at boundaries.

The instability of $M_{23}C_6$ at high temperatures and long ageing times has been reported by several authors[20,37,62,63] some of whom have observed the replacement of this carbide by other more stable phases such as NbC, TiC or intermetallic phases such as σ and χ. On some occasions it has been reported that $M_{23}C_6$ may act as a nucleation site for σ and χ phases. In the present work, as we have seen, the $M_{23}C_6$, in the process of dissolving, goes through an intermediate compound, χ' phase, leading to the formation of χ phase rather than σ phase.

The σ phase frequently reported in austenitic stainless steel AISI type 316 was very limited in REX 734 aged specimens. The phase made its appearance after 100 hours at 900°C, which is beyond the stability range of $M_{23}C_6$ (Fig 9.1). The composition of the tetragonal σ phase in REX 734 is 51Fe, 31Cr, 9Mo, 4Ni (wt %) which is richer in chromium and more depleted in Mo than χ phase. The preferred formation of χ phase, rather than σ phase, in REX 734 aged specimens is not straightforward since both phases compete for the same elements (composition shown above).

Wiegand et al[69] explained the effect of carbon on the precipitation sequence of austenitic stainless steel suggesting that carbon in solid solution prevents the formation of σ phase due to its inability to dissolve carbon, while χ phase can form simultaneously with the carbides because of its capacity to incorporate carbon into the crystal lattice. The χ phase ability to dissolve carbon has been previously postulated by Goldschmidt[25]. Thier et al[170] have shown that, in their 17Cr, 13Ni wt % alloys, increasing the level of nitrogen from 0.039 wt % to 0.145 wt % totally suppresses any σ phase formation, while χ phase tends to occur at higher temperatures.

According to Andrews et al[182], the preference for χ phase rather than σ phase does not depend on the actual value of the molybdenum content of the steel in the range 2 and 5 wt % Mo, however χ phase was never found in steels which did not contain some molybdenum. Furthermore, Leitnaker[142] has shown that, in 16Cr, 8Ni (wt %) stainless steel, the precipitation of χ phase was observed when the Mo content was increased from 1 to 2 wt %. In the present investigation we observed that about 3 wt % Mo in the steel led to the formation of χ phase which contains double the amount of Mo in

relation to σ phase. This suggests that Mo can be dissolved in χ phase at larger quantities.

This brief discussion of previous workers' observations suggests that there may be a chemical effect which determines the preferred precipitation of either χ or σ phase in austenitic stainless steel. Because of χ phase capacity to dissolve interstitials, in REX 734 containing Mo, high nitrogen (0.4 wt %) and relatively high carbon (0.058 wt %) the χ phase forms in preference to σ phase.

In REX 734 weld deposits, a similar tendency is observed with relation to the preferred formation of χ phase; however the precipitation of both σ and χ phases is faster than that observed during ageing treatments. The faster precipitation of χ phase and σ phase is attributed to the presence of δ ferrite, which is known to enhance the precipitation of intermetallic phases[58,59]. According to Singhal and Martin[56] the interface α/γ provides appropriate high energy nucleation sites for intermetallic precipitates. In the present work, in similar circumstances (δ/γ), the ferrite was found to be preferentially absorbed during growth of σ and χ phases, presumably because it is richer in chromium than austenite. The presence of alloying elements such as Mo may achieve a further acceleration of growth of σ and χ phase as reported by Beattie and Hagel[60]. In fact, Wegrzyn et al[138] have shown that, in the presence of δ ferrite, σ phase occurred in areas of multi-run weld deposits which had been exposed to the temperature range of σ formation for not more than 60 seconds. They also observed that additions of Mo, Nb, V and Si accelerated the intermetallic precipitation which was then observed after 30 seconds.

The presence of intermetallic χ and σ phases in aged specimens and weld deposits may affect the mechanical properties of REX 734, particularly the susceptiblity of the material to embrittlement. The reduction in impact properties of austenitic stainless steels through σ phase precipitation has been reported by several workers[145,183-186]. It was found for instance that the embrittling effect of σ phase depends on its amount and distribution[184,185], and that as little as 3% of σ phase by volume may reduce the impact toughness to one half of the original value[145]. It has also been reported that continuous networks of σ phase

in duplex weld metal markedly decrease the impact strength of the weld deposits[186]. While the brittleness of σ phase has been extensively discussed in the literature, very little is known about the effect of χ phase on the impact strength of austenitic stainless steels. Although the crystal structure of χ and σ phases is different, their similarity in chemical composition has led to suggestions that χ phase may be as brittle as σ phase. Reports on impact properties of type 316 stainless steel at liquid nitrogen temperature as a function of ageing treatment[20] have shown that χ phase is brittle but its precipitation did not lead to further significant reduction in the impact strength of the steel already impaired by $M_{23}C_6$ precipitation.

Analysing the precipitation reactions observed in the present investigation in the light of the results obtained by the workers mentioned above on the effect of intermetallic phases on the impact properties of austenitic stainless steels, it may be suggested that the weld deposits would have a greater susceptibility to embrittlement than the aged specimens. This may be partially explained by the differences in precipitation behaviour. The aged specimens showed dominant precipitation of $M_{23}C_6$ at lower temperatures and χ and σ phases at high temperatures after long ageing times. In the weld deposits no $M_{23}C_6$ was detected but continuous networks of χ and σ phases, especially in MMA, were observed at γ/δ interfaces. These intermetallic phases form more readily in the presence of δ ferrite, as previously discussed, and their precipitation reactions can also be favoured by high temperatures reached during welding. Furthermore, stresses introduced during the welding process can also contribute to a reduction in the impact properties of the weld deposit.

9.5 Precipitation of Cr_2N

In REX 734 the precipitation of Cr_2N was observed at boundaries in the temperature range 800-900°C after 100 hours. In this type of steel containing less nitrogen (0.12-0.20 wt %) other workers[80,95,97] have observed that the presence of strong nitride-forming elements such as Nb, Ti or V led to the formation of nitrides of these elements without

precipitation of Cr_2N. However, in austenitic stainless steel containing 0.25 wt % N and 0.18 wt % Nb, Colclough[35] observed that Cr_2N was formed at or near the surface of specimens aged in air at 900°C for 18 hrs. The author indicated that the precipitation of Cr_2N had occurred as a result of nitrogen pick-up which increased the nitrogen content in those areas to approximately 0.4 wt %. In agreement with Colclough's observations, the present investigation clearly showed that Cr_2N precipitation occurs in stabilized austenitic stainless steel containing high nitrogen.

In the present work, the high niobium content of the steel led to extensive precipitation of Z phase in the matrix in preference to Cr_2N. At grain boundaries, early precipitation of Z phase followed by $M_{23}C_6$ precipitation, which dominates most of the areas in the boundaries, may have reduced the local concentration of chromium available to form Cr_2N. However, at high temperatures the rapid diffusion of chromium as well as the instability of $M_{23}C_6$ led to the formation of Cr_2N at grain boundaries (energetically more favourable sites). The replacement of $M_{23}C_6$ by χ phase containing much less chromium than the carbide would replenish the matrix with chromium, which then combines with the nitrogen available to form Cr_2N. This may explain the alternating disposition of χ phase and Cr_2N particles at grain boundaries observed at 800°C during the dissolving process of $M_{23}C_6$.

In the weld deposits no Cr_2N was observed despite the high temperatures reached during welding. While the absence of $M_{23}C_6$ in the weld deposits, as explained earlier, may be understood on the basis of the effect of nitrogen in delaying the carbide precipitation, a question may arise on the non-occurrence of Cr_2N in these weld deposits.

Looking at the precipitation behaviour of REX 734 during ageing treatments, it can be seen that Cr_2N is stable in a very limited temperature range (800-900°C), Fig 9.1, and that precipitation occurs after quite a long ageing time (100 hours). From the viewpoint of the Fe-Cr-N phase diagram[17] the equilibrium between Cr_2N and γ + ferrite occurs in the temperature range of 900-1000°C for a chromium and nitrogen content of 20 wt % and 0.3 wt % respectively. The precipitation of Cr_2N in the duplex structure also depends on the length of time for which the steel has been

held at the temperature which forms Cr_2N. Herbsleb et al[181] have shown that, in duplex ($\gamma+\delta$) steels (wt %) 0.03C, 21-23Cr, 4.5-6.5Ni, 2.5-3.5Mo and 0.08-0.2N, the Cr_2N forms at ferrite-austenite grain boundaries after 2 minutes at the temperature range 750-900°C. According to thermal cycle measurements done by Wegrzyn et al[138] in a MMA weld of 18Cr 8Ni (wt %) duplex weld deposits, the longest dwell time of the weld metal layers at temperatures in the range of 920-740°C is about 61 seconds. This value was obtained using weld heat input of 8 to 10 kJ/mm.

In the present investigation, the weld heat input was over 3 times less than that used by Wegrzyn et al[138], therefore it is possible that the time for which the weld metal layers were held in the temperature range of Cr_2N formation was less or at least equal to that reported by Wegrzyn et al. This low weld heat input could perhaps prevent the formation of Cr_2N in the weld deposits in the as-welded condition. However, if these welds are subsequently heat-treated the precipitation of Cr_2N, χ phase and σ phase will occur at faster rates than would be the case in fully austenitic steel.

The duplex structure ($\gamma+\delta$) such as occur in welds is a result of the solidification sequence and solid state transformation. Although the δ ferrite could be eliminated by changes in the chemical composition of the steel, the presence of this phase in small amounts in the weld deposits is considered beneficial for its effect in reducing the susceptibility of the welds to hot crack, frequently reported in fully austenitic welds. However, from the viewpoint of precipitation behaviour, this duplex structure will be more prone to the precipitation of phases as studied in this investigation than would be the one-phase austenitic structure as in isothermal heat treatments. Accordingly the mechanical properties and corrosion resistance may be significantly affected.

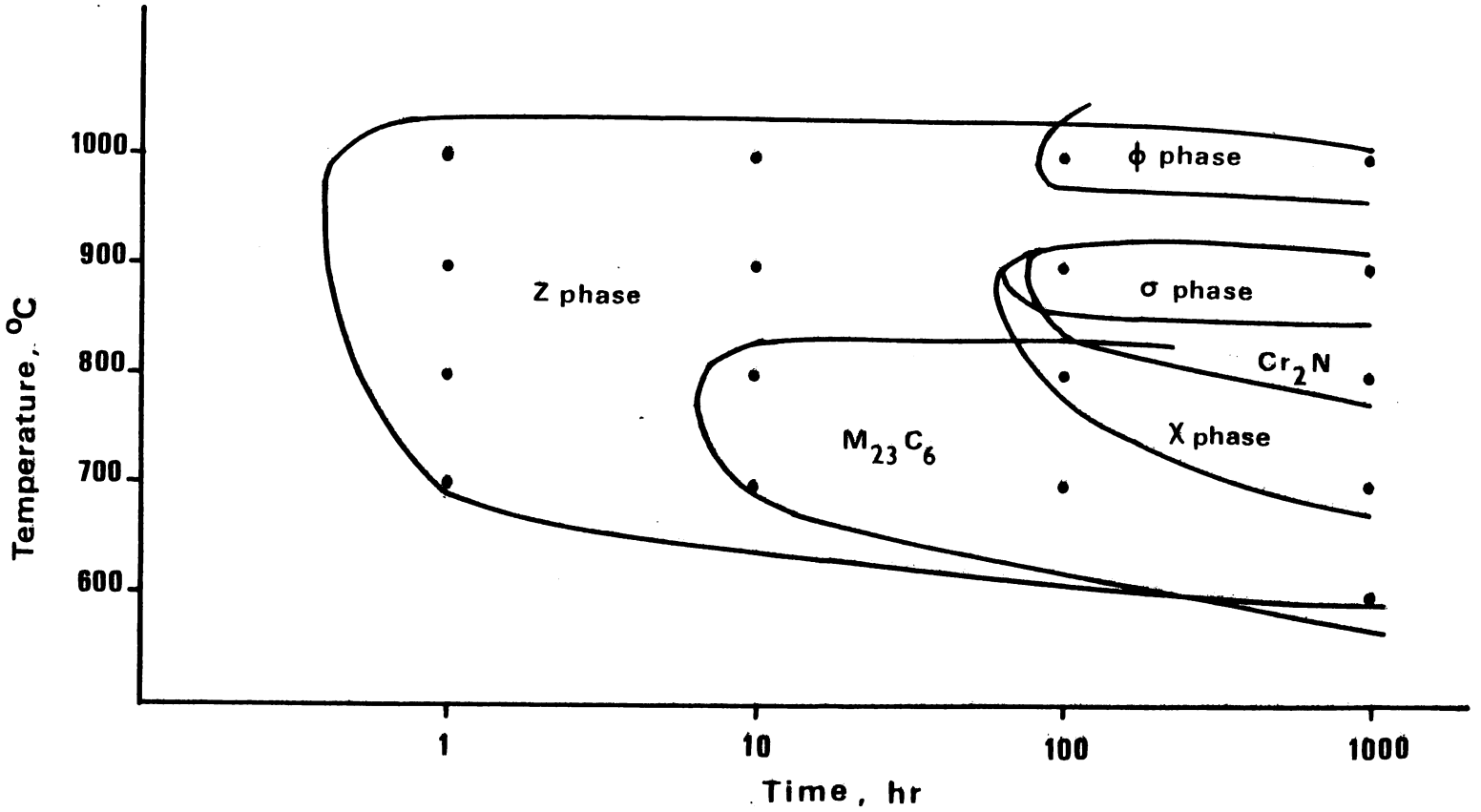

Fig. 9.1 TTT diagram of precipitate reactions in REX 734 stainless steel solution treated for one hour at 1300 °C and water quenched.

10. CONCLUSIONS AND SUGGESTIONS FOR FURTHER WORK

10.1 Conclusion

1) In austenitic stainless steel REX 734 containing niobium and high nitrogen, six different phases may precipitate during ageing in the temperature range 600-1000°C, after solution treatment at 1300°C. These are

(i) A tetragonal niobium-chromium rich nitride (NbCr)N, Z phase.

(ii) A face-centred cubic chromium-rich carbide, $M_{23}C_6$.

(iii) A hexagonal chromium nitride, Cr_2N.

(iv) A body-centred cubic intermetallic compound, χ phase.

(v) A tetragonal intermetallic compound, σ phase.

(vi) A face-centred cubic ϕ phase.

2) Precipitation of Z phase precedes all other precipitation reactions with the particles being formed after 100 hrs at 600°C and after one hour in the temperature range 700-100°C. Z phase occurs at grain boundaries, twin boundaries and on dislocations in the austenitic matrix. The morphology of Z phase follows a distinctive growth sequence viz

rounded equiaxed particles → cuboids → plate-like

The Z phase precipitates with the following orientation relationship with the austenitic matrix

$$(001)\ \gamma\ //\ (001)\ Z\ \text{phase}$$
$$[100]\ \gamma\ //\ [110]\ Z\ \text{phase}$$

Its composition may be represented by the formula (NbCr)N, but some Fe may also be present. The lattice parameter of Z phase is a=3.01 A, c=7.28 A.

3) Precipitation of $M_{23}C_6$ predominates at low ageing temperature, especially at 700°C. The particles always show the familiar cube-on-cube

orientation relationship with the austenite matrix. It appears that the carbide does not dissolve nitrogen and its composition may be written as $(Cr_{16}Fe_{4.5}Mo_{1.5}Ni)C_6$. The lattice parameter of $M_{23}C_6$ carbide is a=10.65 A.

4) Precipitation of Cr_2N occurs exclusively at grain boundaries and only after high temperature ageing. The formation of Cr_2N appears to be related to the $M_{23}C_6$ carbide dissolution which replenishes the matrix with chromium. The particles are massive and do not seem to contain carbon. The lattice parameter of Cr_2N is a=2.77 A, c=4.45 A.

5) χ phase precipitation is always preceded by $M_{23}C_6$ precipitation and occurs at the temperature range 700-900°C. Short term ageing (less than 100 hrs) shows a predominance of $M_{23}C_6$, however the longer ageing product is χ phase, the $M_{23}C_6$ redissolving. The χ phase precipitation appears to be related to $M_{23}C_6$ precipitation with an intermediate compound being formed. This intermediate compound, designated as χ' phase, is a body-centred cubic phase having a lattice parameter a=10.18 A with composition 48Cr, 32Fe, 13Mo, 3Ni (wt %). The equilibrium composition of χ phase is 48Fe, 27Cr, 18Mo, 5Ni (wt %) with a lattice parameter a=8.81 A. The intragranular morphology of χ phase is in the form of faceted rods and its orientation relationship with the matrix is the familiar

$$(111)\ \gamma\ //\ (110)\ \chi \text{ phase}$$
$$(100)\ \gamma\ //\ (11\bar{2})\ \chi \text{ phase}$$
$$[01\bar{1})\ \gamma\ //\ [\bar{1}10]\ \chi \text{ phase}$$

6) Precipitation of σ phase is limited and is preceded by χ phase precipitation which is the preferred intermetallic phase formed in this steel. The σ phase lattice parameter is a=8.86 A, c=4.60 A and its chemical composition is 51Fe, 31Cr, 9Mo, 4Ni (wt %).

7) The f.c.c ϕ phase which has a lattice parameter a=8.3 A forms around Z phase particles after the latter phase approaches its optimum volume. This may be explained by either the instability of Z phase or depletion of solute in the areas surrounding Z phase.

8) In the austenitic stainless steel REX 734 containing niobium and high

nitrogen, a duplex structure ($\gamma+\delta$) may occur after welding by MMA and TIG process as a result of segregation during solidification. The amount of δ ferrite changes with variations of nitrogen content in the weld deposits. A reduction in nitrogen level in the weld tends to increase the amount of δ ferrite in the weld deposit.

9) The precipitating phases observed in the weld metal in the as-welded condition are

(i) Z phase

(ii) χ phase

(iii) σ phase

Precipitation of these phases occurs only in weld areas subjected to weld thermal cycles arising from the multi-run technique, and is more extensive in MMA weld deposits where higher weld heat inputs are used.

10) The presence of δ ferrite has enhanced the precipitation of χ and σ phases which precipitates more readily at the γ/δ interfaces.

11) Z phase precipitates in weld deposits but only on dislocations in the austenite matrix.

10.2 Suggestions for Further Work

During the study of the microstructural behaviour of REX 734 in the present work, it was observed that one of the characteristics of this austenitic stainless steel containing niobium and high nitrogen was the inhibition of the nucleation of $M_{23}C_6$ carbides, which are frequently reported as the main cause for the increased susceptibility to intergranular corrosion of austenitic stainless steels. This should be further investigated in the light of the present work. Another aspect of the precipitation in this material was the observation that χ phase formed preferentially to the brittle σ phase. To conclude that the precipitation sequences and trends established for this alloy are consistent for all alloys within the compositional range of REX 734, it is necessary to investigate several other alloys within its compositional range in order to determine the overall precipitation behaviour.

b) As pointed out in the introduction and in the last chapter of this work, the high nitrogen austenitic stainless steels are claimed to have increased strength and good impact properties in comparison with other austenitic steels. Since the applications of this material may require good mechanical properties after heat treatments or welding it will be useful to correlate the effects of precipitation behaviour in these conditions with certain mechanical properties such as tensile strength and impact resistance. It would be interesting to study whether the large volume fractions of intergranular second phases observed during ageing treatments and under weld conditions cause a marked reduction in the impact properties of this steel.

c) Another property claimed for high nitrogen austenitic stainless steels is its good corrosion resistance, especially pitting corrosion in the presence of nitrogen in solid solution. Although it has been shown that little nitrogen can be removed from solid solution during Z phase precipitation, the effect of this on the pitting corrosion resistance of the material is unknown. Furthermore, the general precipitation behaviour observed in the present work in as heat treated specimens is different from that resulting from welding conditions. Therefore the corrosion behaviour of the heat treated REX 734 as well as the corrosion resistance of the welds need to be established in order to ascertain the precise effects of the various precipitating phases.

d) To complete the microstructural characterization of REX 734 welds an investigation into the precipitation behaviour of heat-affected zones would be necessary.

References

1 Mahla, E.M. and Nielsen, N.A., (1951), Trans. ASM, 43, 290.

2 Beckett, F.M. and Franks, R., (1934), Trans. AIME, 113, 143.

3 Irvine, K.J., Llewellyn, D.T. and Pickering, F.B.,(1961), JISI, 199, 153.

4 Tofaute, W. and Schottky, H., (1940), Arch. Eisen., 14, 71.

5 Truman, J.E., (1978), Stainless Steel Ind., 6, 21.

6 Wedl, W. and Kohl, H., (1979), Berg Huttenmann Monatsch., 124, 508.

7 Liljestrand, L.G. and Omsen, A., (1975), Met. Trans., 6A, 279.

8 Fujita, T., Sato, T. and Takahashi, N., (1978), Trans. ISIJ, 18, 115.

9 Rohlin, L. and Aronsson, B., (1980), Scand. J. Met., 9, 237.

10 Takashi, M., Takayuki, S. and Ryohei, T., (1973), Tetsuo-to-Hagane, 59, 907.

11 Bungardt, K., Von Den Steinen, A. and Lennartz, G., (1969), Dew. Techn. Ber., 9, 218.

12 Class, I. and Jesper, H., Chem. Ing. Techn., (1964), 36, 546.

13 Jesper, H. and Wessling, W., (1965), Werkstoffe u Korrosion, 16, 453.

14 Tuma, H., Landa, V. and Lobl, K., (1981), Mem. Sci. Rev. Met., 78, 255.

15 Bain, E.C. and Aborn, R.H., (1948) Metals Handbook, ed. American Society for Metals.

16 Colombier, L. and Hoffman, J., (1967), "Stainless and Heat Resisting Steels", Edward Arnold.

17 Metals Handbook, (1973), 8th Edition, Vol. 8, American Society for Metals.

18 Hansen, M., (1958) "Constitution of Binary Alloys", 2nd Edition, McGraw Hill.

19 Tisinai, G.P., Stanley, J.K. and Samans, C.H., (1954), Trans. AIME, 200, 1259.

20 Weiss, B. and Stickler, R., (1972), Met. Trans., 3, 851.

21 Jones, F.W. and Pumphrey, W.I. (1949), JISI, 163, 121.

22 Pickering, F.B., (1978), "Physical Metallurgy and Design of Steels", Applied Science Publishers Ltd.

23 Metal Prog. Data Book, (1977), Vol. 112, American Society for Metals.

24 Kautz, H.R. and Gerlach, H., (1968), Arch. Eisen., 39, 151.

25 Goldschmidt, H., (1967), "Interstitial Alloys", Plenum Press, New York.

26 Metals & Alloys Data Book, (1978), Vol. 1 and Vol. 2, JCPDS International Centre for Diffraction Data.

27 Lewis, M.H. and Hattersley, B., (1965), Acta Met., 13, 1159.

28 Dulis, E.J., (1964), ISI Special Report, No 86, 162.

29 Hillert, M. and Lagneborg, R., (1971), J. Mat. Sci., 6, 208.

30 Hatwell, H. and Berghezan, A., (1959), ISI Special Report, No 64, 88.

31 Wolff, U.E., (1966), Trans. Met. Soc. AIME, 19, 236.

32 Beckitt, F.R. and Clark, B.R., (1967), Acta Met., 15, 113.

33 Singhal, L.K. and Martin, J.W., (1968), Trans. Met. Soc. AIME, 242, 814.

34 Singhal, L.K. and Martin, J.W., (1968), Acta Met., 16, 1159.

35 Colclough, G.J., (1981), Ph.D. Thesis, University of Leeds.

36 White, W.E. and Le May, I., (1972), Metallography, 5, 333.

37 Summerling, R. and Nutting, J., (1965), JISI, 203, 398.

38 Irani, J.J. and Weiner, R.D., (1965), JISI, 203, 913.

39 Van Aswegen, J.S.T., Honeycombe, R.W.K. and Warrington, D.H., (1964), Acta Met., 12, 1.

40 Silcock, J.M., (1963), JISI, 201, 409.

41 Harding, H.J. and Honeycombe, R.W.K., (1966), JISI, 204, 259.

42 Silcock, J.M., (1973), JISI, 211, 792.

43 Froes, F.H., Honeycombe, R.W.K. and Warrington, D.R., (1967), Acta Met., 15, 157.

44 Silcock, J.M. and Tunstall, W.J., (1964), Phil. Mag, 10, 361.

45 Shepherd, J.P., (1976), Met. Sci., 10, 174.

46 Silcock, J.M., (1966), 3rd International Conference on "Electron Microscopy", Kyoto.

47 Decker, R.F. and Floreen, S., (1963), "Precipitation from Iron-base Alloys", p.69, Editor G.R. Speich, Gordon & Breach, Cleveland, Ohio.

48 Hall, E.O. and Algie, J.H., (1966), Met. Rev., 11, 61.

49 Nenno, S., Tagaya, M. and Nishiyama, Z., (1962), Trans. Jap. Inst. Metals, 3, 82.

50 Kasper, J.S., (1954), Acta Met., 2, 456.

51 Bechtoldt, C.J. and Vacher, H.C., (1957), J. Res. Nat. Bur. Stand., 58, 7.

52 Denham, A.W. and Silcock, J.M., (1969), JISI, 207, 585.

53 Bain, E.C. and Griffiths, W.E., (1927), Trans. AIME, 75, 166.

54 Blenkinsop, P.A. and Nutting, J., (1967), JISI, 205, 953.

55 Duhaj, D.P., Ivan, I. and Makovicky, E., (1968), JISI, 206, 1245.

56 Singhal, L.K. and Martin, J.W., (1968) Acta Met., 16, 1441.

57 Singhal, L.K. and Duhaj, D.P., (1969), JISI, 207, 1382.

58 Beckitt, F.R., (1969), JISI, 207, 632.

59 Ellis, R.G. and Pollard, G., (1970), JISI, 208, 783.

60 Beattie, H.J. and Hagel, W.C., (1961), Trans. AIME, 221, 28.

61 Singhal, L.K. and Martin, J.W., (1967), JISI, 205, 947.

62 Pickering, F.B., (1959), ISI Special Report, No 64, 118.

63 Pomey, G., (1960), Trans. AIME, 218, 310.

64 Lewis, M.H., (1966), Acta Met., 14, 1421.

65 Nenno, L., Tagaya, M, Hosomi, H. and Nishiyama, Z., (1963), Trans. Jap. Inst. Met., 4, 222.

66 Spruiell, J.E., Scott, J.A., Ary, C.S. and Hardin, R.L., (1973), Met. Trans., 4, 1533.

67 Grot, A.S. and Spruiell, J.E., (1975), Met. Trans., 6A, 2023.

68 Andrews, K.W., (1949), Nature, 164, 1015.

69 Wiegand, H. and Doruk, M., (1962), Arch. Eisen., 33, 559.

70 Slattery, G.F., O'Riordan, P., Lambert, M.E. and Green, S.M., (1981), J. Microscopy, 122, 109.

71 Lai, J.K. and Meshkat, M., (1978), Met. Sci., 12, 415.

72 Morris, D.G. and Harries, D.R., (1978), Met. Sci., 12, 542.

73 Koh, P.K., (1953), J. Metals, 5, 339.

74 Duhaj, D.P. and Ivan, I., (1968), JISI, 206, 1014.

75 Gerlach, H. and Schmidtmann, E., (1968), Arch. Eisen., 39, 139.

76 Cihal, V. and Jezek, J., (1964), JISI, 202, 124.

77 Jack, D.H. and Jack, K.H., (1973), Mat. Sci. Eng., 11, 1.

78 Leslie, W.C., (1981), "The Physical Metallurgy of Steels", McGraw Hill Book Company.

79 Pearson, W.B., (1967), "Handbook of Lattice Spacing and Structures of Metals", Vol. 2, Pergamon Press.

80 Borland, D.W., (1966), Ph.D. Thesis, Sheffield.

81 Masumoto, T. and Imai, Y., (1969), J. Jpn. Inst. Met., 33, 1364.

82 Baerlecken, E. and Hirsch, W., (1955), Stahl und Eisen., 75, 570.

83 Nakagawa, R. and Otoguro, Y., (1963), Trans. Nat. Res. Inst. Met., 5, 129.

84 Okamoto, M., Tanaka, R. and Fujimoto, R, (1963), Tetsuo-to-Hagane, 49, 1694.

85 Omsen, A. and Eliasson, L., (1971), JISI, 209, 830.

86 Kikuchi, M., Tanaka, T. and Tanaka, R., (1974), Met. Trans., 5, 1520.

87 Wakita, S., Kikuchi, M. and Tanaka, R., (1975), JISI, Japan, 61, 2418.

88 Kikuchi, M., Sekita, T., Wakita, S. and Tanaka, R., (1976) JISI, Japan, 62, 981.

89 Tanaka, T., Kikuchi, M. and Tanaka, R., (1977), J. Japan Inst. Met., 41, 1145.

90 Kikuchi, M., Sekita, T., Wakita, S. and Tanaka, R., (1978) JISI Japan, 64, 440.

91 Kikuchi, M., Nishimura, T., Tanaka, T. and Tanaka, R., (1978), Met. Trans., 9A, 1337.

92 Mukherjee, J.K. and Nijhawan, B.R., (1967), JISI, 205, 62.

93 Fabritius, H., (1963), Arch. Eisen., 34, 489.

94 Dulis, E.J. and Smith, G.V., (1952), Trans. AIME, 194, 1083.

95 Bungardt, K., Lennartz, G. and Oppenheim, R., (1965), Paper at Meeting of V.D.E.R.

96 Huges, H., (1967), JISI, 205, 775.

97 Hull, F.C. and Stickler, R., (1963), Joint International Conference on Creep, New York, Inst. Mech. Eng. London, Publisher.

98 Fountain, R.W. and Shipman, J., (1958), Trans. TMS-AIME, 212, 737.

99 Thorvaldsson, T. and Dunlop, G.L., (1982), Met. Sci., 16, 184.

100 Jarl, M., (1978), Scand. J. Met., 7, 93.

101 Borland, D.W. and Honeycombe, R.W.K., (1970), Met. Sci., 4, 14.

102 Jack, D.H. and Jack, K.H., (1972), JISI, 209, 790.

103 Savage, W.F. and Aronson, A.H., (1966), Weld. J., 45, 85.

104 Bray, R.S., Lozano, L.J. and Willett, R.E., (1969), Weld. J., 48, 181.

105 Nakagawa, H., Kato, M., Matsuda, F. and Senda, T., (1970), Trans. Jap. Weld. Soc., 1, 94.

106 Hellawell, A. and Herbert, P.M., (1962), Proc. Roy. Soc., A269, p.560.

107 Savage, W.F., Lundin, C.D. and Aronson, A.H., (1965), Weld. J., 44, 175.

108 Kato, M., Matsuda, F. and Senda, T., (1972), Trans. Jap. Weld. Soc., 3, 59.

109 Nakagawa, H., Kato, M., Matsuda, F. and Senda, T., (1971), Trans. Jap. Weld. Soc., 2, 1.

110 Matsuda, F., Hashimoto, T. and Senda, T., (1969), Trans. Nat. Res. Inst. Met., 11, 43.

111 Kato, M., Matsuda, F. and Senda, T., (1972), Trans. Jap. Weld. Soc., 3, 69.

112 Calvo, F.A., Bentley, K.P. and Baker, R.G., (1960), Acta. Met., 8, 898.

113 Miller, T.W., (1967), M.Sc. Thesis, Rensselaer Polytechnic Institute, Troy, New York.

114 Bray, R.S. and Lozano, L.J., (1965), Weld. J., 44, 424.

115 Bell, J.R., (1966), M.Sc. Thesis, Rensselaer Polytechnic Institute, Troy, New York.

116 Savage, W.F., Lundin, C.D. and Hrubec, R.J., (1968), Weld. J., 47, 420.

117 Rollason, E.C. and Roberts, D.F.T., (1950), Trans. Inst. Weld., 13, 129.

118 Fukui, T. and Namba, K., (1973), Trans. Jap. Weld. Soc., 4, 49.

119 Castro, R., (1961), Mem. Sci. Rev. Met., 58, 881.

120 Blanc, G. and Tricot, R., (1971), Mem. Sci. Rev. Met., 58, 735.

121 Fredriksson, H., (1978), Met. Trans., 3A, 2989.

122 Arata, Y., Matsuda, F. and Katayama, S., (1976), Trans. JWRI, 5, 35.

123 Suutala, N., Takalo, T. and Moisio, T., (1979), Met. Trans., 10A, 512.

124 Suutala, N., Takalo, T. and Moisio, T., (1979), Met. Trans., 10A, 1183.

125 Suutala, N., Takalo, T. and Moisio, T., (1980), Met. Trans., 11A, 717.

126 David, S.A., Goodwin, G.M. and Braski, D.N., (1979), Weld. J., 58, 330.

127 Lyman, C.E., Manning, P.E., Duquette, D.J. and Hall, E., (1978), Scann. Electron Microscopy, 1, 213.

128 Lippold, J.C. and Savage, W.F., (1979), Weld. J., 58, 362.

129 Lippold, J.C. and Savage, W.F., (1980), Weld. J., 59, 48.

130 Takalo, T., Suutala, N. and Moisio, T., (1979), Met. Trans., 10A, 1173.

131 Leone, G.L. and Kerr, H.W., (1982), Weld. J., 61, 13.

132 Cieslak, M.J., Ritter, A.M. and Savage, W.F., (1982), Weld. J., 61, 1.

133 Hull, F.C., (1967), Weld. J., 46, 399.

134 Taylor, J.W., (1958), J. Inst. Met., 86, 456.

135 Borland, J.C. and Younger, R.N., (1960), Brit. Weld. J., 7, 22.

136 Fredriks, H. and Van Der Toorn, L.J., (1968), Brit. Weld. J., 15, 178.

137 Lai, J.K. and Haigh, J.R., (1979), Weld. J., 58, 1.

138 Wegrzyn, J. and Klimpel, A., (1981), Weld. J., 60, 146.

139 Slattery, G.F., Keown, S.R. and Lambert, M.E., (1983), Met. Technology, 10, 373.

140 Slattery, G.F. and O'Riordan, P., (1980), Metallography, 13, 59.

141 Keown, S.R. and Thomas, R.G., (1981), Met. Sci., 15, 386.

142 Leitnaker, J.M., (1982), Weld, J., 61, 9.

143 Dyson, D.J. and Keown, S.R., (1969), Acta Met., 17, 1095.

144 Komura, Y., Sly, W.G. and Shoemaker, D.P.S., (1960), Acta Crystallogr., 13, 575.

145 Klemetti, K., Hänninen, H. and Kivilahti, J., (1984), Weld. J., 68, 17.

146 Iwamoto, N., Murata, K. and Taniguchi, Y., (1976), Trans. JWRI, 5, 53.

147 Binder, O.W., Brown, C.M. and Franks, R., (1949), Trans. ASM, 41, 1301.

148 Marshall, M.W., (1959), Weld. J., 38, 247.

149 Auld, J.R., (1965), "Effect of heat treatment and welding on corrosion resistance of austenitic stainless steels", Special Technical Publication of Am. Soc. Testing Materials, No 369, p.183.

150 Gooch, T.G., (1968), Brit. Weld. J., 15, 345.

151 Stickler, R. and Vinckier, A., (1961), Trans. ASM, 54, 362.

152 Stickler, R. and Vinckier, A., (1963), Corrosion Sci., 3, 1.

153 Pinnow, K.E. and Moskowitz, A., (1970), Weld. J., 49, 278.

154 Schuller, H.J., Schwaab, P. and Ternes, H., (1964), Arch. Eisen., 35, 659.

155 Fontana, M.G. and Greene, N.D., (1967), "Corrosion Engineering", p.64, McGraw Hill, New York.

156 Angerman, C.L., and Kranzlein, P., (1961), Trans. ASM, 53, 443.

157 Bourrat, J. and Hochmann, J., (1962), Mem. Sci. Rev. Met., 59, 863.

158 Pouillard, E. and Choida, J.P., (1967), Mem. Sci. Rev. Met., 64, 1025.

159 Cihal, V., Kasova, I., Masarik, V. and Lehka, N., (1968), 15, 14.

160 Cihal, V., Kasova, I., Masarik, V. and Lehka, N., (1968), Kovove Materialy, 4, 21.

161 Cihal, V., Kasova, I. and Kubelka, J., (1969), Metaux Corros. Inds., 44, 281.

162 Cihal, V. and Jarman, R.A., (1979), Scand. J. Met., 8, 284.

163 Andersen, C.A., (1973), "Microprobe Analysis , Editor A. Wiley, Interscience Publications, New York.

164 Isaacson, M. and Johnson, D., (1975), Ultramicroscopy, 1, 33.

165 Maher, D.M., (1979), "Introduction to Analytical Electron Microscopy", p.259, Editors J.J. Hren, J.I. Goldstein and D.C. Joy, Plenum Press, New York.

166 Joy, D.C., (1979), "Introduction to Analytical Electron Microscopy", p.223, Editors J.J. Hren, J.I. Goldstein and D.C. Joy, Plenum Press, New York.

167 Gullberg, R., (1971), JISI, 209, 71.

168 Andersson, T., and Lundberg, B., (1977), Met. Trans., 8A, 787.

169 Edmonds, D.V. and Honeycombe, R.W.K., (1979), "Precipitation Processes in Solids", ed. K.C. Russel and H.J. Aaronson, Symp. Proc., 1976, TMS Fall Meeting, Niagara Falls, New York, Sept., 1976, Metall. Soc. of AIME, 121.

170 Thier, V.H., Bäumel, A. and Schmidtmann, E., (1969), Arch. Eisen., 40, 333.

171 Schneider, H., (1960), Foundry Trade J., 108, 562.

172 Baeslack, W.A., Savage, W.F., and Duquette, D.J., (1979), Weld. J. 58, 83.

173 Arata, Y., Matsuda, F. and Saruwatari, S., (1974), Trans. of J.W.R.I., 3, 79.

174 David, S.A., (1981). Weld. J., 60, 63.

175 Weiss, B., Hughes, W. and Stickler, R., (1971), Prakt. Metall., 8, 528.

176 Osozawa, K. and Okamoto, N., (1976), "Passivity and its Breakdown on Iron and Iron Base Alloys", USA-Japan Seminar, 135.

177 Sakamoto, T., Abo, H., Okazaki, T., Ogawa, T., Ogawa, H. and Zaizen, T., (1980), "Alloys for the Eighties". ed. R.Q. Barr, Climax Molybdenum Company, 269.

178 kass, J.N., Bell, W.L., Wang, M.T. and Bobick, J., (1979), Met. Trans., 10, 715.

179 Jenkinson, E.A., Day, M.F., Smith, A.I. and Hopkin, L.M.T., (1962), JISI, 200, 1011.

180 Silcock, J.M., Raynor, D. and Willoughby, G., (1977), Met. Sci., 11, 551.

181 Herbsleb, G. and Schwaab, P., (1983), "Duplex Stainless Steels", ed. R.A. Lula, published by American Society for Metals, 15.

182 Andrews, K.W. and Brookes, P.E., (1951), Met. Treatment, 18, 301.

183 Lena, A., (1954), Met. Prog., 66, 86.

184 Talbot, A.M. and Furman, D.E., (1953), Trans. ASM, 45, 429.

185 Creamer, E.L., Rozalsky, I. and Leonard, R.W., (1969), Weld. J., 48, 239.

186 Spruiell, J.E., Fett, W.E. and Lundin, C.D., (1977), Weld. J., 56, 289.

187 Egerton, R.F., (1979), Ultramicroscopy, 4, 169.

188 Egerton, R.F., (1981), Proc. 39th Ann. Meeting Elect. Mic. Soc. Am., Atlanta, p.198.

189 Bourdillon, A.J., Hall, D.J., Morrison, C.D., and Stobbs, W.M., (1983), J. Microscopy, 130, 177.

APPENDIX 1

Electron energy-loss spectroscopy can be used to measure the inner-shell excitation directly through its effect on the transmitted electrons and can be employed as a standardless technique. That is, the absolute amount of a particular element within a given area of a specimen (defined, for example, by the incident-electron beam) is measured.

The information that can be obtained is contained in the angular and energy distribution of the electrons that have passed through the specimen (Fig A.1). By studying these distributions, which result from interactions between the electrons and the specimen, and analysing them in terms of an appropriate model, the required information can be found. This is done by measuring both the angle θ through which an electron is scattered, and E its change in energy relative to its incident energy E_0.

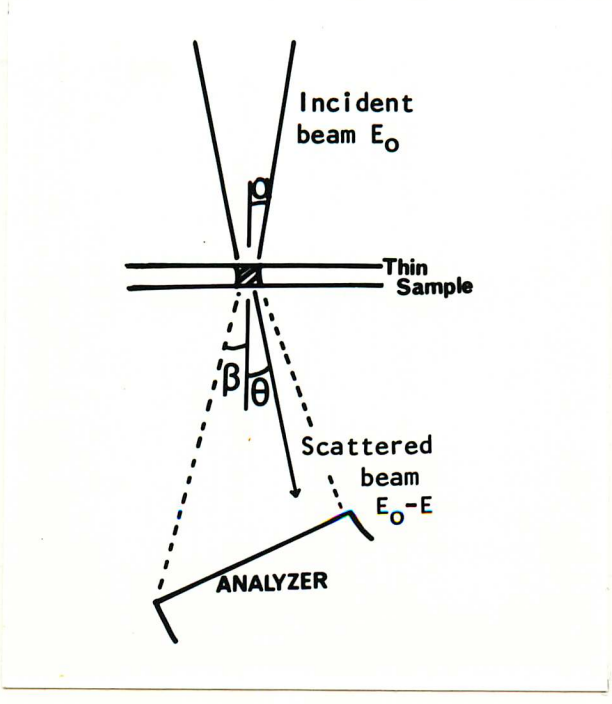

Fig A.1 The geometry of energy-loss spectroscopy in the electron microscope illustrating the scattering angle θ, the spectrometer acceptance semi-angle β and the incident beam convergence angle α.

Usually, however, it is sufficient to collect all the transmitted electrons lying within a cone of some semi-angle β about the incident beam direction, and then to analyse these for their energy loss. The result that is obtained from such an experiment is then an Electron Energy-Loss Spectrum in which the transmitted signal intensity I(E) is plotted as a function of the energy-loss E for all the electrons scattered within the angular cone β accepted by the spectrometer. A schematic electron energy-loss spectrum is shown in Fig A.2.

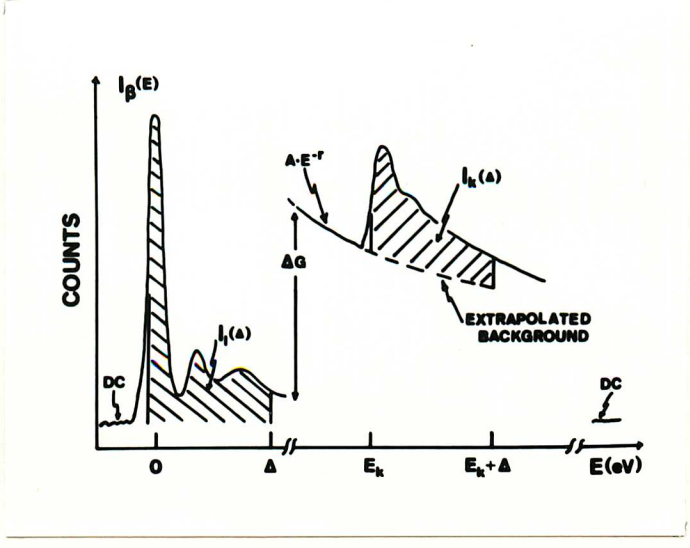

Fig A.2 Schematic electron energy-loss spectrum of the signal intensity I(E) versus energy loss E. All the quantities are defined in the text.

The quantity N of a particular element contributing to the measured intensity in an inner-shell edge ($E>E_K$, Fig A.2) can be obtained from the equation:

$$N = \frac{I_K(\Delta,\beta)}{I_1(\Delta,\beta)} \cdot \frac{1}{\sigma(\Delta,\beta)}$$

where $I_K(\Delta,\beta)$ is the integrated intensity under the edge and above the background measured over an energy-loss window Δ and for a scattering semi-angle β; $I_1(\Delta,\beta)$ is the integrated intensity under the loss region of the spectrum measured from the zero-loss peak up to Δ and for the same

angle β; and $\sigma(\Delta,\beta)$ a partial cross-section from excitations to continuum states from an inner shell, which cover a range Δ of energy losses and a range of scattering angles from zero to β. The semi-angle β is normally determined by an aperture placed between the specimen and electron spectrometer, which in the present investigation was 18mrad. $\sigma(\Delta,\beta)$ is usually expressed in cm^2 per atom, thus the above equation gives N in atoms per cm^2 of surface within the incident electron beam for STEM or within an aperture selected area for CTEM.

In the data systems presently in use, the values of I_k, I_1 are determined through interactive computer programs which read the spectrum from memory of the multi-channel analyser and allow regions of interest (i.e. low-loss; background and edge regions) to be defined. The first step in the quantification of a spectrum is to subtract off the detector dark current (DC). This contribution is recorded at both the beginning and end of each spectral measurement (as depicted schematically in Fig A.2). The next step is to obtain I_k in a form which can be related directly to I_1. Since each channel in the memory of the multi-channel analyser corresponds to a known increment of energy loss (e.g. 1 eV per channel), the relative position of an edge, i.e., E_k, and the energy window Δ over which an integration is to be carried out can both be defined directly from the edge spectral profile. Therefore, with reference to Fig A.2, one specifies E_k, the energy range over which the background is to be modelled (E_{BG}) and the end point for background extrapolation ($E_k+\Delta$). The computer then fits an inverse power law $A.E^{-r}$ (where E is the energy loss and A and r are parameters depending on the acceptance semi-angle β of the spectrometer) to the background, extrapolates this fit to $E_k+\Delta$ and strips the extrapolated intensity from the total intensity. The value of $I_k(\Delta,\beta)$ is then obtained by summing the net number of counts in each channel over the appropriate energy range. The edge region may or may not be recorded at the same detector gain as I_1. Therefore, the appropriate integral for quantification may be $I(\Delta)$ multiplied by a gain factor, $GF = 1/\Delta G$ which is read into the program.

The last step is to calculate $\sigma(\Delta,\beta)$ and this can be done by a method known as Calculated Partial Cross Sections. Egerton's programmes[187,188] for K-shells (SIGMAK) and L-shells loss (SIGMAL) were used in the present

investigation, and are based on the hydrogenic approach. That is, to approximate the initial-state and final state wave functions appropriate for the ionization process by Coulombic wave function, so that the theoretical situation becomes similar to that of the hydrogen atom (single inelastic scattering), for which the generalized oscillator strength (for a given energy and momentum) is known analytically. The only input required for the hydrogenic cross-section programmes (called SIGMAK AND SIGMAL) are the energy of the edge E_K, the energy window Δ, the accelerating voltage E_0, the scattering angle β and the atomic number Z.

Egerton's programmes used in the present work were corrected by a convergent factor F for semi-angle α (effects of a convergent focussed probe) were $\sigma(\Delta,\beta) = F.\sigma(\Delta,\beta)$[189]. Therefore the quantity N of a particular element contributing to the measured intensity in an inner-shell edge was obtained by the equation:

$$N = \frac{I(\Delta,\beta)}{F.\sigma(\Delta,\beta)}$$

One example of the results obtained on Cr/N ratio in Cr_2N (Fig 6.33) using the Egerton's programmes corrected by a convergence factor is given in Table A.1.

Table A.1 Results obtained on Cr/N ratio in CrN precipitate using EELS analysis

ELEMENT	EDGE WINDOW (eV) START	END	INTEGRAL I (counts)	σ PARTIAL CROSS-SECTION (cm^2/atoms)	CONVERGENCE FACTOR	No OF ATOMS	Cr/N RATIO
Cr	400	558.21	187,679	0.4495×10^{-20}	0.848	4.923×10^{25}	2.5
N	323	396.62	62,746	0.3948×10^{-20}	0.871	1.824×10^{25}	